CATASTROPHIC FAILURE OF LARGE STORAGE FACILITIES, CONTAINING CRYOGENIC FLUIDS

A Thesis submitted for the degree of

Doctor of Philosophy of the University of London

by

Ir. ROCHMADI SU

Department of Chemical Engineering and Chemical Technology

Imperial College of Science, Technology and Medicine

February 1991

ABSTRACT

The sudden release of cryogenic liquid resulting from Catastrophic Tank Failure (CTF) and its interaction with vertical bunds has been investigated theoretically. Once the tank wall has ruptured, the phenomenon of CTF itself is regarded as a collapse of a vertical, squat liquid column under its own weight. The resulting flow rushes to and collides with a vertical cylindrical bund, coaxial with the liquid column, and returns to the column axis as a strong hydraulic shock. If the bund is low, overflow occurs. The flow description is based on Shallow Water theory, and the governing equations are solved by the Method of Characteristics. Consistency of the results has been checked against the principle of mass and energy conservation.

In preparation, the first part of the work is concerned with re-investigation of non-boiling liquid release, which has already been examined theoretically and experimentally by several authors. The calculated energy loss at the shock agrees within 1 % with the energy discrepancy, defined as the calculated total energy content at any time level less the total theoretical initial energy content. The calculated amount of overflowing liquid also agrees within 1 % with the mass discrepancy (the calculated total mass less the total theoretical initial mass). The maximum shock height at the bund is equal to that estimated previously (Kleyn, 1983), but such work underestimated the amount of overflowing liquid. The results of this study also roughly agree with the experimental results (Greenspan and Johansson, 1981; Sharifi, 1987).

Cryogenic liquid release is described in the second part of the work. As cryogenic liquids boil vigorously on contact with the ground, the proposed model considers that the cryogenic liquid flow contains vapour, which

forms a two-phase layer on the ground surface. The two-phase layer thickness depends on: boiling rate, horizontal flow velocity, column height and diameter, physical properties of liquid and vapour, and the vapour motion in the flow. The flow region is divided into: non-boiling, density-change and vapour-release regions, with each region having its own governing equations. This work only gives general description of the two-phase, unconfined and confined flow. Further theoretical and experimental investigations are needed. The theoretically predicted propagation velocity of the moving front is around 1.7–1.83. Comparison with results for non-boiling liquid flow has shown that for cryogenic liquid flow, the shock height at the bund and the amount of overflowing liquid are higher than for non-boiling liquid flow. It is concluded that the model for non-boiling flow cannot be used to describe appropriately cryogenic liquid flow.

ACKNOWLEDGEMENTS

I would like to thank Dr. H.J. Michels for his supervision, invaluable guidance and assistance until the completion of this work. I am also very grateful to Dr. S.M. Richardson for advice and guidance, which greatly helped the progress of this work, and to Prof. G.F. Hewitt for the useful discussion on two-phase flow.

Finally, I wish to thank my sponsor, the Engineering Section of Inter University Center, Gadjah Mada University, for providing the scholarship.

CONTENTS

NOMENCLATURE 9

INTRODUCTION 14

CHAPTER 1: UNCONFINED FLOW OF NON-BOILING LIQUID 20

1.1 Introduction 20

1.2 Review of Previous Work 20

1.3 Derivation of Shallow Water Equations 26

1.4 Numerical Solution 30

1.4.1 Method of Characteristics (MOC) 30

1.4.2 The Numerical Calculation of The MOC 33

1.4.3 The Calculation Procedure 41

1.4.4 Selection of The Calculation Procedure 44

1.5 Results and Comparison 46

1.5.1 The Selected Calculation Procedure 46

1.5.2 Comparison with Other Theoretical Results 48

1.5.3 Comparison with The Experimental Results 52

CHAPTER 2: CONFINED FLOW OF NON-BOILING LIQUID 59

2.1 Introduction 59

2.2 Review of Previous Work 59

2.3 The Equations of Shock Conditions 68

2.4 Numerical Solution 71

2.4.1 The Shock Conditions 71

2.4.2 Conditions at The Bund 73
2.4.3 The Early Stage of Shock Formation 75
2.4.4 The Total Mass and Energy Content 77
2.5 Results and Comparison 78
2.5.1 The Initial Conditions 78
2.5.2 Bunds of Unlimited Height 79
2.5.3 Overflow 90
2.5.4 Comparison With The Experimental Results 97

CHAPTER 3: UNCONFINED FLOW OF CRYOGENIC LIQUIDS **102**

3.1 Introduction 102
3.2 Review of Related Work 103
3.3 Model To Be Proposed 112
3.3.1 Heat Sources 112
3.3.2 The Basic Idea: Theoretical Analysis 114
3.3.3 Mathematical Modelling 119
3.4 Numerical Solution 126
3.4.1 Non-boiling Region 127
3.4.2 Density-change Region 127
3.4.3 Vapour-release Region 132
3.4.4 The Initial Conditions 136
3.4.5 Aspects of the Numerical Solution 137
3.5 Results and Discussion 139
3.5.1 The Nature of Two-phase Layer 139
3.5.2 The Selected Procedure 144
3.5.3 The Flow Description 145

CHAPTER 4: CONFINED FLOW OF CRYOGENIC LIQUIDS **157**

4.1 Introduction 157

4.2 Theoretical Description of Shock Flow 158

4.2.1 Conditions at The Bund 160

4.2.2 The Shock Conditions 163

4.3 Numerical Solution 165

4.3.1 Conditions At The Bund 170

4.3.2 The Shock Conditions 173

4.3.3 The Initial Conditions 174

4.4 Results And Discussion 176

4.4.1 Vapour Concentration 176

4.4.2 Mass Discrepancy and Mass Evaporated 179

4.4.3 Bunds of Unlimited Height 183

4.4.4 Bunds of Limited Height 202

4.4.5 Summary 210

CHAPTER 5: CONCLUSIONS **216**

5.1 Introduction 216

5.2 Summary of Assumptions and The Model Description 216

5.3 Discussion of Results 219

5.3.1 Non-boiling Liquid Flow 219

5.3.2 Cryogenic Liquid Flow 222

5.4 Assessment of The Model 225

5.5 Suggestions For Further Work 227

REFERENCES **230**

APPENDIX A: NEWTON-RAPHSON METHOD **235**

APPENDIX B: NORMALISATION OF TIME REFERENCE **238**

1 Trbojevic and Slater's Work 238

2 Martin and Moyce's Work 239

3 Sharifi's Work 241

APPENDIX C **245**

APPENDIX D **257**

D.1 Boiling Rate of Cryogenic Liquid Spills on Land/Soil 257

D.1.1 The Nature of Cryogenic Liquid Boiling on Soil 258

D.1.2 Boiling in a Porous Bed 260

D.2 Stratified Flow Model 263

D.3 Additional Results 268

APPENDIX E **273**

APPENDIX F: The Effect of Vertical Position in Density-change Region on Unconfined and Confined Flows **287**

APPENDIX G: COMPUTER PROGRAMS **292**

NOMENCLATURE

A_n : coefficient of a polynomial or a power series

B_n : coefficient of a polynomial or a power series

C : - wave speed ($= \sqrt{gh}$)

- propagation velocity of sound in a gas

C_A : C at point A ($= C_{i,j+1}$)

C_b : C at the downstream of the shock interface

C_d : C of the bund height ($= \sqrt{gh_d}$)

C_f : C at the upstream of the shock interface

$C_{i,j}$: C at grid-point i and at time step j

C_0 : C of the initial column height ($= \sqrt{gH_0}$)

C_P : C at point P (at the positive characteristic line)

c_p : specific heat

C_Q : C at point Q (at the negative characteristic line)

C_S : C at point S (at the third characteristic line)

C_w : C at the bund

d_p : particle diameter

E_{discr} : energy discrepancy

E_f : a density ratio ($= (\rho_l/\rho_v - 1)$)

E_i : total energy of the upstream flow

E_k : energy content (potential + kinetic energy)

E_o : total energy of the downstream flow

F_{ov} : total volumetric overflow rate

F_{us} : total volumetric upstream flow rate

F_w : total hydrostatic force at the bund

$\mathbf{G_k}$: parameter in the density-change region

G_T : total superficial mass flow rate

g : acceleration of gravity

h : liquid height

h_b : downstream liquid height at the shock interface

h_d : bund height

h_f : upstream liquid height at the shock interface

h_{fg} : latent heat of vaporization

H_l : the enthalpy of liquid

H_0 : initial height of the column/tank

H_v : the enthalpy of vapour

i : grid-point position

j : time step

K : Chezy's resistance coefficient

k_s : thermal conductivity of soil

$\mathbf{K_v}$: parameter in the vapour-release region (in unconfined flow)

k_v : thermal conductivity of vapour

$\mathbf{K_{vb}}$: parameter in the density-increase region

$\mathbf{K_{vs}}$: parameter in the vapour-release region (in shock flow)

L_v : the length of vapour layer

M : ratio of C_b to C_f (in non-boiling liquid shock flow)

m : boiling rate of cryogenic liquid on land

M_c : ratio of C_b to C_f (in cryogenic liquid shock flow)

M_d : ratio of downstream to upstream density

M_{discr} : mass discrepancy

M_{evap} : total mass evaporated

M_{ovf} : total amount of the overflowing liquid

M_{tot} : total mass of the flow

M_{vb} : mass evaporated in the shock flow

M_{vu} : mass evaporated in the surge flow

p : pressure

PI : the term $\int \frac{UC}{r} dt$ in the positive Riemann invariant

P_i : initial impact pressure at the bund

p_0 : ambient pressure

P_w : hydrostatic pressure at the base of the bund

Q : total volumetric amount of the overflow liquid

q_c : convective heat flux

QI : the term $\int \frac{UC}{r} dt$ in the negative Riemann invariant

q_0 : heat flux from the ground

q_w : heat flux at the bund surface

r : radial position ($= i\Delta r$)

r_b : - backward boundary position

- bubble diameter (Azbel, 1981)

r_f : the moving front position (forward boundary)

r_i : position of grid-point i

r_{max} : the highest grid-point position in polynomial fitting

r_{min} : the lowest grid-point position in polynomial fitting

R_0 : initial radius of the column/tank

R_p : jet projection distance

r_P : position of point P (at the positive characteristic line)

r_Q : position of point Q (at the negative characteristic line)

r_S : position of point S (at the third characteristic line)

r_s : the shock position

r_{vr} : the vapour-release position

r_w : the bund position

T : temperature

t : time ($= j\Delta t$)

t_a : the time at which the axis begins to collapse

t_e : the time at which the overflow ends

t_i : the time at which the overflow begins

T_n : Chebychev polynomial term

U : horizontal velocity

U_A : U at point A ($= U_{i,j+1}$)

U_b : U at the downstream of the shock interface

U_f : U at the upstream of the shock interface

$U_{i,j}$: U at grid-point i and at time step j

U_0 : initial velocity of the column (= zero)

U_P : U at point P (at the positive characteristic line)

U_Q : U at point Q (at the negative characteristic line)

U_S : U at point S (at the third characteristic line)

U_s : the shock propagation velocity

U_v : the overflow velocity above the bund

U_{vs} : superficial vapour velocity

U_w : U at the bund

V : total volume of the flow

v : vertical velocity

V_{error} : volume error

v_T : rising velocity of bubbles

v_w : vertical velocity at the bund

X : a geometric polynomial term

x : - horizontal position (in Cartesian coordinates)

- vapour mass fraction

y : - vertical position (in Cartesian coordinates)

- liquid depth (Chan and Benerjee, 1981)

Z : a dimensionless variable (Greenspan and Butler, 1961)

z : axial/vertical position (in cylindrical-coordinates)

Note : symbols in boldface refer to dimensionless form.

Symbol in Greek letters :

α : - thermal diffusivity

- a constant in equation (4.2.1)

γ : ratio of specific heat

ϵ : vapour void fraction

η : dimensionless variable

λ : wavelength

μ : viscosity

ν : momentum diffusivity

ρ : density

ϱ : dimensionless density

ϕ : velocity potential (Penney and Thornhill, 1952)

σ : surface tension

τ : - shear stress

- dimensionless time in the initialization of shock flow

ζ : dimensionless variable in the shock flow

INTRODUCTION

Giant storage tanks on industrial production and terminal sites are a common sight today. Such storage tanks usually accommodate one of various liquids produced or needed by industries, especially liquid fuels. Accompanying the recent increasing world demand for the Liquefied Energy Gases, more LNG and LPG production, storage and transfer facilities have been built. Facilities storing in units of more than 3000 m^3 commonly use large vertical cylindrical tanks; the capacity of each tank can be up to 120,000 m^3.

Any release of the liquid contents from the storage facilities must be considered dangerous, whatever the scale of the release : slow but continuous (in case of a hole or pipe failure) or instantaneous, as a result of tank failure. To limit the arising danger, it is essential to contain any release or spill immediately, especially if the liquid is toxic, volatile or flammable. The common provision for containing any possible release is to surround the storage tanks with a dyke or bund, forming a reservoir. The capacity of the reservoir is traditionally equal to or a litle more than the capacity of storage tanks enclosed, with a safety factor up to 1.5.

However, experience has shown that such a containment facility still offers little protection against liquid release resulting from a Catastrophic Tank Failure (CTF), where the rate of release is a deciding factor. Sudden release of all the liquid contents has proved to result in a powerful radial dispersive surge, which is capable of destroying all but the strongest bund. As an illustration, LNG within a storage tank with a diameter of 50 m and a height of 30 m has potential energy of 3.7×10^6 kJ. Releasing such a huge amount of energy in seconds can obviously destroy many if not all

obstacles. Even with a very strong bund, some liquid will still flow over the bund, indicating the inadequacy of its height. Although this sort of release is quite rare, and the possibility of tank failure is reduced by the progressive improvement of tank design and application of stricter safety regulations, the possibilities of mechanical failures, natural disaster and recently the increasing risk of terrorist attack, leading to CTF, cannot be ignored. It is therefore important to design an effective bund that is capable of containing immediately and completely the worst possible release.

The Imperial College project on Catastrophic Tank Failure was set up with the object of designing such effective containment. The main programme of this project is to understand the resulting flow from CTF as well as its interaction with bunds, so that the requirements for containment of any possible release can be specified accurately. The project was set up along three lines, two of which have already been carried out. The first is theoretical investigation of CTF (Kleyn, 1983), which is considered as the phenomenon of liquid column collapse under its own weight. An idealized mathematical model was proposed to describe the surge flow resulting from the liquid column collapse and the shock flow resulting from the surge flow interaction with the bund. The consequences of inadequate bund height were also evaluated, such as the amount of liquid overflowing the bund and the maximum projection distance of overflow outside the impounding area. This work permitted preliminary recommendations on requirements for a complete containment. To complement this first line, the second examined CTF experimentally (Sharifi, 1987). The collapse of a liquid column was studied by using a small-scale vertical cylindrical water column on a horizontal surface (water-table). The flow was monitored by high-speed photographic and optico-electronic techniques. This experimen-

tal investigation highlighted some aspects which the theoretical one has not examined, such as geometric-scale effects. Such a physical model can also be used to investigate the flow behaviour in more complex conditions, such as liquid release from a slot or hole in a damaged tank wall and the effect of rectangular bunds on the surge flow, which cannot be evaluated easily by the theoretical approach.

The third line, which is the subject of this study, concerns a release of cryogenic liquid. Cryogenic liquids boil vigorously when they spill on the (warm) ground. This particular behaviour is considered to influence the surge flow resulting from the collapse of a cryogenic liquid column. The main objective of this study is, therefore, to describe theoretically the flow behaviour of a cryogenic liquid release, comprising the surge flow and its interaction with bunds.

There has been much previous work on cryogenic liquid spills on land and onto water, especially LNG spills, but surprisingly work on cryogenic release as a result of a CTF is not yet available. Irrespective of the initial size and shape of the spill source, previous work mainly provides estimates of the amount of liquid evaporated and of the size of a spill in a long spill period, as a precursor to the evaluation of vapour dispersion. This is clearly different from the objective of the current study.

Rupture of the tank shell may take place in two ways : vertical (longitudinal) cracking and horizontal or circular cracking along the tank base. These two modes may occur simultaneously. Some tank failure incidents have shown that the tank shell split vertically and was carried away from its original site by the resulting surge flow, or that the tank shell split horizontally at the base and was lifted upward and thrown away. In these cases, the shell cracking presumably propagated much faster than the liquid motion.

Therefore, once the tank shell failed, it became irrelevant to the motion of the liquid content, which allows it to be described as a vertical cylindrical liquid column starting to collapse. This sudden release of the whole liquid contents is regarded as an axisymmetric-flow problem. The other scenario of liquid release may occur when the tank shell ruptures vertically in such a way that liquid is released through a gap or hole in the shell. This case is regarded as an asymmetric-flow problem.

The asymmetric-flow problem is more complex in nature than the axisymmetric one, and solving theoretically such asymmetric flow problems obviously needs very extensive mathematical effort. Such problem is better investigated experimentally (physical model), as carried out by Sharifi.

The liquid column collapse and its resulting surge flow are essentially considered as an unsteady two-dimensional incompressible motion. As in flow problems generally, such motion can be described by solving the continuity and Navier-Stokes equations. Despite their complicated forms, these equations can be solved successfully by using numerical method. Hill et al. (1980) used the Marker and Cell (MAC) method in solving the dam-break problem, which is similar to liquid column collapse problem. Trbojevic and Slater (1989) used the modified-MAC method to simulate a CTF.

It is common practice to make some assumptions to simplify the problem, as long as such assumptions are acceptable. Some authors (Penney and Thornhill, 1952; Greenspan and Young, 1978; Kleyn, 1983) assumed that the surge flow is inviscid. The surge flow resulting from a small-scale water column collapse has a Reynolds number of the order 10^4. This justifies the inviscid flow assumption. It is considered furthermore that, if the column is squat, the horizontal acceleration dominates the flow, and the vertical acceleration is assumed negligible. These two assumptions greatly

simplify the equations, and lead to the so-called Shallow Water Equations (SWEs). The SWEs are unsteady one-dimensional hyperbolic partial differential equations, which can be conveniently solved by the Method of Characteristics (MOC). In reality, most vertical cylindrical storage tanks have a height to diameter ratio of not more than 1, and are thus squat columns. Therefore, the squat column assumption made is acceptable.

Although a model based on the SWEs may give an unrealistic description of the collapse motion at the early stage (Kleyn, 1983), it can generally give as good a flow description as that given by the MAC method. Furthermore, solution of the SWEs by the MOC is much simpler than the solution of the continuity and Navier-Stokes equations by the MAC method, and the computational effort and cost can thus be reduced. Based on this argument, this study will also use the SWEs to describe the surge flow as well as its interaction with bunds.

Most storage tanks are enclosed within a rectangular bunded area. However, like the asymmetric-flow problem mentioned previously, the surge flow interaction with such a rectangular bund is better investigated experimentally than theoretically. The previous theoretical work also simplified the bund configuration into a concentric circular-bund, with the tank at the centre. This study similarly limits its scope to axisymmetric releases within concentric circular bunds.

Although the main objective of this study is to describe cryogenic liquid release, it also re-investigates non-boiling liquid releases, which have already been theoretically examined by Kleyn (1983). The term "non-boiling" is used in this thesis, to distinguish it from cryogenic liquid which boils on contact with the ground. The results of this re-investigation are compared with those of previous theoretical and experimental work, to

assess the accuracy and consistency of the numerical solution as well as the validity of the model used. This is presented in Chapter 1 for unconfined flow (the surge flow) and in Chapter 2 for confined flow (the shock flow). Chapters 3 and 4 are concerned with the main objective of this study, i.e. descriptions of unconfined and confined cryogenic liquid flow. As there are no theoretical and experimental investigations on cryogenic liquid release available, Chapters 3 and 4 also include comparisons with non-boiling liquid releases. The overall conclusions are given in Chapter 5 together with suggestions for further work.

CHAPTER 1

UNCONFINED FLOW OF NON-BOILING LIQUID

1.1 Introduction

While the complete study is concerned with the liquid column collapse motion and the shock flow resulting from the interaction of the surge flow with bunds, this work on unconfined flow will cover the column collapse motion until the resulting surge flow reaches the bund. Such unconfined flow will be theoretically re-investigated in this chapter. This includes the numerical calculation procedures used in previous theoretical work, especially Kleyn's (1983). This work will use the Shallow Water Equations to describe the flow behaviour. Here, the flow description given by the SWEs will be examined, by comparing the results of this investigation with theoretical and experimental results previously obtained by other authors.

1.2 Review of Previous Work

Inspired by the collapse of a big vertical column of water droplets resulting from the atom bomb explosion test at Bikini Lagoon, Penney and Thornhill (1952) considered the dispersive flow following the collapse of such a column as an example of incompressible flow. They assumed that such flow is inviscid and unaffected by ground friction. They used two methods of solution, one of which is more relevant to this study. The first method employs a velocity potential ϕ as a dependent variable in polar coordinates (r, θ), where ϕ is a function of r, θ and time t. To solve the governing equations, the velocity potential ϕ was approximated by a series of trigonometric

functions (cosines), with the coefficients of the series being functions of time. The second method, which is more relevant to this study, is a special case of the solution, i.e. neglect of vertical acceleration in the motion. They considered that for a squat column, i.e. with a height smaller than a base diameter, the resulting surge flow is dominated by horizontal acceleration, and vertical acceleration may be neglected with respect to the horizontal one. As a result of neglecting vertical acceleration, the pressure p at any point in the liquid is equal to the static pressure, which depends only on the depth below the free surface, given by :

$$p = \rho g(h - z) \tag{1.2.1}$$

with ρ = liquid density ,

g = gravity acceleration constant,

h = liquid height, and

z = vertical distance from the basement/ground .

A further consequence of the assumption of negligible vertical acceleration is that any point equidistant from the axis of symmetry has equal horizontal or radial acceleration, regardless of its vertical position. This leads to the derivation of Shallow Water Equations (SWEs), which will be given in the next section. The collapse of a squat liquid column based on such a description is illustrated in Figure 1.1. The SWEs, as the governing equations in this case, are given by :

$$\begin{aligned} \frac{\partial h}{\partial t} + U\frac{\partial h}{\partial r} + h\frac{\partial U}{\partial r} + k\frac{Uh}{r} &= 0 \\ \frac{\partial U}{\partial t} + U\frac{\partial U}{\partial r} + g\frac{\partial h}{\partial r} &= 0 \end{aligned} \tag{1.2.2}$$

with U = horizontal velocity ,

r = horizontal/radial position, and

t = time.

Here, $k = 1$ if the flow is considered in axisymmetric-coordinates (the axisymmetric-model), and $k = 0$ if in cartesian-coordinate (the plane-model). Penney and Thornhill solved equations (1.2.2) numerically by the Method of Characteristics (MOC), but they did not give the calculation procedure in detail. They stated that the surge front has zero thickness and propagates at a speed of $U_{front} = 2\sqrt{gH_0}$, with H_0 being the initial height of the column. In dimensionless form $(U/\sqrt{gH_0})$, this velocity is equal to 2.

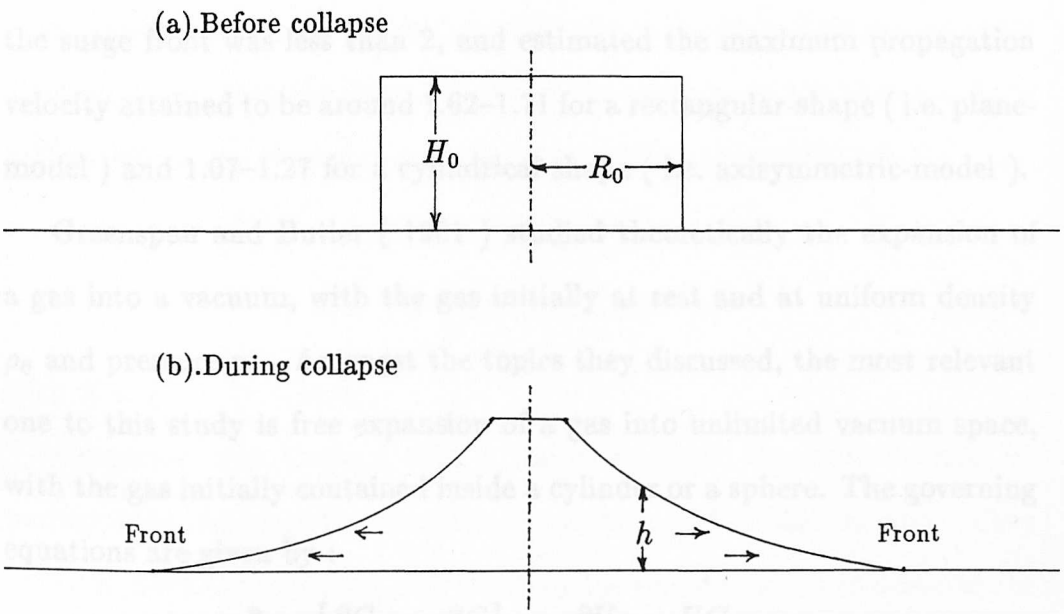


Figure 1.1: The process of liquid column collapse

In the plane-model case, equations (1.2.2) are similar to the governing equations of the dam-break problem. The analytical solution of this problem is known as Ritter's solution (Dressler,1952), given by :

$$\begin{aligned} U &= \tfrac{2}{3}\left(C_0 + (x/t)\right) \\ h &= \tfrac{1}{9}\left(2C_0 - (x/t)\right)^2/g \end{aligned} \qquad (1.2.3)$$

with x = horizontal distance from the initial position of the dam,

$C_0 = \sqrt{gH_0}$.

Concurrent with Penney and Thornhill's investigation, Martin and Moyce conducted an experiment of a liquid column collapse. They used a 5 inch-high water column, with several base sizes and column shapes : rectangular, semi-circular and cylindrical. The liquid was constrained by a very thin waxed paper diaphragm, with its edges glued with a thin layer of beeswax to a metal strip. A short passage of high electric current through this metal strip freed the waxed paper and thus allowed the liquid column to collapse. They observed that the experimental dimensionless propagation velocity of the surge front was less than 2, and estimated the maximum propagation velocity attained to be around 1.62–1.71 for a rectangular-shape (i.e. plane-model) and 1.07–1.27 for a cylindrical-shape (i.e. axisymmetric-model).

Greenspan and Butler (1961) studied theoretically the expansion of a gas into a vacuum, with the gas initially at rest and at uniform density ρ_0 and pressure p_0 . Amongst the topics they discussed, the most relevant one to this study is free expansion of a gas into unlimited vacuum space, with the gas initially contained inside a cylinder or a sphere. The governing equations are given by :

$$\begin{aligned} \frac{2}{(\gamma-1)}\left[\frac{\partial C}{\partial t}+U\frac{\partial C}{\partial r}\right]+C\frac{\partial U}{\partial r}+k\frac{UC}{r} &= 0 \\ \frac{\partial U}{\partial t}+U\frac{\partial U}{\partial r}+\frac{2C}{(\gamma-1)}\frac{\partial C}{\partial r} &= 0 \end{aligned} \qquad (1.2.4)$$

with U = velocity of the gas,

C = sound velocity in the gas $(= \rho^{\frac{(\gamma-1)}{2}})$,

γ = the ratio of specific heats.

For a cylinder, $k = 1$, and for a sphere, $k = 2$. Greenspan and Butler showed that the gas-vacuum interface propagates into vacuum space with a

dimensionless velocity of 2 and the gas density at this interface is considered to be zero, or $C = 0$. Note that equations (1.2.4) will be equivalent to equations (1.2.2), if $\gamma = 2$ and $C = \sqrt{gh}$ are substituted into equations (1.2.4). The cases are in fact analogous, and have the same front condition: zero thickness ($C = 0$) and $U = 2$. To solve equations (1.2.4), Greenspan and Butler used the Method of Characteristics (MOC) and a power series approximation. The power series are given by :

$$\begin{aligned} \phi = \; U + 2C = \; \sum_{i=0}^{n} A_i(\eta) t \\ \psi = \; U - 2C = \; \sum_{i=0}^{n} B_i(\eta) t \end{aligned} \tag{1.2.5}$$

where coefficients A_i and B_i are functions of $\eta = (r-1)/t$. This approximate solution depends on the degree of the power series n. In the case $\gamma = 2$, by taking only a first degree of t in the power series, the results are :

$$\begin{aligned} U &= 2 - 2Z + Zt(5Z^{0.5} - 3Z - 2) \\ C &= Z + \frac{1}{2} Zt(7Z^{0.5} - 3Z - 4) \end{aligned} \tag{1.2.6}$$

with $Z = \frac{1}{3}[2 - (r-1)/t]$.

Greenspan and Young (1978) also investigated theoretically and experimentally the surge flow resulting from the liquid column collapse. They used the SWEs in cartesian-coordinates (the plane-model) to describe the flow behaviour. However, their main objective was to assess the interaction of the surge flow with bunds and its consequences. Following Greenspan and Young's work, Kleyn (1983) examined the same problem in cylindrical polar coordinates (the axisymmetric-model) and compared the results between both models. In the case of the unconfined flow, Kleyn confirmed that the Greenspan and Butler approximate solution is only satisfactory in the early stage of the surge. Kleyn utilized equations (1.2.6) to set up the initial condition of the numerical solution of the axisymmetric-model.

Some authors have used the Marker and Cell method (MAC) to describe the motion of the liquid column collapse. Without neglecting the viscosity effect, the equation of continuity and the Navier-Stokes equation of motion (in unsteady two-dimensional form) are solved numerically, where their finite-difference equation forms are complicated. The MAC method essentially estimates the position and velocity of each element or *cell* of fluid at each time step. Reconstruction of all cell positions at a specific time will illustrate the profile of fluid flow. Hill et al. (1980) used this method to solve the dam-break problem, where following the breaking of a dam, the rushing liquid flows over the quiescent liquid which initially exists. This is a special case of the dam-break problem, as the liquid is initially at both sides of the dam (at different levels). Trbojevic and Slater (1989) recently used the modified MAC in cylindrical polar coordinates to simulate the flow resulting from Catastrophic Tank Failure, and also included flow over the bund.

In parallel with Kleyn's investigation, Sharifi (1987) carried out experiments, mostly on the unconfined flow. She showed that such investigation of the flow resulting from the Catastrophic Tank Failure can best be conducted by using a more realistic cylindrical model, instead of a rectangular/plane model or channel model (as in the dam-break problem) . Her relatively small-scale model, which has a very fast-moving lifting mechanism (around 20 milliseconds), was made from a cylindrical glass jacket with a diameter of 8.7 cm and a height of 10 cm. The glass jacket was initially filled with water, standing on a horizontal surface (water-table). The jacket was then pulled up very fast, leaving a water column standing freely on the table. Sharifi described that a short lifting-time was needed to ensure that the formation of a free vertical water column was not influ-

enced by the lifting mechanism itself, and that the process of the column collapse would only begin after the jacket has been lifted clear of the water column. Included in Sharifi's investigation was a scale-dependence factor, which the theoretical investigation did not account for. She drew attention to the obvious fact that, different from the theoretical investigation, the surge front is in practice blunt (i.e. has non-zero thickness), and that its dimensionless propagation velocity is 1.4 .

1.3 Derivation of Shallow Water Equations

The derivation of the Shallow Water Equations will be started from the basic equations of continuity and of motion. Figure 1.2 illustrates an element in the axisymmetric-coordinates to show the symbols used in the differential equations of unsteady incompressible flow in two-space variables r and z. These differential equations are given by (Bird et al. , 1966) :

* Equation of continuity ;

$$\frac{1}{r}\frac{\partial rU}{\partial r} + \frac{\partial v}{\partial z} = 0 \tag{1.3.1}$$

* Navier-Stokes equations ;

- for the r component,

$$\rho\frac{DU}{Dt} = -\frac{\partial p}{\partial r} - \left[\frac{1}{r}\frac{\partial r\tau_{rr}}{\partial r} + \frac{\partial \tau_{rz}}{\partial z}\right] \tag{1.3.2}$$

- and for the z component,

$$\rho\frac{Dv}{Dt} = -\frac{\partial p}{\partial z} - \rho|g| - \left[\frac{1}{r}\frac{\partial r\tau_{rz}}{\partial r} + \frac{\partial \tau_{zz}}{\partial z}\right] \tag{1.3.3}$$

with $\dfrac{D}{Dt} = \dfrac{\partial}{\partial t} + U\dfrac{\partial}{\partial r} + v\dfrac{\partial}{\partial z}$

and U = radial velocity (in this case, horizontal),

v = axial or z component velocity ,

τ = shear stress (tensor), with its direction indicated by its subscript.

Here, $|g|$ is in absolute value.

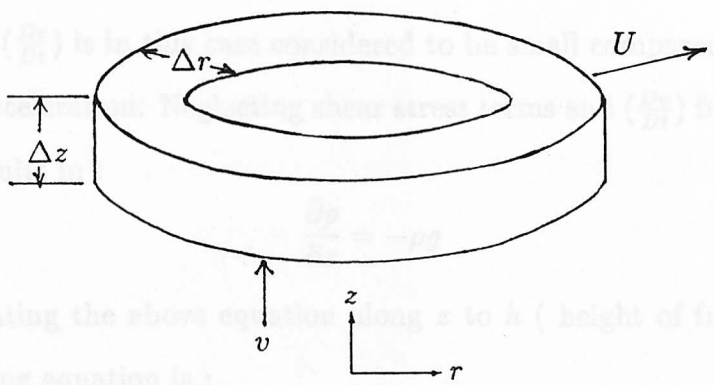


Figure 1.2: The element in axisymmetric-coordinate system

The shear stress terms in equations (1.3.2) and (1.3.3) represent the role of viscous-force on the momentum balance. This viscous effect is, of course, important in laminar flow. In turbulent flow, the viscous effect in the bulk flow may be neglected. In the surge flow following the column collapse, the flow is assumed to be inviscid. The collapse of a small water column with a diameter and a height of only 10 cm results in a surge flow (apart from the surge front) with a Reynolds number of the order of 10^4. This shows that the viscous effect on the surge flow can generally be neglected, and hence the inviscid flow assumption is justified. Fannelop and Waldman (1971) described how the early stages of an oil spill onto water are dominated by gravity and inertia forces, which is identical to inviscid flow. Brighton and Webber (1986) also gave a similar description in their investigation of a liquid spill on land. Their description supports the inviscid flow assumption,

as the period of unconfined flow concerned ranges from the beginning of the column collapse until the surge flow reaches the bund, which is equivalent to the early stage of a liquid spill on land described by Brighton and Webber.

In reality, vertical cylindrical storage tanks commonly have a height-diameter ratio equal to or less than 1, and are then referred to as squat columns. As previously assumed by Penney and Thornhill, the vertical acceleration ($\frac{Dv}{Dt}$) is in this case considered to be small compared with gravitational acceleration. Neglecting shear stress terms and ($\frac{Dv}{Dt}$) from equation (1.3.3) results in :

$$\frac{\partial p}{\partial z} = -\rho g$$

By integrating the above equation along z to h (height of free surface), the resulting equation is :

$$p_0 - p = -\rho g(h - z) \tag{1.3.4}$$

where p_0 is an ambient pressure. The r derivative of the above equation is given by :

$$\frac{\partial p}{\partial r} = \rho g \frac{\partial h}{\partial r} \tag{1.3.5}$$

If ground friction is considered, integration of equation (1.3.2) along z results in :

$$\frac{DU}{Dt} = -\frac{1}{\rho}\frac{\partial p}{\partial r} - \frac{\tau_0}{h} \tag{1.3.6}$$

where τ_0 is the ground resistance stress.

Dressler (1952) and Whitham (1954) employed the Chézy equation to express ground resistance stress. Here, equation (1.3.6) becomes :

$$\frac{DU}{Dt} = -\frac{1}{\rho}\frac{\partial p}{\partial r} - \frac{KU^2}{h} \tag{1.3.7}$$

where K is Chézy's resistance coefficient, which depends on the roughness of the ground surface. Dressler showed that for $K \leq 10^{-6}$, ground resistance

hardly affects the flow. The resistance effect is particularly pronounced at the moving front region. Based on this fact, Greenspan and Young (1978) argued that the error incurred by neglecting ground resistance effect in the early stages of a spill is still acceptable. By assuming the ground surface to be frictionless, equation (1.3.7) becomes :

$$\frac{DU}{Dt} = -g\frac{\partial h}{\partial r} \tag{1.3.8}$$

As shown in the above equation, using liquid height h is more relevant than using vertical velocity v. Integrating equation (1.3.1) along h will result in :

$$\begin{aligned} \int_0^h \left(\frac{1}{r}\frac{\partial rU}{\partial r}\right) + \int_{v_0}^{v_h} dv &= 0 \\ \frac{h}{r}\frac{\partial rU}{\partial r} + v_h - v_0 &= 0 \end{aligned} \tag{1.3.9}$$

The boundary conditions at $z = 0$ and $z = h$ are given by :

$$v = \frac{Dh}{Dt} \quad \text{and} \quad v = 0\,, \quad \text{respectively.}$$

Substituting these boundary conditions into equation (1.3.9) results in :

$$\frac{Dh}{Dt} + h\frac{\partial U}{\partial r} + \frac{hU}{r} = 0 \tag{1.3.10}$$

The Shallow Water Equations mentioned are given by equations (1.3.8) and (1.3.10). The general form of the SWEs is :

$$\begin{aligned} 2\frac{\partial C}{\partial t} + 2U\frac{\partial C}{\partial r} + C\frac{\partial U}{\partial r} + k\frac{UC}{r} &= 0 \\ \frac{\partial U}{\partial t} + U\frac{\partial U}{\partial r} + 2C\frac{\partial C}{\partial r} &= 0 \end{aligned} \tag{1.3.11}$$

with $C = \sqrt{gh}$. In the Shallow Water theory, C is the propagation speed of a surface wave. For $k = 0$, the SWEs are in cartesian coordinates (plane-model), and for $k = 1$ in cylindrical coordinates (axisymmetric-model).

1.4 Numerical Solution

1.4.1 Method of Characteristics (MOC)

Shallow Water Equations (1.3.11) are hyperbolic partial differential equations, which can be solved by several methods (Smith,1977). Amongst these methods, the Method of Characteristics is the most appropriate one (Abbott,1966).

Leaf et al. (1979) confirmed that the Method of Characteristics (MOC) has the best accuracy amongst all methods they have examined. They solved a water-hammer problem (hyperbolic differential equations of transient flow, resulting from a sudden closing of a valve) by several methods : finite-difference method of Lax, Lax-Wendroff (two-step), finite-element method using a Galerkin procedure, and the Method of Characteristics. They concluded that two-step Lax-Wendroff method and the MOC give the best accuracy.

The Method of Characteristics is based on two principles :

- the *entity*, or specific correlation of dependent variables, and
- the *path* or *track*, along which the entity propagates.

The path itself is called a characteristic line or curve.
The following is the basic solution of the SWEs by the MOC. Summing up and subtracting two equations in (1.3.11) results in :

$$(U \pm C)\frac{\partial(U \pm 2C)}{\partial r} + \frac{\partial(U \pm 2C)}{\partial t} = \mp\frac{UC}{r} \qquad (1.4.1)$$

This equation shows that $(U \pm 2C)$ are dependent variables or entities, which are functions of r and t. Their total derivative is given by :

$$d(U \pm 2C) = \frac{\partial(U \pm 2C)}{\partial r}\,dr + \frac{\partial(U \pm 2C)}{\partial t}\,dt \quad ,$$

and this equation can be transformed into the form :

$$\frac{dr}{dt}\frac{\partial(U \pm 2C)}{\partial r} + \frac{\partial(U \pm 2C)}{\partial t} = \frac{d(U \pm 2C)}{dt} \qquad (1.4.2)$$

Comparison of equations (1.4.1) and (1.4.2) shows that entities $(U \pm 2C)$ move along their path with a velocity of :

$$\left.\frac{dr}{dt}\right|_{\pm} = U \pm C \quad ,$$

with their rate of change given by :

$$\frac{d(U \pm 2C)}{dt} = \mp\frac{UC}{r} \quad .$$

Briefly, there are two characteristic lines with their corresponding entity correlations : *positive* and *negative*. The positive characteristic line has a slope of :

$$\left.\frac{dr}{dt}\right|_{+} = U + C \qquad (1.4.3)$$

where along this positive characteristic line, the rate of change of $(U + 2C)$ is given by :

$$\frac{d(U + 2C)}{dt} = -\frac{UC}{r} \qquad (1.4.4)$$

and its general correlation :

$$U + 2C + \int \frac{UC}{r}\,dt = \text{constant} \qquad (1.4.5)$$

Equation (1.4.5) is called the positive Riemann invariant (Abbott,1966). Similarly, along the negative characteristic line,there are :

* a slope of :

$$\left.\frac{dr}{dt}\right|_{-} = U - C \qquad (1.4.6)$$

* and a negative Riemann invariant :

$$U - 2C - \int \frac{UC}{r}\,dt = \text{constant} \qquad (1.4.7)$$

The RHS of equations (1.4.5) and (1.4.7) are constants or parameters. This means that there are two families of characteristic lines in this solution, as illustrated in Figure 1.3. The flow region is bounded by two moving boundaries, which are also members of characteristic lines. They are the forward moving boundary, sometimes called forward moving front or edge, and the inward moving boundary, which moves toward the axis. As shown in Figure 1.3 , the flow region begins at $t = 0$ and $r = R_0$, which is the original position of a tank wall. Furthermore, all negative characteristic lines start from this point as well. This phenomenon shows that the disturbance is dispersed over the whole flow region. In this case, the disturbance is the initial liquid column profile (a step function).

As in the problem of the expansion of a gas into vacuum (Greenspan and Butler, 1961), the horizontal velocity $U = 0$ and C is equal to $C_0 = \sqrt{gH_0}$ at the inward moving boundary. This boundary line is in fact the negative characteristic line with a propagation velocity of $\frac{dr}{dt} = C_0$. This boundary line is then given by :

$$r_b = R_0 - C_0 t \tag{1.4.8}$$

This equation is only valid until it reaches the axis at $t = (R_0/C_0)$, when the axis begins to collapse.

As shown in Figure 1.3, the positive characteristic lines start from the inward boundary line. Because $U_0 = 0$ and $C = C_0$ at the inward boundary line, the value of the positive Riemann invariants are $2C_0$, as can be derived from equation (1.4.4) :

$$U + 2C + \int \frac{UC}{r}\, dt = U_0 + 2C_0 = 2C_0 \quad .$$

At the forward moving boundary, the thickness or height of the front is zero (Saint Venant solution), analogous to the gas- vacuum interface, where the gas density is zero or $C = 0$. Hence, the front velocity can be determined

by the above equation :

$$U_{front} + 2C_{front} + \int \frac{UC}{r}\, dt = 2C_0 \qquad \text{or} \qquad U_{front} = 2C_0 \quad .$$

This means that the front propagates with a constant velocity. The forward moving boundary is then given by :

$$\frac{dr}{dt} = 2C_0 \qquad \text{or} \qquad r_f = R_0 + 2C_0 t \tag{1.4.9}$$

1.4.2 The Numerical Calculation of The MOC

As the solution of the SWEs by the MOC is based on the characteristic lines and Riemann invariants (positive and negative), the condition at any point always depends on these characteristic lines and the correlations of Riemann invariants. Figure 1.4 illustrates the principle of the MOC solution, how to determine the condition at any point along a characteristic line. To simplify the illustration, two families of characteristic lines (positive and negative) are drawn arbitrarily. It is assumed that the condition at points A to E are known. The condition at point P depends on the conditions at points A and B. Along the positive characteristic line AP, $(U_P + 2C_P)$ is correlated to $(U_A + 2C_A)$ in Riemann invariant given by equation (1.4.5). Similarly, along the negative characteristic line BP, $(U_P - 2C_P)$ is correlated to $(U_B - 2C_B)$ in equation (1.4.7). Because the values of U and C at points A and B are known, U and C can be calculated from the two Riemann invariant correlations along AP and BP. The conditions at other points (Q, R and S) can be calculated in a similar way to those at point P, as can points U, V and W.

As commonly carried out in numerical solutions, the SWEs are also solved numerically by using uniform increments Δr and Δt. The method illustrated in Figure 1.4 cannot ensure the uniformity of Δr and Δt. Instead

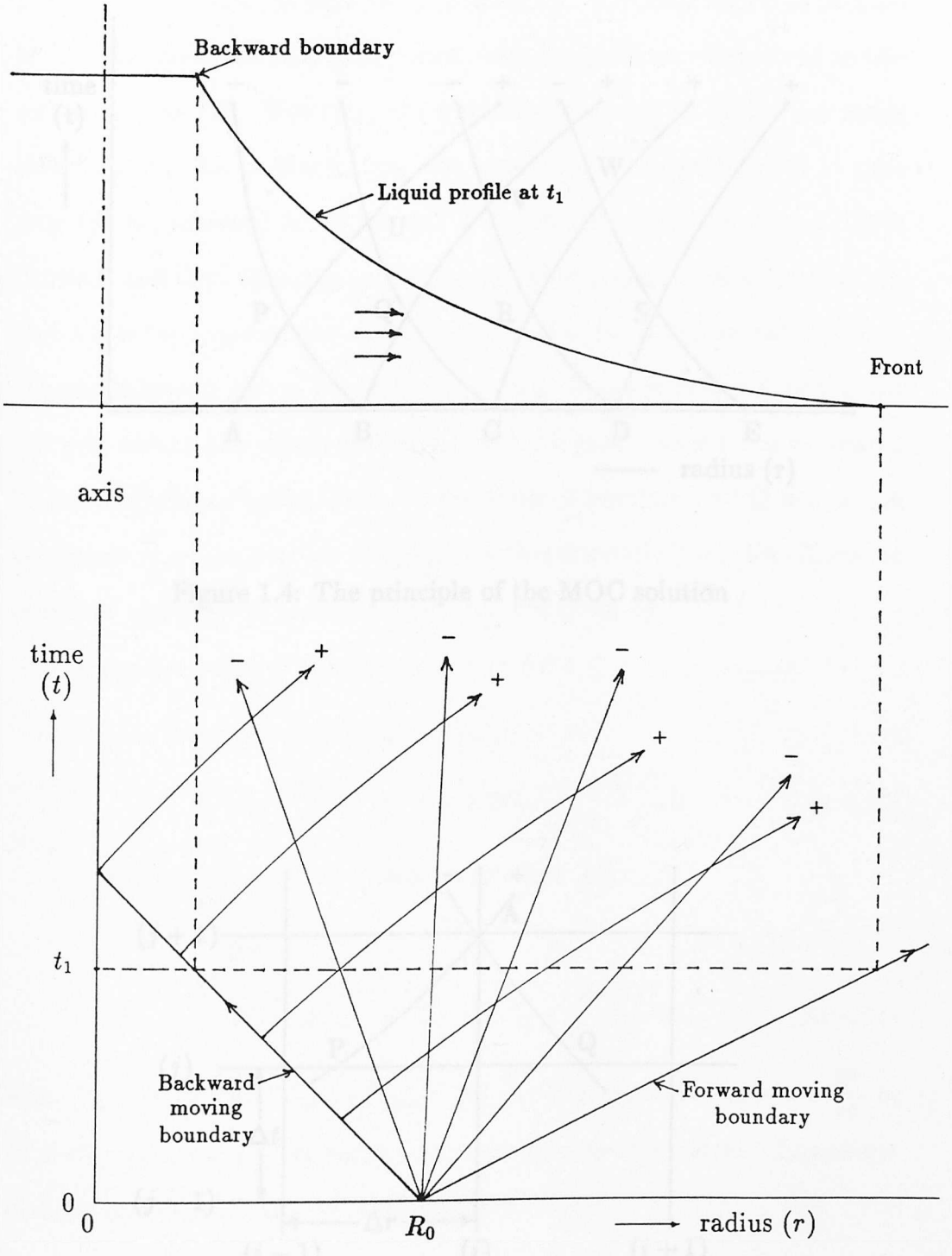


Figure 1.3: Two families of characteristic lines

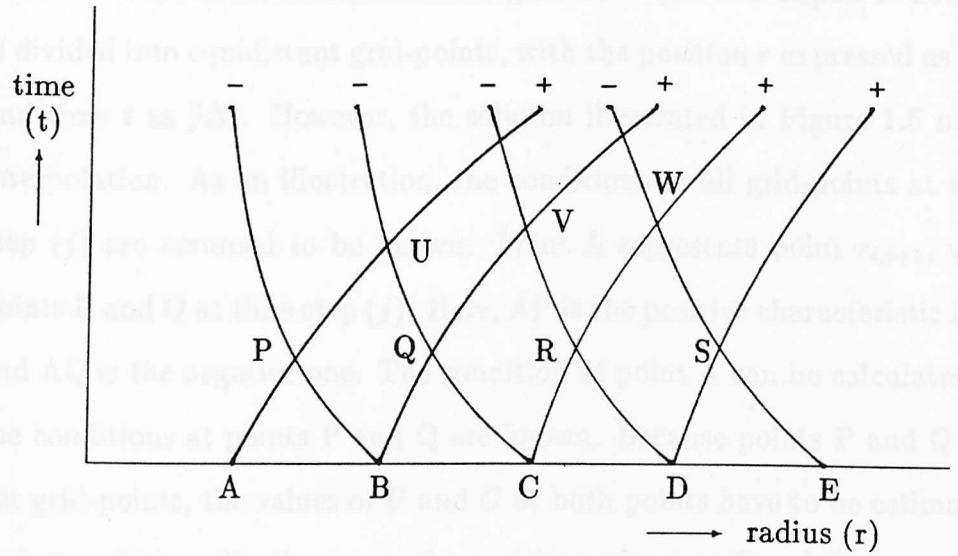


Figure 1.4: The principle of the MOC solution

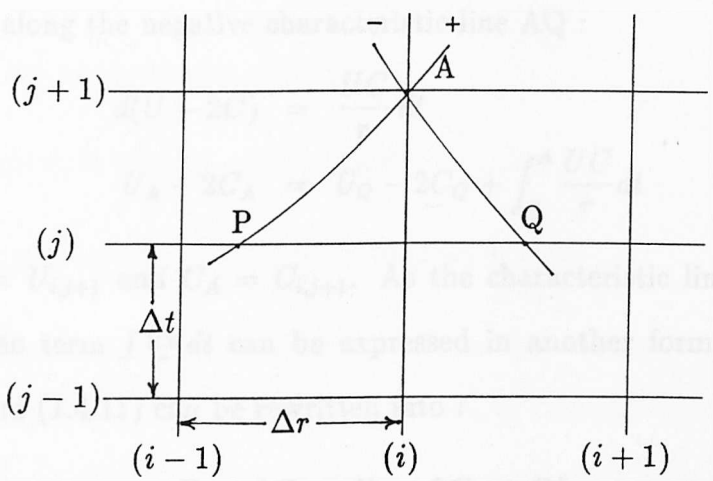


Figure 1.5: Three-point method : A , P and Q

of that illustrated in Figure 1.4, grid-points (mesh or node) with uniform Δr and Δt are used, as depicted in Figure 1.5 . The flow region or domain is divided into equidistant grid-points, with the position r expressed as $i\Delta r$ and time t as $j\Delta t$. However, the solution illustrated in Figure 1.5 needs interpolation. As an illustration, the conditions at all grid-points at time step (j) are assumed to be known. Point A represents point $r_{i,j+1}$, with points P and Q at time step (j). Here, AP is the positive characteristic line, and AQ is the negative one. The condition at point A can be calculated, if the conditions at points P and Q are known. Because points P and Q are not grid-points, the values of U and C at both points have to be estimated by interpolation. Furthermore, the positions of points P and Q depend on the slopes $\frac{dr}{dt}$ of the positive and negative characteristic lines. The Riemann invariant correlations at line AP and AQ are given by :

* along the positive characteristic line AP :

$$\begin{aligned} d(U+2C) &= -\frac{UC}{r}\,dt \\ U_A + 2C_A &= U_P + 2C_P - \int_P^A \frac{UC}{r}dt \end{aligned} \qquad (1.4.10)$$

* and along the negative characteristic line AQ :

$$\begin{aligned} d(U-2C) &= \frac{UC}{r}\,dt \\ U_A - 2C_A &= U_Q - 2C_Q + \int_Q^A \frac{UC}{r}dt \end{aligned} \qquad (1.4.11)$$

with $U_A = U_{i,j+1}$ and $C_A = C_{i,j+1}$. As the characteristic lines are $\frac{dr}{dt} = U \pm C$, the term $\int \frac{UC}{r}dt$ can be expressed in another form. Equations (1.4.10) and (1.4.11) can be rewritten into :

$$U_A + 2C_A = U_P + 2C_P + PI \qquad (1.4.12)$$

with $PI = -\int_P^A \frac{UC}{r}\,dt$ (1.4.12-A),

or $PI = -\int_P^A \frac{UC}{r(U+C)}\,dr$ (1.4.12-B),

and

$$U_A - 2C_A = U_Q - 2C_Q - QI \qquad (1.4.13)$$

with $$QI = -\int_Q^A \frac{UC}{r}\,dt \qquad (1.4.13\text{-A}),$$

or $$QI = -\int_Q^A \frac{UC}{r(U+C)}\,dr \qquad (1.4.13\text{-B}).$$

The values of U and C at point A are then evaluated by solving equations (1.4.12) and (1.4.13) simultaneously, and given by :

$$\begin{aligned} U_A &= \frac{1}{2}(U_P + U_Q + 2C_P + 2C_Q + PI - QI) \\ C_A &= \frac{1}{4}(U_P - U_Q - 2C_P + 2C_Q + PI + QI) \end{aligned} \qquad (1.4.14)$$

These equations clearly show that U and C at point A are determined by iteration, because the position of points P and Q depend on the slopes of lines AP and AQ, and the values of U and C at both points are calculated by interpolation. This method of calculation is called a three-point method (Abbott,1979), because it involves three points A, P and Q. Greenspan and Young(1978), and Kleyn (1983) employed this method in their numerical solution. The accuracy of this method relies on :

- the size of increments Δr and Δt,
- the method of interpolation, and
- the estimate of the slope of characteristic line.

Using finer or smaller increments will increase the accuracy, but this will need more computational effort(computer memory and cost). The usual way is to use a compromise size of increment, that is a moderate size, compensated by iteration (implicit method), to improve the accuracy. The selection of the increment size also has to consider the Courant-Friedriech-Lewy criterion (CFL). This criterion essentially describes the behaviour of

a numerical solution of a differential equation, which depends on the increment size, in relation with its actual solution. To ensure that the numerical solution converges to the actual solution, the CFL criterion must be fulfilled. For the SWEs solution, the CFL criterion is given by (Smith,1977; Abbott,1979) :

$$\frac{\Delta t|U+C|}{\Delta r} \leq 1 \tag{1.4.15}$$

This criterion gives a restriction on the magnitude of Δt to be used with respect to the magnitude of Δr, or vice versa.

The profile of the values of U and C at successive grid points dictates the method of interpolation. If the increment is small or U and C vary linearly with the position, linear interpolation is sufficient. Greenspan and Young used linear interpolation (together with iteration), but they did not mention their accuracy. Kleyn used a Chebychev polynomial as a way of interpolation. To improve the accuracy and convergence of the numerical solution, Abbott(1979) suggested that better interpolation method and slope approximation will both have to be used. For example, the positive and negative characteristic slopes are better estimated by using the conditions at two points than at one point only. Greenspan and Young, and later Kleyn, took the average value of the slope between time steps j and $(j+1)$. The approximate slope of the positive characteristic line AP is then given by :

$$\left.\frac{dr}{dt}\right|_{+} = \frac{1}{2}(U_A + C_A + U_P + C_P) \tag{1.4.16}$$

Likewise, the approximate slope of the negative characteristic line AQ is given by :

$$\left.\frac{dr}{dt}\right|_{-} = \frac{1}{2}(U_A - C_A + U_Q - C_Q) \tag{1.4.17}$$

Kleyn called this method a *three-point second-order* method.

Following this previous work, the current study uses a three-point second order method. It also re-investigates the interpolation method and the method of PI and QI evaluation, as described in equations (1.4.12) and (1.4.13). The interpolation is performed by using a polynomial fitting. Two forms of polynomial fitting are examined. These are :

1. A simple polynomial :

$$U = A_0 + A_1 X + A_2 X^2 + \cdots + A_n X^n \tag{1.4.18}$$

with A_n = coefficients (to be evaluated),

$X = (2r - r_{max} - r_{min})/(r_{max} - r_{min})$.

The X value should be between -1 and +1 , to satisfy the validity of this polynomial fitting.

2. A Chebychev polynomial (Carnahan *et al.* ,1969):

$$U = A_0 + A_1 T_1(X) + A_2 T_2(X) + \cdots + A_n T_n(X) \tag{1.4.19}$$

with X defined as in 1), and

$T_1(X) = X$,

$T_2(X) = 2X - 1$,

$\vdots$

$T_n(X) = 2X T_{n-1}(X) - T_{n-2}(X)$.

A simple polynomial fitting is tried, because it is simpler to use than Chebychev polynomial. The interpolation is carrried out in two ways. These are :

- Using *all nodes* inside the inward-forward boundary lines and presenting them into one polynomial equation. Hence, at each time step, there is only one polynomial fitting.
- Using *4 - 6 nodes* surrounding the point to be calculated (2 in front, and the others behind) and fitting them into one polynomial equation. In this case, each iterated point has a polynomial fitting.

The terms PI and QI in equations (1.4.12) and (1.4.13) are also evaluated in two ways, i.e. :

- By numerical integration of equations (1.4.12-B) and (1.4.13-B) using the trapezoidal rule, as carried out by Kleyn. Here, U and C are interpolated at time step j.

- By arithmetic averaging equations (1.4.12-A) and (1.4.13-A), in the forms :

$$\begin{aligned} PI &= -\left[\frac{U_A C_A}{r_A} + \frac{U_P C_P}{r_P}\right]\frac{\Delta t}{2} \\ QI &= -\left[\frac{U_A C_A}{r_A} + \frac{U_Q C_Q}{r_Q}\right]\frac{\Delta t}{2} \end{aligned} \tag{1.4.20}$$

The liquid at the axis starts to collapse, when the inward moving boundary has reached the axis. Because the horizontal velocity U at the axis is always zero, only C is to be calculated, by using equation (1.4.13). In this case, $U_A = 0$. By using the negative characteristic line passing through $r = 0$, r_Q can be estimated as :

$$r_Q = -(U_Q - C_Q - C_A)\frac{\Delta t}{2} \tag{1.4.21}$$

However, the term $\frac{U_A C_A}{r_A}$ (in QI) at the axis cannot be evaluated directly, because $r_A = 0$. This term is then estimated by employing the l'Hospital rule :

$$\lim_{r\to 0}\frac{U}{r} = \frac{\partial U}{\partial r} \qquad \text{, so :} \qquad \frac{UC}{r} = C\frac{\partial U}{\partial r}$$

Incorporating the above correlation into equation (1.3.11) results in :

$$2\left(\frac{\partial C}{\partial t} + \overbrace{U\frac{\partial C}{\partial r}}^{U=0}\right) + C\frac{\partial U}{\partial r} = -\frac{UC}{r}$$

$$\text{hence} \qquad \frac{UC}{r} = \frac{\partial C}{\partial t} \tag{1.4.22}$$

In numerical solution, this equation is approximated by using :

$$\left.\frac{UC}{r}\right|_{r=0} \approx \frac{(C_{0,j+1} - C_{0,j})}{\Delta t} \tag{1.4.23}$$

where $C_{0,j}$ and $C_{0,j+1}$ are values of C at the axis at time steps j and $(j+1)$.

1.4.3 The Calculation Procedure

In order to obtain the generalized results, all variables involved are expressed in dimensionless form. These are :

$$\mathbf{U} = \frac{U}{C_0}, \mathbf{C} = \frac{C}{C_0}, \mathbf{r} = \frac{r}{R_0}, \mathbf{h} = \frac{h}{H_0}, \mathbf{t} = \frac{tC_0}{R_0}.$$

Hence, the dimensionless velocity of the moving front is 2 , and the dimensionless initial column height and radius are both equal to 1.

To start the calculation, the initial condition is needed. For the plane-model, Ritter's solution in equations (1.2.2) is used to set up the initial conditions. For the axisymmetric-model, the initial condition is set up by using equation (1.2.6). The initial condition is set up at small time after the column begins to collapse.

As mentioned before, the determination of **U** and **C** at each grid point at time step $(j+1)$ is essentially an iterative calculation. Equations (1.4.14) together with the determinations of P and Q positions ($\mathbf{r}_P$ and $\mathbf{r}_Q$) are evaluated simultaneously. Here, the positions $\mathbf{r}_P$ and $\mathbf{r}_Q$ are estimated from equations (1.4.16) and (1.4.17) :

$$\mathbf{r}_P = \mathbf{r}_i - (\mathbf{U}_P + \mathbf{C}_P + \mathbf{U}_A + \mathbf{C}_A)\frac{\Delta \mathbf{t}}{2} \tag{1.4.24}$$

$$\mathbf{r}_Q = \mathbf{r}_i - (\mathbf{U}_Q - \mathbf{C}_Q + \mathbf{U}_A - \mathbf{C}_A)\frac{\Delta \mathbf{t}}{2} \tag{1.4.25}$$

Because this iteration involves several unknown variables ($\mathbf{r}_P, \mathbf{r}_Q, \mathbf{U}_Aand\mathbf{C}_A$), the iteration is conveniently performed by using the Newton-Raphson method

(described in Appendix A). The above equations are regarded as two functions $F_1(\mathbf{r}_P, \mathbf{r}_Q)$ and $F_2(\mathbf{r}_P, \mathbf{r}_Q)$, i.e. :

$$\begin{aligned} F_1(\mathbf{r}_P, \mathbf{r}_Q) &= \mathbf{r}_i - (\mathbf{U}_P + \mathbf{C}_P + \mathbf{U}_A + \mathbf{C}_A)\frac{\Delta \mathbf{t}}{2} - \mathbf{r}_P \\ F_2(\mathbf{r}_P, \mathbf{r}_Q) &= \mathbf{r}_i - (\mathbf{U}_Q - \mathbf{C}_Q + \mathbf{U}_A - \mathbf{C}_A)\frac{\Delta \mathbf{t}}{2} - \mathbf{r}_Q \end{aligned} \qquad (1.4.26)$$

The iteration procedure is performed as follows :

1. At grid point $\mathbf{r}_{i,j+1}$, the positions of P and Q are initially estimated by :

$$\begin{aligned} \mathbf{r}_P &= \mathbf{r}_i - (\mathbf{U}_{i,j} + \mathbf{C}_{i,j})\Delta \mathbf{t} \\ \mathbf{r}_Q &= \mathbf{r}_i - (\mathbf{U}_{i,j} - \mathbf{C}_{i,j})\Delta \mathbf{t} \end{aligned} \qquad (1.4.27)$$

2. For a given $\mathbf{r}_P$ and $\mathbf{r}_Q$, values of $\mathbf{U}_P, \mathbf{C}_P, \mathbf{U}_Q$ and $\mathbf{C}_Q$ are evaluated by interpolation.

3. $\mathbf{U}_A$ and $\mathbf{C}_A$ are calculated by using equations (1.4.14).

4. F_1 and F_2 in equations (1.4.26) are calculated. If absolute values $|F_1|$ and $|F_2|$ are both less or equal than ϵ (a very small number, namely 10^{-6}), then the iteration is regarded as successfull, and calculation is continued for next grid point.

5. If one or both values of $|F_1|$ and $|F_2|$ are greater than ϵ (i.e. $|F_1|,|F_2| > \epsilon$), new $\mathbf{r}_P$ and $\mathbf{r}_Q$ are estimated by using :

$$\begin{aligned} \mathbf{r}_P^{n+1} &= \mathbf{r}_P^n - \frac{\left[F_1 \frac{\partial F_2}{\partial \mathbf{r}_P} - F_2 \frac{\partial F_1}{\partial \mathbf{r}_Q}\right]}{\left[\frac{\partial F_1}{\partial \mathbf{r}_P}\frac{\partial F_2}{\partial \mathbf{r}_Q} - \frac{\partial F_1}{\partial \mathbf{r}_Q}\frac{\partial F_2}{\partial \mathbf{r}_P}\right]} \\ \mathbf{r}_Q^{n+1} &= \mathbf{r}_Q^n + \frac{\left[F_1 \frac{\partial F_2}{\partial \mathbf{r}_Q} - F_2 \frac{\partial F_1}{\partial \mathbf{r}_P}\right]}{\left[\frac{\partial F_1}{\partial \mathbf{r}_P}\frac{\partial F_2}{\partial \mathbf{r}_Q} - \frac{\partial F_1}{\partial \mathbf{r}_Q}\frac{\partial F_2}{\partial \mathbf{r}_P}\right]} \end{aligned} \qquad (1.4.28)$$

with n = iteration step. These equations are described in Appendix A. The calculation operation is then repeated from step 2) onwards.

The flow diagram of this procedure is shown in Figure 1.6 .

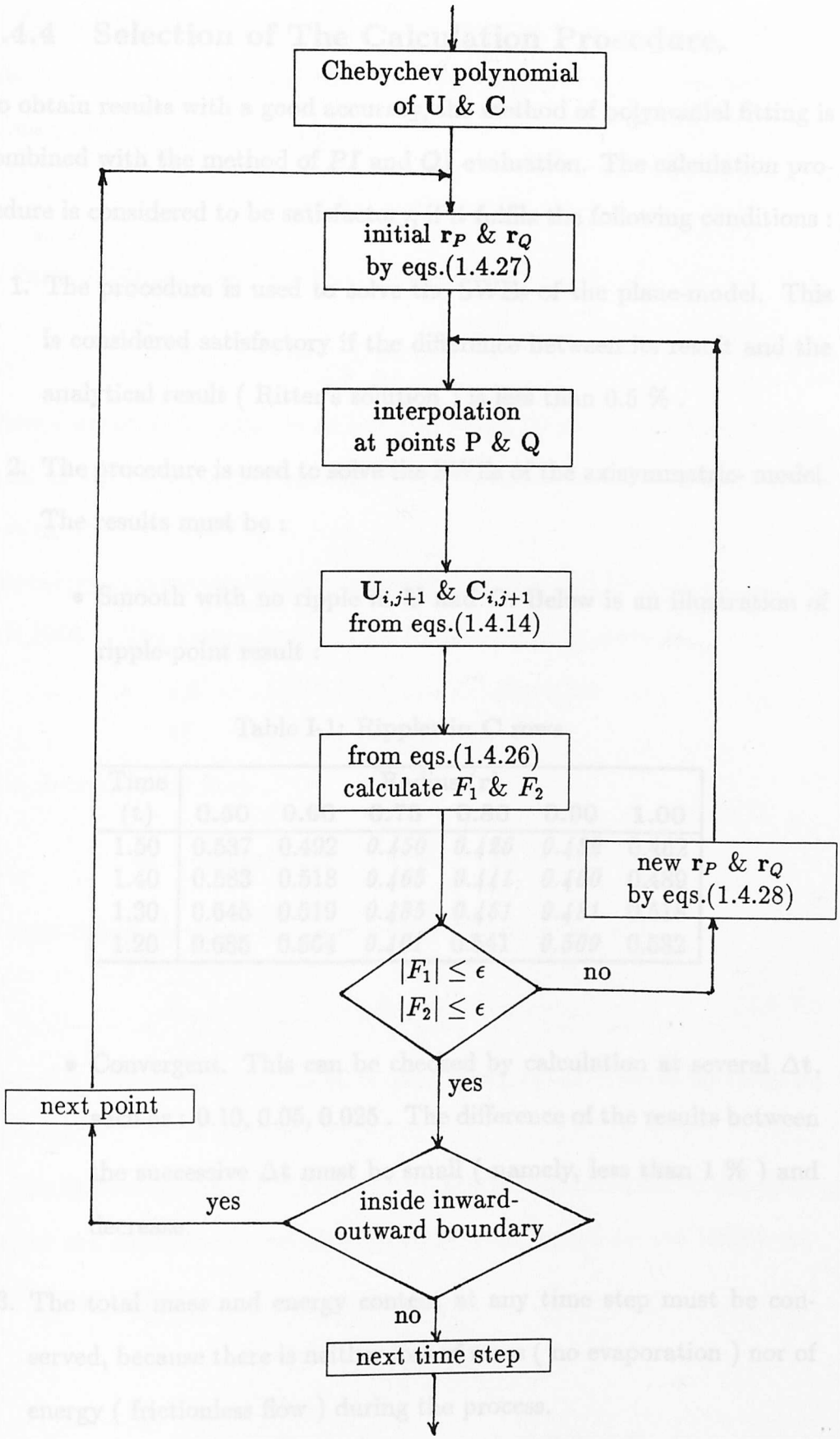


Figure 1.6: Flow diagram of the iteration procedure

1.4.4 Selection of The Calculation Procedure.

To obtain results with a good accuracy, the method of polynomial fitting is combined with the method of PI and QI evaluation. The calculation procedure is considered to be satisfactory, if it fulfils the following conditions :

1. The procedure is used to solve the SWEs of the plane-model. This is considered satisfactory if the difference between its result and the analytical result (Ritter's solution) is less than 0.5 % .

2. The procedure is used to solve the SWEs of the axisymmetric- model. The results must be :

   - Smooth with no ripple in **U** and **C**. Below is an illustration of ripple-point result :

Table I-1: Ripples in **C** rows

Time	Radius (**r**)					
(**t**)	**0.50**	**0.60**	**0.70**	**0.80**	**0.90**	**1.00**
1.50	0.537	0.492	*0.450*	*0.426*	*0.432*	0.462
1.40	0.583	0.518	*0.465*	*0.441*	*0.460*	0.489
1.30	0.645	0.519	*0.485*	*0.461*	*0.481*	0.518
1.20	0.685	0.664	*0.401*	0.541	*0.509*	0.532

   - Convergent. This can be checked by calculation at several Δ**t**, such as : 0.10, 0.05, 0.025 . The difference of the results between the successive Δ**t** must be small (namely, less than 1 %) and decrease.

3. The total mass and energy content at any time step must be conserved, because there is neither loss of mass (no evaporation) nor of energy (frictionless flow) during the process.

Total mass and energy content are calculated numerically. Because the liquid is incompressible, the total volume must remain constant. The volume of a small element is given by :

$$dV = 2\pi r h\, dr \quad .$$

In finite-difference form, the total volume is given by :

$$V = 2\pi \sum_{i=0}^{n-1} (r_i h_i + r_{i+1} h_{i+1}) \frac{\Delta r}{2} \qquad (1.4.29)$$

where i denotes the position of the grid point. This value is theoretically equal to the initial liquid volume $V_0 = \pi R_0^2 H_0$, or in dimensionless form, $\mathbf{V} = \pi$.

The energy content consists of the *potential energy* and *kinetic energy* (Abbott,1966). The energy content of a small element is given by :

$$\begin{aligned} dE &= \left(\tfrac{1}{2}U^2 + \tfrac{1}{h}\int_0^h \rho g z\, dz\right)(2\pi r h)\, dr \quad , \\ dE &= \left(\tfrac{1}{2}U^2 + \tfrac{1}{2}\rho g h\right)(2\pi r h)\, dr \end{aligned}$$

or in dimensionless form :

$$d\mathbf{E} = \mathbf{E}_k (2\pi \mathbf{r h})\, d\mathbf{r} \qquad \text{with} \qquad \mathbf{E}_k = \tfrac{1}{2}\mathbf{U}^2 + \tfrac{1}{2}\mathbf{h}$$

In finite-difference form, the total energy content is equal to :

$$E_{tot} = 2\pi \sum_{i=0}^{n-1} (r_i E_{k,i} h_i + r_{i+1} E_{k,i+1} h_{i+1}) \frac{\Delta r}{2} \qquad (1.4.30)$$

The total initial energy content is $\frac{1}{2}\pi\rho g R_0^2 H_0^2$ or in dimensionless form, $\mathbf{E}_{tot} = \frac{1}{2}\pi$.

The difference between the calculated results and the initial volume/energy content are expressed in relative percent, with regard to the initial volume/energy content :

$$\begin{aligned} V_{err} &= 100\% \times \frac{(\mathbf{V} - \pi)}{\pi} \\ E_{err} &= 100\% \times \frac{(\mathbf{E}_{tot} - \frac{1}{2}\pi)}{\frac{1}{2}\pi} \end{aligned}$$

A satisfactory procedure will give both errors less than 1 % .

1.5 Results and Comparison

1.5.1 The Selected Calculation Procedure

The method of the selection of the calculation procedure was described in Section 1.4.4. The combination between the polynomial forms and the evaluation methods of PI and QI influenced the results. The procedure that is satisfactory for solving the plane-model cannot ensure a satisfactory solution for the axisymmetric-model. Ritter's equation (1.2.3) shows that for the plane-model, **U** and **C** depend linearly on position x. Furthermore, the solution of the plane-model does not include the evaluation of PI and QI, which makes it simpler than the solution of the axisymmetric-model. This may cause the procedure satisfactory for the solution of the plane-model, but unsatisfactory for the solution of the axisymmetric-model.

The following is a description of the results obtained by the combinations of the polynomial fitting with the method of PI & QI evaluations :

1). *The Combination of the Simple Polynomial and the Numerical Integration.*

Polynomial fitting was tried in two ways (i.e. based on all points inside the boundaries, and based on a group of 4 - 6 points surrounding the 'iterated' point), with its coefficients evaluated by the least-squares method. The trapezoidal method was used in the numerical integration, with the interval of integration divided into 8 segments or more. These combinations are not satisfactory. The difference with Ritter's solution is greater than 0.5 % and they sometimes produced ripples.

2). *The Combination of Chebychev Polynomial with the Numerical Integration.*

A Chebychev polynomial fitting was also expressed in two ways, similar

to 1) above. Using Chebychev polynomial fitting in both ways was satisfactory and accurate for solving the plane- model. The latter form (i.e. using 4-6 points) has the best accuracy, and gave average errors less than 0.01 % . However, the combination of the numerical integration with both forms of Chebychev polynomial fitting was still unsatisfactory for solving the axisymmetric-model. They produced ripples.

3). *The Combination of Chebychev Polynomial with the Arithmetic Average.*

Here, equations (1.4.20) were used. Chebychev polynomial fitting from all points still gave ripples, especially for points near the inward and outward moving boundaries. By using one polynomial equation for each iterated point, the combination gave monotonic results and satisfied the first and second conditions mentioned in Section 1.4.4. This combination was then used for further calculation.

Kleyn used $\Delta \mathbf{r} = 0.10$ and refined the increment (mesh) around the axis into $\Delta \mathbf{r} = 0.01$. This study also used $\Delta \mathbf{r} = 0.10$. For comparison purpose, two procedures were tried : with a mesh- refinement around the axis (similar to Kleyn's), and without mesh- refinement. Both methods gave monotonic results. The total mass (volume) and energy content were then calculated for both cases. The results are shown in Table I-2 , together with Kleyn's results. It is shown that the procedure using mesh-refinement around the axis resulted in growing volume and energy errors, while the procedure without mesh-refinement gave small errors. The growing errors are caused by not comforming to the CFL criterion. According to this criterion, to achieve a convergent numerical solution, the mesh-refinement must be followed by time-increment refinement. Using $\Delta \mathbf{t} = 0.10$ also gave volume and energy errors higher than 1 % , although the errors are still

smaller than those of the procedure with mesh-refinement. This may also be caused by not conforming to the CFL criterion in some part of the flow region. In the region from $\mathbf{r} = 1$ to the front edge, the value $|\mathbf{U} + \mathbf{C}|$ is always greater than 1. This means that with $\Delta\mathbf{r} = 0.10$, $\Delta\mathbf{t}$ used must be less than 0.10.

In conclusion, the calculation procedure using :

- a Chebychev polynomial fitting,
- an arithmetic average method, and
- unrefined mesh around the axis,

is selected in this work, with $\Delta\mathbf{t}$ equal to or less than 0.05.

1.5.2 Comparison with Other Theoretical Results

So far, only Kleyn's (1983) and, Trbojevic and Slater's (1989) results can be compared directly.

Kleyn's numerical data comprises the unconfined flow and the shock flow data, with the maximum distance of bund from the axis equal to four times the initial radius. Because this comparison is only concerned with unconfined flow, the data can only be compared until $\mathbf{t} = 1.5$, at which the forward moving front reaches the bund.

The average difference in $\mathbf{U}$ and $\mathbf{C}$ between Kleyn's results and the results of this work was less than 10 % . Large differences were found at points near the moving boundaries and around the axis after the liquid level at the axis collapsed. The total mass and energy content calculation with Kleyn's data showed that his data resulted in growing volume and energy errors, as shown in Table I-2 , although the errors are less than 10 % . This is caused by refining $\Delta\mathbf{r}$ around the axis without refining $\Delta\mathbf{t}$ (CFL criterion), as described before.

Table I-2: Comparison of Volume and Energy errors

Volume errors (%)

Time (t)	Kleyn's Data	With Mesh-refinement $\Delta t = 0.10$	With Mesh-refinement $\Delta t = 0.05$	No Mesh-refinement $\Delta t = 0.10$	No Mesh-refinement $\Delta t = 0.05$
0.10	0.844	0.844	0.912	0.844	0.912
0.20	-0.218	0.407	0.406	0.407	0.406
0.30	0.359	0.453	-0.009	0.951	-0.078
0.40	0.882	0.449	-0.050	0.973	-0.143
0.50	1.485	0.441	-0.130	0.933	-0.238
0.60	1.779	0.476	-0.091	0.903	-0.212
0.70	2.299	0.449	-0.171	0.940	-0.232
0.80	2.851	0.509	-0.116	0.964	-0.249
0.90	3.504	0.472	-0.161	0.993	-0.267
1.00	3.656	0.147	-0.569	1.007	-0.296
1.10	4.382	1.504	0.917	1.182	-0.137
1.20	4.911	2.895	2.425	1.187	-0.139
1.30	5.169	4.182	3.710	1.196	-0.105
1.40	5.394	5.334	4.911	1.157	-0.088
1.50	5.572	6.335	5.982	1.149	-0.097
1.60				1.116	-0.058
1.80				1.241	-0.026
2.00				1.199	-0.105

Energy errors (%)

Time (t)	Kleyn's Data	With Mesh-refinement $\Delta t = 0.10$	With Mesh-refinement $\Delta t = 0.05$	No Mesh-refinement $\Delta t = 0.10$	No Mesh-refinement $\Delta t = 0.05$
0.10	1.758	1.758	1.904	1.758	1.904
0.20	0.328	0.996	0.985	0.996	0.985
0.30	0.849	1.141	0.182	2.292	0.027
0.40	1.502	1.129	0.058	2.325	-0.128
0.50	2.254	1.114	-0.075	2.220	-0.285
0.60	2.857	1.160	-0.007	2.198	-0.257
0.70	3.571	1.117	-0.160	2.246	-0.318
0.80	4.321	1.227	-0.073	2.289	-0.359
0.90	5.185	1.174	-0.168	2.371	-0.382
1.00	5.916	1.429	-0.086	2.410	-0.438
1.10	6.644	3.757	2.527	2.646	-0.179
1.20	7.306	6.111	5.127	2.650	-0.216
1.30	7.614	8.258	7.450	2.648	-0.195
1.40	7.803	10.159	9.564	2.566	-0.168
1.50	7.955	11.752	11.408	2.523	-0.212
1.60				2.495	-0.159
1.80				2.680	-0.128
2.00				2.655	-0.245

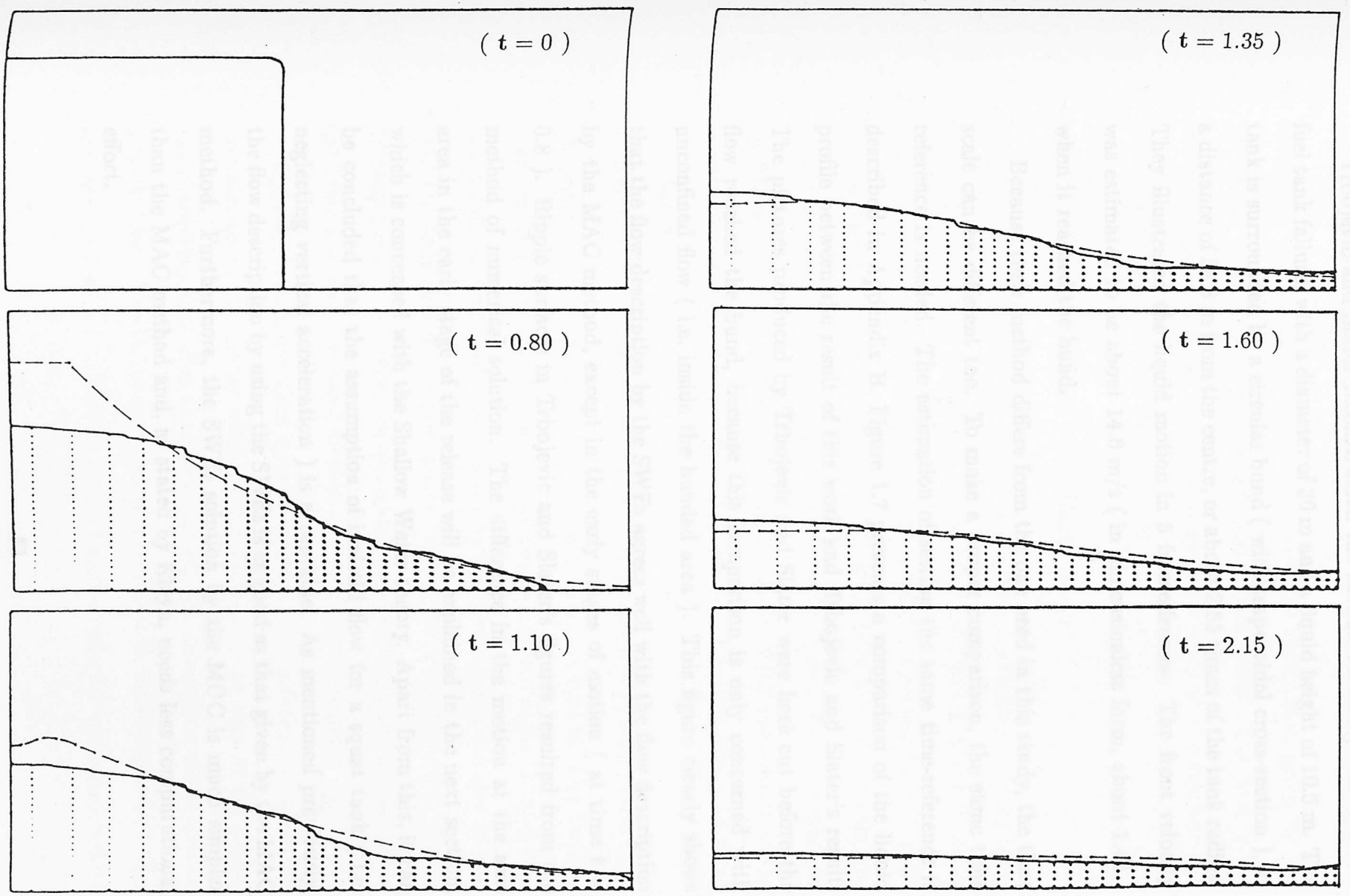


Figure 1.7: Comparison of the results of current work with Trbojevic and Slater's results (dashlines refer to the current work)

Trbojevic and Slater reconstructed the motion resulting from a diesel fuel tank failure, with a diameter of 30 m and a liquid height of 10.5 m. The tank is surrounded by a circular bund (with trapezoidal cross-section), at a distance of 38.3 m from the centre, or about 2.55 times of the tank radius. They illustrated the liquid motion in 5 freeze-frames. The front velocity was estimated to be about 14.6 m/s (in dimensionless form, about 1.44) when it reached the bund.

Because their method differs from the one used in this study, the time scale can be different too. To make a proper comparison, the same time reference is needed. The estimation of setting the same time-reference is described in Appendix B. Figure 1.7 presents a comparison of the liquid profile between the result of this work and Trbojevic and Slater's result. The pictures produced by Trbojevic and Slater were here cut before the flow reached the bund, because this comparison is only concerned with unconfined flow (i.e. inside the bunded area). This figure clearly shows that the flow description by the SWEs agrees well with the flow description by the MAC method, except in the early stages of motion (at time $t = 0.8$). Ripple surfaces in Trbojevic and Slater's figures resulted from the method of numerical solution. The difference in the motion at the axis area in the early stage of the release will be explained in the next section, which is concerned with the Shallow Water theory. Apart from this, it can be concluded that the assumption of inviscid flow for a squat tank (i.e. neglecting vertical acceleration) is acceptable. As mentioned previously, the flow description by using the SWEs is as good as that given by the MAC method. Furthermore, the SWEs solution by the MOC is much simpler than the MAC method and, as stated by Kleyn, needs less computational effort.

1.5.3 Comparison with The Experimental Results

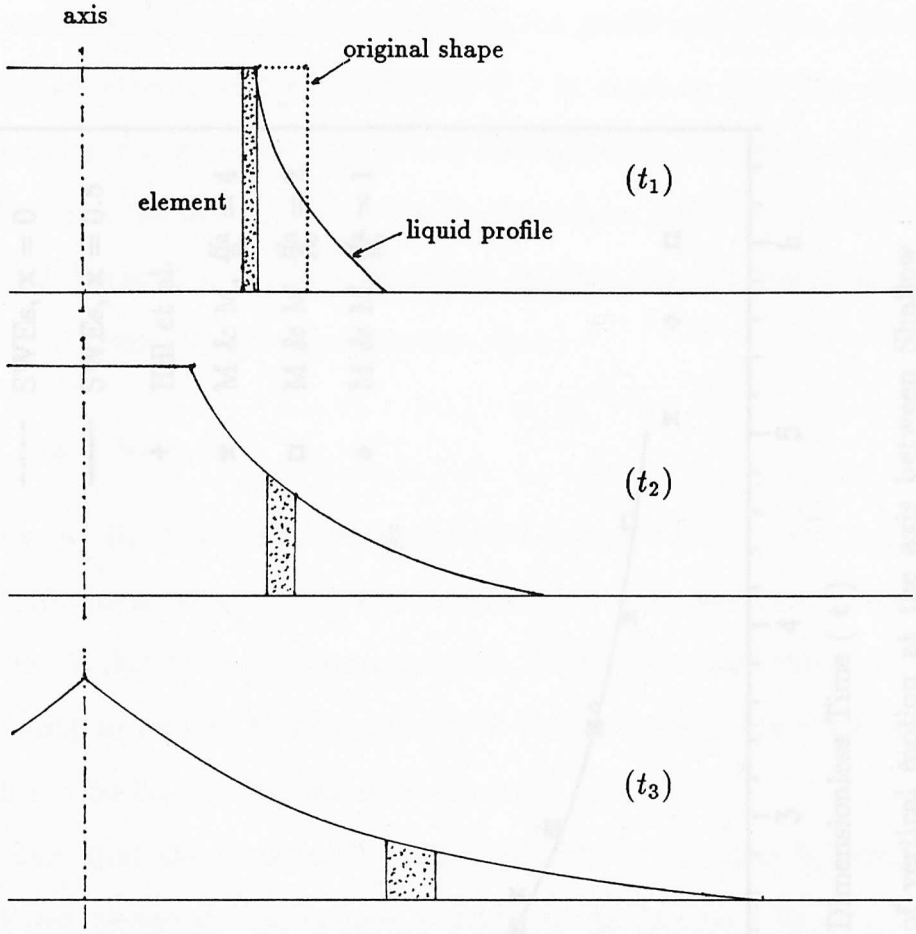
There are two prominent aspects in which the description given by the SWEs are different from the experimental observation. The first is the motion of the column at the early stages, especially at the original site area, and the second is the front velocity.

1.5.3.1 Vertical Motion at The Early Stage

Sharifi (1987) observed the motion of the column collapse by using high-speed film. The film shows that the body of the column first falls down and subsequently the liquid disperses horizontally. Kleyn roughly estimated that beyond one and a third column radii away from the column axis, the vertical acceleration can be neglected, as beyond that point the horizontal motion is dominant. The vertical acceleration is of the same order as the horizontal one inside the region of one and a quarter column radii away from the column axis.

The Shallow Water theory implies that an element of fluid moves horizontally, while its height gradually decreases along its motion. This concept is shown in Figure 1.8. When this concept is applied to the collapse of a liquid column, the liquid level at the axis of the column remains at rest until the backward moving boundary reaches the axis at $\mathbf{t} = 1$. This is different from the experimental observation, where the liquid at the axis of the column moves downward as soon as the column collapses.

However, within the time span of interest, this difference is tolerable. Comparison of the theory with the experiment in the case of the plane-model confirms that after the axis collapsed, the description of the motion given by the SWEs in the axis area agrees well with the experimental one, as shown in Figure 1.9. This picture is based on Martin and Moyce's data



(a).Motion of an element according to the Shallow Water theory

(b).A column collapse motion based on the experiment

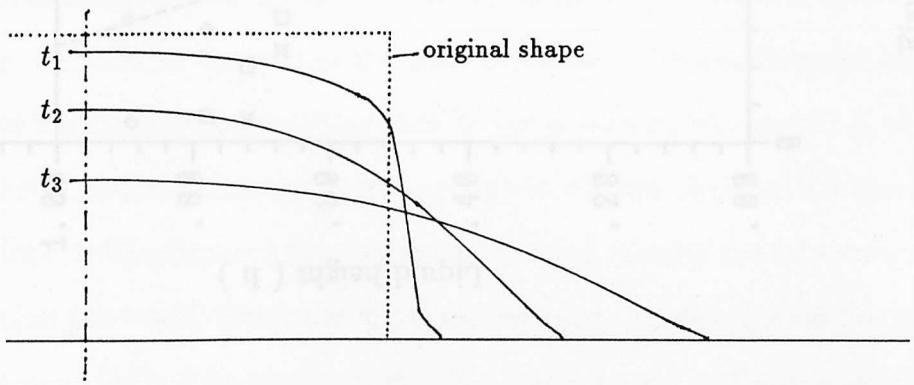


Figure 1.8: Comparison of SWE's concept with the experiment

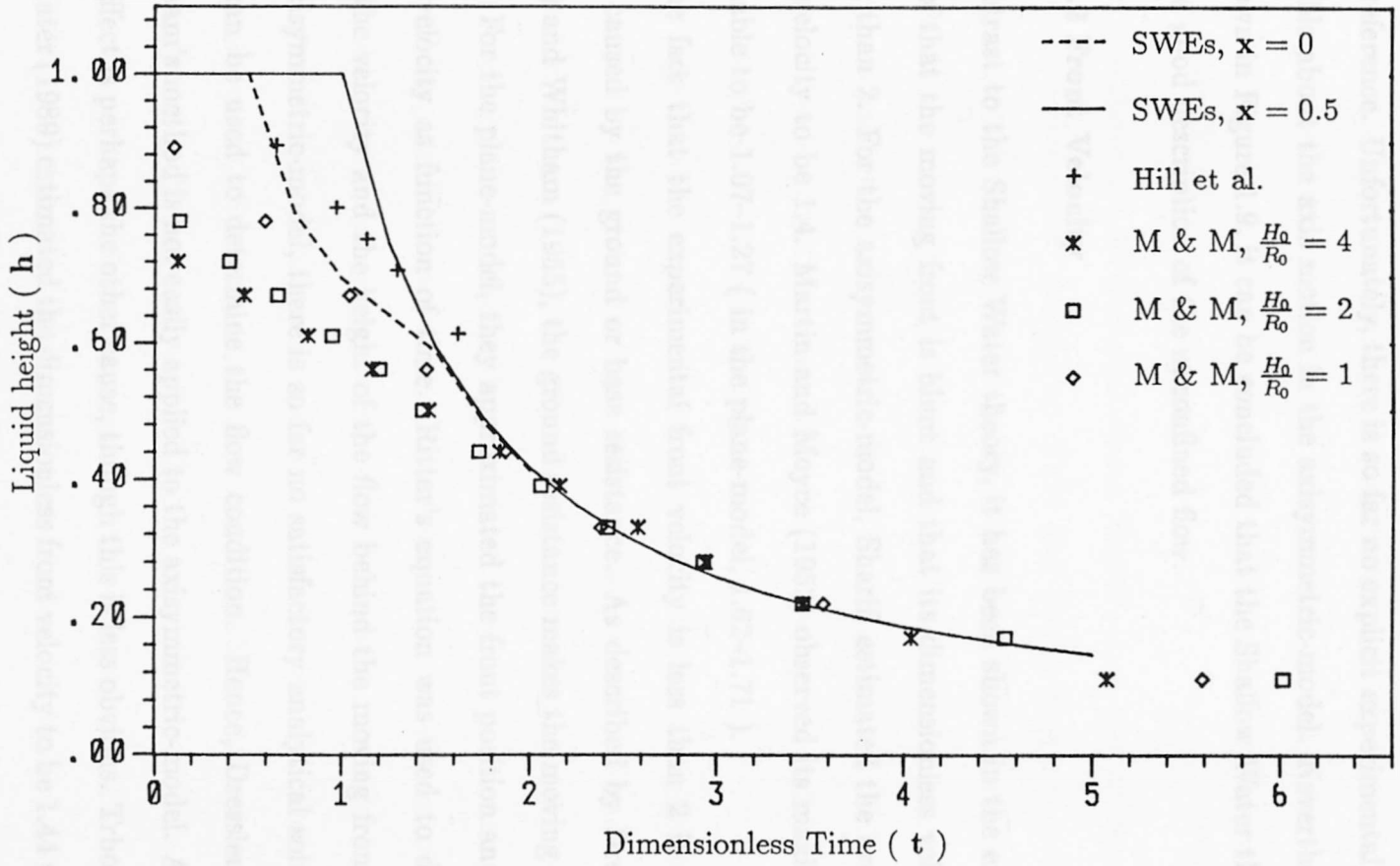


Figure 1.9: Comparison of vertical motion at the axis between Shallow Water theory (SWEs) and Martin and Moyce's data (M & M)

of the motion of the top of the column in the plane model case. Their data were re-interpreted (see Appendix B) in order to have the same time-reference. Unfortunately, there is so far no explicit experimental data available about the axis motion in the axisymmetric-model. Nevertheless, as shown in Figure 1.9, it can be concluded that the Shallow Water theory gives a good description of the unconfined flow.

1.5.3.2 Front Velocity

In contrast to the Shallow Water theory, it has been shown in the experiments that the moving front is blunt and that its dimensionless velocity is less than 2. For the axisymmetric-model, Sharifi estimated the average front velocity to be 1.4. Martin and Moyce (1952) observed its maximum attainable to be 1.07–1.27 (in the plane-model, 1.62–1.71).

The fact that the experimental front velocity is less than 2 is most likely caused by the ground or base resistance. As described by Dressler (1952) and Whitham (1955), the ground resistance makes the moving front blunt. For the plane-model, they approximated the front position and the front velocity as function of time. Ritter's equation was used to determine the velocity and the height of the flow behind the moving front. In the axisymmetric-model, there is so far no satisfactory analytical solution that can be used to determine the flow condition. Hence, Dressler and Whitham's method is not easily applied to the axisymmetric-model. A viscous effect is perhaps the other cause, though this is less obvious. Trbojevic and Slater (1989) estimated the dimensionless front velocity to be 1.44 when it arrives at the bund. Here, the MAC method they employed does not ignore viscous effects (in the form of shear stress terms). Unfortunately, they only investigated one tank size, so their estimate of the front velocity

cannot be regarded as general. Although there is a difference between the front velocity estimated theoretically and that of experimentally, as previously mentioned by Greenspan and Young (1978), the error incurred from neglecting the ground resistance effect is believed to be acceptable.

1.5.3.3 Flow Profile

Figure 1.10 shows the comparison between Sharifi's data and the results of this work. Although her description of the flow profile does not cover the original site of the column, it is very useful, for there are no other experimental data available. Figure 1.10 was prepared after the time reference and scale dependence had been normalized (see Appendix B). This figure shows that liquid height in experiments tend to be higher than predicted by the theory. Here, two possible causes can be given.

The first possibility might be the slight variation of the roughness of the base plate. Sharifi used a light diffuse glass plate as the base of the water table. In her experiments, the front was observed to propagate at a different velocity for different radial direction. In other words, the surge front position, which is supposed to be in circular shape, is not concentric to the original column. She suggests that this is most likely caused by a slight variation of the plate roughness, which leads to different flow resistance. As a consequence, there is a variation in liquid height at the same radius from the axis but different radial direction.

The second cause might be inaccuracy of the liquid height measurement. Sharifi used a photo-diode unit to determine the liquid height, by measuring the loss of light intensity across the liquid flow. Although she had standardized and corrected the photo-diode unit for water flow condition, the unit apparently gave higher values for liquid height than the true

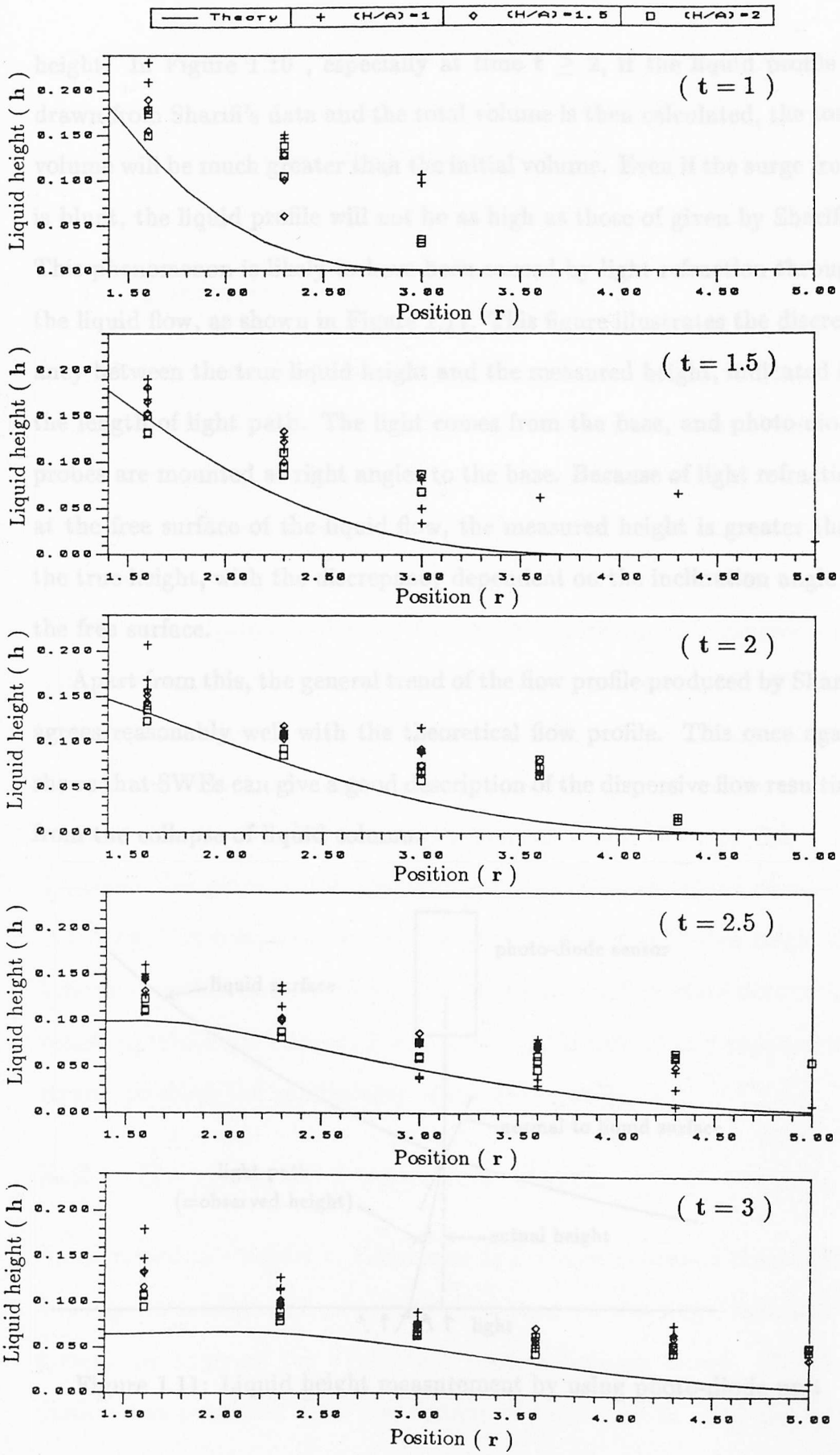


Figure 1.10: Comparison of flow profiles between the results of current work with Sharifi's results

height. In Figure 1.10 , especially at time $t \geq 2$, if the liquid profile is drawn from Sharifi's data and the total volume is then calculated, the total volume will be much greater than the initial volume. Even if the surge front is blunt, the liquid profile will not be as high as those of given by Sharifi. This phenomenon is likely to have been caused by light refraction through the liquid flow, as shown in Figure 1.11. This figure illustrates the discrepancy between the true liquid height and the measured height, indicated by the length of light path. The light comes from the base, and photo-diode probes are mounted at right angles to the base. Because of light refraction at the free surface of the liquid flow, the measured height is greater than the true height, with the discrepancy dependent on the inclination angle of the free surface.

Apart from this, the general trend of the flow profile produced by Sharifi agrees reasonably well with the theoretical flow profile. This once again shows that SWEs can give a good description of the dispersive flow resulting from the collapse of liquid column.

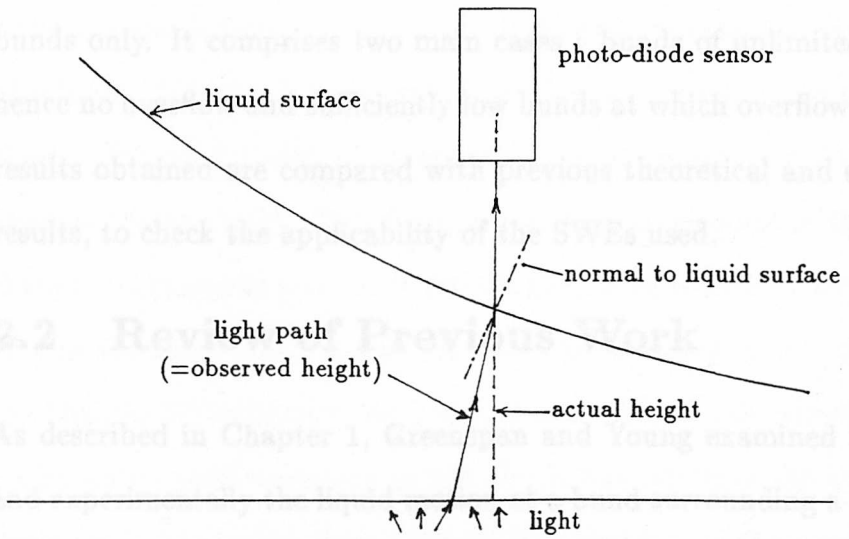


Figure 1.11: Liquid height measurement by using photo-diode unit

CHAPTER 2

CONFINED FLOW OF NON-BOILING LIQUID

2.1 Introduction

To complement the unconfined flow investigation described in Chapter 1, the SWEs will now be applied to describe confined flow, where the surge flow resulting from the liquid column collapse is obstructed by a bund or dyke. This obstruction causes the surge flow to form a shock : a hydraulic jump or bore.

This investigation will cover the shock motion and its consequences. The fundamental theory used follows Greenspan and Young's (1978) work. Initially, this study would include the flow behaviour at an inclined bund as well, but it was eventually realized such flow over an inclined surface required the use of a different theory from that used so far in this study. Therefore the scope of this investigation had to be restricted to vertical bunds only. It comprises two main cases : bunds of unlimited height and hence no overflow and sufficiently low bunds at which overflow occurs. The results obtained are compared with previous theoretical and experimental results, to check the applicability of the SWEs used.

2.2 Review of Previous Work

As described in Chapter 1, Greenspan and Young examined theoretically and experimentally the liquid motion at a bund surrounding a tank storage system, by applying the SWEs to a plane-coordinate model. The fluid motion was simulated from the instant of tank rupture until the shock

resulting from collision with a vertical bund moves back towards the centre of the original tank position. They also estimated theoretically the total amount of overflow. For their experiments, Greenspan and Young used a 9×9 inch rectangular column, with various bund positions and heights. Although their theoretical investigation was only concerned with a vertical bund, they explored the effect of the bund inclination angle ($30°$ and $60°$ to the horizontal) in their experiments. They claimed that their theoretical description of shock motion is in good agreement with their observations. Their numerical calculation of the amount of the overflowing liquid for vertical bund also showed good agreement with their experimental results. In the case of inclined bunds, their experiment showed that a decrease in the bund inclination angle (from $90°$) resulted in an increase of the amount of overflow. They concluded that bund height is an important factor in the overflow phenomenon.

When the surge front collides with the bund, the liquid rapidly piles up at the bund, forming a shock, as illustrated in Figure 2.1. Initially, the shock height or shock level rises fast (the liquid climbs up along the bund), while the shock front slowly moves backwards, toward the initial position of column. The shock level rapidly reaches a maximum and then declines slowly. Figure 2.1 also illustrates the shock formation according to the Shallow Water theory. This figure shows how an element of the surge flow changes its shape as soon as it crosses the shock interface: from short and fat (in the surge flow) to tall but slim (in the shock flow). According to the Shallow Water theory, the shock is formed from tall elements arranged horizontally; their sequence in the shock flow remains the same as their sequence in the surge flow. Hence, the element at the surge front will become the element of the shock flow at the bund position. Unless overflow

occurs, its position remains unchanged.

Greenspan and Young illustrated the shock motion into a position x versus time t diagram, as shown in Figure 2.2. The moving front of the surge flow arrives at the bund (x_w) at time t_w. The shock formed moves towards the initial column position, where the shock front propagation velocity increases gradually. The shock eventually converges into the axis of symmetry ($x = 0$), and is then reflected from the axis. The shock will repeatedly move forward and backwards between the axis of symmetry and the bund. This motion is called sloshing.

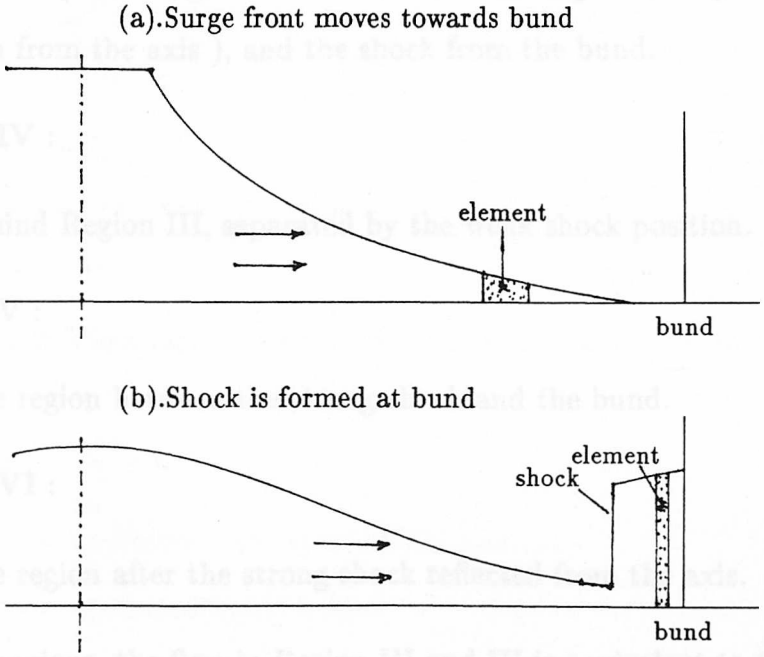


Figure 2.1: Illustration of shock formation

The backward moving boundary (in the unconfined flow) reaches the axis at $t_a = (x_0/C_0)$, and is reflected in the form of a weak shock (wave). This weak shock will be swallowed by the strong shock coming from the bund, previously described. Based on the diagram in Figure 2.2, Greenspan and Young divide the flow domain into several regions, i.e. ;

Region I ($0 \leq x \leq x_0$, $0 < t \leq t_a$):

The undisturbed liquid region, which has not yet been affected by the collapse.

Region II ($x_0 < x \leq x_w$, $0 < t \leq t_w$):

Ahead of the surging front, where there is no liquid.

Region III :

The region between the backward moving boundary and the forward moving boundary, and later between the weak shock motion (resulting from the backward moving boundary reflection from the axis), and the shock from the bund.

Region IV :

Behind Region III, separated by the weak shock position.

Region V :

The region between the strong shock and the bund.

Region VI :

The region after the strong shock reflected from the axis.

Of these regions, the flow in Region III and IV is equivalent to the unconfined flow described in Chapter 1.

Greenspan and Young derived the shock condition equations from mass and momentum balances across the shock. The shock propagation velocity U_s is considered to depend on the upstream flow conditions (Region III and IV):

$$U_s = U_f - \sqrt{\frac{gh_f}{2}} M^2 \left(1 + \frac{1}{M^2}\right)^{0.5} \qquad (2.2.1)$$

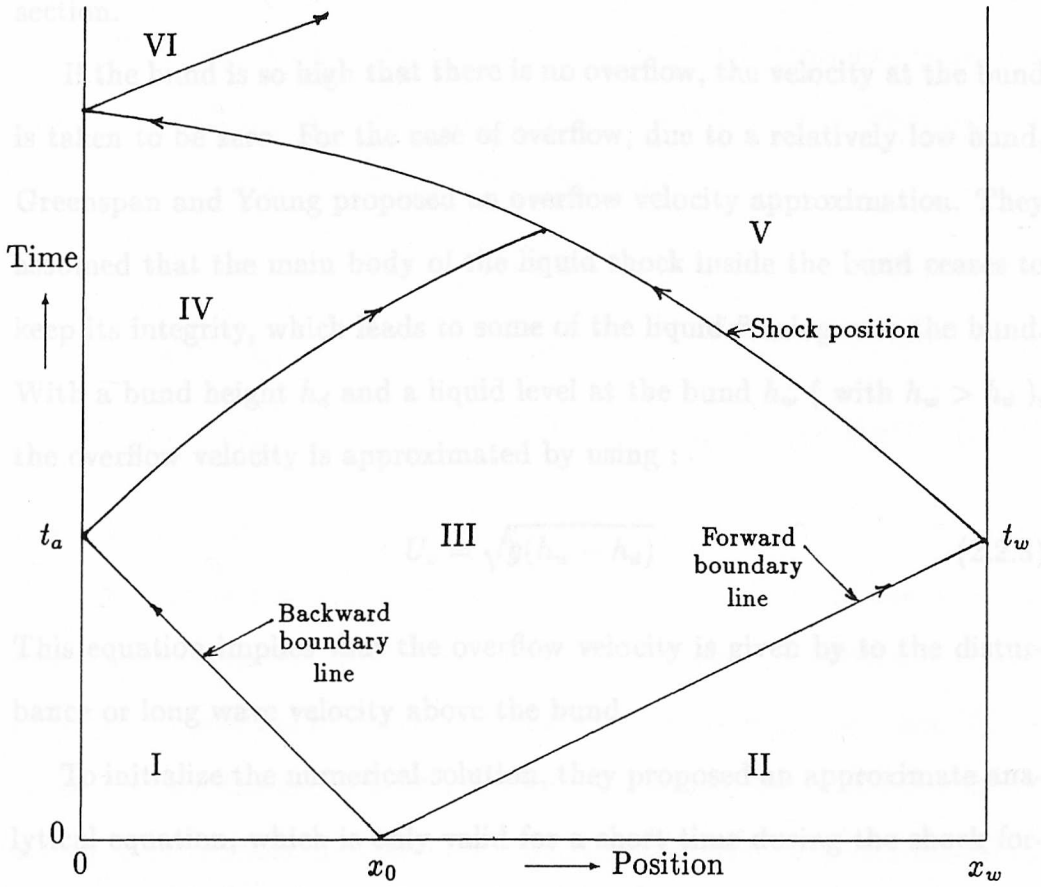


Figure 2.2: Flow region division, according to Greenspan and Young

with $M^2 = \dfrac{h_b}{h_f}$

U_f = upstream velocity at shock position,

h_f = upstream liquid height,

h_b = downstream liquid height (shock height).

Here, subscripts f and b denote repectively *in front of* and *behind* the shock position. The liquid velocity at the shock position (downstream) is given by :

$$U_b = U_f - \sqrt{\frac{gh_f}{2}}(M^2 - 1)\left(1 + \frac{1}{M^2}\right)^{0.5} \qquad (2.2.2)$$

The complete derivation of both equations will be described in the next

section.

If the bund is so high that there is no overflow, the velocity at the bund is taken to be zero. For the case of overflow, due to a relatively low bund, Greenspan and Young proposed an overflow velocity approximation. They assumed that the main body of the liquid shock inside the bund ceases to keep its integrity, which leads to some of the liquid flowing over the bund. With a bund height h_d and a liquid level at the bund h_w (with $h_w > h_d$), the overflow velocity is approximated by using :

$$U_v = \sqrt{g(h_w - h_d)} \tag{2.2.3}$$

This equation implies that the overflow velocity is given by to the disturbance or long wave velocity above the bund.

To initialize the numerical solution, they proposed an approximate analytical equation, which is only valid for a short time during the shock formation, and before the overflow takes place. New space and time variables are introduced by :

$$\eta = \frac{(x_w - x)}{t_w} \quad , \quad \tau = \frac{(t - t_w)}{t_w} \qquad \text{and} \qquad \zeta = \frac{\eta}{\tau^2}$$

with U and C behind the shock approximated by a power series in τ :

$$\begin{aligned} U &= \tau f_0(\zeta) + \tau^2 f_1(\zeta) + \ldots \\ C &= \tau^{0.5} \left[g_0(\zeta) + \tau g_1(\zeta) + \ldots \right] \end{aligned} \tag{2.2.4}$$

and the shock position (locus) ζ_s is defined by :

$$\zeta_s = z(\tau) = z_0 + z_1 \tau \tag{2.2.5}$$

The shock propagation velocity is derived from the above equation :

$$U_s = -\frac{d\eta_s}{d\tau} = -2z_0\tau - 3z_0\tau^2 \tag{2.2.6}$$

The coefficients f_0, f_1, g_0 and g_1 in equation (2.2.4) are evaluated by substituting the power series into the SWEs and the shock conditions (equations (2.2.1) and (2.2.2)). In this case, Ritter's solution is used to determine the upstream conditions U_f and h_f. The results are :

$$\begin{aligned} f_0 &= \zeta \quad , \quad f_1 = \frac{5}{3}\frac{\zeta^3}{{k_0}^2} + 2\frac{k_1\zeta}{k_0} \quad , \\ g_0 &= k_0 \quad , \quad g_1 = -\frac{\zeta^2}{2k_0} + k_1 \quad , \\ z_0 &= \frac{8}{27{k_0}^2}, \quad z_1 = -\frac{1}{4}[f_1(z_0) + \frac{6z_0}{k_0}g_1(z_0) + 8z_0 - 6{z_0}^2] \end{aligned} \tag{2.2.7}$$

where $k_0 = 2^{1.25}3^{-0.5}$ and $k_1 = -\frac{5}{9}\frac{3^{0.5}}{2^{0.25}}\left(2^{0.5} - \frac{1}{9}\right)$.

According to this approximate solution, the liquid level of the shock is nearly uniform in the early period of the shock motion, i.e. the liquid level at the shock position is almost equal to the liquid level at the bund. Based on this result, the shock level can then be assumed to be uniform in the early period of shock motion, and it can alternatively be approximated by using the principle of mass conservation behind the shock position. As illustrated in Figure 2.3, the total mass behind the shock position is given by :

$$\begin{aligned} \int_{x_s}^{x_f} h_{III}dx &= \int_{x_s}^{x_w} h_b dx \\ h_b &= \frac{1}{(x_w - x_s)}\int_{x_s}^{x_f} h_{III}dx \end{aligned} \tag{2.2.8}$$

where h_{III} = liquid height in Region III (unconfined flow),

h_b = shock height ,

x_s = shock position ,

x_f = position of the surge front.

This approximation gave the same result as that given by equation (2.2.4).

Greenspan and Johansson (1981) investigated experimentally the overflow phenomena, in the axisymmetric-model. The main aim of their inves-

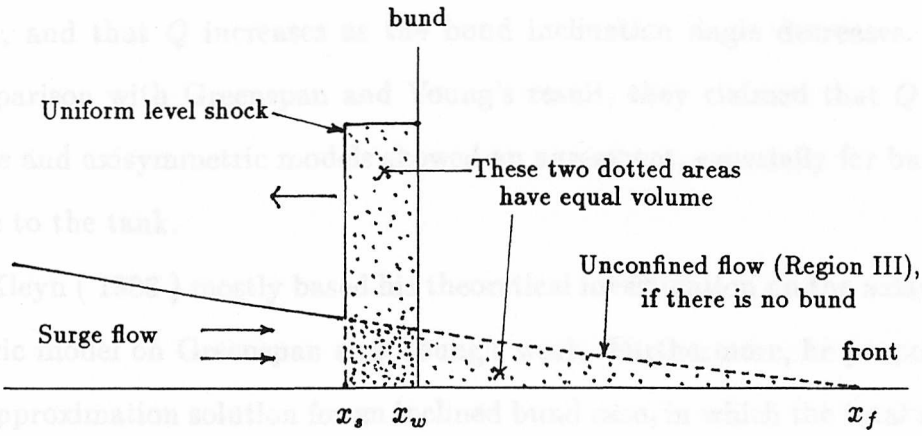


Figure 2.3: Uniform shock height approximation

tigation was to measure accurately the amount of overflow for various bund conditions. This included several possible bund shapes, which may reduce or prevent the overflow. They also investigated the sudden release of liquid through a slot or orifice simulating partial rupture of the tank wall. They used a vertical cylindrical column with a diameter of 7.5 inches and a height of 11 inches, with a circular bund set up at several distances and with several inclination angles. It was theoretically considered that the total amount of overflow Q (expressed as a fraction of the initial column volume) is a function of four dimensionless variables :

$$Q = F\left[\frac{h_d}{H_0}, \frac{r_w}{H_0}, \frac{R_0}{H_0}, \Theta\right] \tag{2.2.9}$$

where r_w is the bund distance from the axis of the column and Θ is the bund inclination angle (with respect to the horizontal surface). During the experiment, variation of (h_d/H_0) was obtained by changing the initial height of liquid column H_0 and retaining constant bund height h_d. Greenspan and Johansson confirmed the Greenspan and Young's conclusion that the amount of overflow Q strongly depends upon (h_d/H_0). They also concluded that radial spreading (indicated by the term $\frac{UC}{r}$ in the SWEs given by

equation (1.3.11)) reduces Q when the bund is moved further from the tank, and that Q increases as the bund inclination angle decreases. In comparison with Greenspan and Young's result, they claimed that Q for plane and axisymmetric models showed an agreement, especially for bunds close to the tank.

Kleyn (1983) mostly based his theoretical investigation on the axisymmetric model on Greenspan and Young's work. Furthermore, he proposed an approximation solution for an inclined bund case, in which the total momentum behind the shock is regarded to be constant. Based on Greenspan and Young's argument, he simplified the shock level to be uniform at any instant. Kleyn claimed that such simplification reduced numerical calculation effort and that the results were still as good as those without simplification. Contrary to Greenspan and Johansson's conclusion, Kleyn showed that the amount of overflow in the axisymmetric-model is far less than that in the plane-model. He also showed that the shock level at the bund in the axisymmetric-model is lower than that in the plane-model. His estimate of overflow on an inclined bund agreed with the trend of Greenspan and Young's experiments, where a decrease in an inclination angle resulted in greater overflow.

Based on the assumption of a uniform shock level, the shock height in the overflow case was estimated by using :

$$\pi(h_{w,0} - h_w)(r_w - r_s) = \int \sqrt{g(h_w - h_d)^3}\,dt \qquad (2.2.10)$$

where r_s = shock position ,

$h_{w,0}$ = shock level when no-overflow occurs
(bund of unlimited height),

h_w = shock level in the case of overflow.

The RHS of the above equation is the total overflow, which is derived from

equation (2.2.3). Here, $h_{w,0}$ and h_w are calculated at the same time level.

Kleyn also explored one further aspect of overflow. When the liquid flows over the bund, it forms a jet flow. He assumed that the jet motion behaves similarly to the motion of a projectile under gravitational force, the distance where the liquid hits the ground can be estimated. This distance could be used to recommend safe distances for units built near storage tank facilities. As there is no explicit vertical velocity in the Shallow Water theory, Kleyn approximated the vertical velocity of overflow liquid leaving the bund by using :

$$v_w \approx \frac{dh_w}{dt} \tag{2.2.11}$$

which is the rate of change of shock height at bund. The distance of jet projection can be calculated by using :

$$\begin{aligned} R_p(t) &= r_w + U_w t_p \\ t_p &= \frac{v_w}{g} + \left[\left(\frac{v_w}{g} \right)^2 + \frac{2h_d}{g} \right]^{0.5} \end{aligned} \tag{2.2.12}$$

The horizontal velocity U_w is calculated from equation (2.2.3).

In parallel with Kleyn's work, Sharifi (1987) tried to investigate confined flow experimentally, although she mainly concentrated on unconfined flow investigation. Her investigation included an inclined bund (40°) and variation of (H_0/R_0). She emphasized once more that the bund height has a major influence on the overflow, as concluded by Greenspan and Young, and Greenspan and Johansson. Her observation on the liquid motion at the bund agrees well with that given by the theoretical description of Kleyn. On the other hand, she showed that Kleyn underestimated the amount of overflow.

By using the MAC method, Trbojevic and Slater (1989) simulated the flow over inclined bund, as described previously in Chapter 1. They

stated that the dynamic pressure at the bund wall can be three times of the corresponding hydrostatic pressure. Unfortunately, they did not describe further aspects of shock motion and overflow. Instead, they presented their results in several freeze frames, which illustrate the fluid motion.

2.3 The Equations of Shock Conditions

The shock conditions are determined from the conservation of mass and momentum across the shock. It is assumed that the flow is incompressible flow and there is no mass loss at the shock interface. Several symbols used in deriving the shock conditions are shown in Figure 2.4.

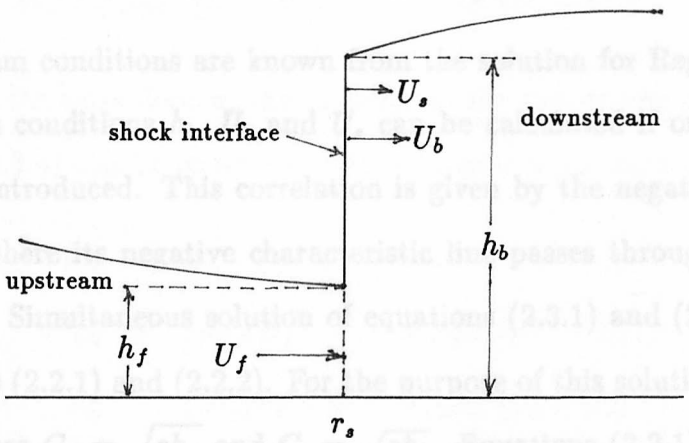


Figure 2.4: Description of symbols at the shock position

With respect to the shock interface (the plane that separates the upstream and downstream flows), the incoming mass flow rate is $\rho h_f(U_f - U_s)$. Similarly, the outgoing mass flow rate is $\rho h_b(U_b - U_s)$. The mass balance is given by :

$$h_f(U_f - U_s) = h_b(U_b - U_s) \qquad (2.3.1)$$

The momentum balance involves two quantities : the momentum flux and

the force acting at the shock interface. The upstream momentum concentration is $\rho(U_f - U_s)$. Based on the shock interface motion point of view (Galilean frame), the incoming momentum rate is $\rho h_f(U_f - U_s)^2$. In the Shallow Water theory, the force concerned is a hydrostatic force. In this case, the upstream hydrostatic force is $\frac{1}{2}\rho g {h_f}^2$. Likewise, the output momentum rate (downstream) is $\rho h_b(U_b - U_s)^2$, with its hydrostatic force $\frac{1}{2}\rho g {h_b}^2$. The momentum balance is given by :

Input momentum rate − Output momentum rate =Net force acting at the interface,

$$h_f(U_f - U_s)^2 - h_b(U_b - U_s)^2 = \tfrac{1}{2}g{h_b}^2 - \tfrac{1}{2}g{h_f}^2 \qquad (2.3.2)$$

The upstream conditions are known from the solution for Region III. The downstream conditions h_b, U_b and U_s can be calculated if one more correlation is introduced. This correlation is given by the negative Riemann invariant, where its negative characteristic line passes through the shock position r_s. Simultaneous solution of equations (2.3.1) and (2.3.2) results in equations (2.2.1) and (2.2.2). For the purpose of this solution, it is convenient to use $C_f = \sqrt{gh_f}$ and $C_b = \sqrt{gh_b}$. Equations (2.2.1) and (2.2.2) then become :

$$\begin{aligned} U_s &= U_f - \frac{C_f}{\sqrt{2}} M^2 \left(1 + \frac{1}{M^2}\right)^{0.5} \\ U_b &= U_f - \frac{C_f}{\sqrt{2}} (M^2 - 1) \left(1 + \frac{1}{M^2}\right)^{0.5} \end{aligned} \qquad (2.3.3)$$

On the other hand, the total energy across the interface does not remain constant (Stoker, 1957 ; Abbott, 1966). The fluid will lose some of its energy as it traverses the shock interface. To keep the shock interface standing against the upstream flow, a counter-force is needed and hence

work is done at the interface. The energy loss is equal to the difference between the total upstream and downstream energy content. As in the case of the momentum balance, two quantities are involved : the energy flux and the work arising from the hydrostatic force. The upstream energy concentration is $\rho(\frac{1}{2}(U_f - U_s)^2 + \frac{1}{2}gh_f)$, which consists of kinetic and potential energy (equation (1.4.30) in Chapter 1). The total energy influx is then equal to $\rho(\frac{1}{2}(U_f - U_s)^2 + \frac{1}{2}gh_f)h_f(U_f - U_s)$. The work resulting from the hydrostatic force is $\frac{1}{2}\rho g{h_f}^2(U_f - U_s)$. The outflow condition is derived in a similar way. The energy balance is given by :

$$-(\textit{Outflux energy} - \textit{Influx energy}) \;=\; \textit{Total work},$$

$$-\rho h_b(\tfrac{1}{2}(U_b - U_s)^2 + \tfrac{1}{2}gh_b)(U_b - U_s) \;+\; \rho h_f(\frac{1}{2}(U_f - U_s)^2 + \frac{1}{2}gh_f)(U_f - U_s) = W_s + \frac{1}{2}\rho g{h_b}^2(U_b - U_s) \;-\; \frac{1}{2}\rho g{h_f}^2(U_f - U_s) \qquad (2.3.4)$$

where W_s is the work done at the interface or the energy loss per unit time. Equation (2.3.4) can be re-written into a simpler form, such as :

$$W_s = E_i - E_o \quad , \qquad \text{with}$$

$$E_i = \tfrac{1}{2}\rho h_f(U_f - U_s)^3 + \rho g{h_f}^2(U_f - U_s) \qquad (2.3.5)$$

$$E_o = \tfrac{1}{2}\rho h_b(U_b - U_s)^3 + \rho g{h_b}^2(U_b - U_s) \qquad (2.3.6)$$

This energy will be absorbed by the liquid and converted into heat. Because W_s is very small compared with the sensible heat, the liquid temperature effectively does not change.

2.4 Numerical Solution

The numerical solution and calculation procedures performed in Region V are essentially the same as those for Regions III and IV (described in Chapter 1), including interpolation by using Chebychev polynomial fitting

and arithmetic averaging on PI and QI evaluation. This section will only describe special aspects of the numerical solution in Region V, such as determination of the shock position and the flow condition at the bund.

2.4.1 The Shock Conditions

The shock conditions are determined from equations (2.3.3) together with the negative Riemann invariant. As shown in Figure 2.5, the negative characteristic line AQ passes through the shock position at time step $(j+1)$, which is represented by point A. The position of point Q is estimated by using :

$$r_Q = r_{s,j+1} - (U_A - C_A + U_Q - C_Q)\frac{\Delta t}{2} \tag{2.4.1}$$

where $r_{s,j+1}$ = the shock position at time step $(j+1)$,

U_A,C_A = shock conditions at time step $(j+1)$.

Along this line, the negative Riemann invariant correlation is given by :

$$U_A - 2C_A = U_Q - 2C_Q \left(\frac{U_A C_A}{r_{s,j+1}} + \frac{U_Q C_Q}{r_Q}\right)\frac{\Delta t}{2} \tag{2.4.2}$$

The shock position is estimated by using :

$$r_{s,j+1} = r_{s,j} + (U_{s,j} + U_{s,j+1})\frac{\Delta t}{2} \tag{2.4.3}$$

where $r_{s,j}$ is the shock position at time step (j). The conditions at time step (j): $U_{s,j}$,$r_{s,j}$, U and C of the downstream flow, as well as the upstream conditions U_f and C_f at time step $(j+1)$, are known. There are 5 unknown quantities : $U_{s,j+1}$, $r_{s,j+1}$, r_Q, U_A and C_A, with 5 available equations : two in (2.3.3), and the other (2.4.1), (2.4.2) and (2.4.3). Hence, these five equations can be solved in principle. The Newton-Raphson iteration method is employed, with equations (2.4.1) to (2.4.3) regarded as :

$$F_1 = r_{s,j+1} - (U_A - C_A + U_Q - C_Q)\frac{\Delta t}{2} - r_Q = 0$$

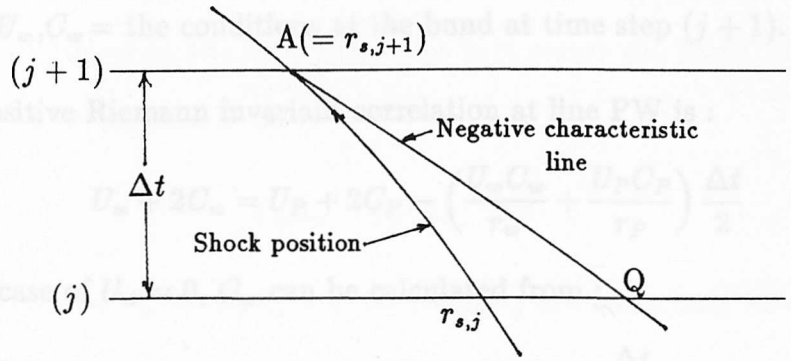


Figure 2.5: Determination of the shock conditions

$$F_2 = U_A - 2C_A - U_Q + 2C_Q - \left(\frac{U_A C_A}{r_{s,j+1}} + \frac{U_Q C_Q}{r_Q}\right)\frac{\Delta t}{2} = 0$$
$$F_3 = r_{s,j} + (U_{s,j} + U_{s,j+1})\frac{\Delta t}{2} - r_{s,j+1} = 0 \qquad (2.4.4)$$

where F_1, F_2 and F_3 are functions of $r_{s,j+1}$, r_Q and C_A. Here, U_A and $U_{s,j+1}$ are calculated from equations (2.3.3). The values of U_f and C_f are approximated by interpolation at position $r_{s,j+1}$. The algorithm for iteration is the same as that mentioned in Section 1.4.3.

2.4.2 Conditions at The Bund

Two bund conditions are considered : bunds of unlimited height, where no overflow occurs and, relatively low bunds.

In the case of bunds of unlimited height, the velocity at the bund U_w is considered to be zero at all times. Hence, only the liquid height or level at the bund will be determined. As illustrated in Figure 2.6, the conditions at the bund can be calculated from the positive Riemann invariant, where its positive characteristic line passes through the bund position at time step $(j+1)$. Here, the position of point P is given by :

$$r_P = r_w - (U_w + C_w + U_P + C_P)\frac{\Delta t}{2} \qquad (2.4.5)$$

where r_w = the position of bund,

U_w,C_w = the conditions at the bund at time step $(j+1)$.

The positive Riemann invariant correlation at line PW is :

$$U_w + 2C_w = U_P + 2C_P - \left(\frac{U_w C_w}{r_w} + \frac{U_P C_P}{r_P}\right)\frac{\Delta t}{2} \qquad (2.4.6)$$

In the case of $U_w = 0$, C_w can be calculated from :

$$r_P = r_w - (C_w + U_P + C_P)\frac{\Delta t}{2}$$

$$\text{or} \qquad F(r_P) = r_w - (C_w + U_P + C_P)\frac{\Delta t}{2} - r_P = 0 \qquad (2.4.7)$$

$$\text{with} \qquad C_w = \frac{1}{2}\left[U_P + 2C_P - \left(\frac{U_P C_P}{r_P}\right)\frac{\Delta t}{2}\right] \qquad (2.4.8)$$

The above equation can be solved easily by the Newton-Raphson method.

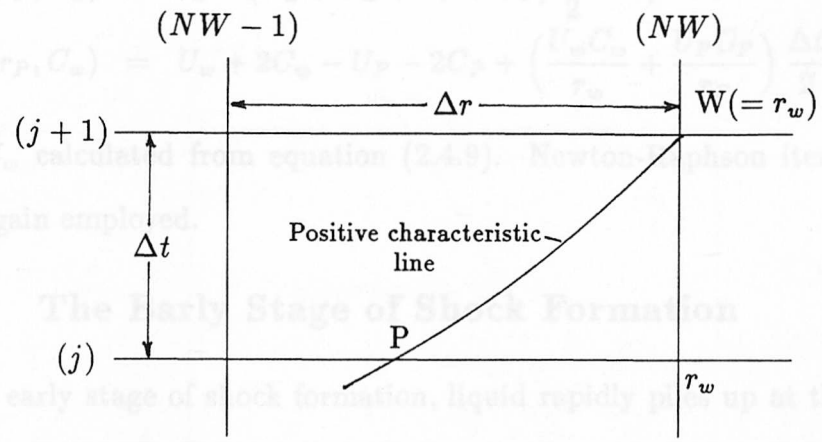


Figure 2.6: Determination of the conditions at bund

When overflow occurs, due to relatively low bunds, the velocity U_w has to be determined, together with C_w. Following Greenspan and Young's (1978) method, the rate of overflow is approximated from equation (2.2.3). This equation estimates the velocity above the bund. According to the Shallow Water theory, the horizontal velocity involved in the Riemann invariant correlation is an average velocity throughout the liquid height. Equation

(2.2.3) is hence adjusted into the average value along the liquid height at the bund. Based on the total mass flow rate across the bund, the velocity U_w can be determined from :

$$U_w h_w = U_v(h_w - h_d) \quad ,$$

The quantities $C_w = \sqrt{gh_w}$ and $C_d = \sqrt{gh_d}$ are commonly used. Hence, the velocity U_w is better expressed in the form :

$$U_w = \frac{(C_w{}^2 - C_d{}^2)^{\frac{3}{2}}}{C_w{}^2} \tag{2.4.9}$$

Three unknown quantities are involved : r_P, U_w and C_w, with 3 available equations : (2.4.5), (2.4.6) and (2.4.9). The problem is regarded as :

$$\begin{aligned} F_1(r_P, C_w) &= r_w - (U_w + C_w + U_P + C_P)\frac{\Delta t}{2} - r_P = 0 \qquad (2.4.10) \\ F_2(r_P, C_w) &= U_w + 2C_w - U_P - 2C_P + \left(\frac{U_w C_w}{r_w} + \frac{U_P C_P}{r_P}\right)\frac{\Delta t}{2} = 0 \end{aligned}$$

with U_w calculated from equation (2.4.9). Newton-Raphson iteration is once again employed.

2.4.3 The Early Stage of Shock Formation

At the early stage of shock formation, liquid rapidly piles up at the bund but the shock moves very slowly. Its position r_s is still very close to the wall. The distance $(r_w - r_s)$ is very small compared with Δr used in the calculation (i.e. $\Delta \mathbf{r} = 0.1$). According to the CFL criterion (equation (1.4.15)), the time increment Δt must be less than or equal to $\frac{\delta r}{|U + C|}$. With $\delta r = r_w - r_s < \Delta r$, the time increment Δt in the early stage of shock formation must be much smaller than Δt used in the previous calculation. Figure 2.7 illustrates the determination of the time increment to be employed, with respect to the shock position. The appropriate Δt to be used in the early stage of shock formation depends on both the positive

characteristic line through points P and W_1 and the negative characteristic line through points Q and S_1. Here, points P and Q are situated at time step (j). To satisfy the CFL criterion, both points must lie between the shock and the bund positions, or r_P must be greater than $r_{s,j}$ and r_Q must be less than r_w. The previous Δt is then divided into smaller increments, namely $\delta t = \dfrac{\Delta t}{K}$, where K is an integer number to be determined, until the conditions :

$$\begin{aligned} r_P &= r_w - (U_{w,j} + C_{w,j})\delta t > r_{s,j} \quad \text{and} \\ r_Q &= r_{s,j} - (U_{b,j} - C_{b,j})\delta t < r_w \end{aligned} \tag{2.4.11}$$

are satisfied. Here, $U_{b,j}$ and $C_{b,j}$ are U and C at the shock position $r_{s,j}$. Briefly, the time mesh is refined into K sections, where the shock conditions

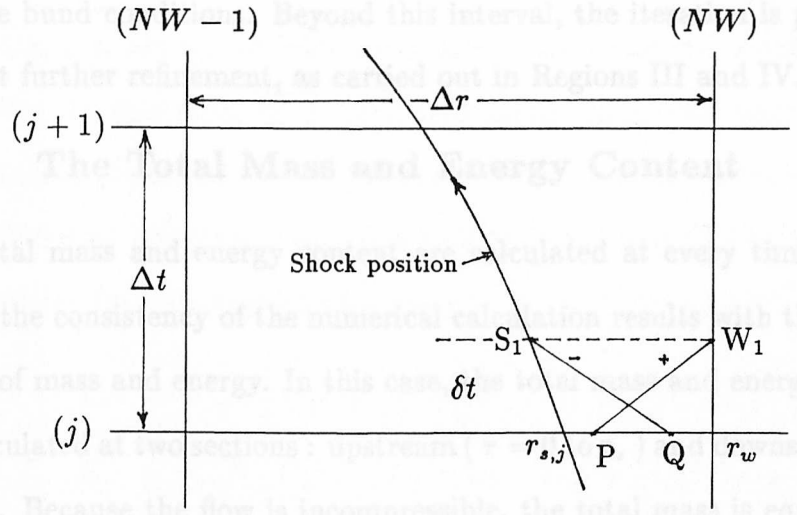


Figure 2.7: Determination of the time increment in the early stage of shock formation

are determined at each section (i.e. refined time step). Because of this time mesh refinement, the upstream conditions U_f and C_f in equations (2.3.3) also have to be evaluated at each refined time step. Hence, U and C in the upstream flow are then interpolated from two directions : position r and

time t. This interpolation can be performed by using Chebychev polynomial fitting. The procedure to determine appropriate δt can be summarized as follows :

1. For an initial trial, K is taken to be equal to 2, i.e. $\delta t = \Delta t/2$.

2. Based on the conditions at time step (j) : U_b, C_b, U_w and C_w, the position r_P and r_Q are estimated from equations (2.4.11).

3. If both are fulfilled, then δt is considered as a refined time increment. Otherwise, a new K is taken, bigger than the previous one, such as $K_{new} = 2K_{old}$, and step 2) is repeated.

Refinement of the time increment is carried out only if r_s is situated between r_{NW-1} and r_w, where there is no grid point to be iterated except the shock and the bund conditions. Beyond this interval, the iteration is performed without further refinement, as carried out in Regions III and IV.

2.4.4 The Total Mass and Energy Content

The total mass and energy content are calculated at every time step, to ensure the consistency of the numerical calculation results with the conservation of mass and energy. In this case, the total mass and energy content are calculated at two sections : upstream ($r = 0$ to r_s) and downstream (r_s to r_w). Because the flow is incompressible, the total mass is equal to the total volume multiplied by the (constant) density. The difference between the calculated volume V and the initial volume V_{init} (in dimensionless, $\mathbf{V}_{init} = \pi$) is expressed as a percentage of the initial volume :

$$V_{error} = 100\,\% \frac{(V - V_{init})}{V_{init}} \quad .$$

Unlike in unconfined flow, where the total energy content remains constant, the total energy content in confined flow decreases gradually, due to energy

loss at the shock, as given by equation (2.3.4). The discrepancy between the calculated energy content E_{tot} and the initial energy content E_{init} is expressed as a percentage of the initial energy content :

$$E_{discr} = 100\,\% \frac{(E_{tot} - E_{init})}{E_{init}} \quad .$$

As described in Chapter 1, the dimensionless initial energy content is equal to $\frac{1}{2}\pi$.

The total amount of the overflowing liquid is estimated by using :

$$Q = \int_{t_i}^{t_e} U_w {C_w}^2 (2\pi r_w)\, dt \quad .$$

Incorporation of equation (2.4.9) into the above equation results in :

$$Q = 2\pi r_w \int_{t_i}^{t_e} ({C_w}^2 - {C_d}^2)^{\frac{3}{2}}\, dt \qquad (2.4.12)$$

where t_i and t_e are respectively the moments at which the overflow begins and ends. In this case, Q is calculated numerically, and expressed as a percentage of the initial volume. The total energy loss at the shock interface is calculated by integrating equation (2.3.4). Equations (2.3.5) and (2.3.6) are rewritten into dimensionless-forms :

$$\begin{aligned} \mathbf{E}_i &= \mathbf{C}_f{}^2(\frac{1}{2}\mathbf{U}_f{}^2 + \frac{1}{2}\mathbf{C}_f{}^2)(\mathbf{U}_f - \mathbf{U}_s) + \frac{1}{2}\mathbf{C}_f{}^4\mathbf{U}_f \\ \mathbf{E}_o &= \mathbf{C}_b{}^2(\frac{1}{2}\mathbf{U}_b{}^2 + \frac{1}{2}\mathbf{C}_b{}^2)(\mathbf{U}_b - \mathbf{U}_s) + \frac{1}{2}\mathbf{C}_b{}^4\mathbf{U}_f \end{aligned} \qquad (2.4.13)$$

The total energy loss is given by :

$$\mathbf{E}_{loss} = 2\pi \mathbf{r}_w \int_{t_w}^{t} (\mathbf{E}_i - \mathbf{E}_o) dt \qquad (2.4.14)$$

Likewise, $\mathbf{E}_{loss}$ is calculated numerically, and also expressed as a percentage of the initial energy content.

2.5 Results and Comparison

2.5.1 The Initial Conditions

Equations (2.2.4) to (2.2.7) are derived from the SWEs of the plane-model, with the upstream conditions ($\mathbf{U}_f$ and $\mathbf{C}_f$) are determined from Ritter's solution. The upstream conditions for the axisymmetric-model are different from those for the plane-model. Hence, equations (2.2.4) to (2.2.7) may be modified, if they will be used to set up the initial conditions for the axisymmetric-model. The modification was carried out in a similar way to Greenspan and Young's (1978) approximation method, i.e. by substituting equations (2.2.4) into the SWEs of the axisymmetric-model. Because there is no analytical solution for the SWEs of the axisymmetric-model, Greenspan and Butler's (1961) approximation was used to determine the upstream conditions. The result obtained was in fact the same as equations (2.2.4) to (2.2.7). Hence, these equations were also used to set up the initial conditions for the numerical solution in the axisymmetric-model.

The other method to set up the initial conditions was tried, by using equation (2.2.8) together with (2.2.1). As described by Greenspan and Young, the shock height is almost uniform in the early stage of shock formation. Following Greenspan and Young's description, this method of setting-up the initial conditions assumed $\mathbf{C}_w = \mathbf{C}_b$ (uniform shock flow height). Because the shock moves slowly, the shock propagation velocity $\mathbf{U}_s$ can be approximated by using :

$$\mathbf{U}_s \approx \frac{(\mathbf{r}_s - \mathbf{r}_w)}{\delta \mathbf{t}_w} \tag{2.5.1}$$

with $\delta \mathbf{t}_w = \mathbf{t} - \mathbf{t}_w$.

The shock position $\mathbf{r}_s$ is then calculated iteratively from equations (2.2.1) and (2.2.8). Because the value of $\mathbf{U}_s$ in the early stage is very small, the iteration is insensitive to the variation of $\mathbf{U}_s$. This method of setting-

up the initial condition also proved satisfatory. The numerical calculation performed in this work used both methods.

2.5.2 Bunds of Unlimited Height

This section discusses the results in several sub-sections.

2.5.2.1 Shock Profile

Figures 2.8 and 2.9 are two examples of the results, which illustrate the shock motion from the beginning of shock formation until the shock approaches the axis. The other results are enclosed in Appendix C.

The shock level is almost uniform at the early stage of its formation, as described by Greenspan and Young. As the shock moves towards the axis and away from the bund, the liquid height at the shock front $\mathbf{r}_s$ is always lower than the height behind it. The height profile in the shock front region forms a curved surface, not a flat one. When the shock front is far away from the bund, the liquid level of the shock is almost uniform, i.e. the height gradient is very small. As soon as the shock front approaches the axis, it rises sharply, with its level higher than the liquid level behind it. This is clearly seen in Figures 2.8 and 2.9, when the shock position is situated around $\mathbf{r} = 0.1$, close to the axis. This description agrees with Greenspan and Young's illustration, where the shock converges and a new reflected shock departing from the axis is formed. Figure 2.10 shows the other aspect of the shock motion in the early stages. This figure depicts the shock level $\mathbf{h}_b$ and the downstream velocity $\mathbf{U}_b$ at the shock interface as a function of time. After the shock has been formed, the downstream velocity $\mathbf{U}_b$ increases sharply, reaches a maximum value and then falls steadily. When the velocity $\mathbf{U}_b$ is equal to zero, this corresponds to the shock level $\mathbf{h}_b$ reaching its maximum. This coincidence can be explained by using

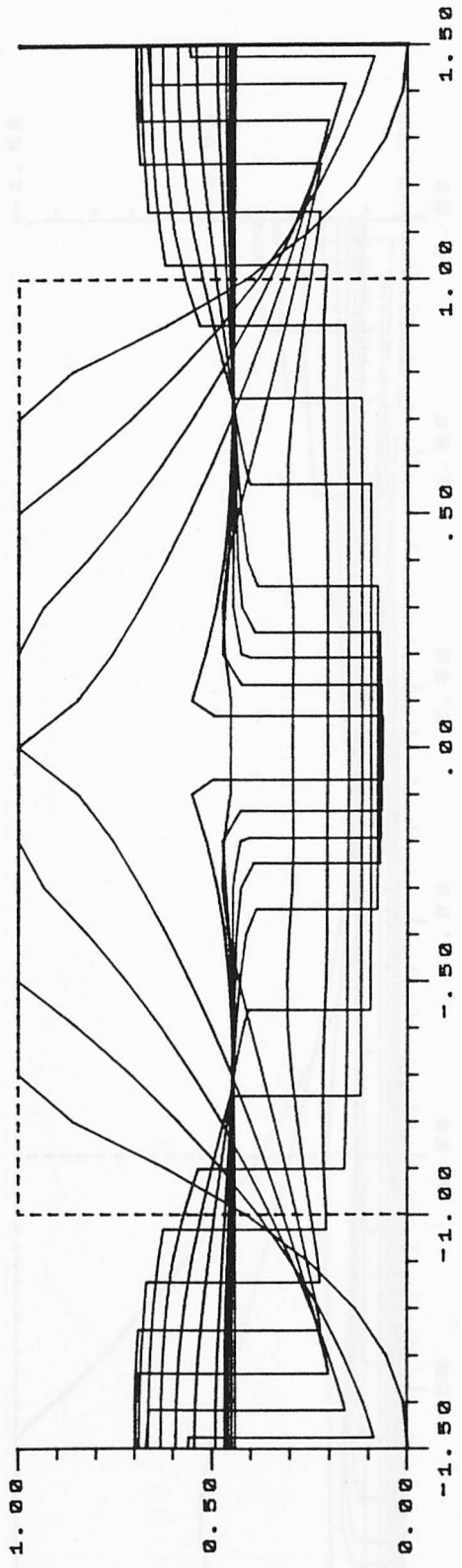


Figure 2.8: The shock profiles for $\mathbf{r}_w = 1.5$

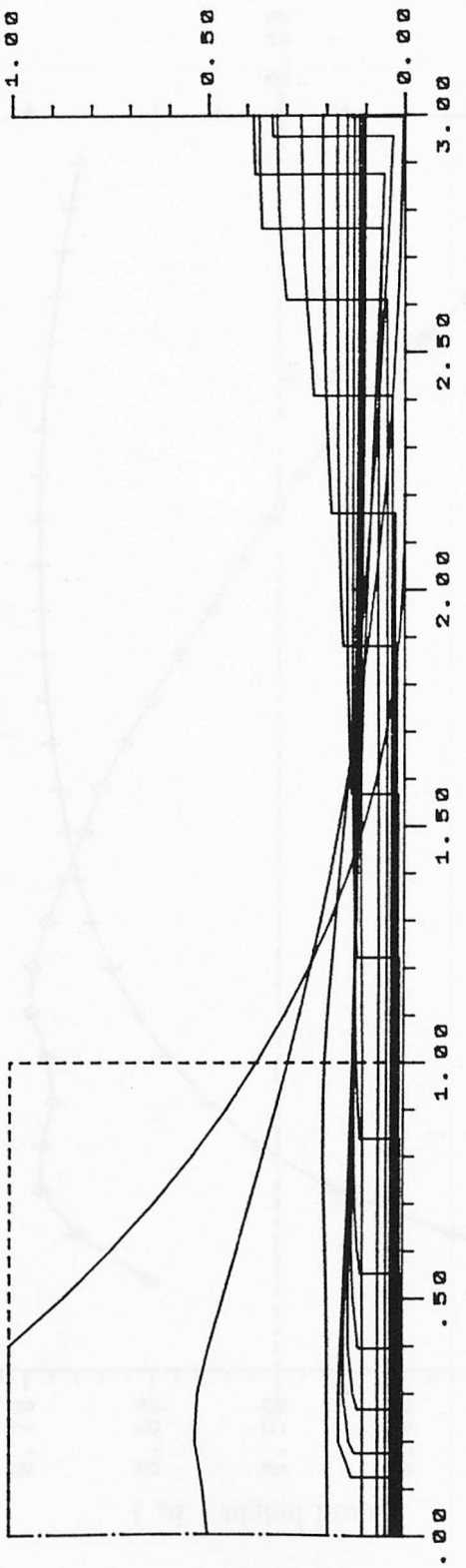


Figure 2.9: The shock profiles for $\mathbf{r}_w = 3$

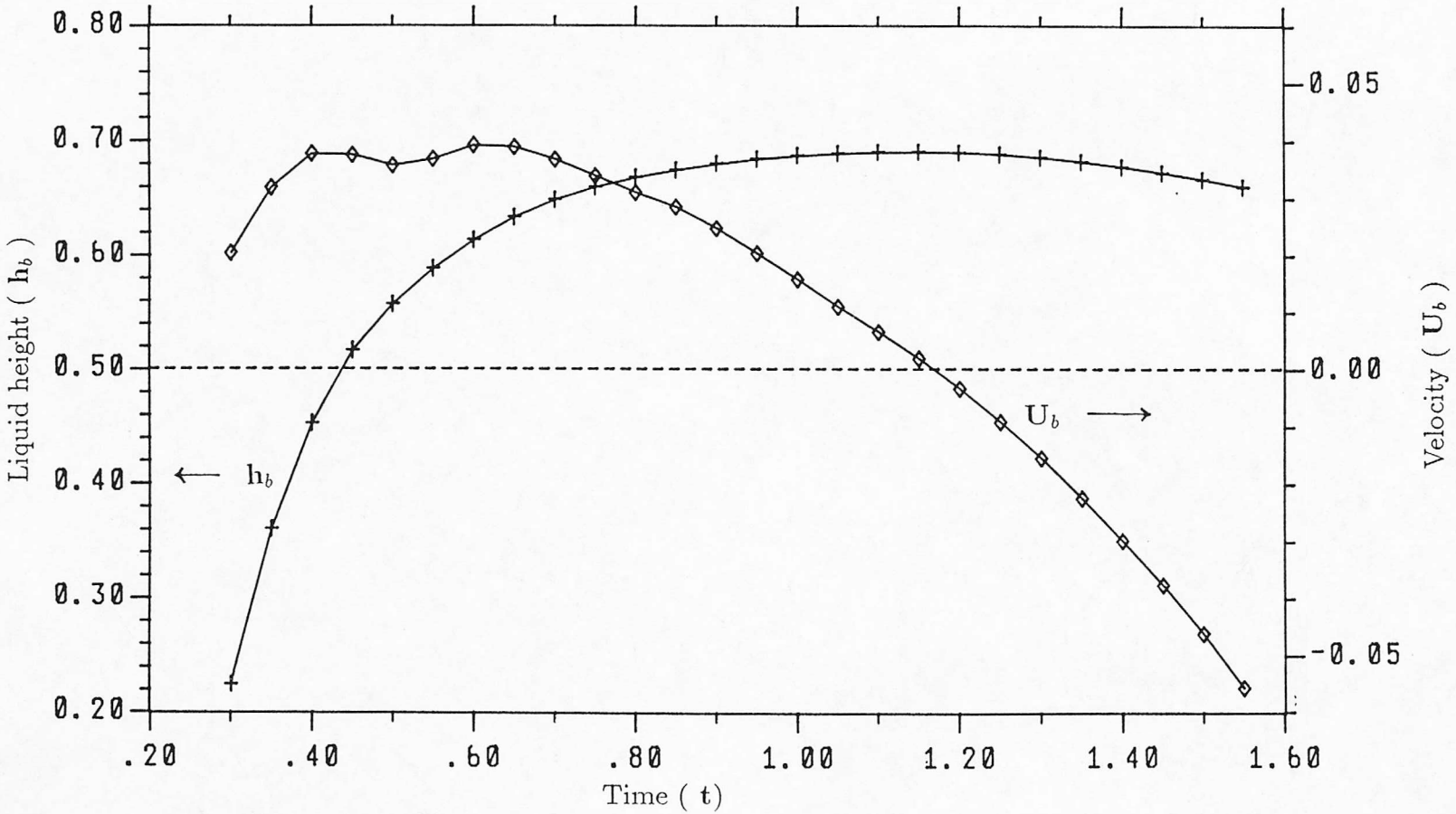


Figure 2.10: The downstream height $\mathbf{h}_b$ and velocity $\mathbf{U}_b$ when the shock level reaches a maximum

equation (1.3.10). When the shock level $\mathbf{h}_b$ reaches a maximum, $\frac{D\mathbf{h}}{Dt} = 0$. Equation (1.3.10) becomes :

$$\frac{D\mathbf{h}}{Dt} + \mathbf{h}\frac{\partial \mathbf{rU}}{\mathbf{r}\partial \mathbf{r}} = 0 \quad \text{or} \quad \frac{\partial \mathbf{rU}}{\partial \mathbf{r}} = 0 \quad .$$

This means that the velocity **U** in the shock flow is uniform ; the downstream velocity is equal to the velocity at the bund. This agrees with the calculation result, i.e. $\mathbf{U}_b = 0$, while the velocity at the bund $\mathbf{U}_w$ is known to be zero.

2.5.2.2 Mass and Energy Content

The mass and energy content were calculated for each time step after $\mathbf{t}_w$. One of the results is presented in Table II-1 and the others are given in Appendix C. It is shown that the mass (volume) error is still less than 1 %. As described in a previous section, the difference between the calculated energy content and the initial energy content is expressed as the energy discrepancy E_{discr}. This energy discrepancy should be equal to the total energy loss at the shock. This is shown in Table II-1 and Appendix C, where E_{discr} agrees very well with the energy loss at the shock. Their difference is less than 1 %. This shows that the numerical calculation results are consistent with the conservation of mass and energy.

By the time the shock converges into the axis, the rest of the energy content is close to the final energy level. This is illustrated in Figure 2.11 . The total initial energy content is $\frac{1}{2}\pi \mathbf{R}_0{}^2\mathbf{H}_0{}^2$. If the final liquid level inside the impounding area is $\mathbf{H}_{w,f}$, the final energy level is $\frac{1}{2}\pi \mathbf{r}_w{}^2\mathbf{H}_{w,f}{}^2$. As there is no mass loss, the conservation of mass is given by :

$$\pi \mathbf{r}_w{}^2\mathbf{H}_{w,f} = \pi \mathbf{R}_0{}^2\mathbf{H}_0 \quad , \quad \text{or} \quad \mathbf{H}_{w,f} = \left(\frac{\mathbf{R}_0}{\mathbf{r}_w}\right)^2 \mathbf{H}_0 \quad .$$

Table II-1: Mass error (V_{error}) and energy discrepancy (E_{discr}) for $\mathbf{r}_w = 1.5$

Time	V_{error}	E_{discr}	E_{loss}
0.40	-0.05	-2.63	2.80
0.50	-0.15	-6.68	6.72
0.60	-0.22	-10.85	10.79
0.70	-0.29	-14.82	14.66
0.80	-0.41	-18.54	18.22
0.90	-0.48	-21.87	21.44
1.00	-0.52	-24.86	24.37
1.10	-0.35	-27.30	27.03
1.20	-0.26	-29.63	29.46
1.30	-0.25	-31.84	31.66
1.40	-0.25	-33.86	33.67
1.50	-0.22	-35.66	35.50
1.60	-0.20	-37.30	37.17
1.70	-0.08	-38.67	38.67
1.80	-0.07	-40.02	40.03
1.90	-0.06	-41.21	41.22
2.00	-0.05	-42.22	42.25
2.10	-0.02	-43.07	43.12
2.20	-0.01	-43.80	43.86
2.30	0.00	-44.43	44.49
2.40	0.03	-44.95	45.04
2.50	0.05	-45.41	45.50
2.60	0.07	-45.79	45.90
2.70	0.12	-46.11	46.24
2.80	0.18	-46.37	46.52
2.90	0.25	-46.57	46.76
3.00	0.34	-46.60	46.94

It can be shown that the ratio of final energy level to the total initial energy content is $\left(\frac{\mathbf{R}_0}{\mathbf{r}_w}\right)^2$. For $\mathbf{r}_w = 2$, the final energy level is 25 % of the initial energy content, while the remaining total energy content when the shock reaches the axis is about 34 %. Hence at that instant, the system only has an energy of 9 % of the initial energy content available for subsequent flow (i.e. sloshing). With such a little energy remained, the reflected shock motion or sloshing flow is weaker than the (first) surge flow, hence the interaction of such sloshing flow with the bund is less impor-

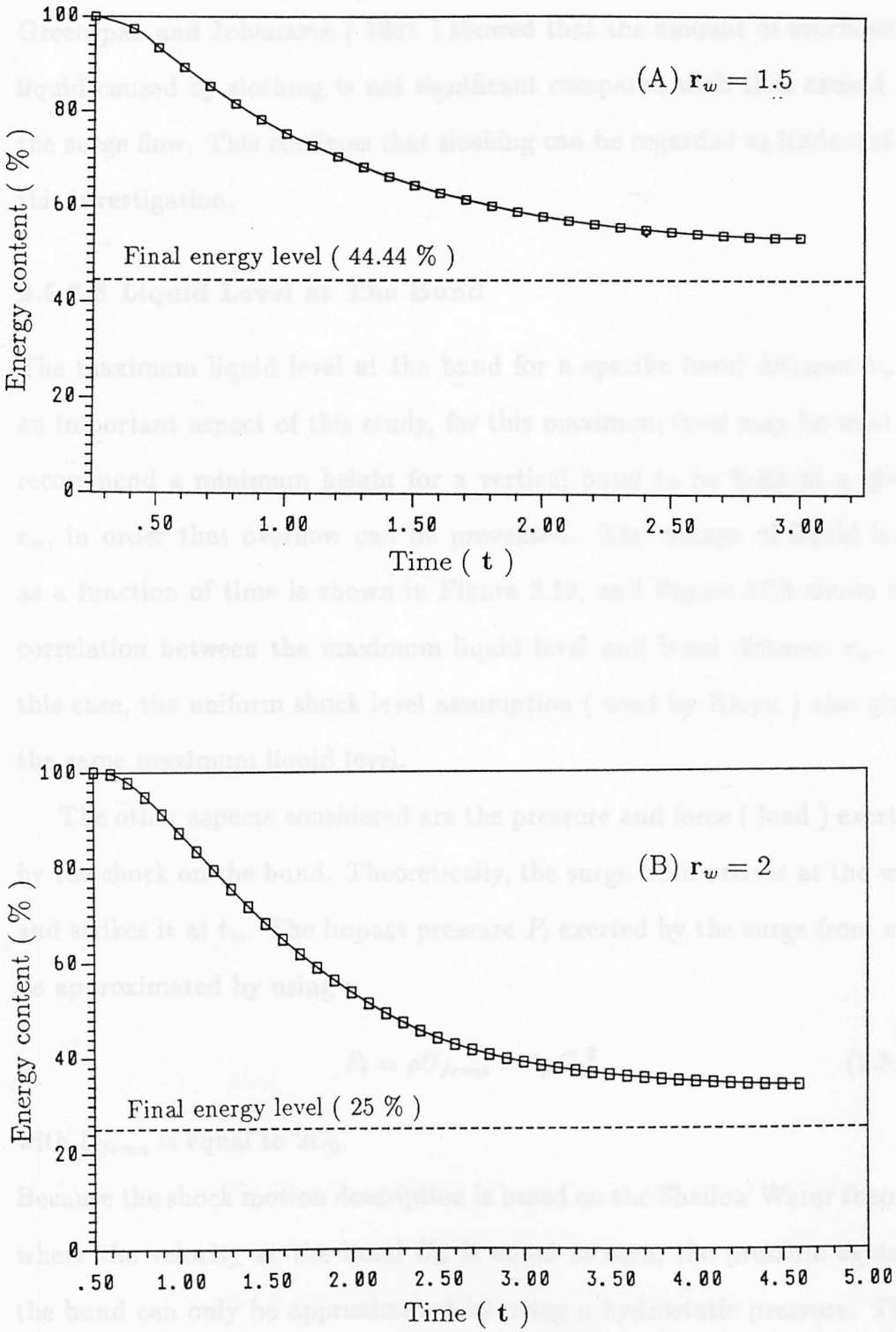


Figure 2.11: Energy content profiles for $r_w = 1.5$ and 2

tant than that of the surge flow. Based on this argument, the reflected shock motion or sloshing (Region VI) can be regarded as irrelevant in this study. The experimental observation by Greenspan and Young (1978) and Greenspan and Johansson (1981) showed that the amount of overflowing liquid caused by sloshing is not significant compared with that caused by the surge flow. This confirms that sloshing can be regarded as irrelevant in this investigation.

2.5.2.3 Liquid Level at The Bund

The maximum liquid level at the bund for a specific bund distance $\mathbf{r}_w$ is an important aspect of this study, for this maximum level may be used to recommend a minimum height for a vertical bund to be built at a given $\mathbf{r}_w$, in order that overflow can be prevented. The change of liquid level as a function of time is shown in Figure 2.12, and Figure 2.13 shows the correlation between the maximum liquid level and bund distance $\mathbf{r}_w$. In this case, the uniform shock level assumption (used by Kleyn) also gives the same maximum liquid level.

The other aspects considered are the pressure and force (load) exerted by the shock on the bund. Theoretically, the surge front arrives at the wall and strikes it at $\mathbf{t}_w$. The impact pressure P_i exerted by the surge front can be approximated by using :

$$P_i = \rho U_{front} = 4\rho {C_0}^2 \tag{2.5.2}$$

with U_{front} is equal to $2C_0$.

Because the shock motion description is based on the Shallow Water theory, where the velocity at the bund U_w is equal to zero, the pressure against the bund can only be approximated by using a hydrostatic pressure. This approximation may not be sufficient in the early stage of the shock forma-

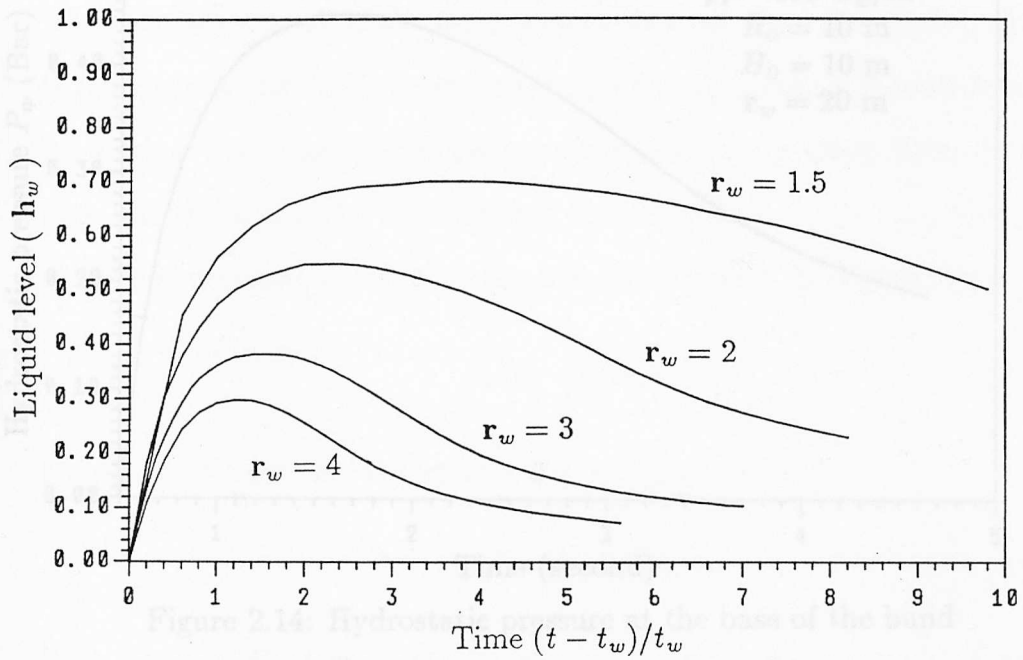


Figure 2.12: Liquid level at the bund

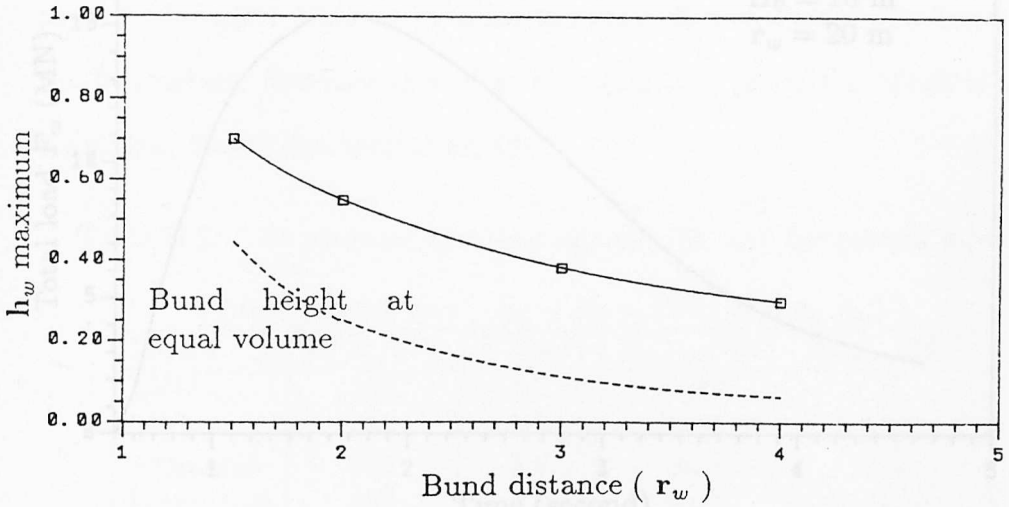


Figure 2.13: Maximum liquid level at the bund

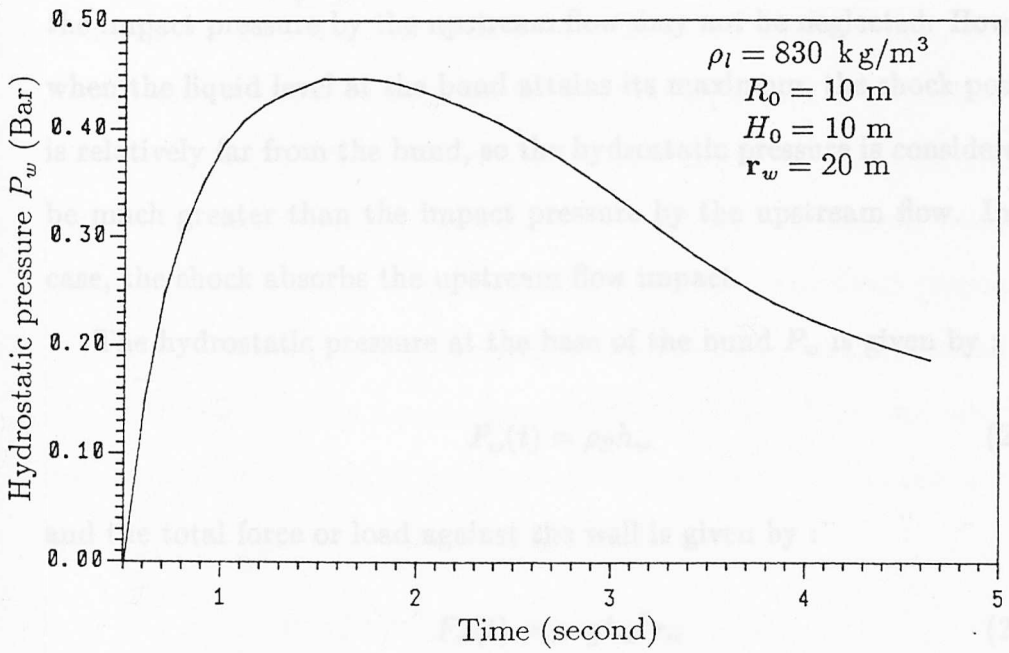


Figure 2.14: Hydrostatic pressure at the base of the bund

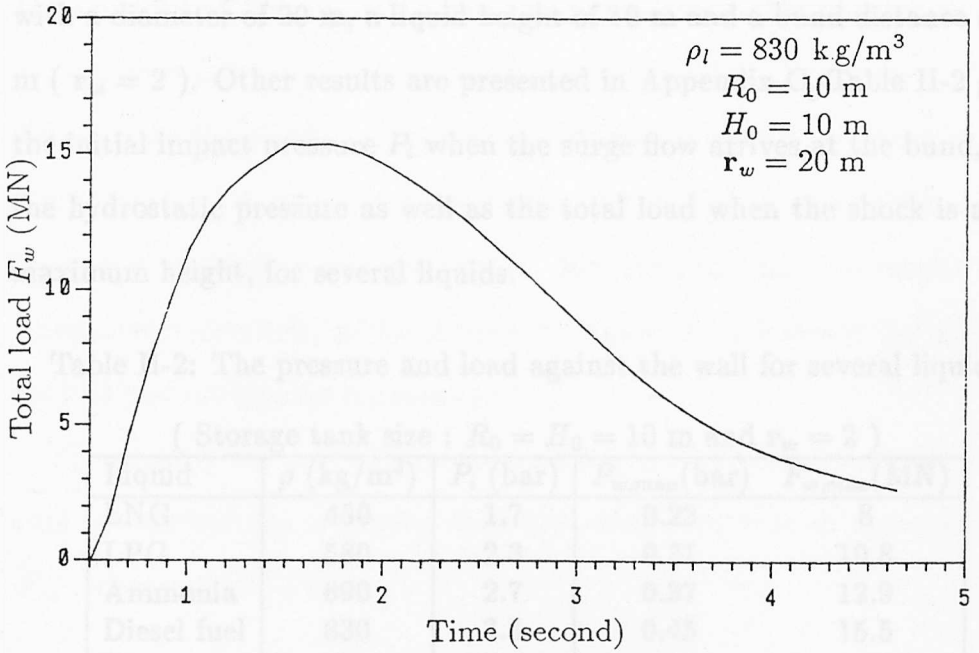


Figure 2.15: Total hydrostatic load against the bund

tion, where the shock position is very close to the wall. At this condition, the impact pressure by the upstream flow may not be neglected. However, when the liquid level at the bund attains its maximum, the shock position is relatively far from the bund, so the hydrostatic pressure is considered to be much greater than the impact pressure by the upstream flow. In this case, the shock absorbs the upstream flow impact.

The hydrostatic pressure at the base of the bund P_w is given by :

$$P_w(t) = \rho g h_w \tag{2.5.3}$$

and the total force or load against the wall is given by :

$$F_w(t) = \rho \pi g {h_w}^2 r_w \tag{2.5.4}$$

Here, P_w and F_w depend on the dimension of the storage tank. Figures 2.14 and 2.15 are examples of the hydrostatic pressure and total load at the bund as function of time for the storage tank containing diesel fuel, with a diameter of 20 m, a liquid height of 10 m and a bund distance of 20 m ($\mathbf{r}_w = 2$). Other results are presented in Appendix C. Table II-2 gives the initial impact pressure P_i when the surge flow arrives at the bund, and the hydrostatic pressure as well as the total load when the shock is at its maximum height, for several liquids.

Table II-2: The pressure and load against the wall for several liquids

(Storage tank size : $R_0 = H_0 = 10$ m and $\mathbf{r}_w = 2$)

Liquid	ρ (kg/m^3)	P_i (bar)	$P_{w,max}$(bar)	$F_{w,max}$(MN)
LNG	430	1.7	0.23	8
LPG	580	2.3	0.31	10.8
Ammonia	690	2.7	0.37	12.9
Diesel fuel	830	3.3	0.45	15.5
Water	1000	3.9	0.54	18.6

2.5.3 Overflow

In the case of overflow, the velocity at the bund $\mathbf{U}_w$ is estimated by equation (2.4.9) and the total volume of the overflowing liquid is calculated from equation (2.4.12). The overflow was found to affect the shock propagation velocity $\mathbf{U}_s$ and the shock position $\mathbf{r}_s$. The overflow reduces the volume of the shock flow (Region V), which in turn decreases the shock propagation velocity. Higher overflow rates result in lower shock propagation velocity. If the bund is so low that the overflow rate becomes very high, the volumetric rate of overflow F_{ov} can be greater than the volumetric rate of the upstream flow F_{us} (i.e. the inflow of the shock interface) :

$$\begin{aligned} \textit{overflow } F_{ov} &> \textit{upstream flow } F_{us} \quad , \\ 2\pi \mathbf{r}_w \mathbf{U}_w \mathbf{C}_w{}^2 &> 2\pi \mathbf{r}_s \mathbf{U}_f \mathbf{C}_f{}^2 \end{aligned} \tag{2.5.5}$$

At this condition, the shock slows down progressively until it finally stops. The shock then moves back, towards the bund and eventually disappears. Greenspan and Young, and Kleyn did not describe this phenomenon, although they also estimated the velocity at the bund $\mathbf{U}_w$ by equation (2.4.9). To estimate the overflow, it is initially considered that if the shock reaches the bund ($\mathbf{r}_s = \mathbf{r}_w$), overflow stops. After that, a new shock will be formed, and overflow will start again. However, this method results in an intermittent overflow, as illustrated in Figure 2.16, because the shock is formed and disappears repeatedly.

To simplify the problem, it is assumed that if the calculated volumetric rate of overflow F_{ov} is greater than the volumetric rate of upstream flow F_{us} (equation (2.5.5)) :

- the shock stops moving ($\mathbf{U}_s = 0$) and,
- the volumetric rate of overflow is taken to be equal to the volumetric

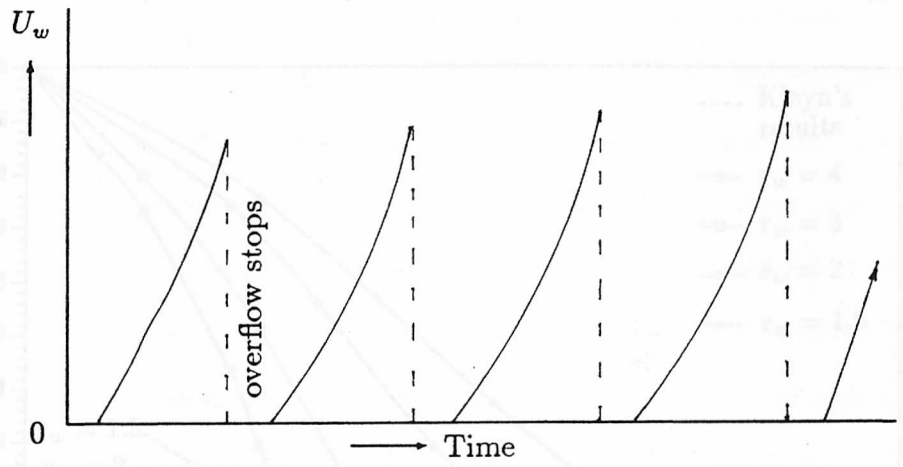


Figure 2.16: Illustration of an intermittent overflow

rate of upstream flow ($F_{ov} = F_{us}$).

Based on this assumption, the velocity at the bund $\mathbf{U}_w$ is then given by :

$$\mathbf{U}_w = \mathbf{U}_f \left(\frac{\mathbf{r}_s}{\mathbf{r}_w}\right) \left(\frac{\mathbf{C}_f}{\mathbf{C}_w}\right)^2 \tag{2.5.6}$$

From the viewpoint of numerical calculation, this method is simpler than the previous method, because there is no intermittent flow. This method also resulted in the same amount of the overflowing liquid as that given by the intermittent flow method. This work used either equation (2.4.9) or equation (2.5.6) to estimate the velocity $\mathbf{U}_w$, depending on the condition of overflow given by equation (2.5.5).

The total volume of the overflowing liquid at various bund distances and heights is presented in Figure 2.17, together with Kleyn's results. Figure 2.18 presents the amount of overflow as a function of bund height, which corresponds to the equal volume between the impounding area and the tank. Figure 2.18 shows that further bund distance ($\mathbf{r}_w >> 1$) gives larger amount of the overflowing liquid.

Figures 2.17 and 2.18 show that Kleyn underestimated the amount of overflow, as also confirmed by Sharifi. This is caused by his method of the

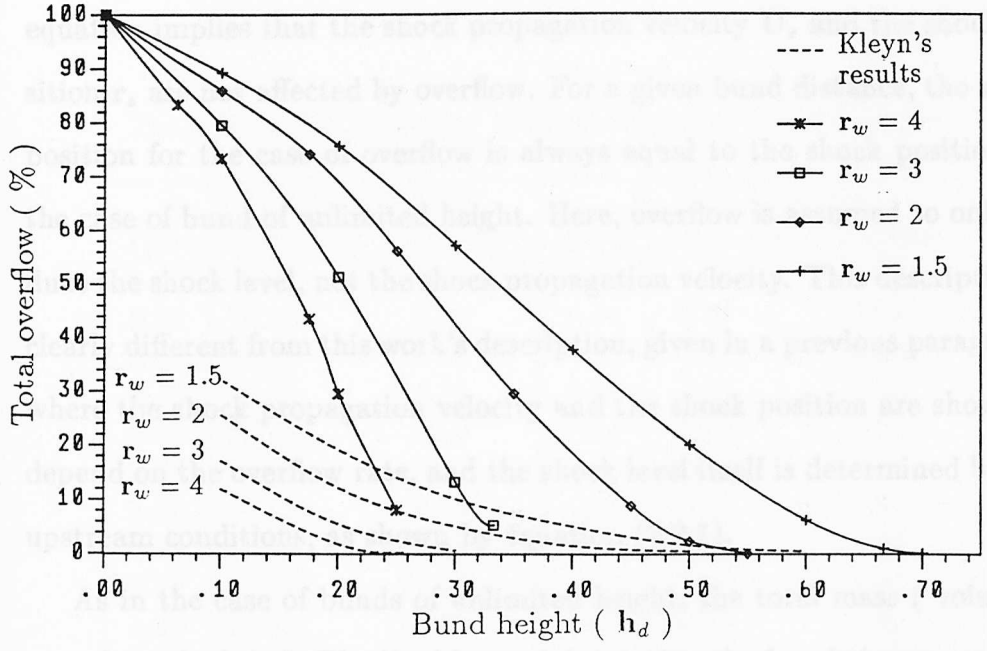


Figure 2.17: Total overflow for various values of $\mathbf{h}_d$ and $\mathbf{r}_w$

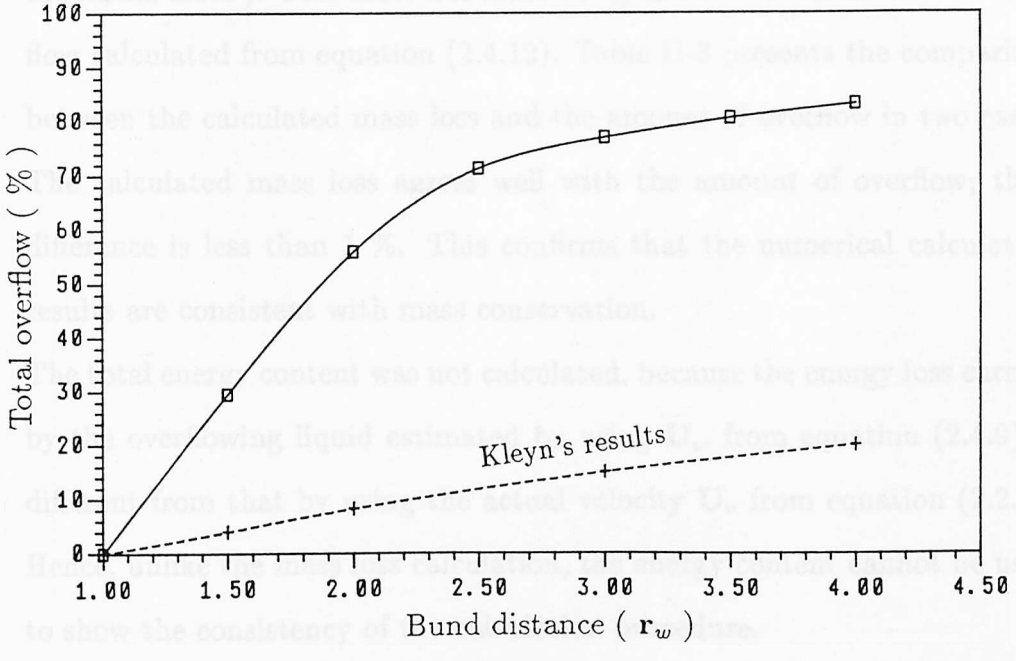


Figure 2.18: Total overflow for $\mathbf{h}_d$ corresponding to equivalent volume of tank capacity

amount of overflow estimation, which is based on equation (2.2.10). This equation implies that the shock propagation velocity $\mathbf{U_s}$ and the shock position $\mathbf{r_s}$ are not affected by overflow. For a given bund distance, the shock position for the case of overflow is always equal to the shock position for the case of bund of unlimited height. Here, overflow is assumed to only reduce the shock level, not the shock propagation velocity. This description is clearly different from this work's description, given in a previous paragraph, where the shock propagation velocity and the shock position are shown to depend on the overflow rate, and the shock level itself is determined by the upstream conditions, as shown by equation (2.2.1).

As in the case of bunds of unlimited height, the total mass (volume) was also calculated. The liquid remaining inside the bunded area was numerically calculated, and the difference between the remaining liquid and the initial mass (volume) is expressed as the mass loss (as a percentage of the initial mass). This mass loss must be equal to the total amount of overflow calculated from equation (2.4.12). Table II-3 presents the comparison between the calculated mass loss and the amount of overflow in two cases. The calculated mass loss agrees well with the amount of overflow; their difference is less than 1 %. This confirms that the numerical calculation results are consistent with mass conservation.

The total energy content was not calculated, because the energy loss carried by the overflowing liquid estimated by using $\mathbf{U_w}$ from equation (2.4.9) is different from that by using the actual velocity $\mathbf{U_v}$ from equation (2.2.3). Hence, unlike the mass loss calculation, the energy content cannot be used to show the consistency of the calculation procedure.

Overflow occurs, when the liquid jumps above the bund and falls onto the ground outside the bunded area. The distance between the bund and

Table II-3: The mass loss and the total amount of overflow

$r_w = 1.5$, $h_d = 0.4444$			$r_w = 2$, $h_d = 0.25$		
Time	Mass-Loss	Overflow	Time	Mass-Loss	Overflow
0.40	0.05	0.00	0.60	0.04	0.00
0.50	0.59	0.42	0.70	0.16	0.09
0.60	1.78	1.53	0.80	1.05	0.95
0.70	3.43	3.12	0.90	2.75	2.63
0.80	5.38	5.00	1.00	5.09	4.95
0.90	7.45	7.02	1.10	7.75	7.74
1.00	9.57	9.10	1.20	10.72	10.80
1.10	11.56	11.18	1.30	13.91	14.02
1.20	13.54	13.23	1.40	17.21	17.32
1.30	15.53	15.24	1.50	20.55	20.66
1.40	17.47	17.18	1.60	23.89	23.99
1.50	19.31	19.02	1.70	27.16	27.24
1.60	21.00	20.71	1.80	30.32	30.40
1.70	22.56	22.27	1.90	33.35	33.42
1.80	23.97	23.69	2.00	36.23	36.29
1.90	25.23	24.95	2.10	38.95	39.01
2.00	26.33	26.06	2.20	41.50	41.54
2.10	27.25	26.99	2.30	43.87	43.89
2.20	28.02	27.76	2.40	46.04	46.03
2.30	28.60	28.36	2.50	47.98	47.96
2.40	29.03	28.79	2.60	49.74	49.68
2.50	29.29	29.06	2.70	51.24	51.18
2.60	29.42	29.19	2.80	52.51	52.46
2.70	29.46	29.21	2.90	53.57	53.52
			3.00	54.42	54.36
			3.10	55.05	55.00
			3.20	55.51	55.45
			3.30	55.79	55.74
			3.40	55.96	55.90
			3.50	56.04	55.97
			3.60	56.06	55.98
			3.70	56.07	55.98

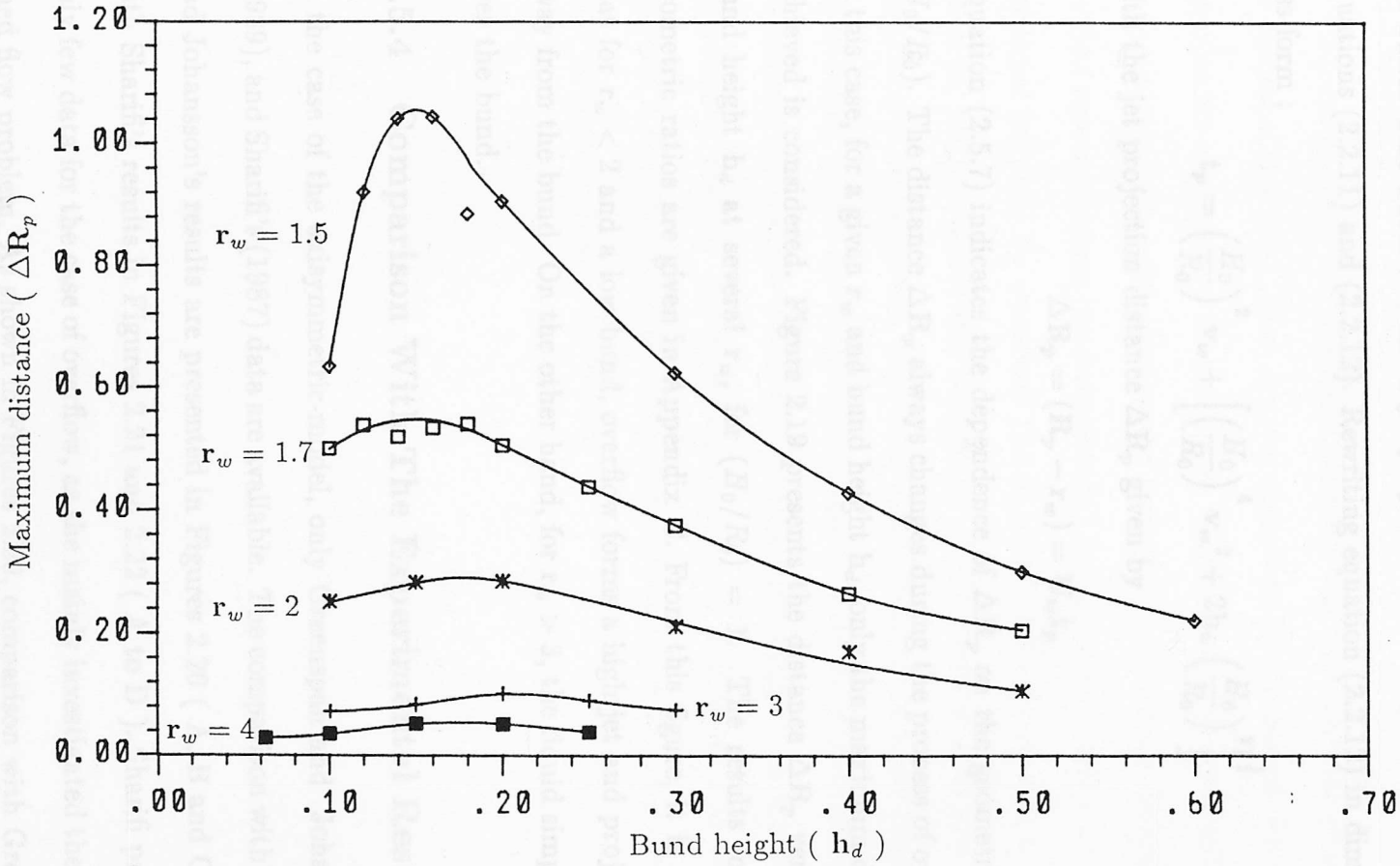


Figure 2.19: Maximum jet projection distance for $(H_0/R_0) = 1$

the position where the liquid jet falls can be important, for this can be used to consider the minimum acceptable distance of the units or equipment from the bund. This distance (called jet projection distance) is calculated from equations (2.2.11) and (2.2.12). Rewriting equation (2.2.12) in dimensionless form :

$$\mathbf{t}_p = \left(\frac{H_0}{R_0}\right)^2 \mathbf{v}_w + \left[\left(\frac{H_0}{R_0}\right)^4 \mathbf{v}_w{}^2 + 2\mathbf{h}_w \left(\frac{H_0}{R_0}\right)^2\right]^{\frac{1}{2}} \tag{2.5.7}$$

with the jet projection distance $\Delta\mathbf{R}_p$ given by :

$$\Delta\mathbf{R}_p = (\mathbf{R}_p - \mathbf{r}_w) = \mathbf{U}_w \mathbf{t}_p \tag{2.5.8}$$

Equation (2.5.7) indicates the dependence of $\Delta\mathbf{R}_p$ on the geometric ratio (H_0/R_0). The distance $\Delta\mathbf{R}_p$ always changes during the process of overflow. In this case, for a given $\mathbf{r}_w$ and bund height $\mathbf{h}_d$, only the maximum distance achieved is considered. Figure 2.19 presents the distance $\Delta\mathbf{R}_p$ versus the bund height $\mathbf{h}_d$ at several $\mathbf{r}_w$, for $(H_0/R_0) = 1$. The results for other geometric ratios are given in Appendix C. From this figure, it is obvious that for $\mathbf{r}_w < 2$ and a low bund, overflow forms a high jet and projects far away from the bund. On the other hand, for $\mathbf{r}_w > 3$, the liquid simply slips over the bund.

2.5.4 Comparison With The Experimental Results

In the case of the axisymmetric-model, only Greenspan and Johansson's (1989), and Sharifi's (1987) data are available. The comparison with Greenspan and Johansson's results are presented in Figures 2.20 (A, B and C), and with Sharifi's results in Figures 2.21 and 2.22 (A to D). Sharifi produced only few data for the case of overflow, as she mainly investigated the unconfined flow problem. As shown in Figures 2.20, comparison with Greenspan and Johansson's data shows that this theoretical work appears to overestimate the amount of overflow at low bunds, and to underestimate it at

high bunds. On the other hand, comparison with Sharifi's data (Figure 2.21) shows that this work overestimates the amount of overflow for all bund heights.

Concerning with the difference between the experimental results and the results of this work, there are two aspects to be considered. Firstly, the experiments used small-scale models, at which the overflow may suffer from the geometric-scale ratio, viscous and surface tension effects. Secondly, the overflow rate at extreme bund conditions (low and high bunds) may not be estimated properly by equations (2.4.9) and (2.5.6). In view of these two concerns, further theoretical estimation of the overflow rate and further experimental investigation, especially using larger models, are needed. Nevertheless, within the range of uncertainty of the experimental accuracy, the amount of overflow predicted by this work roughly agrees with the experimental results. The comparison of liquid level motion at the bund (Figures 2.22) also shows an agreement with that given by this theoretical work, as already claimed by Sharifi.

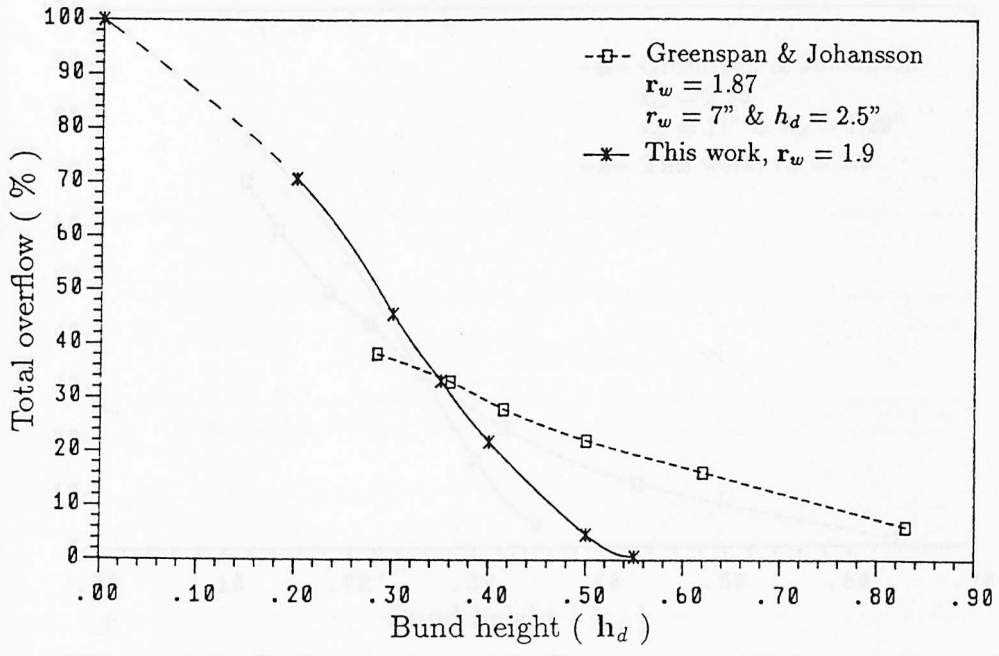


Figure 2.20-A: Comparison with Greenspan and Johansson's results

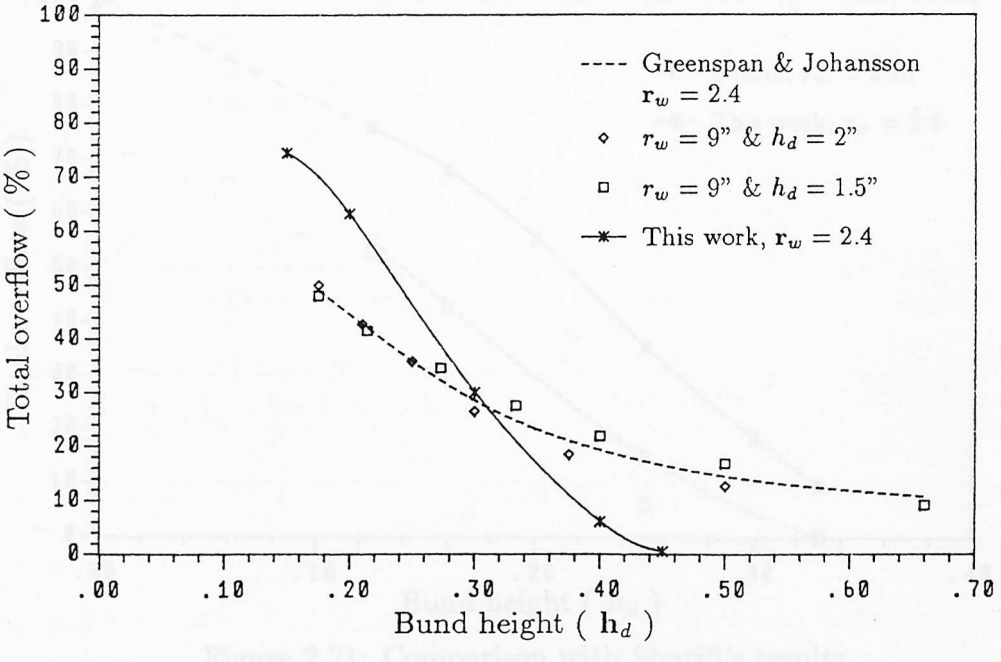


Figure 2.20-B: Comparison with Greenspan and Johansson's results

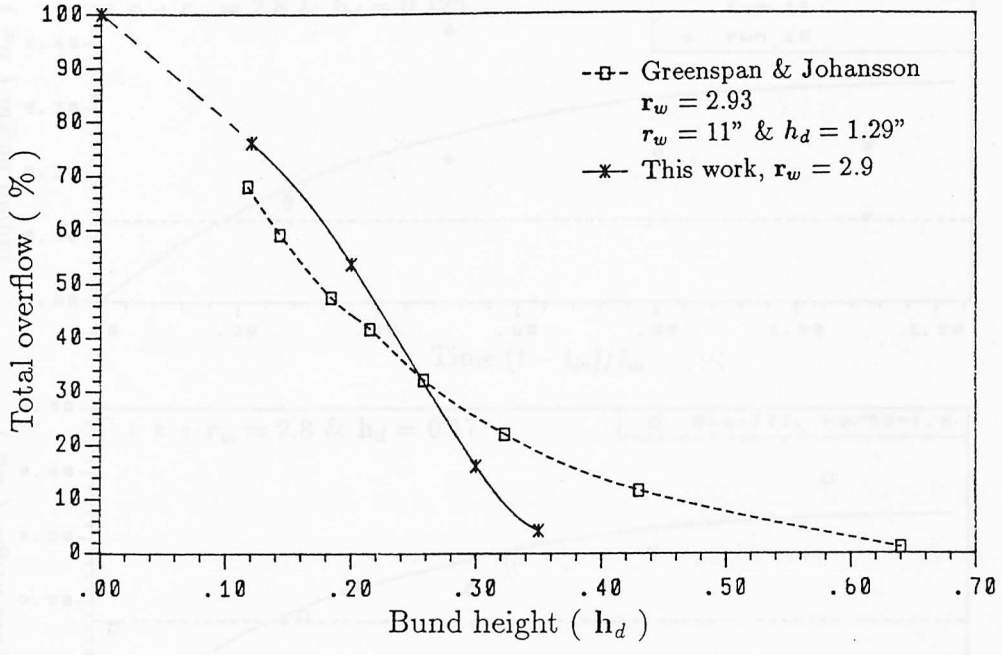


Figure 2.20-C: Comparison with Greenspan and Johansson's results

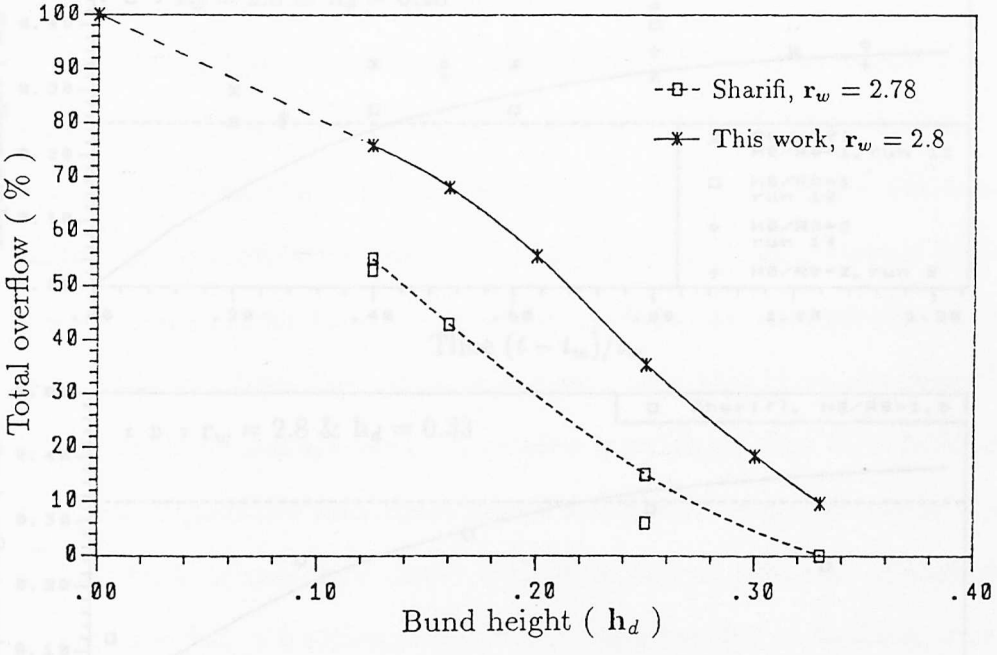


Figure 2.21: Comparison with Sharifi's results

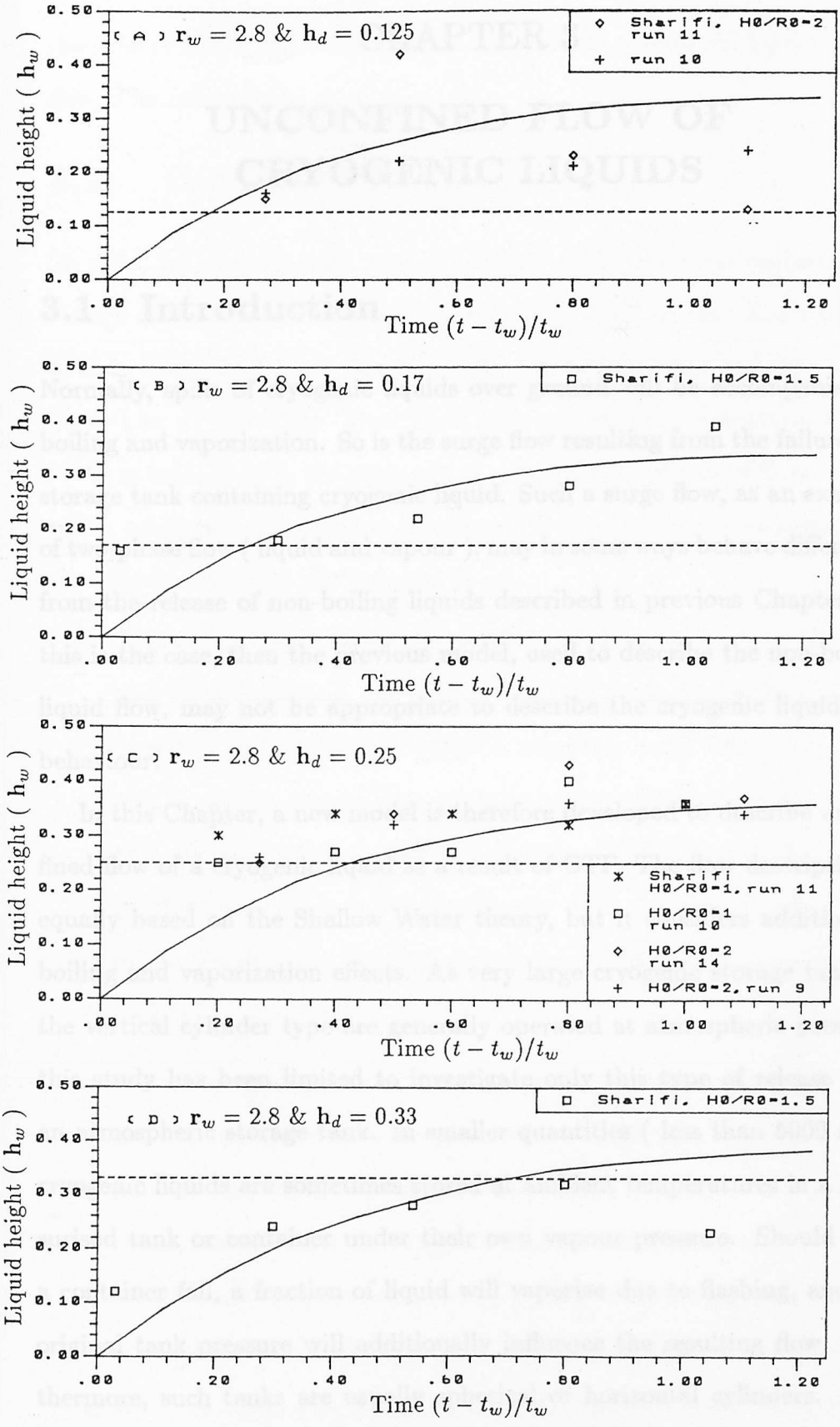


Figure 2.22: Comparison of h_w between the results of this work and Sharifi's results

CHAPTER 3

UNCONFINED FLOW OF CRYOGENIC LIQUIDS

3.1 Introduction

Normally, spills of cryogenic liquids over ground will be accompanied by boiling and vaporization. So is the surge flow resulting from the failure of a storage tank containing cryogenic liquid. Such a surge flow, as an example of two-phase flow (liquid and vapour), may in some ways behave differently from the release of non-boiling liquids described in previous Chapters. If this is the case, then the previous model, used to describe the non-boiling liquid flow, may not be appropriate to describe the cryogenic liquid flow behaviour.

In this Chapter, a new model is therefore developed to describe unconfined flow of a cryogenic liquid as a result of CTF. The flow description is equally based on the Shallow Water theory, but it considers additionally boiling and vaporization effects. As very large cryogenic storage tanks of the vertical cylinder type are generally operated at atmospheric pressure, this study has been limited to investigate only this type of release from an atmospheric storage tank. In smaller quantities (less than 5000 m^3), cryogenic liquids are sometimes stored at ambient temperatures in a pressurised tank or container under their own vapour pressure. Should such a container fail, a fraction of liquid will vaporize due to flashing, and the original tank pressure will additionally influence the resulting flow. Furthermore, such tanks are usually spherical or horizontal cylinders. Such conditions are clearly not those of this study, which is concerned only with

the flow resulting from the collapse of a vertical cylindrical liquid column due to its own weight.

3.2 Review of Related Work

To date, no work directly relevant to this study has been reported. Although much work concerning cryogenic liquid spills on land and water has already been carried out, some aspects of these investigations are different from those in this study. Their main purpose has been to estimate the size of the spreading pool, the evaporation rate and the amount of liquid evaporated, which are main factors considered in vapour dispersion assessment. The different aspects just referred to are :

- The scope of interest of the previous work extends up to when the spill stops spreading, due to loss of driving force, where the spill layer is very thin. This occurs over a relatively long time span, which may comprise several flow regimes: gravity-inertia, gravity-viscous and viscous-surface tension (Fannelop and Waldman, 1971). By contrast, this study is concerned only with the early stages of spill, in the gravity-inertia regime, as pointed out by Webber and Brighton (1986).
- Because in previous work the interest in the nature of the flow is less specific and the flow takes place over a large time span, the governing flow equations are simple, and apply irrespective of the initial shape/form of the source of spill (such as a cylindrical tank). Hence, models used in the previous work may not describe properly the flow behaviour resulting from CTF, which is of interest for this study.

To show the governing equations used in the previous work, the following is a quotation of three such papers on cryogenic liquid spills on land. They

are those of Shaw and Briscoe (1978), Raj (1981) and Webber and Brighton (1986).

Shaw and Briscoe, and Raj, considered that the whole spreading process (from start to finish) occurs only in the gravity-inertia regime, and that the propagation velocity of the front edge only depends on the average liquid height throughout the spreading pool. They neglected viscous and surface tension effects in the later stages of the spreading process.
Shaw and Briscoe estimated the propagation velocity U of the moving front edge by :

$$U = \frac{dR}{dt} = (2gh)^{0.5} \tag{3.2.1}$$

with $h = \dfrac{V}{\pi R^2}$,

where h = the average liquid height throughout the pool,

R = the radius of the pool,

t = time

V = total volume of the remaining liquid.

Based on the rate of the liquid release, Raj classified cryogenic liquid spills into: instantaneous, semi-continuous and continuous releases. The sudden release of liquid from the rupture of a storage tank is an example of an instantaneous release. Raj used a different estimate for the propagation velocity of the moving front edge from that of Shaw and Briscoe. He assumed that the ground is smooth and frictionless. Raj used the equation :

$$R\frac{d^2R}{dt^2} = -\frac{gh}{P} \tag{3.2.2}$$

where P is a factor, representing the ratio of the inertia of the liquid to the inertia of the liquid if it was everywhere moving with the acceleration of the moving front. Raj evaluated the factor P and found it equal to 0.754.

Webber and Brighton claimed that their model represents an improvement over previous work, as it included the viscous effect that influences the later stages of the spreading process. The governing equations of their model are :

$$\frac{dV}{dt} = -\pi R^2 m \tag{3.2.3}$$

$$\frac{dU}{dt} = \frac{4g(1-s)h}{R} - F \tag{3.2.4}$$

with $F = C_L \frac{U^2}{h} + \left(\frac{3}{2}\right)^5 \frac{\nu U}{h^2}$,

where U = the propagation velocity of the front,

h = the average liquid height throughout the pool,

m = the mass rate of vaporization,

s = a shape factor,

F = friction term,

C_L = Chezy friction coefficient,

ν = kinematic viscosity,

Here, the shape factor s is defined by $h_{front} = sh$; s depends on the shape of the moving front edge, and is related to the stages of the spreading process. Webber and Brighton described that, in the early stages of spread, the gravity force is balanced by the inertia force (i.e. in the gravity-inertia regime). Later, the inertia force may become negligible, and the ground resistance and viscous forces will then balance the gravitational force (i.e. the gravity-viscous regime). Over the whole period of the spread, Webber and Brighton considered that the flow profile gradually changes (represented by shape factor s), where :

- $s = 0$ in the early stages of the spread, with zero height of the front edge. After that,

- $0 < s < 1$ where the spreading pool is thicker in the middle and thinner at the front, and

- $s > 1$ where the pool is thick at the edge and thin in the middle.

Unfortunately, they did not describe in detail how the shape of the moving front edge changes from one stage to another stage of the spread.
In the early stage of spread, their front edge condition (i.e. $h_{front} = 0$) is equivalent to that in the Shallow Water theory described in Chapter 1. Webber and Brighton pointed out that, their model cannot describe the details of the acceleration from rest with an arbitrary initial height profile at the early stage of spread, as their model does not consider the initial form/shape of the spill source. It therefore differs from the dam-break problem (described in Chapter 1), which is similar to the problem of this study and is concerned only with the early stages of the spreading process. All this explains the difference in the point of interest between previous work on cryogenic liquid spills and that of this study.

Although not concerned with cryogenic liquid spread, very relevant to this study is the work of Chan and Banerjee (1981), who simulated an injection of an emergency coolant into a reactor core cooling system during a Loss of Coolant Accident (LOCA), in the CANDU (Canadian Deuterium-Uranium) nuclear reactor. Fuel rods of the CANDU reactor are in horizontal position, inside horizontal cooling tubes. Under normal operation, heavy water as a coolant flows through the annulus between the fuel rod and the cooling tube. In a LOCA, cooling tubes become dry, because the coolant suddenly stops flowing into the reactor, while heat is continuously generated from nuclear reaction. This makes the temperature of the reactor core rise rapidly. To prevent an excessive temperature rise of the reactor core and the possibility of fuel melting, an Emergency Core Cool-

ing (ECC) must be carried out, by injecting water into the cooling tubes. Chan and Banerjee simulated this phenomenon theoretically and experimentally. They used a hot horizontal tube, into which water is suddenly injected. From the heat transfer point of view, this process is commonly called quenching, where a hot surface is brought in direct contact with a cold liquid, in order to reduce the surface temperature quickly.

When a cold liquid contacts a hot surface at a significantly higher temperature, initially film boiling occurs whenever there is a relatively high temperature difference. A thin vapour layer covers the hot surface, separating the liquid from the surface and thus preventing direct contact between them. If the temperature of the hot surface decreases, the boiling mode can change from film boiling to transition and subsequently to nucleate boiling. In nucleate boiling, the hot surface is covered by liquid and bubbles; the liquid contacts directly with the hot surface over the area not covered by bubbles. During transition boiling *rewetting* may take place, where the hot surface is rewetted with liquid, or the vapour-liquid interface in film boiling collapses. In pool boiling, the transition from film boiling to transition boiling occurs at a specific temperature, which is sometimes called the Leidenfrost temperature.

Figure 3.1 illustrates Chan and Banerjee's flow description. As water is injected into a hot horizontal tube, the front part of the flow forms a tongue-like shape. They identified three regions: the totally quenched (A – A′), the partially quenched (B – B′) and the film boiling region (C – C′). In the totally quenched region, the tube is fully filled with liquid, which may contain vapour bubbles resulting from nucleate or transition boiling. The heat transfer mode in this region is a forced convective boiling. In the film boiling region, the liquid tongue has no contact with the tube wall, due to

the existence of a thin film of vapour. In this description, quenching begins when film boiling ceases and changes into transition boiling; the vapour-liquid interface in film boiling collapses and the tube wall is rewetted by liquid. Rewetting takes place between the totally quenched and the film boiling regions, starting from the bottom, then at the middle and finally at the top of the inside surface of the tube. Here, rewetting does therefore not occur simultaneously at the same cross-sectional position.

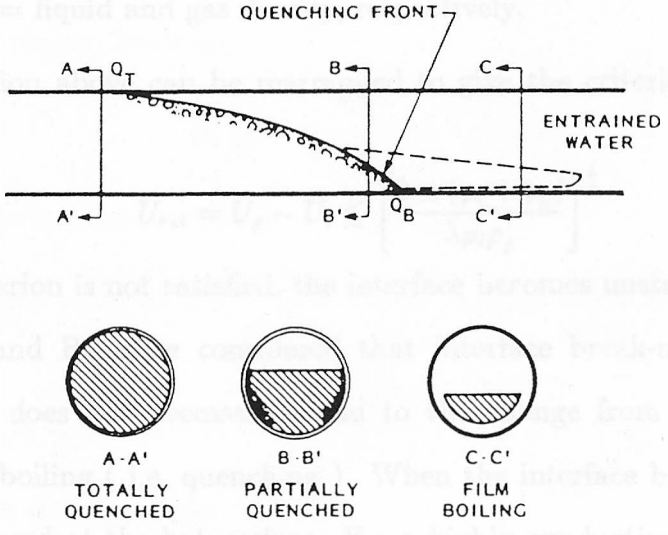


Figure 3.1: Characteristics of channel rewetting according to Chan and Banerjee

To describe the rewetting phenomenon in an Emergency Core Cooling, Chan and Banerjee used Zuber's theory (Zuber, 1958) on the instability of the liquid-vapour interface of film boiling in pool boiling. Zuber based his theory on the Kelvin-Helmholtz instability of an interfacial wave.

Zuber considered that film boiling exists as long as an interfacial wave (with a wavelength of λ) at the vapour-liquid interface is stable; the wavelength λ is less than critical wavelength λ_c. Conversely, when the interfacial wave grows so that its wavelength exceeds λ_c, the interface becomes unstable. The interface will break up or the hot surface will be rewetted, and

the boiling mode will change from film boiling to transition boiling. Based on the Kelvin-Helmholtz theory on interface wave, λ_c is given by:

$$\lambda_c = \frac{2\pi\sigma(\rho_l + \rho_g)}{\rho_l \rho_g {U_{rel}}^2}$$

with U_{rel} = relative velocity between vapour (U_g) and liquid (U_l) at the interface,

σ = interfacial tension,

λ = wavelength at the interface,

ρ_l,ρ_g = liquid and gas density, respectively.

The equation above can be rearranged to give the criterion for interface stability :

$$U_{rel} = U_g - U_l \leq \left[\frac{2\pi\sigma(\rho_l + \rho_g)}{\lambda \rho_l \rho_g}\right]^{\frac{1}{2}} \qquad (3.2.5)$$

If this criterion is not satisfied, the interface becomes unstable.

Chan and Banerjee considered that interface break-up, and surface rewetting, does not necessarily lead to the change from film boiling to transition boiling (i.e. quenching). When the interface breaks up, a wet spot is formed at the hot surface. For a highly conductive and high heat capacity surface, the wet spot just formed may dry up rapidly due to sufficiently rapid heat transfer, thus the vapour film in boiling is restored. On the other hand, for a low heat capacity surface, such as a thin tube wall, rewetting that leads to the change from film boiling to transition boiling can take place the first time the wet spot forms, even at a temperature higher than the Leidenfrost temperature. Their flow experiments support this argument: in their case, rewetting does not always occur at the Leidenfrost temperature. Instead, it can happen at a higher temperature. Their theoretical prediction of the rewetting position along the tube, based on the stability criterion of an interfacial wave mentioned above, is in very good agreement with their experimental results.

To estimate the rewetting position, the vapour flow conditions below the liquid phase must be known. Chan and Banerjee derived the governing equations for the vapour-phase beneath the liquid-phase by conservation of mass and momentum. Figure 3.2 illustrates the cross-sectional view of the tube in the film boiling region, which underlies their analysis. In this case, it is assumed that heat from the wall is transferred merely by molecular conduction across the vapour film (as in film boiling theory), and that the vapour density is constant along the channel.

Mass conservation leads to :

$$\rho_g \frac{\partial \delta}{\partial t} + \rho_g \frac{\partial \delta U_g}{\partial x} = \frac{k\Delta T}{h_{fg}} \frac{1}{\delta} \tag{3.2.6}$$

and momentum conservation to :

$$\frac{\partial \delta U_g}{\partial t} + \frac{\partial \delta {U_g}^2}{\partial x} = -\frac{1}{\rho_g} \frac{\partial \delta p}{\partial x} - \frac{1}{\rho_g}(\tau_g + \tau_i) + \frac{k\Delta T}{\rho_g h_{fg}} \frac{U_i}{\delta} \tag{3.2.7}$$

with $p - p_0 = \rho_l g(h_l - y) - \frac{1}{\rho_g}\left(\frac{k\Delta T}{h_{fg}}\frac{1}{\delta}\right)^2 - \sigma\left[1 + \left(\frac{\partial \delta}{\partial x}\right)^2\right]^{-\frac{3}{2}} \frac{\partial^2 \delta}{\partial x^2}$

and p = local pressure,

τ = shear stress,

δ = vapour film thickness,

U_i = interfacial velocity,

x = peripheral position (see in Figure 3.2),

h_l = liquid level (see in Figure 3.2),

y = hydraulic depth,

h_{fg} = latent heat of vaporization,

k = thermal conductivity of vapour,

ΔT = temperature difference between liquid and hot surface.

Subscripts g and i respectively denote vapour and interfacial. Equations (3.2.6) and (3.2.7) are essentially solved numerically by using an explicit

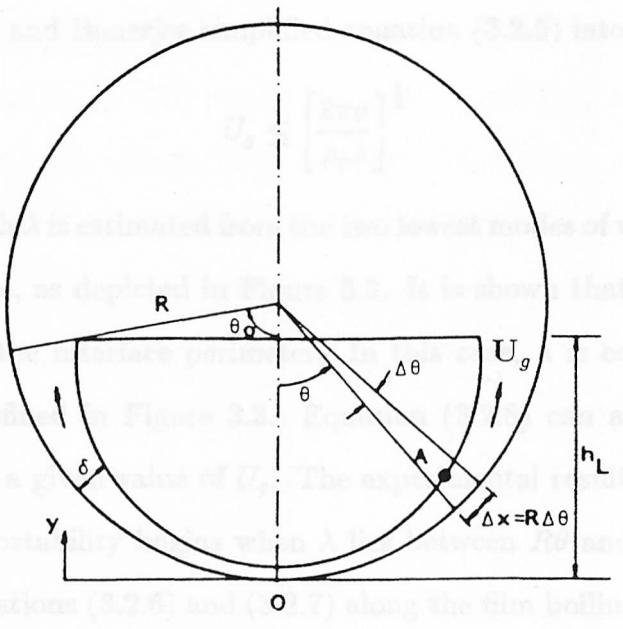


Figure 3.2: Chan and Banerjee's analysis on film boiling

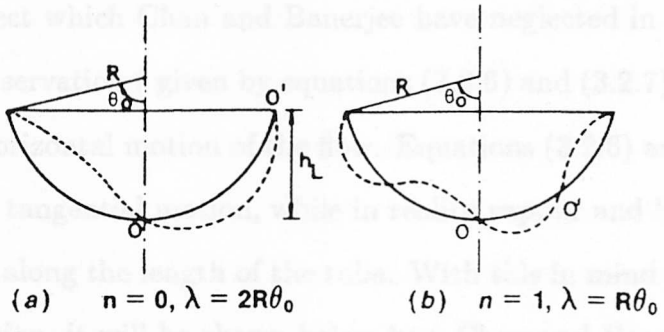


Figure 3.3: Two possible modes of oscillation

finite-difference technique. The results show that δ is nearly constant in the first half of the vapour channel and opens up rapidly after that. The vapour velocity U_g rises linearly from zero at the bottom, goes to a maximum at the point where δ starts to increase rapidly, then decreases due to the increase of δ. By using the average value of U_g along x (corresponding to the liquid height), the stability of the vapour-liquid interface can be checked from equation (3.2.5). As U_l (with the same direction as U_g) can be neglected (being very small compared with U_g) and ρ_l is generally much greater

than ρ_g, Chan and Banerjee simplified equation (3.2.5) into :

$$U_g \leq \left[\frac{2\pi\sigma}{\rho_g \lambda}\right]^{\frac{1}{2}} \tag{3.2.8}$$

The wavelength λ is estimated from the two lowest modes of wave oscillation at the interface, as depicted in Figure 3.3. It is shown that λ depends on the length of the interface perimeter. In this case, λ is equal to $2R\theta$ or $R\theta$, with θ defined in Figure 3.3. Equation (3.2.8) can also be used to estimate λ for a given value of U_g. The experimental result confirms that the interface instability begins when λ lies between $R\theta$ and $2R\theta$. Briefly, by solving equations (3.2.6) and (3.2.7) along the film boiling and partially quenched regions, together with the criterion given by equation (3.2.8), the rewetting position can be predicted.

The aspect which Chan and Banerjee have neglected in mass and momentum conservation (given by equations (3.2.6) and (3.2.7)) is the longitudinal or horizontal motion of the flow. Equations (3.2.6) and (3.2.7) only describe the tangential motion, while in reality vapour and liquid also flow horizontally along the length of the tube. With this in mind and with suitable adaptation, it will be shown below how Chan and Banerjee's method for the determination of a stable vapour-liquid interface in a transient two-phase flow can be applied to the model of a cryogenic liquid flow resulting from a CTF.

3.3 Model To Be Proposed

3.3.1 Heat Sources

As the model to be proposed will consider boiling and vaporization effects, the input of heat into cryogenic liquid flow is essential to the model. Because the temperature of cryogenic liquids is much lower than the temperature of

the surroundings (ground/soil and air), when cryogenic liquids spill on the ground, the heat received by cryogenic liquids comes from the ground and the atmosphere (air). In addition, heat also comes from solar radiation. Drake et al. (1974) and Shaw and Briscoe (1978) confirmed that in the early stages of cryogenic liquid spills, heat from solar radiation and the atmosphere can be neglected, compared with the heat flux from the ground. The following is an illustration of comparison of heat flux from the three heat sources mentioned, which is based on existing work on LNG spills on soil.

Drake and Reid (1975) and Reid and Wang (1978) measured the boiling rate of LNG on soil. This boiling rate depends on the nature of soil, such as compactness, surface roughness and moisture content, which all affect the apparent thermal properties of the soil. They found that within such variations the boiling rate is very high at the early stages of spills. The heat flux from the soil was estimated by using an unsteady one-dimensional conductive heat transfer equation with the soil being regarded as a semi-infinite solid. Based on the results of Reid and Wang (see Appendix D), the average LNG boiling rate during the first second of spill is around 1 kg/m^{2}s, or equivalent to a heat flux of 510 kW/m^2. Shaw and Briscoe estimated that the average boiling rate during the first second of spill is 0.7 kg/m^{2}s. Shaw and Briscoe also estimated the solar radiation energy on a cloudless day to be around 0.8 kW/m^2. They evaluated the convective heat flux from the atmosphere by using a heat-mass transfer analogy and some related empirical equations. Their equation is :

$$q_c = CU^{0.78}(2r)^{-0.11}\Delta T \rho_m c_{pm} \left(\frac{Sc}{Pr}\right)^{\frac{2}{3}} \quad \text{W/m}^2 \qquad (3.3.1)$$

with $C = 4.8 \times 10^{-3} Sc^{\frac{2}{3}}$,

U = wind velocity (m/s),

r = radius of the liquid pool (m),

ΔT = temperature difference between the air and liquid (°C),

ρ_m,c_{pm} = average density and heat capacity,

Sc,Pr = Schmidt and Prandtl numbers.

For an LNG spill with a spill radius of 30 m, wind velocity of 10 m/s and and air temperature of 25°C, equation (3.3.1) gave a convective heat flux q_c equal to 4.8 kW/m^2. Drake et al. also estimated q_c based on a convective heat transfer on a horizontal flat plate. For a similar condition of spill, their calculated heat transfer coefficient is 25 W/m^2°C, and this corresponds to a heat flux q_c of 4.6 kW/m^2.

The above estimates clearly show that heat flux from the ground dominates during the early stage of spills, and that at that stage solar radiation energy as well as convective heat transfer from the atmosphere can be neglected. In deriving the governing equation, this study will therefore only consider heat flux from the ground. It is assumed that this heat flux is constant during the early stage of spill that covers the timespan relevant to this study. For liquid methane, heat flux from the ground is equivalent to the evaporation rate m = 0.54 kg/m^{2}s. Details of this assumption are given in Appendix D.

3.3.2 The Basic Idea: Theoretical Analysis

In a cryogenic liquid spill over the ground, there is much analogous to the quenching process described in Chan and Banerjee's work. If the radius in Figure 3.2 is increased until the tube diameter is large enough to be considered infinite, the bottom will become flat and horizontal, and the vapour will effectively flow on a horizontal surface. Although the liquid in Figure 3.2 does not flow in the same direction as the vapour, such a

concept can be used to describe the collapse of the cryogenic liquid column on a horizontal surface at ambient temperature, as depicted in Figure 3.4. Based on this analogy, the flow resulting from the collapse of a cryogenic liquid column is considered to consist initially of two layers: the liquid layer on top and the vapour produced below (beneath the liquid layer). If it is assumed that in this case, the liquid-vapour interface is equally stable if the Kelvin-Helmholtz stability criterion (equation (3.2.5)) is satisfied, as in Chan and Banerjee's work, then the wavelength λ of the interfacial wave must be determined from the length of the interface, in the flow direction. Here, the two lowest modes of the interfacial wave oscillation are considered, as shown in Figure 3.5(a). These two possible modes of oscillation are $\frac{1}{2}\lambda$ and λ, which correspond to the length of vapour layer L_v of $\frac{1}{4}\lambda$ or $\frac{1}{2}\lambda$, respectively.

As there are two phases which flow separately from each other, such two-phase flow is called a stratified flow. By using the Shallow Water theory, the governing equations for the (upper) liquid-layer are given by :

$$\begin{aligned} \frac{\partial h_l}{\partial t} + U_l\frac{\partial h_l}{\partial r} + h_l\frac{\partial U_l}{\partial r} + \frac{h_l U_l}{r} &= -\frac{m}{\rho_l} \\ \frac{\partial U_l}{\partial t} + U_l\frac{\partial U_l}{\partial r} + g\frac{\partial h_l}{\partial r} &= 0 \end{aligned}$$

and the governing equations for the (lower) vapour-layer are given by :

$$\begin{aligned} \frac{\partial h_v}{\partial t} + U_v\frac{\partial h_v}{\partial r} + h_v\frac{\partial U_v}{\partial r} + \frac{h_v U_v}{r} &= +\frac{m}{\rho_v} \\ \frac{\partial U_v}{\partial t} + U_v\frac{\partial U_v}{\partial r} + g\frac{\rho_l}{\rho_v}\frac{\partial h_l}{\partial r} &= 0 \end{aligned}$$

where h_l, h_v = the thickness/height of liquid and vapour layer,

U_l, U_v= liquid and vapour velocity,

ρ_l, ρ_v = liquid and vapour density, and

m = boiling rate of liquid.

Details of the derivation of the above equations are described in Appendix D. These governing equations are solved by using the Method of Characteristics. An example of the calculation results for liquid methane (as a major component of LNG) is shown in Appendix D, where the boiling rate of methane is assumed to be constant, $m = 0.54\,\mathrm{kg/m^2s}$. The results show that the vapour-layer velocity is around $0\text{–}12\sqrt{gH_0}$ and the liquid-layer velocity is $0\text{–}1.9\sqrt{gH_0}$. The velocity of both vapour-layer and liquid-layer for a liquid methane column with a radius and a height of 10 cm, as may be used in scaled down experiments, are also shown in Figure 3.5(b). To examine the length of the stable liquid-vapour interface in the stratified flow resulting from the collapse of such a small column, the maximum value of U_{rel} (i.e. $U_{rel,crit}$) is calculated from equation (3.2.5). With a liquid and vapour density of 424 kg/m^3 and 1.8 kg/m^3, respectively, an interfacial tension σ of 0.014 N/m, and the length of interface L_v taken to be equal to $\frac{1}{2}\lambda$, the value of $U_{rel,crit}$ in equation (3.2.6) is given by:

L_v (cm) :	1	2	3	4	5
$U_{rel,crit}$ (m/s) :	1.57	1.10	0.91	0.79	0.70

If these values are added to the velocity of the liquid-layer, they will give the maximum velocity of the vapour-layer for which the interface is still stable, according to the Kelvin-Helmholtz criterion. This is also shown in Figure 3.5(b). Based on this result, it is obvious that the length of a stable liquid-vapour interface in the stratified flow resulting from the collapse of a column with a radius and a height of 10 cm is only around 1 cm, i.e. the interface becomes unstable beyond $1.1R_0$. Because :

$$U_{rel} = U_v - U_l \sim \sqrt{gH_0} \quad , \quad \text{and} \quad U_{rel,crit} \sim \frac{1}{\sqrt{\lambda}} \text{ or } \frac{1}{\sqrt{L_v}}$$

(see equation (3.2.5)), the length of such a stable liquid-vapour interface in the stratified flow resulting from the collapse of a large column is therefore

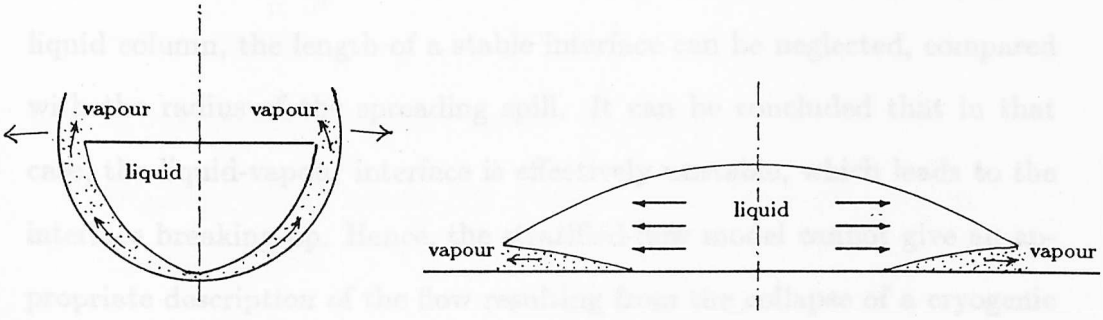


Figure 3.4: Analogy between Chan and Banerjee's experiment and cryogenic liquid spills on the ground

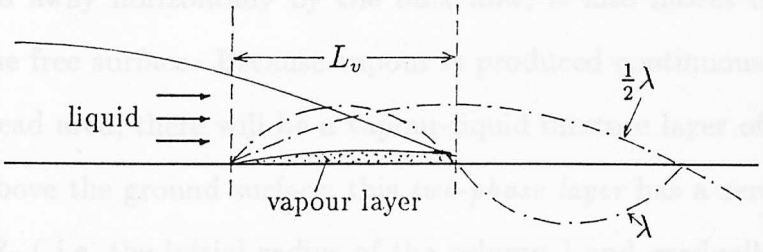


Figure 3.5:(a) Two possible modes of interfacial wave oscillation

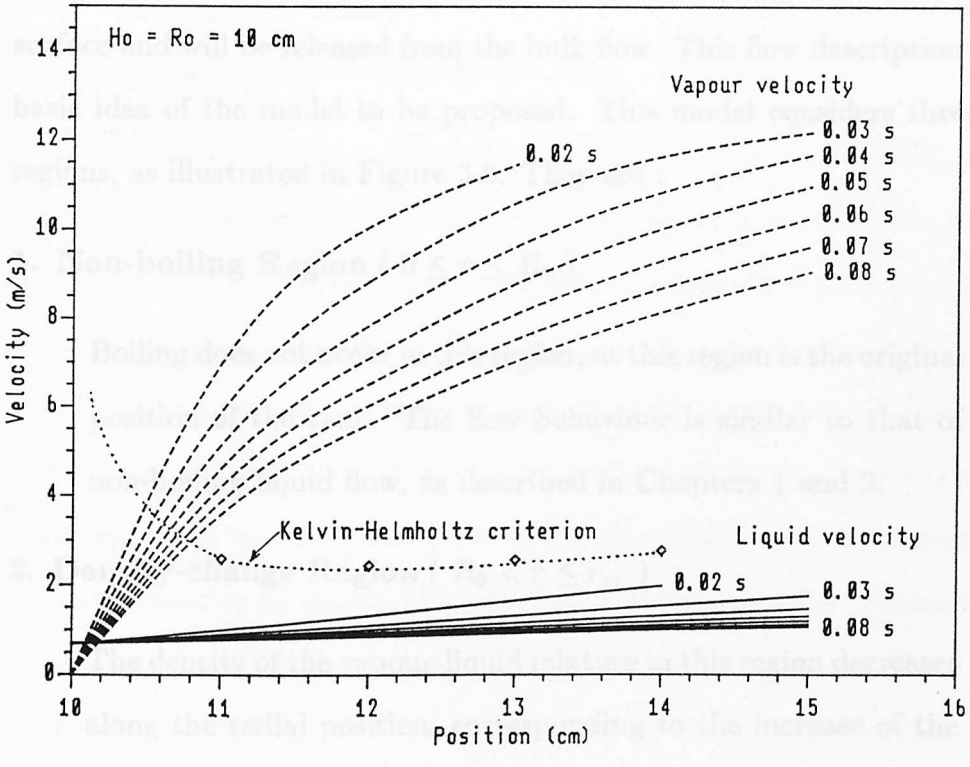


Figure 3.5: (b) Velocity of stratified flow from a column with $R_0 = H_0 = 10$ cm

much less than $1.1R_0$. Hence, in the case of the collapse of a large cryogenic liquid column, the length of a stable interface can be neglected, compared with the radius of the spreading spill. It can be concluded that in that case, the liquid-vapour interface is effectively unstable, which leads to the interface breaking-up. Hence, the stratified-flow model cannot give an appropriate description of the flow resulting from the collapse of a cryogenic liquid column.

Instead of flowing separately in a lower layer, the vapour produced from the boiling process will mix with the liquid. In this case, while the vapour is carried away horizontally by the bulk flow, it also moves upward, towards the free surface. Because vapour is produced continuously over the spill/spread area, there will be a vapour-liquid mixture layer of increasing height above the ground surface; this *two-phase layer* has a zero thickness at $r = R_0$ (i.e. the initial radius of the column) and gradually increases along the flow direction. At some position, the vapour will reach the free surface and will be released from the bulk flow. This flow description is the basic idea of the model to be proposed. This model considers three flow regions, as illustrated in Figure 3.6. They are :

1. Non-boiling Region ($0 \leq r \leq R_0$)

Boiling does not occur in this region, as this region is the original position of the tank. The flow behaviour is similar to that of non-boiling liquid flow, as described in Chapters 1 and 2.

2. Density-change Region ($R_0 < r \leq r_{vr}$)

The density of the vapour-liquid mixture in this region decreases along the radial position, corresponding to the increase of the two-phase layer thickness. Here, r_{vr} is the position where the

vapour begin to reach the free surface, to be called the *vapour-release* position.

3. Vapour-release Region ($r_{vr} < r \leq r_f$)

Vigorous vapour release due to vapour break-through occurs at the free surface.

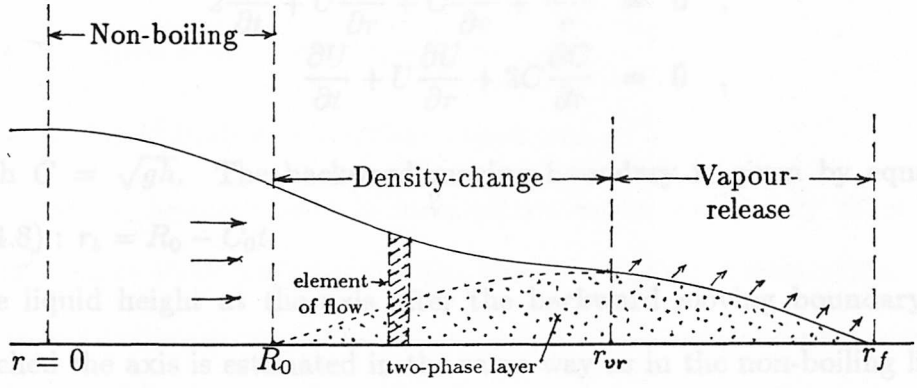


Figure 3.6: Division of flow region

3.3.3 Mathematical Modelling

As described in the Introduction (Section 3.1), the flow description is equally based on the Shallow Water theory. An illustration of the motion of a flow element, according to this theory, is shown in Figure 1.8 (Chapter 1). This theory implies that any point at the same horizontal (radial) position propagates at the same velocity, regardless of its vertical position. Application of the Shallow Water theory to the model to be proposed means that vapour in the two-phase layer in the density-change region moves at the same velocity as the liquid layer. Figure 3.6 shows a flow element that is used as a basis for the derivation of the governing equations.

Each region of the flow has specific and different characteristics. The following describes the governing equations for each region described above.

3.3.3.1 Non-boiling Region

There is no evaporation in this region, and the flow in this region can be treated in the same way as non-boiling liquid flow (Chapters 1 and 2). Without being described in detail again, the governing equations of this region are equations (1.3.11) :

$$\begin{aligned} 2\frac{\partial C}{\partial t} + U\frac{\partial C}{\partial r} + C\frac{\partial U}{\partial r} + \frac{UC}{r} &= 0 \quad , \\ \frac{\partial U}{\partial t} + U\frac{\partial U}{\partial r} + 2C\frac{\partial C}{\partial r} &= 0 \quad , \end{aligned}$$

with $C = \sqrt{gh}$. The backward moving boundary is given by equation (1.4.8) : $r_b = R_0 - C_0 t$.

The liquid height at the axis after the backward moving boundary has reached the axis is estimated in the same way as in the non-boiling liquid case.

3.3.3.2 Density-change Region

Besides liquid height h and velocity U, the density ρ is introduced as a new dependent variable. Here, density ρ is defined as an average density of the vapour-liquid mixture from $z = 0$ to $z = h$, as is the velocity U. The derivation of the governing equations starts from :

- equation of continuity :

$$\frac{\partial \rho}{\partial t} = -\left(\frac{1}{r}\frac{\partial r\rho U}{\partial r} + \frac{\partial \rho v}{\partial z}\right) \tag{3.3.2}$$

- equation of motion :

  – r component :

$$\rho\frac{DU}{Dt} = -\frac{\partial p}{\partial r} \tag{3.3.3}$$

– z component :

$$\rho \frac{Dv}{Dt} = -\frac{\partial p}{\partial z} - \rho g \tag{3.3.4}$$

The energy balance involves potential and kinetic energies, the work done and the heat flow to and from the surroundings. In this case, because the phase changes from liquid to vapour, an enthalpy is likely to be the most appropriate term to be used. It is assumed that :

- the liquid is at its boiling temperature,
- the liquid boils at a constant temperature.

As cryogenic liquids stored in atmospheric tanks are usually at or only slightly below their boiling point, the first assumption is reasonable.

There is a boiling temperature range for a multicomponent liquid, such as LNG and LPG. Because this study is concerned only with the early stage of spills, it is expected that only a small amount of liquid will evaporate during that stage, and that its composition changes so little that the boiling temperature does not change. Hence, the second assumption is also acceptable.

It is considered that the vapour formed in boiling is in equilibrium with the liquid, i.e. the vapour is in its saturated condition. The enthalpy of the mixture is given by :

$$H = xH_v + (1-x)H_l \quad \text{or} \quad H = H_l + (H_v - H_l)x \quad ,$$

with x = vapour mass fraction,

H_l,H_v = enthalpy of liquid and vapour, respectively.

The enthalpy can be further simplified, by taking $H_l = 0$ (reference enthalpy), and $(H_v - H_l) = h_{fg}$, the latent heat of evaporation. Hence, the enthalpy becomes :

$$H = h_{fg}x \tag{3.3.5}$$

Because during the initial stages relevant to this study the heat flux from the ground is very high (see Section 3.3.2), the phase-change process dominates the energy balance. The latent heat of evaporation of cryogenic liquids is of the order of 100 kJ/kg, while the kinetic and potential energy change, as well as the work done to and from the surroundings, are only of the order of 1 to 100 J/kg. As a third assumption, the other energy changes in the energy balance are negligible, compared with the enthalpy change. Hence, the energy balance is given by :

$$\rho \frac{DH}{Dt} = -\frac{\partial q_z}{\partial z} \tag{3.3.6}$$

where q_z is the conductive heat flux.

The relation between the density ρ and the vapour mass fraction x is given by :

$$\frac{1}{\rho} = \frac{x}{\rho_v} + \frac{(1-x)}{\rho_l} \tag{3.3.7}$$

where ρ_v and ρ_l are respectively the vapour and liquid density. By using this relation, the enthalpy can be substituted by the density. Equation (3.3.7) is transformed into :

$$x = \frac{\rho_v(\rho_l - \rho)}{\rho(\rho_l - \rho_v)} \tag{3.3.8}$$

Substitution of this equation into equation (3.3.6) results in :

$$\frac{h_{fg}\rho_l}{E_f \rho} \frac{D\rho}{Dt} = -\frac{\partial q_z}{\partial z} \tag{3.3.9}$$

with $E_f = (\frac{\rho_l}{\rho_v} - 1)$. With the density independent of z, integration of equation (3.3.9) along z results in :

$$\begin{aligned} \int_0^h \frac{h_{fg}\rho_l}{E_f \rho} \frac{D\rho}{Dt} dz &= -\int_{q_0}^{q_h} dq_z \\ h \frac{h_{fg}\rho_l}{E_f \rho} \frac{D\rho}{Dt} &= -(q_h - q_0) \end{aligned}$$

At the ground surface, q_0 is equal to the heat flux from the ground, and q_h is zero, as there is no significant heat flux or evaporation at the top/free surface of the liquid (see Section 3.3.2). The above equation becomes :

$$\frac{h}{\rho}\frac{D\rho}{Dt} = -\left(\frac{q_0 E_f}{h_{fg}\rho_l}\right) \tag{3.3.10}$$

In this case, $(\frac{q_0}{h_{fg}})$ is the boiling rate m per unit area; the governing equation (3.3.10) represents the rate of density change.

Derivation of equations of continuity and motion is as in Chapter 1. Because ρ is regarded as independent of z, equation (3.3.2) becomes :

$$\frac{\partial \rho}{\partial t} = -\frac{1}{r}\frac{\partial r\rho U}{\partial r} - \rho\frac{\partial v}{\partial z}$$

Integration of the above equation along z results in :

$$h\frac{\partial \rho}{\partial t} = -\frac{h}{r}\frac{\partial r\rho U}{\partial r} - \rho(v_h - v_0) \tag{3.3.11}$$

With the boundary conditions given by :

$$v_0 = 0 \qquad \text{and} \qquad v_h = \frac{Dh}{Dt} \quad ,$$

equation (3.3.11) becomes :

$$h\frac{\partial \rho}{\partial t} + \frac{h}{r}\frac{\partial r\rho U}{\partial r} + \rho\frac{Dh}{Dt} = 0$$

$$h\frac{\partial \rho}{\partial t} + hU\frac{\partial \rho}{\partial r} + \rho h\frac{\partial U}{\partial r} + \rho\frac{hU}{r} + \rho\frac{Dh}{Dt} = 0$$

Substitution of $\frac{D\rho}{Dt} = \frac{\partial \rho}{\partial t} + U\frac{\partial \rho}{\partial r}$ into the above equation results in :

$$\rho\frac{Dh}{Dt} + h\frac{D\rho}{Dt} + \rho h\frac{\partial U}{\partial r} + \rho\frac{hU}{r} = 0 \tag{3.3.12}$$

By neglecting the vertical acceleration $\frac{Dv}{Dt}$ in equation (3.3.4) with respect to $|g|$ and integrating it along z to h, the equation becomes :

$$p - p_h = \rho g(h - z) \tag{3.3.13}$$

where p_h is ambient pressure. Substitution of the r-derivative of equation (3.3.13) into equation(3.3.3) results in:

$$\rho\frac{DU}{Dt} = -g\frac{\partial \rho h}{\partial r} + gz\frac{\partial \rho}{\partial r} \tag{3.3.14}$$

Equation (3.3.14) still depends on z. As this work is based on Shallow Water theory, which only considers horizontal motion, the value of z has to be somewhere between 0 and h. However, as shown in Appendix F, the flow behaviour is not significantly affected by the value of z. Therefore, the term $g\frac{\partial \rho}{\partial r}$ in equation (3.3.14) can be neglected, which then becomes:

$$\rho\frac{DU}{Dt} + g\frac{\partial \rho h}{\partial r} = 0 \tag{3.3.15}$$

The governing equations in the density-change region are equations (3.3.10), (3.3.12) and (3.3.15). Below is a summary of those mentioned :

$$\begin{aligned} \rho\frac{Dh}{Dt} + h\frac{D\rho}{Dt} + \rho h\frac{\partial U}{\partial r} + \rho\frac{hU}{r} &= 0 \\ \rho\frac{DU}{Dt} + g\frac{\partial \rho h}{\partial r} &= 0 \\ h\frac{D\rho}{Dt} + K_b\rho &= 0 \end{aligned} \tag{3.3.16}$$

with $K_b = \frac{q_0 E_f}{h_{fg}\rho_l}$.

As the density is defined as an average density along the height of the flow, the two-phase layer thickness can be calculated from the density:

$$\rho h = \rho_l(h - h_b) + \rho_b h_b \qquad \text{or} \qquad h_b = h\frac{(\rho_l - \rho)}{(\rho_l - \rho_b)} \tag{3.3.17}$$

where ρ_b is two-phase layer density and h_b is two-phase layer thickness. The two-phase layer density ρ_b depends on the concentration of vapour in the two-phase layer; it is determined by :

$$\rho_b = \rho_l - \epsilon_v(\rho_l - \rho_v) \tag{3.3.18}$$

where ϵ_v is vapour void fraction in the two-phase layer. The concentration of vapour in the two-phase layer will be discussed in Section 3.5 (Results and Discussion).

As the density at the vapour-release position r_{vr} is equal to the two-phase layer density, r_{vr} can be determined on the basis of ρ_b. Furthermore, the smallest density in the density-change region is at r_{vr}; the two-phase layer density ρ_b is also called ρ_{min}.

3.3.3.3 Vapour-release Region

The height of flow reduces as time and the distance from the axis increase, but this region is characterized by additional thinning of the flow height, due to mass loss or massive vapour release at the free surface. It is assumed that the vapour void fraction or the density in this region is constant and equal to the two-phase layer density given by equation (3.3.18). The constant density assumption makes equation (3.3.6) become :

$$\frac{\partial qz}{\partial z} = 0 \qquad \text{or} \qquad q_0 = q_h \quad .$$

Here, the boiling rate (the vapour production rate) is equal to the rate of vapour release at the free surface. The rate of mass loss at the free surface m_s is given by :

$$m_s = \frac{q_0}{h_{fg}(1-x)} \tag{3.3.19}$$

where x is the vapour mass fraction corresponding to the minimum density ρ_{min} or ρ_b. The term $\left(\frac{q_0}{h_{fg}}\right)$ is equal to the amount of liquid changed into vapour, while the mass loss at the free surface due to vapour release is equal to the loss of liquid (which changed into vapour) plus its vapour content. Hence, the term $(1-x)$ is to correct $\left(\frac{q_0}{h_{fg}}\right)$ for the rate of mass loss. However, the value of x in the vapour-release region is relatively small; for a vapour void fraction of 0.7, the corresponding value of x is only around 0.01, so in equation (3.3.19) x can effectively be neglected.

The governing equations of this region are derived from :

- the equation of continuity :

$$\frac{1}{r}\frac{\partial r\rho U}{\partial r}+\frac{\partial \rho v}{\partial z}=0 \tag{3.3.20}$$

- the equation of motion :

  - r component :

$$\rho\frac{DU}{Dt}=-\frac{\partial p}{\partial r} \tag{3.3.21}$$

  - z component :

$$\rho\frac{Dv}{Dt}=-\frac{\partial p}{\partial z}-\rho g \tag{3.3.22}$$

where ρ in this case is equal to ρ_{min}. Integration of equation (3.3.20) along z results in :

$$\begin{aligned}\int_0^h \frac{1}{r}\frac{\partial r\rho U}{\partial r}\,dz+\int_0^h d\rho v &= 0\\ \rho\frac{h}{r}\frac{\partial rU}{\partial r}+(\rho v_h+m_s-\rho v_0) &= 0\\ \longrightarrow \frac{Dh}{Dt}+\frac{h}{r}\frac{\partial rU}{\partial r} &= -\frac{m_s}{\rho_{min}}\end{aligned} \tag{3.3.23}$$

Equations (3.3.21) and (3.3.22) are treated in a similar way to that in non-boiling liquid flow. The result is :

$$\frac{\partial U}{\partial t}+U\frac{\partial U}{\partial r}+g\frac{\partial h}{\partial r}=0 \tag{3.3.24}$$

The governing equations in this region are given by equations (3.3.23) and (3.3.24).

3.4 Numerical Solution

The solution of the governing equations in all regions is again based on the Method of Characteristics (MOC), with a three-point method, an interpolation by using Chebychev polynomials and evaluation of PI and QI (equations (1.4.12) and (1.4.13)) by the arithmetic average method. As

carried out previously, all variables are expressed in dimensionless form : the symbols and their meanings have already been mentioned in Chapter 1. In addition, the dimensionless density ϱ is equal to $\left(\frac{\rho}{\rho_l}\right)$. Hence, the dimensionless liquid density ϱ_l is equal to 1.

3.4.1 Non-boiling Region

Rearrangement of the governing equations results in :

$$\frac{\partial(\mathbf{U} \pm 2\mathbf{C})}{\partial \mathbf{t}} + (\mathbf{U} \pm \mathbf{C})\frac{\partial(\mathbf{U} \pm 2\mathbf{C})}{\partial \mathbf{r}} = \mp\frac{\mathbf{UC}}{\mathbf{r}} \tag{3.4.1}$$

The slope of the characteristic lines (positive and negative) is given by :

$$\frac{d\mathbf{r}}{dt} = \mathbf{U} \pm \mathbf{C} \tag{3.4.2}$$

with the (positive and negative) Riemann invariants :

$$\frac{d(\mathbf{U} \pm 2\mathbf{C})}{dt} = \mp\frac{\mathbf{UC}}{\mathbf{r}} \tag{3.4.3}$$

No further explanation is needed here, for details of the numerical solution have been described in Chapter 1. The only additional statement for this region is that $\varrho = 1$ at all grid points and at all time levels.

3.4.2 Density-change Region

Solution in this region by the MOC involves three dependent variables **U**, **h** and ϱ, with three equations. Substitution of $C = \sqrt{gh}$ in the governing equations (3.3.16) results in :

$$2\frac{D\mathbf{C}}{D\mathbf{t}} + \mathbf{C}\frac{\partial \mathbf{U}}{\partial \mathbf{r}} = -\frac{\mathbf{UC}}{\mathbf{r}} - \frac{\mathbf{C}}{\varrho}\frac{D\varrho}{D\mathbf{t}} \tag{3.4.4}$$

$$\frac{D\mathbf{U}}{D\mathbf{t}} + 2\mathbf{C}\frac{\partial \mathbf{C}}{\partial \mathbf{r}} = -\frac{\mathbf{C}^2}{\varrho}\frac{\partial \varrho}{\partial \mathbf{r}} \tag{3.4.5}$$

$$\frac{1}{\varrho}\frac{D\varrho}{D\mathbf{t}} = -\frac{\mathbf{G_k}}{\mathbf{C}^2} \tag{3.4.6}$$

with $\mathbf{G_k} = \dfrac{K_b R_0}{C_0 H_0} = \dfrac{q_0 E_f}{h_{fg}\rho_l}\dfrac{R_0}{C_0 H_0}$. The term $\mathbf{G_k}$ can also be expressed in another form :

$$\mathbf{G_k} = \frac{U_{vs}}{C_0}\left(\frac{\rho_l - \rho_v}{\rho_l}\right)\frac{R_0}{H_0} \quad , \quad \text{with} \quad U_{vs} = \frac{q_0}{h_{fg}\rho_v} \quad .$$

The physical meaning of U_{vs} is a superficial velocity of the vapour produced in boiling. As ρ_v is generally much smaller than ρ_l, the term $\left(\frac{\rho_l - \rho_v}{\rho_l}\right)$ is effectively equal to 1. The horizontal velocity U is of the order of C_0, as shown in the case of non-boiling liquid flow. Hence, the term $\mathbf{G_k}$ does in fact indicate the ratio of the superficial velocity of the vapour to the horizontal velocity of flow.

Abbott (1966) described the method to find the characteristic line equations and their corresponding Riemann invariants from a set of differential equations, which may consist of more than two equations. Because three variables are involved in this region, there will be three characteristic lines and three Riemann invariants. Instead of Abbott's method, equations (3.4.4) and (3.4.5) can be manipulated in another simple way to obtain the characteristic lines and their Riemann invariants. The result is equivalent to that obtained by the method described by Abbott.

Addition of the LHS of equations (3.4.4) and (3.4.5) results in :

$$\frac{D(\mathrm{U}+2\mathrm{C})}{D\mathrm{t}} + \mathrm{C}\frac{\partial(\mathrm{U}+2\mathrm{C})}{\partial \mathrm{r}} = \frac{\partial(\mathrm{U}+2\mathrm{C})}{\partial \mathrm{t}} + (\mathrm{U}+\mathrm{C})\frac{\partial(\mathrm{U}+2\mathrm{C})}{\partial \mathrm{r}}$$

and addition of the RHS of both equations results in :

$$\begin{aligned} -\frac{\mathrm{UC}}{\mathrm{r}} - \frac{\mathrm{C}}{\varrho}\frac{D\varrho}{D\mathrm{t}} - \frac{\mathrm{C}^2}{\varrho}\frac{\partial \varrho}{\partial \mathrm{r}} &= -\frac{\mathrm{UC}}{\mathrm{r}} - \frac{\mathrm{C}}{\varrho}\left[\frac{\partial \varrho}{\partial \mathrm{t}} + \mathrm{U}\frac{\partial \varrho}{\partial \mathrm{r}} + \mathrm{C}\frac{\partial \varrho}{\partial \mathrm{r}}\right] \\ &= -\frac{\mathrm{UC}}{\mathrm{r}} - \frac{\mathrm{C}}{\varrho}\left[\frac{\partial \varrho}{\partial \mathrm{t}} + (\mathrm{U}+\mathrm{C})\frac{\partial \varrho}{\partial \mathrm{r}}\right] \end{aligned}$$

By combining the above equations, they become :

$$\frac{\partial(\mathrm{U}+2\mathrm{C})}{\partial \mathrm{t}} + (\mathrm{U}+\mathrm{C})\frac{\partial(\mathrm{U}+2\mathrm{C})}{\partial \mathrm{r}} + \frac{\mathrm{C}}{\varrho}\left[\frac{\partial \varrho}{\partial \mathrm{t}} + (\mathrm{U}+\mathrm{C})\frac{\partial \varrho}{\partial \mathrm{r}}\right] = -\frac{\mathrm{UC}}{\mathrm{r}} \quad (3.4.7)$$

This equation shows that the entities $(\mathbf{U}+2\mathbf{C})$ and ϱ propagate along the path with a slope of $(\mathbf{U}+\mathbf{C})$. Based on the principle of the MOC, equation (3.4.7) corresponds to :

- the slope of the positive characteristic line :

$$\left.\frac{d\mathbf{r}}{d\mathbf{t}}\right|_{+} = (\mathbf{U}+\mathbf{C}) \tag{3.4.8}$$

- with its positive Riemann invariant :

$$\frac{d(\mathbf{U}+2\mathbf{C})}{d\mathbf{t}} + \frac{\mathbf{C}}{\varrho}\frac{d\varrho}{d\mathbf{t}} = -\frac{\mathbf{UC}}{\mathbf{r}}$$

or in another form :

$$\frac{d(\mathbf{U}+2\mathbf{C})}{d\mathbf{t}} + \mathbf{C}\frac{d\ln\varrho}{d\mathbf{t}} = -\frac{\mathbf{UC}}{\mathbf{r}} \tag{3.4.9}$$

Similarly, subtraction of equations (3.4.4) and (3.4.5) results in :

- the slope of the negative characteristic line :

$$\left.\frac{d\mathbf{r}}{d\mathbf{t}}\right|_{-} = (\mathbf{U}-\mathbf{C}) \tag{3.4.10}$$

- with its negative Riemann invariant :

$$\frac{d(\mathbf{U}-2\mathbf{C})}{d\mathbf{t}} - \mathbf{C}\frac{d\ln\varrho}{d\mathbf{t}} = \frac{\mathbf{UC}}{\mathbf{r}} \tag{3.4.11}$$

Also based on the principle of the MOC, equation (3.4.6) corresponds to :

- the slope of the third characteristic line :

$$\frac{d\mathbf{r}}{d\mathbf{t}} = \mathbf{U} \tag{3.4.12}$$

- with its Riemann invariant given by :

$$\frac{1}{\varrho}\frac{d\varrho}{d\mathbf{t}} = -\frac{\mathbf{G_k}}{\mathbf{C}^2} \quad \text{or} \quad \frac{d\ln\varrho}{d\mathbf{t}} = -\frac{\mathbf{G_k}}{\mathbf{C}^2} \tag{3.4.13}$$

In this case, instead of two characteristic lines, three characteristic lines are used to determine the condition of the flow, as shown in Figure 3.7. These three characteristic lines are PA as the positive characteristic line, QA as the negative characteristic line and SA as the third characteristic line. Note that SA is actually the path of an element (in the Shallow Water theory) with a propagation velocity of **U**. Point A represents point $\mathbf{r}_{i,j+1}$, whose

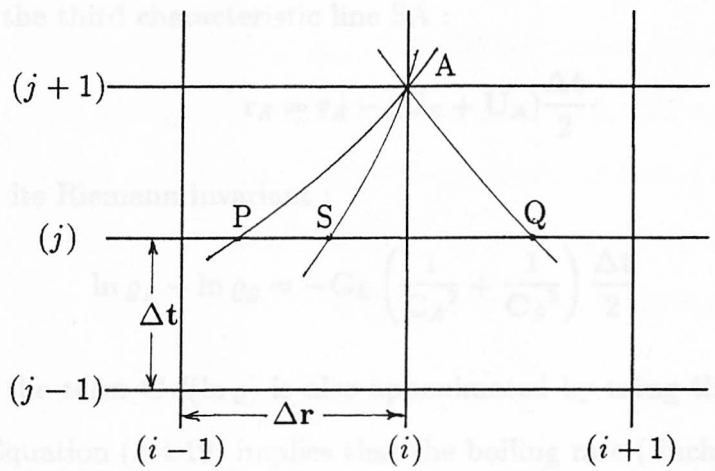


Figure 3.7: Characteristic lines PA, QA and SA in the density-change region

conditions is to be determined. By using a similar way to that described in Chapter 1, the values of **U**, **C** and ϱ are determined from equations (3.4.8) to (3.4.13) in the forms of :

- the positive characteristic line PA :

$$\mathbf{r}_P = \mathbf{r}_A - (\mathbf{U}_P + \mathbf{C}_P + \mathbf{U}_A + \mathbf{C}_A)\frac{\Delta \mathbf{t}}{2} \qquad (3.4.14)$$

with its Riemann invariant :

$$\mathbf{U}_A + 2\mathbf{C}_A - (\mathbf{U}_P + 2\mathbf{C}_P) + \frac{1}{2}(\mathbf{C}_A + \mathbf{C}_P)(\ln \varrho_A - \ln \varrho_P) = - \left(\frac{\mathbf{U}_A \mathbf{C}_A}{\mathbf{r}_A} + \frac{\mathbf{U}_P \mathbf{C}_P}{\mathbf{r}_P}\right)\frac{\Delta \mathbf{t}}{2} \qquad (3.4.15)$$

- the negative characteristic line QA :

$$\mathbf{r_Q = r_A - (U_Q - C_Q + U_A - C_A)\frac{\Delta t}{2}} \tag{3.4.16}$$

with its Riemann invariant :

$$\mathbf{U_A - 2C_A - (U_Q - 2C_Q) - \frac{1}{2}(C_A + C_Q)(\ln \varrho_A - \ln \varrho_Q) = + \left(\frac{U_A C_A}{r_A} + \frac{U_Q C_Q}{r_Q}\right)\frac{\Delta t}{2}} \tag{3.4.17}$$

- and the third characteristic line SA :

$$\mathbf{r_S = r_A - (U_S + U_A)\frac{\Delta t}{2}} \tag{3.4.18}$$

with its Riemann invariant :

$$\ln \varrho_A - \ln \varrho_S = -\mathbf{G_k}\left(\frac{1}{{C_A}^2} + \frac{1}{{C_S}^2}\right)\frac{\Delta t}{2} \tag{3.4.19}$$

Note that the term $\mathbf{C}\, d(\ln \varrho)$ is also appoximated by using the arithmetic average. Equation (3.4.19) implies that the boiling rate (included in $\mathbf{G_k}$) is constant for all positions and at all time, as already described in Section 3.3.2. For a particular case, where the boiling rate is not constant, due to variation of the surface temperature or variation of the boiling mode, equation (3.4.19) can be rewritten in the form of:

$$\ln \varrho_A - \ln \varrho_S = -\left(\frac{G_{kA}}{{C_A}^2} + \frac{G_{kS}}{{C_S}^2}\right)\frac{\Delta t}{2}$$

It is obvious that equations (3.4.14) to (3.4.19) are non-linear. By regarding them as quasi-linear equations, the solution can be obtained through the use of the Newton-Raphson method described in Appendix A. In this case, the solution is regarded as a simultaneous solution of six equations: (3.4.14) to (3.4.19) with six unknown variables: r_P, r_Q, r_S, U_A, C_A and ϱ_A. The basic algorithm of the numerical calculation procedure (iteration) is equivalent to that described in Chapter 1.

The other aspect of the numerical calculation in this region is the determination of the vapour-release position $\mathbf{r}_{vr}$. This corresponds to the position at which $\varrho = \varrho_{min}$. The vapour-release position $\mathbf{r}_{vr}$ can essentially be determined by iteration, i.e. by assuming $\mathbf{r}_{vr}$ at an arbitrary value and then calculating **U**, **C** and ϱ at that point, until ϱ at $\mathbf{r}_{vr}$ is found to be equal to ϱ_{min}. However, this method needs extensive iteration. Instead, by using an interpolation method, $\mathbf{r}_{vr}$ can also be determined easily without performing numerous iterations. As an illustration, suppose the calculated density at $\mathbf{r}_{i,j+1}$ is greater than ϱ_{min}, but the calculated density at $\mathbf{r}_{i+1,j+1}$ is less than ϱ_{min}. Hence, the position $\mathbf{r}_{vr}$ lies between $\mathbf{r}_i$ and r_{i+1}. By taking $\varrho_{i-1,j+1}$, $\varrho_{i,j+1}$ and $\varrho_{i+1,j+1}$ into Chebychev polynomial form (as a function of position **r**), the position $\mathbf{r}_{vr}$ can be determined by interpolation, where $\varrho = \varrho_{min}$. After that, the density at $\mathbf{r}_{i+1,j+1}$ is taken to be equal to ϱ_{min}.

3.4.3 Vapour-release Region

The governing equations (3.3.23) and (3.3.24) are transformed into :

$$2\frac{DC}{Dt} + \mathbf{C}\frac{\partial \mathbf{U}}{\partial \mathbf{r}} = -\frac{\mathbf{UC}}{\mathbf{r}} - \frac{\mathbf{K_v}}{\mathbf{C}} \qquad (3.4.20)$$

$$\frac{DU}{Dt} + 2\mathbf{C}\frac{\partial \mathbf{C}}{\partial \mathbf{r}} = 0 \qquad (3.4.21)$$

with $$\mathbf{K_v} = \frac{m_s}{\rho_{min} C_0}\frac{R_0}{H_0} \quad .$$

The evaporation rate m_s is calculated from equation (3.3.19). The MOC solution of the above equations is given by :

- the slope of the positive characteristic line :

$$\left.\frac{d\mathbf{r}}{dt}\right|_{+} = \mathbf{U} + \mathbf{C} \qquad (3.4.22)$$

with its Riemann invariant :

$$\frac{d(\mathbf{U} + 2\mathbf{C})}{dt} = -\frac{\mathbf{UC}}{\mathbf{r}} - \frac{\mathbf{K_v}}{\mathbf{C}} \qquad (3.4.23)$$

- and the slope of the negative characteristic line :

$$\left.\frac{d\mathbf{r}}{d\mathbf{t}}\right|_{-} = \mathbf{U} - \mathbf{C} \tag{3.4.24}$$

with its Riemann invariant :

$$\frac{d(\mathbf{U} - 2\mathbf{C})}{d\mathbf{t}} = \frac{\mathbf{UC}}{\mathbf{r}} + \frac{\mathbf{K_v}}{\mathbf{C}} \tag{3.4.25}$$

As shown in Figure 3.8, there are two characteristic lines AP and AQ used to determine **U** and **C** at point A. Here, the density ϱ of this region is always equal to ϱ_{min}. The numerical solution of equations (3.4.22) to (3.4.25) is

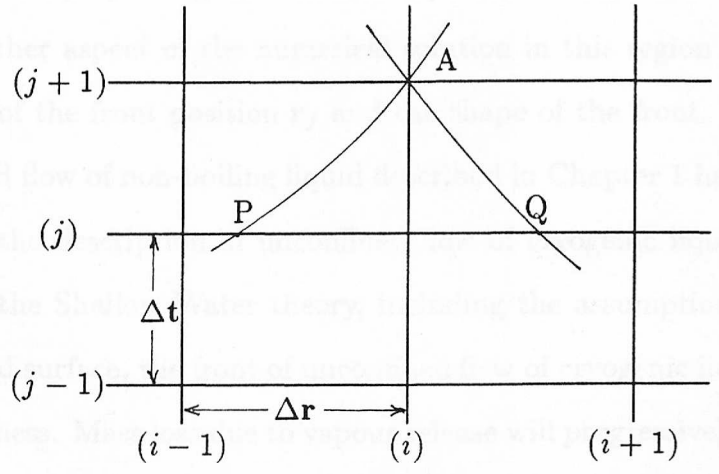


Figure 3.8: Characteristic lines PA and QA in the vapour-release region

given by :

- the positive characteristic line PA :

$$\mathbf{r}_P = \mathbf{r}_A - (\mathbf{U}_P + \mathbf{C}_P + \mathbf{U}_A + \mathbf{C}_A)\frac{\Delta \mathbf{t}}{2} \tag{3.4.26}$$

with its Riemann invariant :

$$\begin{aligned} \mathbf{U}_A + 2\mathbf{C}_A - (\mathbf{U}_P + 2\mathbf{C}_P) \;=\; & -\left(\frac{\mathbf{U}_A\mathbf{C}_A}{\mathbf{r}_A} + \frac{\mathbf{U}_P\mathbf{C}_P}{\mathbf{r}_P}\right)\frac{\Delta \mathbf{t}}{2} \\ & -\mathbf{K_v}\left(\frac{1}{\mathbf{C}_A} + \frac{1}{\mathbf{C}_P}\right)\frac{\Delta \mathbf{t}}{2} \end{aligned} \tag{3.4.27}$$

- and the negative characteristic line QA :

$$\mathbf{r}_Q = \mathbf{r}_A - (\mathbf{U}_Q - \mathbf{C}_Q + \mathbf{U}_A - \mathbf{C}_A)\frac{\Delta \mathbf{t}}{2} \qquad (3.4.28)$$

with its Riemann invariant :

$$\mathbf{U}_A - 2\mathbf{C}_A - (\mathbf{U}_Q - 2\mathbf{C}_Q) = \left(\frac{\mathbf{U}_A\mathbf{C}_A}{\mathbf{r}_A} + \frac{\mathbf{U}_Q\mathbf{C}_Q}{\mathbf{r}_Q}\right)\frac{\Delta \mathbf{t}}{2} + \mathbf{K_v}\left(\frac{1}{\mathbf{C}_A} + \frac{1}{\mathbf{C}_Q}\right)\frac{\Delta \mathbf{t}}{2} \qquad (3.4.29)$$

These four equations are non-linear, with four unknown variables : $\mathbf{r}_P$, $\mathbf{r}_Q$, $\mathbf{U}_A$ and $\mathbf{C}_A$. As described in the previous section, these four equations can be solved easily by using the Newton-Raphson method.

The other aspect of the numerical solution in this region is the determination of the front position $\mathbf{r}_f$ and the shape of the front. The front of unconfined flow of non-boiling liquid described in Chapter 1 has zero thickness. As the description of unconfined flow of cryogenic liquid is equally based on the Shallow Water theory, including the assumption of frictionless ground surface, the front of unconfined flow of cryogenic liquid also has zero thickness. Mass loss due to vapour release will progressively reduce the height/thickness of flow from $\mathbf{r}_{vr}$ up to the front position $\mathbf{r}_f$, as illustrated in Figure 3.9.

Estimation of the front position $\mathbf{r}_f$ is illustrated in Figure 3.10. To avoid the term $(\frac{\mathbf{K_v}}{\mathbf{C}})$ in equations (3.4.23) and (3.4.25) becoming infinite due to $\mathbf{C}_{fr} = 0$, the Riemann invariant is changed into :

$$\mathbf{C}\frac{d(\mathbf{U} \pm 2\mathbf{C})}{dt} = \mp\left(\frac{\mathbf{U}\mathbf{C}^2}{\mathbf{r}} + \mathbf{K_v}\right) \qquad (3.4.30)$$

By taking $\mathbf{C}_{front} = 0$, the estimate of the positive characteristic line that passes through the front point becomes :

$$\mathbf{r}_P = \mathbf{r}_f - (\mathbf{U}_P + \mathbf{C}_P + \mathbf{U}_{front})\frac{\Delta \mathbf{t}}{2} \qquad (3.4.31)$$

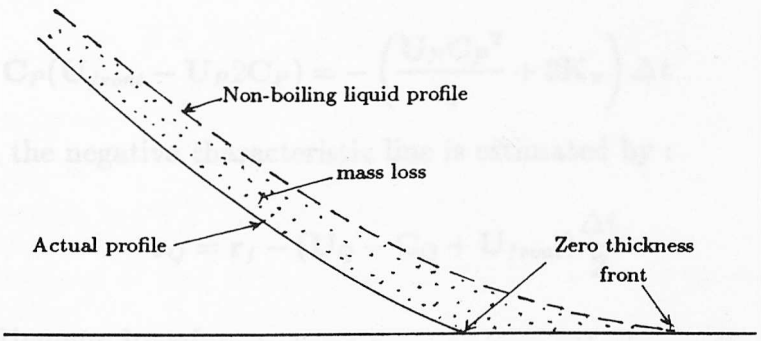


Figure 3.9: Illustration of the effect of mass loss on flow profile in the front region

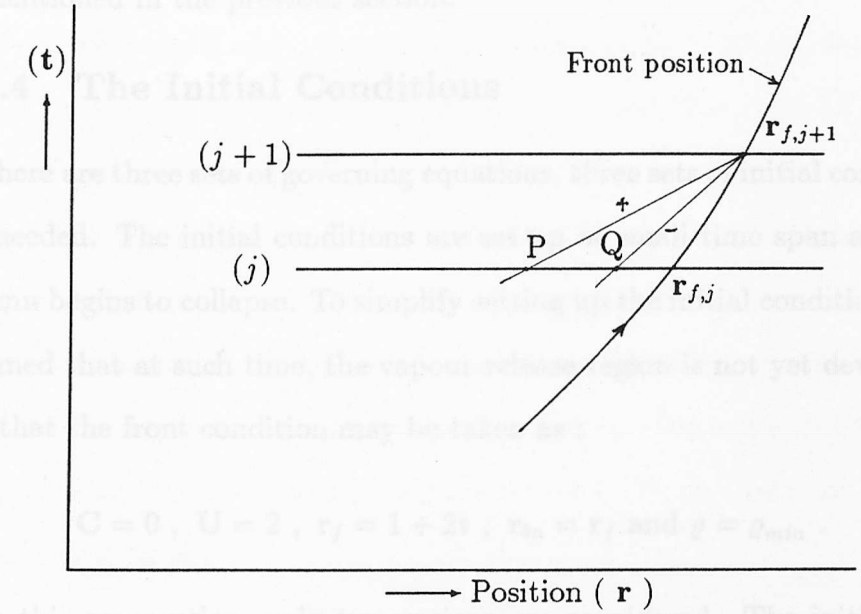


Figure 3.10: The front position determination

with its Riemann invariant given by :

$$\frac{(C_P + C_{fr})}{2}[(U + 2C)_{front} - (U_P + 2C_P)] = - \left(\frac{U_P C_P{}^2}{r_P} + \frac{UC^2}{r}\bigg|_{front} \right) \frac{\Delta t}{2} - K_v \Delta t$$

$$C_P(U_{front} - U_P 2C_P) = - \left(\frac{U_P C_P{}^2}{r_P} + 2K_v \right) \Delta t \qquad (3.4.32)$$

Likewise, the negative characteristic line is estimated by :

$$r_Q = r_f - (U_Q - C_Q + U_{front}) \frac{\Delta t}{2} \qquad (3.4.33)$$

with its Riemann invariant :

$$C_Q(U_{front} - U_Q + 2C_Q) = \left(\frac{U_Q C_Q{}^2}{r_Q} + 2K_v \right) \Delta t \qquad (3.4.34)$$

There are four unknown variables : r_P, r_Q, r_f and U_{front}. Equations (3.4.32) to (3.4.35) are again solved by using the Newton-Raphson method, as mentioned in the previous section.

3.4.4 The Initial Conditions

As there are three sets of governing equations, three sets of initial conditions are needed. The initial conditions are set up at small time span after the column begins to collapse. To simplify setting up the initial conditions, it is assumed that at such time, the vapour-release region is not yet developed, and that the front condition may be taken as :

$$C = 0 \ , \ U = 2 \ , \ r_f = 1 + 2t \ , \ r_{bu} = r_f \text{ and } \varrho = \varrho_{min} \ .$$

With this assumption, only two regions are considered. The initial condition in the non-boiling region is set up by using equations (1.1.6), i.e. Greenspan and Butler's approximate solution of the SWEs of the axisymmetric-model. Following their method of solution, the initial condition in the

density-change region is also given by approximate solution of equations (3.4.4) to (3.4.6). The resulting equations are :

$$\begin{aligned} \mathbf{U} &= 2 - 2Z + [5Z^{1.5} - (E_1 + 5\mathbf{G_k} + 2)Z - 3Z^2]\mathbf{t} \\ \mathbf{C} &= Z + [7Z^{1.5} - (2E_1 + 7\mathbf{G_k} + 4)Z - 3Z^2]\frac{\mathbf{t}}{2} \\ \varrho &= \left(\frac{3Z}{2}\right)^{3\mathbf{G_k}t} \end{aligned} \tag{3.4.35}$$

with $E_1 = 3\mathbf{G_k} \ln\left(\frac{3Z}{2}\right)$, and $Z = \frac{1}{3}[2 - \frac{(\mathbf{r}-1)}{\mathbf{t}}]$.
The estimates of **U** and **C** in equations (3.4.36) are seen as the result of modification of equations (1.1.6), with additional terms E_1 and $\mathbf{G_k}$.

3.4.5 Aspects of the Numerical Solution

As shown in equation (3.4.6), $\mathbf{G_k}$ depends on the physical properties of the liquid and the dimensions/size of the column/tank. This equation shows that the value of $\mathbf{G_k}$ is high for a high boiling rate (high superficial velocity U_{vs}) and for a small tank (low horizontal velocity C_0). As an illustration, for LNG columns with radii of respectively 0.1, 1 and 10 m, with $(H_0/R_0) =$ 1 and the boiling rate of LNG $m = 0.54\,\mathrm{kg/m^2s}$ (see Appendix D), the values of $\mathbf{G_k}$ are respectively 0.3, 0.096 and 0.03. Hence, the highest value of $\mathbf{G_k}$ is likely to be of the order of 0.3. This study will therefore investigate the effect variation of $\mathbf{G_k}$ up to 0.5, which is believed to cover all possible scenarios for cryogenic liquid storage tank failure. From the definition of $\mathbf{G_k}$ in equation (3.4.6) and $\mathbf{K_v}$ in equation (3.4.20), the value of $\mathbf{K_v}$ can be calculated from :

$$\mathbf{K_v} = \frac{\mathbf{G_k}}{E_f(1-x)\varrho_{min}} \tag{3.4.36}$$

where $E_f = \left(\frac{\rho_l}{\rho_v} - 1\right)$ and x is the mass fraction of vapour corresponding to ϱ_{min}.

From physical property data, the density ratio $\frac{\rho_l}{\rho_v}$ of cryogenic liquid (nitrogen , oxygen , methane to propane) at their normal boiling point is found to be in the range 150 to 250. In order to represent this property in general, this study takes a typical density ratio $\frac{\rho_l}{\rho_v}$ of 200.

As in the case of non-boiling liquid flow, $\mathbf{U}$ and $\mathbf{C}$ are calculated by interpolation, using a Chebychev polynomial fitting. In this study, a density interpolation will also be carried out by using a Chebychev polynomial fitting. To obtain the results with a satisfactory accuracy and consistent with the mass conservation, density as a dependent variable is expressed in three ways :

1. Density ϱ as a function of $\mathbf{r}$: $\varrho = f_1(\mathbf{r})$.
2. The term $\ln \varrho$ as a function of $\mathbf{r}$: $\ln \varrho = f_2(\mathbf{r})$. This term is used, because it appears in Riemann invariant equations.
3. The term $\varrho \mathbf{C}^2$ as a function of $\mathbf{r}$: $\varrho \mathbf{C}^2 = f_3(\mathbf{r})$.

The accuracy and consistency of the numerical calculation procedure will be checked on a mass error basis, as carried out in the non-boiling liquid flow. The total mass can be calculated numerically by using :

$$\mathbf{M}_{tot} = 2\pi \sum_{i=0}^{N_{front}-1} (\varrho_i \mathbf{r}_i \mathbf{h}_i + \varrho_{i+1} \mathbf{r}_{i+1} \mathbf{h}_{i+1}) \frac{\Delta \mathbf{r}}{2} \qquad (3.4.37)$$

The dimensionless initial value of total mass is π. Instead of using the term "mass error", the difference between $\mathbf{M}_{tot}$ and the initial mass is called a mass discrepancy M_{discr}, expressed as a percentage of the initial value of total mass :

$$M_{discr} = \frac{(\mathbf{M}_{tot} - \pi)}{\pi} 100\,\% \quad ,$$

because M_{discr} also includes the mass loss due to vapour escape. The mass

loss or evaporated mass is calculated by :

$$\Delta M_v = \pi m \left({r_f}^2 - {r_{vr}}^2 \right) \quad ,$$

or in dimensionless form :

$$\Delta \mathrm{M}_v = \pi \frac{\mathrm{G_k}}{E_f} \left({\mathrm{r}_f}^2 - {\mathrm{r}_{vr}}^2 \right) \tag{3.4.38}$$

This evaporated mass is also expressed as a percentage of the initial value of total mass :

$$M_{evap} = \frac{\Delta \mathrm{M}_v}{\pi} 100\,\% \quad .$$

The calculation procedure is considered to be satisfactory and consistent with the conservation of mass if the difference between M_{discr} and M_{evap} is 1 % or less.

The energy content is not checked in this solution, because during the derivation of the governing equations, the potential and kinetic energies are neglected in the energy balance, and only thermal energy is considered. Hence, checking the total potential and kinetic energies, as carried out in non-boiling liquid flow, is not appropriate. Furthermore, checking the heat balance of cryogenic liquid flow is in fact equivalent to checking the vapour production (density change). This is also equivalent to the calculation of the evaporated mass, because the heat flux from the ground is related to the vapour production rate. In other words, checking the mass discrepancy also includes checking the heat balance.

3.5 Results and Discussion

3.5.1 The Nature of Two-phase Layer

As the two-phase layer is the main aspect of the model proposed in this study, it is essential to describe the nature of the two-phase layer, such as its

height and vapour concentration. The solution of the governing equations for the density-change region only results in an average density profile for the whole spill, but it does not identify the individual heights of the liquid and the two-phase layers. The relation between the height or thickness (h_b) and the density (ρ_b) of the two-phase layer is given by equation (3.3.17). In this case, density ρ_b indicates the vapour concentration in the two-phase layer. If the vapour void fraction ϵ_v in the two-phase layer is known, ρ_b can be determined from equation (3.3.18). To describe completely the nature of the two-phase layer, one more piece of information (equation or correlation) is needed; either the height of the two-phase layer h_b or its vapour concentration (ρ_b or ϵ_v).

The height of the two-phase layer essentially depends on :

1. the boiling rate or vapour generation rate m,
2. the horizontal velocity of the flow U,
3. the dimensions of the column (H_0 and R_0),
4. the physical properties of liquid and vapour,
5. the motion of vapour in the two-phase layer.

Parameter $\mathbf{G_k}$ of the model proposed in fact covers points 1 to 4 (see equation (3.4.6)). The motion of vapour in the two-phase layer is influenced by buoyancy, turbulence and acceleration of the flow resulting from the collapse of a liquid column: the vapour moves upward due to buoyancy, while turbulence may break up the vapour into bubbles and may balance buoyancy, which could slow down or accelerate the upward motion of the vapour. Unfortunately, no appropriate and reliable work or theory is available that can be used to describe the precise motion of the vapour under

these conditions, and hence the nature of the two-phase layer. Further thorough theoretical and experimental investigation is needed. However, a general and qualitative description of the two-phase layer can at least be given in this study.

If buoyancy dominates the upward motion of the vapour, the height of the two-phase layer h_b, or alternatively the vapour void fraction ϵ_v, can be estimated from such motion of bubbles in liquid. In this work, such an estimate is likely to give a higher value of h_b. On the other hand, if turbulence dominates the motion of the vapour, the estimate of h_b is likely to be lower than the actual value of h_b. The actual value of h_b may lie between these two estimates; buoyancy domination or turbulence domination.

Weisman et al. (1979) described the transition from dispersed flow to intermittent flow for two-phase flow in horizontal pipes. They defined dispersed flow as a flow in which the discontinuous phase is finely dispersed in a continuous phase; if the vapour or gas is the discontinuous phase, it is dispersed into small bubbles in the liquid; if the liquid is the discontinuous phase, there is mist flow. Weisman et al. also described that intermittent flow comprises slug, plug and bubbly flow, where the vapour or gas is contained in "large bubbles". They considered that in dispersed flow, turbulence can overcome buoyancy and break the vapour or gas into finely dispersed bubbles, and hence control the motion of bubbles. Based on their theoretical and experimental investigations, they estimated that dispersed flow exists when the total superficial mass flow rate G_T (gas and liquid) is equal to or greater than 10^7 kg/m^{2}hr. Unfortunately, this criterion can only give a qualitative description of one aspect of two-phase flow, but cannot be used to determine the vapour concentration in two-phase flow. Never-

theless, it may serve to describe the sort of liquid-vapour mixture in the two-phase layer in cryogenic liquid spills, which can be regarded as two-phase flow in a horizontal conduit with increasing height. For a methane column with a height and a radius of 10 m, the horizontal flow velocity is of the order of 10 m/s; with $\rho_l = 424$ kg/m^3 and a vapour void fraction $\epsilon_v = 0.5$, the total superficial mass flow rate $G_T = 7.6 \times 10^6$ kg/m^{2}hr, which is close to the criterion threshold above. It is therefore likely that the two-phase layer in the flow resulting from the collapse of a large column ($H_0 \geq 10$ m) is likely in dispersed flow.

Barnea (1986) also investigated dispersed two-phase flow in an inclined pipe; in this case, he was only concerned with gas dispersed in liquid. He considered that in the transition from dispersed bubbly flow to intermittent slug or plug flow, the turbulent force is in balance with buoyancy as well as with interfacial forces. At this transition condition, he assumed that finely dispersed bubbles are packed at maximum capacity. Above this maximum capacity, bubbles will coalesce. Here, bubbles are considered as uniform spheres in cubic packing. The maximum gas void fraction in such a structure is 0.52. However, this does not mean that maximum gas void fraction in the dispersed flow is always 0.52. Froth flow can have a higher void fraction of gas.

Larsen and Tong (1969) studied the critical heat flux in subcooled flow boiling inside a tube. They considered that the critical heat flux corresponds to the transition condition where the tube wall is fully covered with crowded bubbles, which are almost to coalesce to form a vapour layer. Larsen and Tong approximated this condition by assuming that the bubble-layer at the wall consists of liquid containing uniform size spherical bubbles, arranged in an octahedral structure. The maximum theoretical vapour void

fraction in such a structure is 0.74. They estimated that the void fraction of the bubble-layer at the tube wall is around 0.7. A similar study was also carried out by Weisman and Pei (1983). On the basis of experimental observation, they estimated that bubbles in the bubble-layer at the wall are of an elliptic shape, with a short to long axis ratio of about 1 : 3, rather than a spherical shape. They found that the maximum void fraction in this structure is around 0.82. All this shows that the vapour void fraction at the transition from dispersed flow (with vapour is finely dispersed) into intermittent flow may be in the range of 0.5–0.8.

If estimation of the upward motion of the vapour, and hence of the height of the two-phase layer, is only based on buoyancy, the vapour void fraction in the two-phase layer can be calculated from :

$$\epsilon_v = \frac{U_{vs}}{v_T} \quad ,$$

where U_{vs} is vapour superficial velocity and v_T is rising velocity of bubbles. For methane, with $m = 0.54$ kg/m^{2}s, the superficial velocity $U_{vs} = 0.30$ m/s.

Because such value of the superficial velocity is relatively high, bubbles tend to coalesce and form a large bubble, hence an estimate of the rising velocity of bubbles has to account for bubble concentration. At such condition, Wallis (1969) estimated v_T as given by:

$$v_T = K_0 U_{vs} + 1.53 \left[\frac{\sigma g(\rho_l - \rho_v)}{{\rho_l}^2} \right]^{0.25}$$

where K_0 is a flow distribution parameter; its value is around 1–1.5, and it is generally taken to be equal to 1.2. Based on this equation, for methane, $v_T = 0.56$ m/s or $\epsilon_v = 0.54$.

Levich (1962) estimated v_T of an oblate ellipsoid shape bubble in a mass-

bubbling process, given by:

$$v_T = \left[\frac{4\sigma^2 g(\rho_l - \rho_v)}{\alpha \mu_l {\rho_l}^2}\right]^{0.20}$$

where α is a constant, equal to 30. For methane, this equation gives $v_T =$ 0.35 m/s, or $\epsilon_v = 0.86$.

In summary, turbulence effects on two-phase flow just mentioned cannot as yet be used to estimate the concentration of vapour in the two-phase layer. Thus the concentration of vapour in the two-phase layer is not yet known. The calculation in this study mainly uses $\epsilon_v = 0.7$; the results presented in this Chapter are based on this value. Other results for $\epsilon_v = 0.5$ and 0.8 are enclosed in Appendix D. This therefore gives a general description of the two-phase layer, while precise description has to be further investigated theoretically and experimentally at a later date, by considering buoyancy, turbulence and transient condition together.

3.5.2 The Selected Procedure

In non-boiling liquid flow, the time increment $\Delta \mathbf{t}$ used was 0.05 and $\Delta \mathbf{r}$ was 0.10, which conforms with the CFL criterion, given by equation (1.4.15). In cryogenic liquid flow, the value of $|\mathbf{U} + \mathbf{C}|$ at some positions can be higher than 2, because the height of flow is affected by the two-phase layer thickness. Hence, to conform with the CFL criterion, $\Delta \mathbf{t}$ used may be less than 0.05. The time increment $\Delta \mathbf{t}$ used in the current calculation was then taken to be equal to 0.025.

The density interpolation was carried out using three methods, as mentioned before. Using ϱ as a dependent variable was unsatisfactory, where the difference between M_{discr} and M_{evap} was sometimes greater than 5%. This may be caused by the uncertainty about the density profile. As will be shown in the next section, for small values of $\mathbf{G_k}$, the density changes

rapidly at the vapour-release position $\mathbf{r}_{vr}$. At this position, the drastic density change may make interpolation insufficiently accurate. Using the term $\ln \varrho$ as a dependent variable improved the accuracy, but for large values of $\mathbf{G_k}$, this method still gave unacceptably low accuracy. According to equation (3.4.6), the density is calculated from :

$$\varrho_A = \varrho_P \exp - \int \frac{\mathbf{G_k}}{\mathbf{C}^2} dt \quad .$$

This means that a small variation or fluctuation in $\mathbf{C}$ can result in a large fluctuation in density, and this leads to a large difference between M_{discr} and M_{evap} for large values of $\mathbf{G_k}$. Finally, using the term $\varrho \mathbf{C}^2$ as a dependent variable gave $(|M_{discr}| - M_{evap}) \leq 1\%$. Table III-1 shows the mass discrepancy M_{discr} and the mass evaporated M_{evap} for $\mathbf{G_k} = 0.005$, 0.05 and 0.5. It is also shown that, within the dimensionless time span 0 to 2.5, the mass evaporated is very small (less than 1 %), except for $\mathbf{G_k} = 0.5$ at $\mathbf{t} > 1.5$. In this case, $\mathbf{G_k} = 0.5$ is regarded as an extreme condition, which is likely to arise in practice only for a small tank with a very high boiling rate. In general, the difference between the mass discrepancy and the mass evaporated is less than 1 %. In conclusion, interpolation using $\varrho \mathbf{C}^2$ was therefore used in this study.

3.5.3 The Flow Description

This comprises the front and vapour-release positions, the flow profile, and the density and velocity profiles. The results are presented in several figures, with $\mathbf{G_k}$ as a parameter. The density ratio $\frac{\rho_l}{\rho_v}$ is taken to be 200. With a vapour void fraction of 0.7, the corresponding minimum density is 0.3035. Other calculation results for several values of vapour void fractions are given in Appendix D.

As there is no relevant experimental and theoretical work available for

Table III-1: The mass discrepancy and the amount of mass evaporated for $(\rho_l/\rho_v) = 200$

Time	$G_k = 0.005$		$G_k = 0.05$		$G_k = 0.5$	
(t)	M_{discr}	M_{evap}	M_{discr}	M_{evap}	M_{discr}	M_{evap}
0.10	0.832	0.670E-5	0.818	0.620E-4	0.595	0.621E-3
0.20	0.066	0.807E-4	0.131	0.738E-3	-0.063	0.631E-2
0.30	-0.118	0.163E-3	-0.048	0.141E-2	-0.262	0.125E-1
0.40	-0.194	0.247E-3	-0.111	0.182E-2	-0.154	0.246E-1
0.50	-0.238	0.327E-3	-0.144	0.358E-2	-0.176	0.442E-1
0.60	-0.269	0.386E-3	-0.159	0.524E-2	-0.152	0.739E-1
0.70	-0.294	0.495E-3	-0.173	0.670E-2	-0.228	0.116E+0
0.80	-0.307	0.606E-3	-0.180	0.872E-2	-0.253	0.173E+0
0.90	-0.317	0.696E-3	-0.202	0.114E-1	-0.256	0.248E+0
1.00	-0.327	0.848E-3	-0.178	0.149E-1	-0.310	0.341E+0
1.10	-0.251	0.102E-2	-0.097	0.193E-1	-0.468	0.457E+0
1.20	-0.222	0.120E-2	-0.042	0.248E-1	-0.694	0.596E+0
1.30	-0.208	0.144E-2	-0.019	0.316E-1	-0.998	0.762E+0
1.40	-0.189	0.172E-2	0.021	0.397E-1	-1.135	0.956E+0
1.50	-0.177	0.206E-2	0.022	0.494E-1	-1.377	0.118E+1
1.60	-0.169	0.247E-2	0.025	0.608E-1	-1.542	0.144E+1
1.70	-0.163	0.296E-2	0.058	0.741E-1	-1.522	0.172E+1
1.80	-0.156	0.353E-2	0.085	0.894E-1	-1.459	0.205E+1
1.90	-0.142	0.421E-2	0.074	0.107E+0	-1.684	0.241E+1
2.00	-0.132	0.498E-2	0.092	0.127E+0	-1.822	0.281E+1
2.10	-0.124	0.586E-2	0.132	0.150E+0	-1.708	0.325E+1
2.20	-0.119	0.686E-2	0.119	0.175E+0	-1.902	0.373E+1
2.30	-0.106	0.800E-2	0.132	0.204E+0	-1.948	0.426E+1
2.40	-0.096	0.928E-2	0.136	0.235E+0	-1.911	0.483E+1
2.50	-0.092	0.107E-1	0.153	0.271E+0	-2.016	0.545E+1

comparison purposes, the results of this study are compared only with the theoretical results of non-boiling liquid flow. Below are descriptions of some aspects of the flow.

3.5.3.1 The Front and The Vapour-release Positions

Figures 3.11, 3.12 and 3.13 show the front position $\mathbf{r}_f$, the vapour-release position $\mathbf{r}_{vr}$ and the amount of evaporated mass M_{evap} as functions of time.

As shown in Figure 3.11, it is obvious that the propagation velocity of

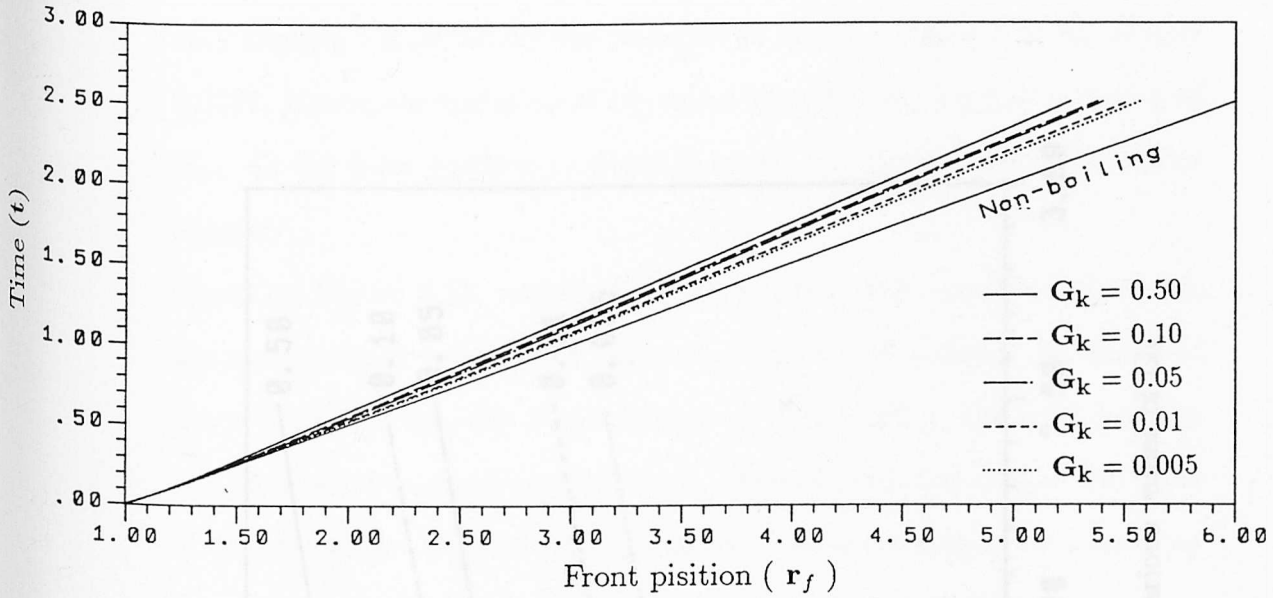


Figure 3.11: The front position for various values of G_k

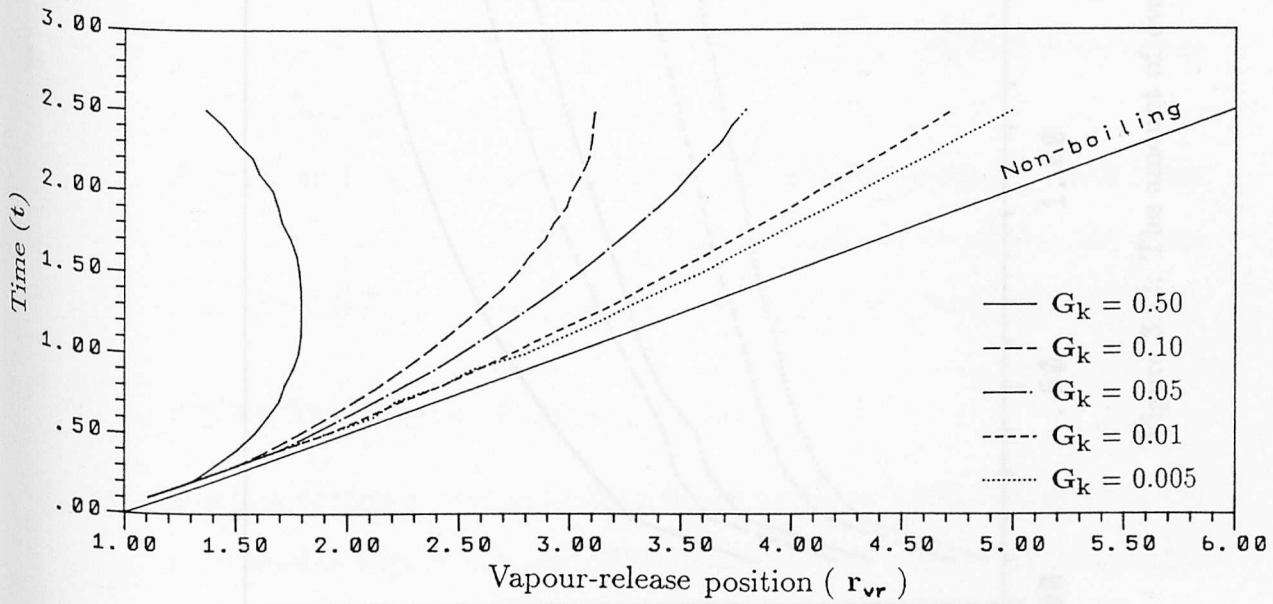


Figure 3.12: The vapour-release position for various values of G_k

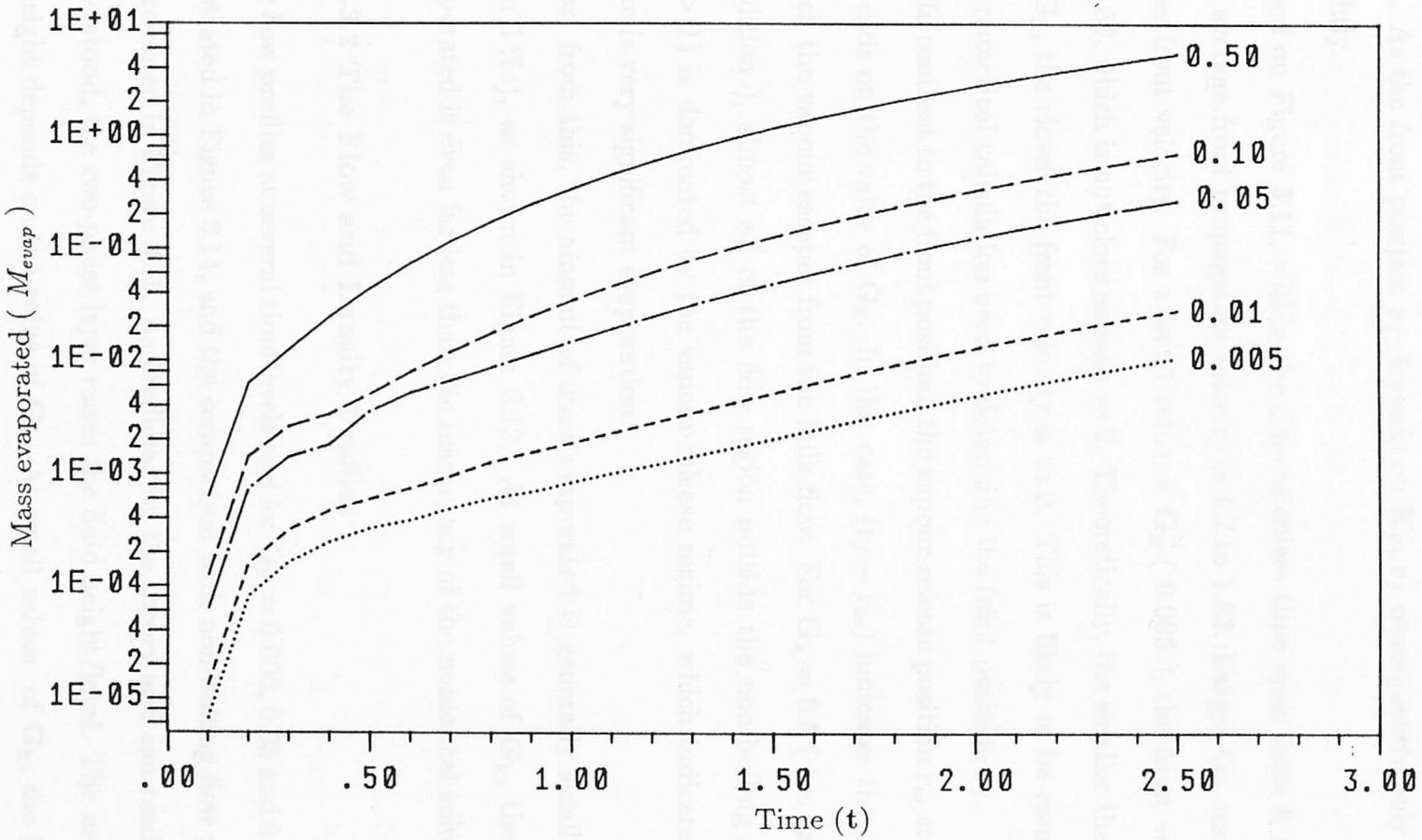


Figure 3.13: The amount of evaporated mass for various values of G_k

the front is less than 2. It is also not surprising that the front position is only slightly influenced by the variation of $\mathbf{G_k}$. For $\mathbf{G_k} = 0.5$, $\mathbf{K_v}$ is only 0.0084. Hence, the variation of $\mathbf{G_k}$ up to 0.5 gives only a small variation of $\mathbf{K_v}$. As the front position $\mathbf{r}_f$ depends on $\mathbf{K_v}$, $\mathbf{r}_f$ consequently only varies slightly.

Based on Figure 3.11, within the dimensionless time span from 0 to 2.5, the average front propagation velocity is 1.7 to 1.83. Larger $\mathbf{G_k}$ results in lower front velocity. For a small value of $\mathbf{G_k}$ (0.005), the front velocity is 1.83, which is not close enough to 2. Theoretically, the smaller the value of $\mathbf{G_k}$, the closer the front velocity is to 2. This is likely to be caused by the numerical calculation used to determine the front position $\mathbf{r}_f$.

In contrast to the front position, the vapour-release position $\mathbf{r}_{vr}$ strongly depends on the value of $\mathbf{G_k}$. In this case, $(\mathbf{r}_f - \mathbf{r}_{vr})$ indicates the area in which the vapour escapes from the bulk flow. For $\mathbf{G_k} = 0.5$ (i.e. extreme condition), almost all of the flow region outside the non-boiling region ($\mathbf{r} > 1$) is dominated by the vapour-release regime, which indicates that there is very significant evaporation.

Apart from this, the amount of mass evaporated is generally small (less than 1 %), as shown in Figure 3.13. At small values of $\mathbf{G_k}$, the mass evaporated is even far less than the inaccuracy of the numerical solution.

3.5.3.2 The Flow and Density Profiles

The flow profiles at several time levels and for $\mathbf{G_k} = 0.005$, 0.05 and 0.5, are illustrated in Figure 3.14, and the comparison with non-boiling flow profile is presented in Figure 3.15. As predicted by the theory and can readily be understood, the two-phase layer raises the fluid height/level. The increase in height depends on the value of $\mathbf{G_k}$. At small values of $\mathbf{G_k}$, the height

only increases slightly, and it is even difficult to distinguish the difference with the non-boiling liquid level, as can be seen in Figure 3.15. The two-phase layer in Figure 3.14 is drawn as a dotted line. This figure shows the effect of $\mathbf{G_k}$ upon the two-phase layer thickness.

At the extreme condition, such as at $\mathbf{G_k} = 0.5$, the height increase is very high. As $\mathbf{G_k}$ indicates the ratio of the superficial velocity of the vapour produced to the horizontal velocity of the flow (see equation (3.4.6)), the flow at $\mathbf{G_k} = 0.5$ is an example of the flow resulting from the collapse of a small column with a high boiling rate.

Figure 3.16 illustrates the density profiles at various $\mathbf{G_k}$ values. As mentioned before, the density profiles indicate the thickness and behaviour of the two-phase layer. From Figure 3.16, the nature of the density profile can be identified with two types of curve : A-type and B-type, as depicted in Figure 3.17. The A-type curve represents the flow with a thin two-phase layer and the B-type represents two-phase layer dominated flow. The flow dominated by the two-phase layer indicates that significant evaporation takes place. Line PQRS in Figure 3.17 is used to show the relative height of the two-phase layer, with respect to the total fluid height. The relative height of the two-phase layer for an A-type curve is shown by the ratio of PQ to PS. Similarly, the relative height of the two-phase layer for a B-type curve is given by the ratio of PR to PS. Briefly, by identifying the form of the density curve, the flow behaviour can be known. The A-type curve is encountered at small values of $\mathbf{G_k}$ and at a very early stage of spill/spread for moderate values of $\mathbf{G_k}$, such as 0.05 . On the other hand, for large values of $\mathbf{G_k}$ and at a late time of spill, the density profile has a B-type curve. It can be concluded that the density profile actually begins with an A-type curve, and gradually changes into a B-type curve, and that at a late

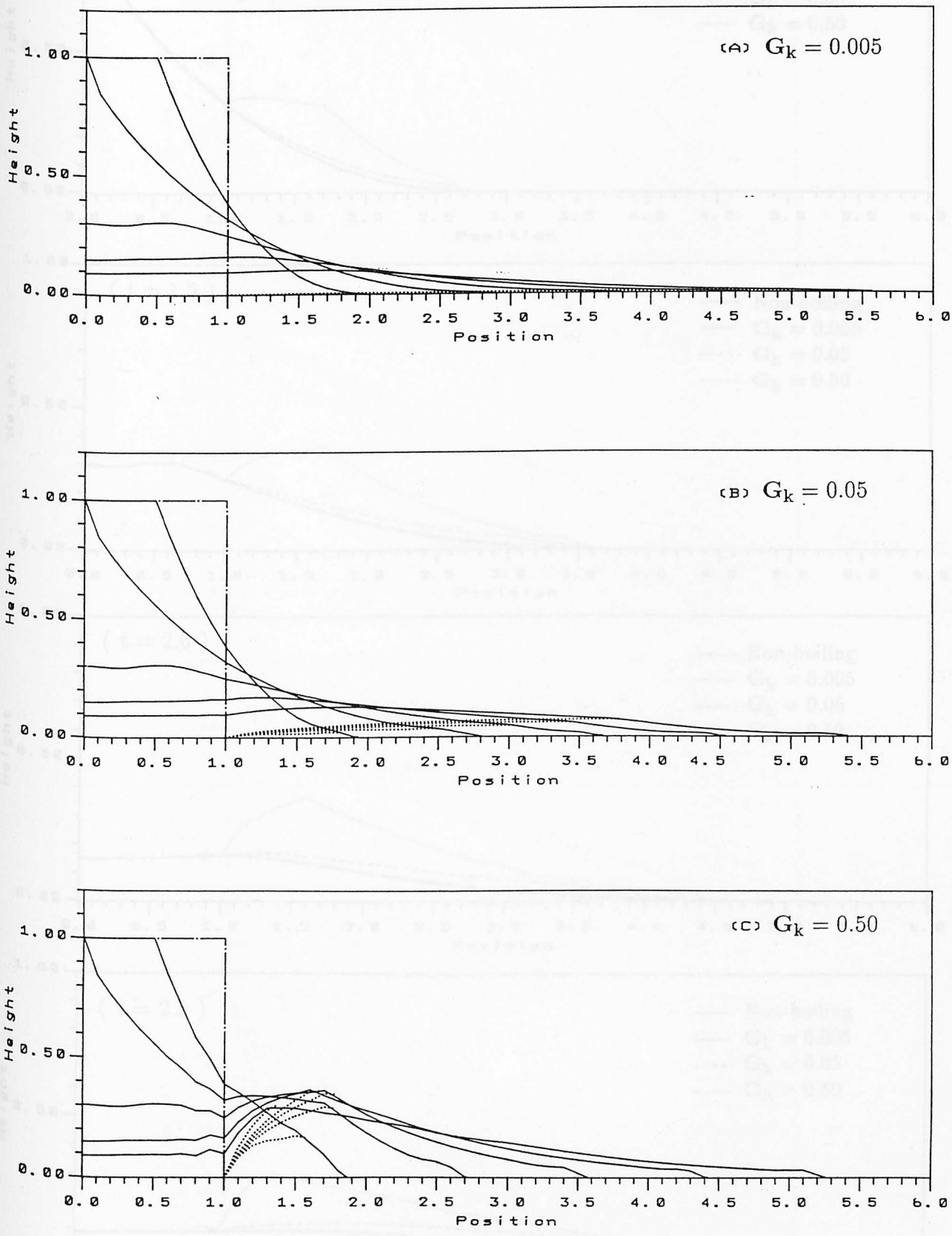


Figure 3.14: Flow profiles of cryogenic liquid flow for various values of G_k

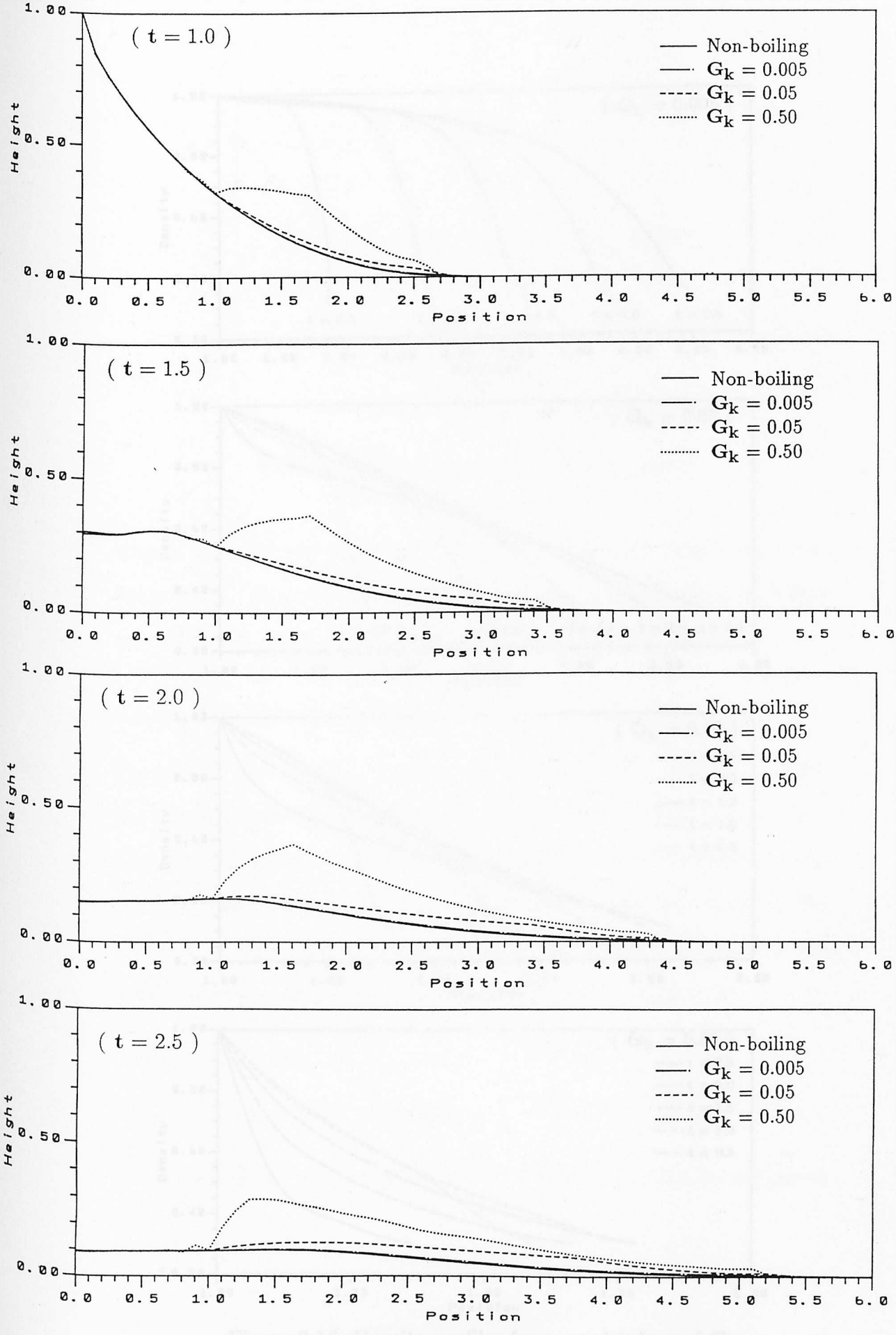


Figure 3.15: Comparison of flow profile between non-boiling liquid flow and cryogenic liquid flow

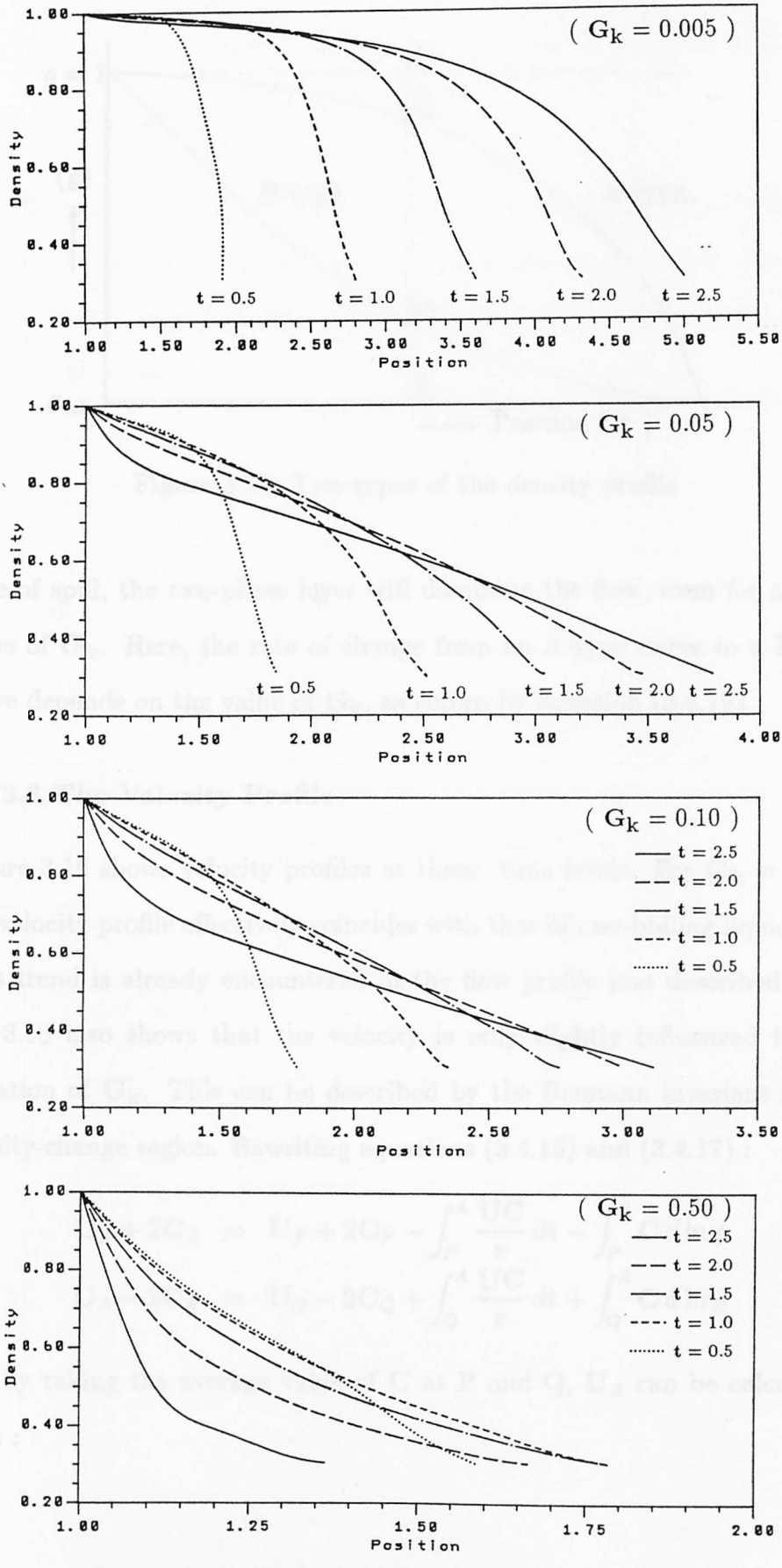


Figure 3.16: Density profiles for several values of G_k

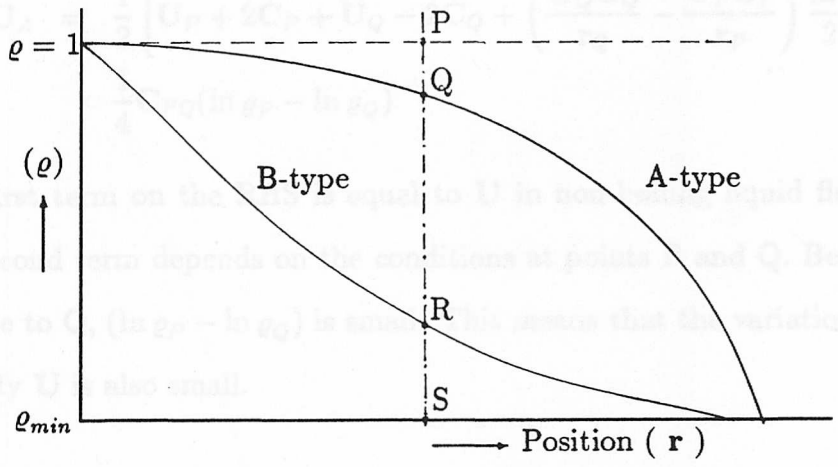


Figure 3.17: Two types of the density profile

time of spill, the two-phase layer will dominate the flow, even for a small value of $\mathbf{G_k}$. Here, the rate of change from an A-type curve to a B-type curve depends on the value of $\mathbf{G_k}$, as shown by equation (3.4.19).

3.5.3.3 The Velocity Profile

Figure 3.18 shows velocity profiles at three time levels. For $\mathbf{G_k} = 0.005$, the velocity profile effectively coincides with that of non-boiling liquid flow. This trend is already encountered in the flow profile just described. Figure 3.18 also shows that the velocity is only slightly influenced by the variation of $\mathbf{G_k}$. This can be described by the Riemann invariant in the density-change region. Rewriting equations (3.4.15) and (3.4.17) :

$$\mathbf{U}_A + 2\mathbf{C}_A = \mathbf{U}_P + 2\mathbf{C}_P - \int_P^A \frac{\mathbf{UC}}{\mathbf{r}}\,dt - \int_P^A \mathbf{C}\,d\ln\varrho$$

$$\mathbf{U}_A - 2\mathbf{C}_A = \mathbf{U}_Q - 2\mathbf{C}_Q + \int_Q^A \frac{\mathbf{UC}}{\mathbf{r}}\,dt + \int_Q^A \mathbf{C}\,d\ln\varrho$$

and by taking the average value of C at P and Q, $\mathbf{U}_A$ can be calculated from :

$$\mathbf{U}_A = \frac{1}{2}\left[\mathbf{U}_P + 2\mathbf{C}_P + \mathbf{U}_Q - 2\mathbf{C}_Q + \left(\frac{\mathbf{U}_Q\mathbf{C}_Q}{\mathbf{r}_Q} - \frac{\mathbf{U}_P\mathbf{C}_P}{\mathbf{r}_P}\right)\frac{\Delta \mathbf{t}}{2}\right]$$
$$\frac{1}{4}\mathbf{C}_{PQ}(\ln \varrho_P - \ln \varrho_Q)$$

The first term on the RHS is equal to U in non-boiling liquid flow, and the second term depends on the conditions at points P and Q. Because P is close to Q, $(\ln \varrho_P - \ln \varrho_Q)$ is small. This means that the variation of the velocity U is also small.

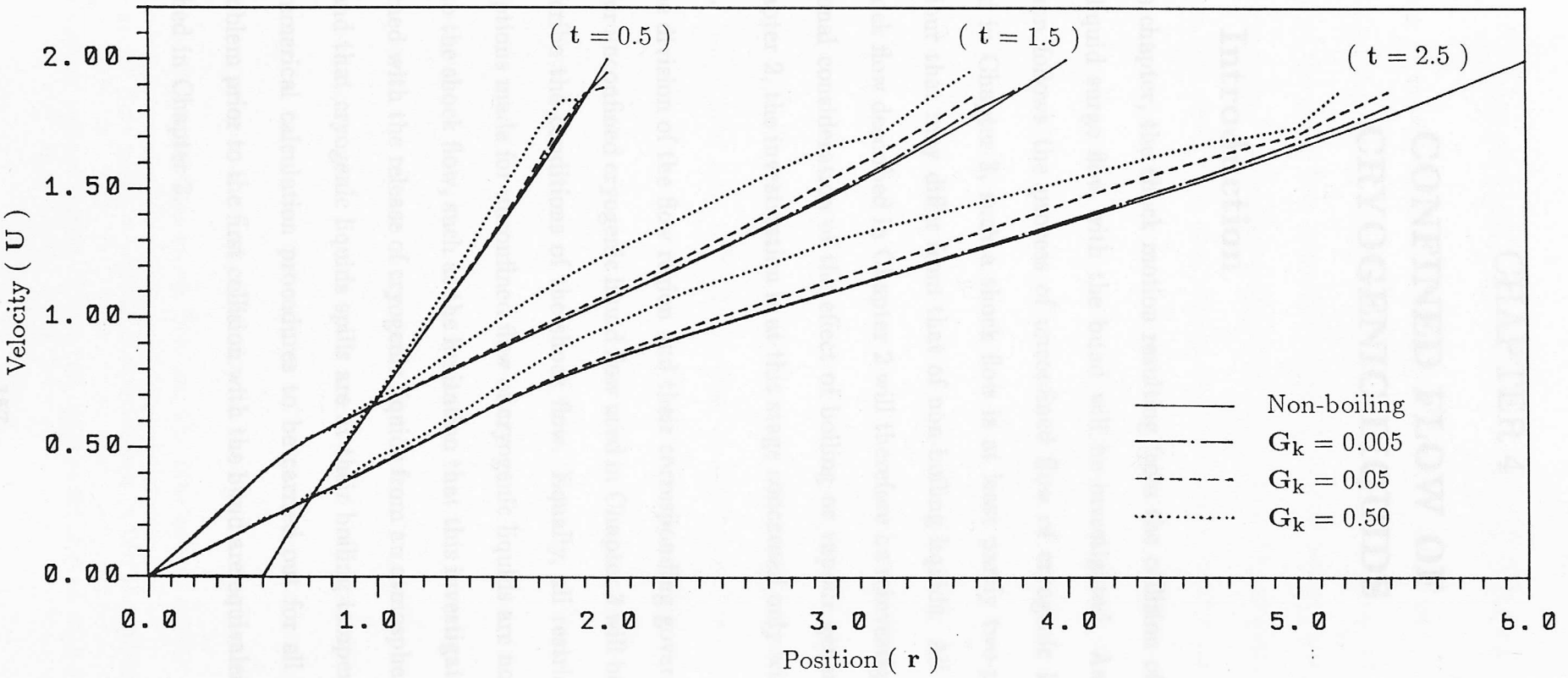


Figure 3.18: Comparison of velocity profiles between non-boiling liquid flow and cryogenic liquid flow

CHAPTER 4

CONFINED FLOW OF CRYOGENIC LIQUIDS

4.1 Introduction

In this chapter, the shock motion resulting from the collision of the cryogenic liquid surge flow with the bund will be investigated. As this phenomenon follows the process of unconfined flow of cryogenic liquids described in Chapter 3, such a shock flow is at least partly two-phase with behaviour that may differ from that of non-boiling liquids. All aspects of the shock flow described in Chapter 2 will therefore be reinvestigated, with additional consideration of the effect of boiling or vapour generation. As in Chapter 2, the investigation is at this stage concerned only with vertical bunds.

The division of the flow region and their corresponding governing equations for unconfined cryogenic liquid flow used in Chapter 3 will be extended to describe the conditions of the shock flow. Equally, all restrictions and assumptions made for unconfined flow of cryogenic liquids are now also applied to the shock flow, such as the limitation that this investigation is only concerned with the release of cryogenic liquids from an atmospheric storage tank and that cryogenic liquids spills are at their boiling temperature. The numerical calculation procedures to be carried out for all aspects of the problem prior to the first collision with the bund are equivalent to those described in Chapter 3.

4.2 Theoretical Description of Shock Flow

As soon as the cryogenic liquid surge flow has collided with a bund surrounding the original storage tank, a shock is formed. Some of the kinetic energy of the surge flow is converted into potential energy, and the height of the shock flow becomes much greater than that of the original surge flow. Because this shock flow of cryogenic liquid contains vapour, as in the case of unconfined flow of cryogenic liquids described in Chapter 3, its analysis is more complicated than that of non-boiling liquids. Here, the density of the vapour-liquid mixture is also a dependent variable, which is related to the vapour concentration in the flow.

The front of the cryogenic liquid surge flow is effectively in the vapour-release region, i.e. it is uniform vapour-liquid mixture. Hence, when this moving front collides with the bund and the shock is formed, this shock flow must also be in the vapour-release region, although the vapour motion in the shock flow may differ from that in the surge flow (i.e. the "as yet", unconfined flow). This is illustrated in Figure 4.1. Subsequently, when the returning shock swallows the density-change region of the, until then undisturbed, outgoing flow, the shock flow region will become divided into *density-change* and *vapour-release* regions. The density-change region covers the area in which the vapour does not yet reach the free surface and escapes, while the vapour-release region is characterized by the release of vapour and hence mass loss at the free surface. The nature of this density-change region is however different from that in the unconfined flow.

As in the case of unconfined flow of cryogenic liquids, the essential aspects of the two-phase shock flow are the presence of vapour and liquid in the shock flow and the vapour concentration in the two-phase layer and in the vapour-release region. These can only be estimated with some degree

of accuracy if the vapour motion in the shock flow is well understood. As

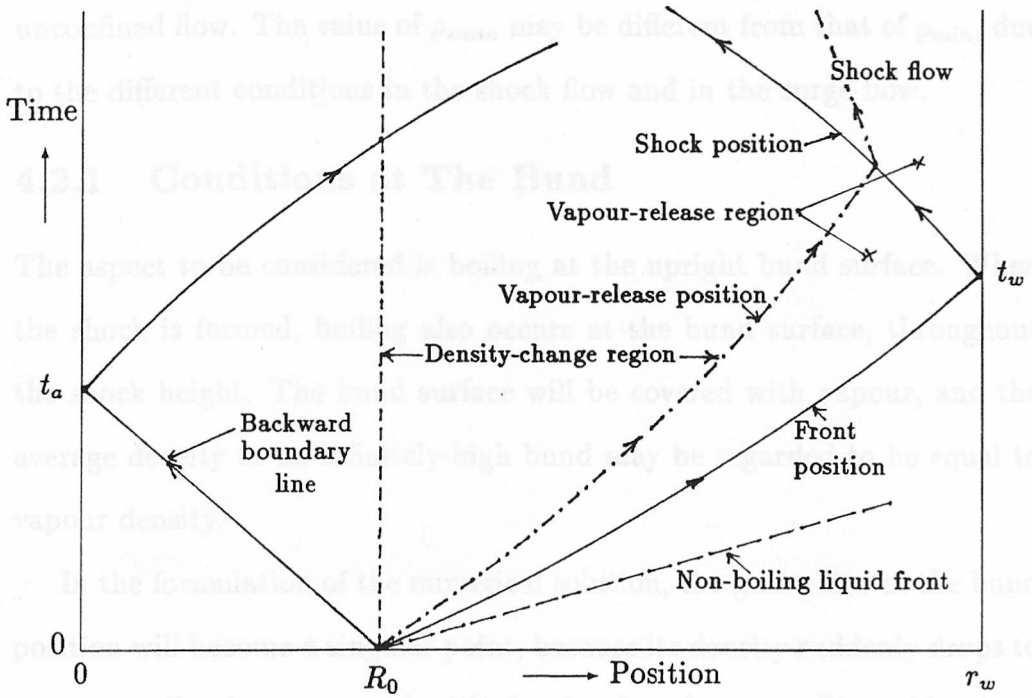


Figure 4.1: Illustration of the shock flow region division

the two-phase shock flow is a complex flow phenomenon, allowance has to be made for the constraints of the Shallow Water theory. The concept of the Shallow Water theory on the shock formation was described briefly in Section 2.2. However, an estimation of the vapour motion in the shock flow is still as difficult as that in the surge flow (in Chapter 3), as no related and reliable theoretical or experimental work is available. Our estimate of the vapour concentration in the two-phase layer and in the vapour-release region of the shock flow will be described in the section of Results and Discussion (Section 4.4).

Because the flow density is the dependent variable of the shock flow, the equations used to determine the conditions at the shock interface and at the bund are also different from those in the case of non-boiling liquids

described in Chapter 2. The minimum density for the shock flow is defined as ρ_{smin}, in order to distinguish it from the minimum density ρ_{min} for unconfined flow. The value of ρ_{smin} may be different from that of ρ_{min}, due to the different conditions in the shock flow and in the surge flow.

4.2.1 Conditions at The Bund

The aspect to be considered is boiling at the upright bund surface. When the shock is formed, boiling also occurs at the bund surface, throughout the shock height. The bund surface will be covered with vapour, and the average density at an infinitely-high bund may be regarded to be equal to vapour density.

In the formulation of the numerical solution, the grid-point at the bund position will become a singular point, because its density suddenly drops to a very small value compared with the density of surrounding grid-points. This makes the numerical solution difficult, if not impossible, to be carried out. To simplify the problem, the grid-point at the bund position is assumed to be represented by point W which is very close to the bund position r_w (see Figure 4.2(a)). The position of point W is $(r_w - \delta r)$, where δr is small. The conditions at the bund are assumed to be equal to those at point W, such that :

$$\rho_w = \lim_{r_W \to r_w} \rho_r \quad .$$

Boiling at the bund surface is then considered to affect only the horizontal velocity at the bund. The rate of boiling can be calculated from the heat flux from the bund surface. Here, boiling is considered to take place at a vertical surface. As an illustration, the estimate of film boiling coefficient of liquid methane at a vertical surface is about 0.31 kW/m^{2}C°. This corresponds to a heat flux $q_w = 57.7$ kW/m^2. For an infinitely-high bund, the

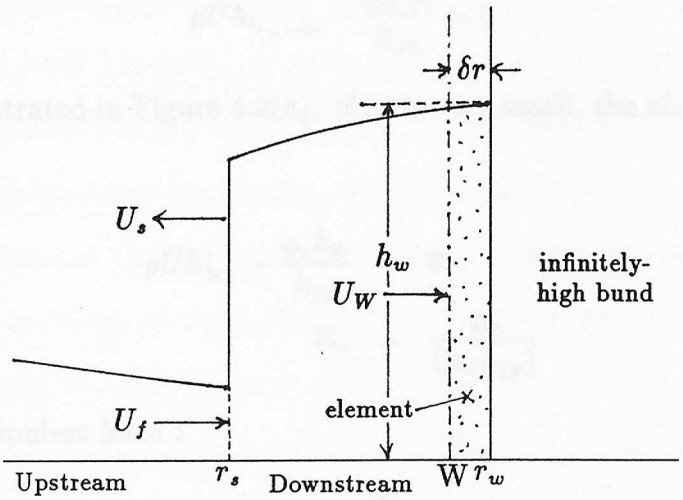


Figure 4.2 (a): Approximation of U_w at infinitely-high bund

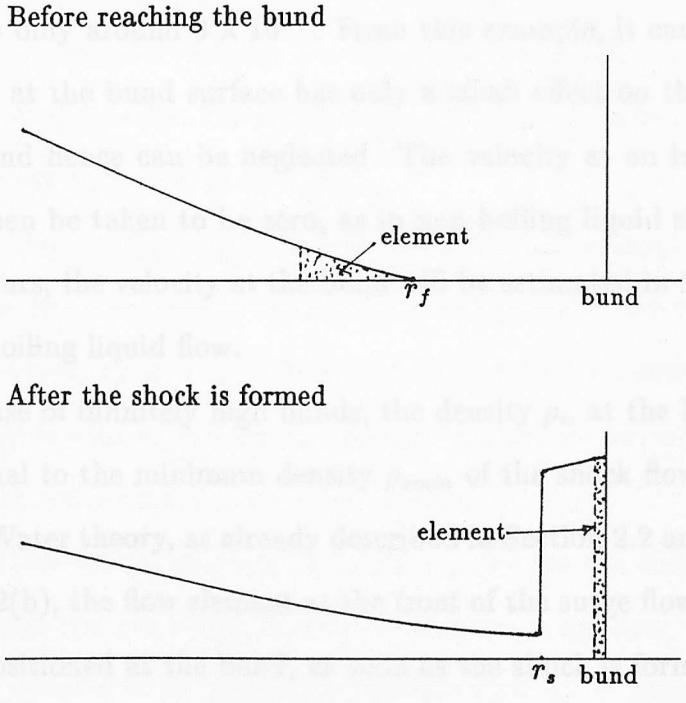


Figure 4.2: (b): Illustration of the shock formation

steady-state the mass balance in a very thin element between point W and the bund position may be given by :

$$\rho U h|_{r_w - \delta r} - \frac{q_w h_w}{h_{fg}} = 0$$

which is illustrated in Figure 4.2(a). If δr is very small, the above equation becomes :

$$\begin{aligned} \rho U h|_{r_w} - \frac{q_w h_w}{h_{fg}} &= 0 \\ U_w &= \frac{q_w}{(\rho_w h_{fg})} \end{aligned} \tag{4.2.1}$$

or in dimensionless form :

$$\mathbf{U}_w = \frac{q_w}{\rho_w h_{fg} C_0} \tag{4.2.2}$$

Equation (4.2.2) is used to approximate the velocity at an infinitely high bund. For liquid methane released from a storage tank with a height of 10 m, $\mathbf{U}_w$ is only around 3×10^{-5}. From this example, it can be deduced that boiling at the bund surface has only a small effect on the velocity at the bund, and hence can be neglected. The velocity at an infinitely-high bund can then be taken to be zero, as in non-boiling liquid shock flow. If overflow occurs, the velocity at the bund will be estimated in the same way as for non-boiling liquid flow.

In the case of infinitely high bunds, the density ρ_w at the bund is theoretically equal to the minimum density ρ_{smin} of the shock flow. According to Shallow Water theory, as already described in Section 2.2 and illustrated in Figure 4.2(b), the flow element at the front of the surge flow will be permanently positioned at the bund, as soon as the shock is formed. Because the density of the element at the front of the surge flow is equal to ρ_{min} (i.e. in the vapour-release region of unconfined flow), the density of the element at the bund will also be at its minimum value.

4.2.2 The Shock Conditions

To clarify the description, the flow in front of the shock interface (i.e. the surge flow) is called *upstream*, and that behind the shock interface (i.e. the shock flow itself) is called *downstream* (see Figure 4.2(a)). Symbols used in this description are identical to those in Chapter 2: subscripts f and b respectively denote upstream and downstream flows.

The conditions at the downstream, including density ρ_b, essentially depend on the conditions at the upstream. According to the Shallow Water theory, the shape of a flow element changes into tall but slim, as soon as the flow element crosses the shock interface. This flow element has a high potential energy but low horizontal velocity when it becomes a part of the shock flow. However, this description still cannot be used to estimate the downstream density ρ_b, because the density of the flow element may in reality change when it crosses the shock interface. In this case, it is difficult to estimate such a change of density. To simplify the estimation, assumptions are made, which depend on the value of the upstream density ρ_f and of the minimum density of the shock flow ρ_{smin}.

If $\rho_f > \rho_{smin}$, i.e. the upstream flow is in the density-change region, the density of the flow element is assumed to be constant, while it crosses the shock interface, or $\rho_b = \rho_f$. In this case, the downstream flow of the shock interface is also in the density-change region, in which the density subsequently decreases until ρ_{smin} is reached.

As mentioned before, the minimum density ρ_{smin} of the the shock flow may be different from the minimum density ρ_{min} of the surge flow. In the case when ρ_{smin} is greater than ρ_{min}, it is possible that $\rho_f < \rho_{smin}$, i.e. when the upstream density ρ_f is low (i.e. in the density-change region close to the vapour-release position and in the vapour-release region). If that is so, the density of the flow element will increase from ρ_f to ρ_{smin}, while it

crosses the shock interface. However, as previously described, it is difficult to estimate gradual change of the density at the shock interface. It is therefore assumed that in the case $\rho_f < \rho_{smin}$, for the purpose of the shock conditions calculation, the downstream density ρ_b is taken to be equal to ρ_{smin}.

As in non-boiling liquid flow, the conditions at the shock interface of cryogenic liquid flow are determined from mass and momentum balances across the shock interface. To derive the equations that can be used to determine the shock conditions in the general case, it is first considered that the upstream density ρ_f is not equal to the downstream density ρ_b, as in the case $\rho_f < \rho_{smin}$. Because the density changes when an element of fluid crosses the shock interface from the upstream to the downstream flow, there is mass loss at the shock interface, due to vapour release in this process of density change. The steady-state mass balance across the shock interface is given by :

$$\rho_f h_f (U_f - U_s) = \rho_b h_b (U_b - U_s) + M \tag{4.2.3}$$

with U_s = propagation velocity of the shock ,

M = mass loss rate at the shock interface.

The magnitude of M can be illustrated from this example : if the upstream and the downstream dimensionless densities are respectively $\varrho_f = 0.30$ and $\varrho_b = 0.70$, such a change from the upstream to the downstream density corresponds to a change of vapour mass fraction from 0.0115 to 0.0021. This example shows that the amount of vapour M released at the shock interface due to the density change is very small compared with other terms in equation (4.2.3). It is therefore assumed that the density change does not reduce the mass flow across the interface, and thus M may be neglected in the mass balance. Equation (4.2.3) now becomes :

$$\rho_f h_f (U_f - U_s) = \rho_b h_b (U_b - U_s) \tag{4.2.4}$$

The above equation is equivalent to the mass balance in non-boiling liquid shock flow (see equation (2.3.1)). Also neglecting the vapour release effect, the steady-state momentum balance is given by :

$$\rho_f h_f (U_f - U_s)^2 - \rho_b h_b (U_b - U_s)^2 = \frac{1}{2}\rho_b g {h_b}^2 - \frac{1}{2}\rho_f g {h_f}^2 \qquad (4.2.5)$$

If M_c^2 and M_d are respectively the ratio of height and density between the downstream and the upstream flows, i.e. $M_c = \sqrt{\frac{h_b}{h_f}} = \frac{C_b}{C_f}$ and $M_d = \frac{\rho_b}{\rho_f}$, the simultaneous solution of equations (4.2.4) and (4.2.5) results in :

$$U_s = U_f - \frac{C_f}{\sqrt{2}} \left[\frac{M_d {M_c}^2 (M_d {M_c}^4 - 1)}{(M_d {M_c}^2 - 1)} \right]^{\frac{1}{2}} \qquad (4.2.6)$$

$$U_b = \frac{U_f}{M_d {M_c}^2} + \left(1 - \frac{1}{M_d {M_c}^2}\right) U_s \qquad (4.2.7)$$

These two equations determine the shock conditions. In the special case when the upstream density is equal to the downstream density, i.e. $M_d = 1$, equations (4.2.6) and (4.2.7) become equivalent to equations (2.3.3) in the non-boiling liquid case.

4.3 Numerical Solution

Except at the shock position r_s and the bund position r_w, the numerical solution used is equivalent to that for unconfined flow of cryogenic liquids described in Chapter 3. There are also two sets of governing equations: one for the density-change region and one for the vapour-release region. Of particular interest is the equation (3.3.14) for the density-change region, which still depends on z. It is shown in Appendix F that the value of z has little effect for for $\mathbf{r}_w \geq 3$; its effect is only pronounced for $\mathbf{r}_w \leq 2$. In this case, $z = 0$ gives the highest estimate of liquid height at the bund. To provide for the worst case, this work therefore only considers $z = 0$, where equation (3.3.15) is used for the the governing equation in the density-change region.

The vapour-release position r_{vs} in the shock flow, which separates both regions, is also determined by using interpolation, as carried out for unconfined flow. The following is a summary of the solution by the MOC in both regions. Unless described, symbols of all variables used in this section onwards are written in their dimensionless form.

The solution in the density-change region has three sets of characteristic lines and Riemann invariants, as shown in Figure 4.3. These characteristic lines are PA as a positive characteristic line, QA as a negative characteristic line and SA as the third one.

The conditions at point A are determined by using :

- along the positive characteristic line PA :

$$\mathbf{r}_P = \mathbf{r}_i - (\mathbf{U}_P + \mathbf{C}_P + \mathbf{U}_A + \mathbf{C}_A)\frac{\Delta \mathbf{t}}{2} \tag{4.3.1}$$

with its Riemann invariant :

$$\begin{aligned} \mathbf{U}_A + 2\mathbf{C}_A = \mathbf{U}_P + 2\mathbf{C}_P \; &- \; \frac{1}{2}(\mathbf{C}_A + \mathbf{C}_P)(\ln \varrho_A - \ln \varrho_P) \\ &- \; \left(\frac{\mathbf{U}_A\mathbf{C}_A}{\mathbf{r}_A} + \frac{\mathbf{U}_P\mathbf{C}_P}{\mathbf{r}_P}\right)\frac{\Delta \mathbf{t}}{2} \end{aligned} \tag{4.3.2}$$

- along the negative characteristic line QA :

$$\mathbf{r}_Q = \mathbf{r}_i - (\mathbf{U}_Q - \mathbf{C}_Q + \mathbf{U}_A - \mathbf{C}_A)\frac{\Delta \mathbf{t}}{2} \tag{4.3.3}$$

with its Riemann invariant :

$$\begin{aligned} \mathbf{U}_A - 2\mathbf{C}_A = \mathbf{U}_Q - 2\mathbf{C}_Q \; &+ \; \frac{1}{2}(\mathbf{C}_A + \mathbf{C}_Q)(\ln \varrho_A - \ln \varrho_Q) \\ &+ \; \left(\frac{\mathbf{U}_A\mathbf{C}_A}{\mathbf{r}_A} + \frac{\mathbf{U}_Q\mathbf{C}_Q}{\mathbf{r}_Q}\right)\frac{\Delta \mathbf{t}}{2} \end{aligned} \tag{4.3.4}$$

- and along the characteristic line SA :

$$\mathbf{r}_S = \mathbf{r}_i - (\mathbf{U}_S + \mathbf{U}_A)\frac{\Delta \mathbf{t}}{2} \tag{4.3.5}$$

with its Riemann invariant :

$$\ln \varrho_A - \ln \varrho_S = -\mathbf{G_k}\left(\frac{1}{\mathbf{C}_A{}^2} + \frac{1}{\mathbf{C}_S{}^2}\right)\frac{\Delta \mathbf{t}}{2} \tag{4.3.6}$$

with $\mathbf{G_k}$ defined in equation (3.4.6).

Equations (4.3.1) to (4.3.6) are solved simultaneously by using the Newton-Raphson method.

Two characteristic lines in the vapour-release region are shown in Figure 4.4. They are : PA, which is a positive characteristic line, and QA, which is a negative one. The equations used to determine the conditions at point A are given by :

- along the positive characteristic line PA :

$$\mathbf{r}_P = \mathbf{r}_i - (\mathbf{U}_P + \mathbf{C}_P + \mathbf{U}_A + \mathbf{C}_A)\frac{\Delta \mathbf{t}}{2} \tag{4.3.7}$$

with its Riemann invariant :

$$\begin{aligned} \mathbf{U}_A + 2\mathbf{C}_A = \mathbf{U}_P \; &+ \; 2\mathbf{C}_P - \mathbf{K}_{\mathbf{vs}} \left(\frac{1}{\mathbf{C}_A} + \frac{1}{\mathbf{C}_P}\right) \frac{\Delta \mathbf{t}}{2} \\ &- \left(\frac{\mathbf{U}_A \mathbf{C}_A}{\mathbf{r}_A} + \frac{\mathbf{U}_P \mathbf{C}_P}{\mathbf{r}_P}\right) \frac{\Delta \mathbf{t}}{2} \end{aligned} \tag{4.3.8}$$

- and along the negative characteristic line QA :

$$\mathbf{r}_Q = \mathbf{r}_i - (\mathbf{U}_Q - \mathbf{C}_Q + \mathbf{U}_A - \mathbf{C}_A)\frac{\Delta \mathbf{t}}{2} \tag{4.3.9}$$

with its Riemann invariant :

$$\begin{aligned} \mathbf{U}_A - 2\mathbf{C}_A = \mathbf{U}_Q \; &- \; 2\mathbf{C}_Q + \mathbf{K}_{\mathbf{vs}} \left(\frac{1}{\mathbf{C}_A} + \frac{1}{\mathbf{C}_Q}\right) \frac{\Delta \mathbf{t}}{2} \\ &+ \left(\frac{\mathbf{U}_A \mathbf{C}_A}{\mathbf{r}_A} + \frac{\mathbf{U}_Q \mathbf{C}_Q}{\mathbf{r}_Q}\right) \frac{\Delta \mathbf{t}}{2} \end{aligned} \tag{4.3.10}$$

where $\mathbf{K}_{\mathbf{vs}}$ is defined in equation (3.4.37), with ϱ_{min} substituted by ϱ_{smin}. The Newton-Raphson method is also used to solve the above equations simultaneously.

At the early stage of shock formation, when the shock position $\mathbf{r}_s$ is still very close to the bund position $\mathbf{r}_w$, the time increment is refined in order to satisfy the CFL criterion. The method of time increment selection has already been described in Chapter 2 (Section 2.4.3).

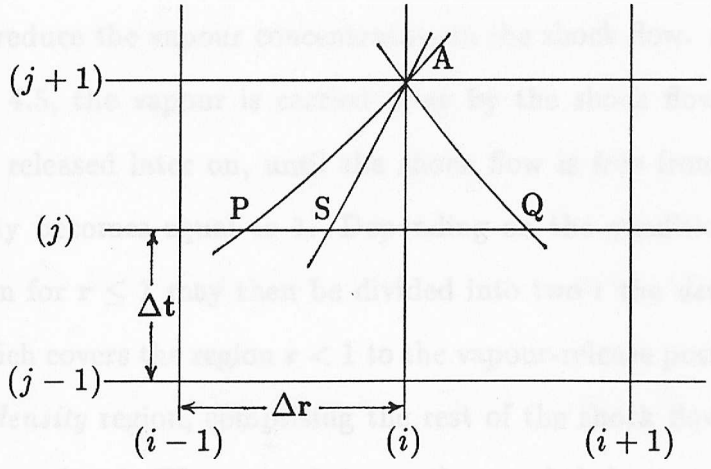


Figure 4.3: Characteristic lines PA, QA and SA in the density-change region

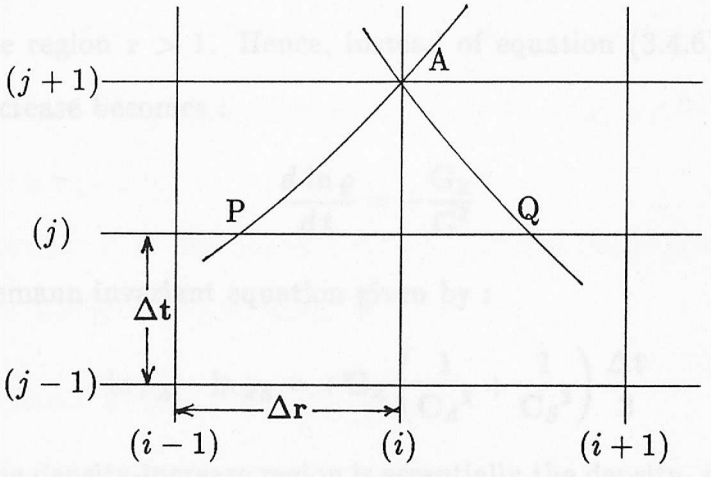


Figure 4.4: Two characteristic lines PA and QA in the vapour-release region

When the shock position $\mathbf{r_s}$ is less than $\mathbf{r} = 1$, the density of the shock flow in the region between $\mathbf{r_s}$ and $\mathbf{r} = 1$ will increase, because there is no boiling or no vapour production in the region $\mathbf{r} \leq 1$, while the vapour contained in the flow is gradually released at the free surface. This in turn will reduce the vapour concentration in the shock flow. As illustrated in Figure 4.5, the vapour is carried away by the shock flow and will be gradually released later on, until the shock flow is free from vapour and the density becomes equal to 1. Depending on the condition, the shock flow region for $\mathbf{r} \leq 1$ may then be divided into two : the *density-increase* region which covers the region $\mathbf{r} < 1$ to the vapour-release position, and the *constant-density* region, comprising the rest of the shock flow region with a density equal to 1. The governing equations and their numerical solution in the constant-density region are equivalent to those for non-boiling liquid shock flow. Of particular interest is the density-increase region. Because the density rises, the equation of density change rate given by equation (3.4.6) has to be adjusted. To simplify the problem, it is assumed that the rate of vapour release in the density-increase region is equal to the boiling rate in the region $\mathbf{r} > 1$. Hence, instead of equation (3.4.6), the rate of density increase becomes :

$$\frac{d \ln \varrho}{d\,\mathbf{t}} = +\frac{\mathbf{G_k}}{\mathbf{C}^2}$$

with a Riemann invariant equation given by :

$$\ln \varrho_A - \ln \varrho_S = +\mathbf{G_k} \left(\frac{1}{\mathbf{C_A}^2} + \frac{1}{\mathbf{C_S}^2} \right) \frac{\Delta \mathbf{t}}{2} \qquad (4.3.11)$$

Because the density-increase region is essentially the density- change region as well, the characteristic line equations are also given by equations (4.3.1), (4.3.3) and (4.3.5). In this case, positive and negative Riemann invariants need adjustment, due to density change and vapour release taking place

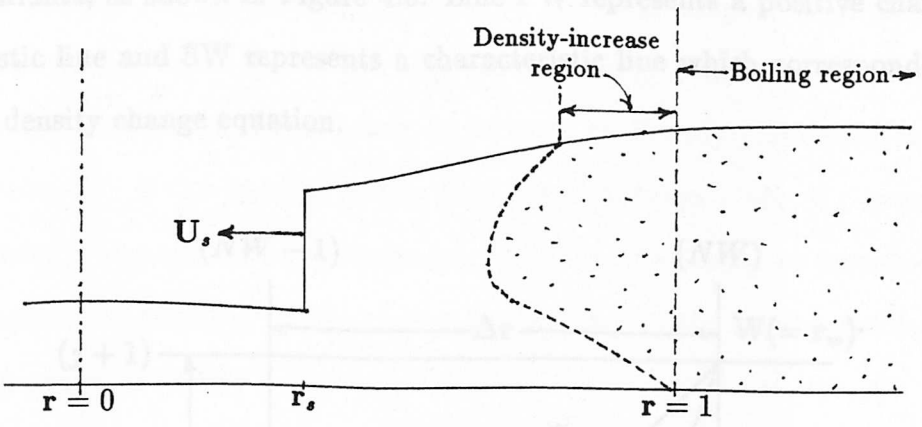


Figure 4.5: Illustration of the density-increase region when $r_s < 1$

simultaneously. The positive Riemann invariant is given by :

$$U_A + 2C_A = U_P + 2C_P - \frac{1}{2}(C_A + C_P)(\ln \varrho_A - \ln \varrho_P) - \left(\frac{U_A C_A}{r_A} + \frac{U_P C_P}{r_P}\right)\frac{\Delta t}{2} + K_{vb}\left(\frac{1}{\varrho_A C_A} + \frac{1}{\varrho_P C_P}\right)\frac{\Delta t}{2} \quad (4.3.12)$$

and similarly, the negative Riemann invariant is given by :

$$U_A - 2C_A = U_Q - 2C_Q + \frac{1}{2}(C_A + C_Q)(\ln \varrho_A - \ln \varrho_Q) + \left(\frac{U_A C_A}{r_A} + \frac{U_Q C_Q}{r_Q}\right)\frac{\Delta t}{2} - K_{vb}\left(\frac{1}{\varrho_A C_A} + \frac{1}{\varrho_Q C_Q}\right)\frac{\Delta t}{2} \quad (4.3.13)$$

with $K_{vb} = \dfrac{G_k}{\left(\frac{1}{\varrho_v} - 1\right)}$. Equations (4.3.11) to (4.3.13) are only valid until the density is equal to 1.

The conditions at the shock position and the bund position will be described in the following section.

4.3.1 Conditions at The Bund

Two regimes are also considered in the determination of the conditions at the bund. If the density ϱ_w at the bund is greater than minimum density ϱ_{smin} of the shock flow, the condition at the bund is determined in the density-change regime, by using two characteristic lines and their Riemann

invariants, as shown in Figure 4.6. Line PW represents a positive characteristic line and SW represents a characteristic line which corresponds to the density change equation.

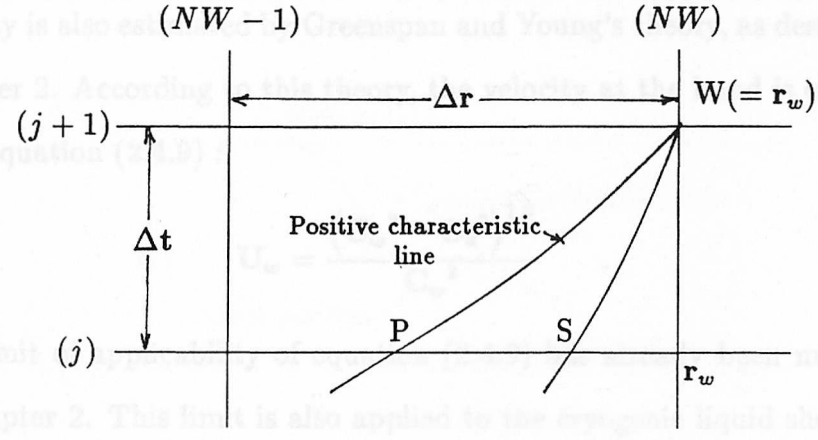


Figure 4.6: Determination of conditions at bund

The equations used to determine the condition at the bund are given by :

- the positive characteristic line PW :

$$\mathbf{r}_P = \mathbf{r}_w - (\mathbf{U}_w + \mathbf{C}_w + \mathbf{U}_P + \mathbf{C}_P)\frac{\Delta \mathbf{t}}{2} \tag{4.3.14}$$

with its Riemann invariant :

$$\mathbf{U}_w + 2\mathbf{C}_w = \mathbf{U}_P + 2\mathbf{C}_P - \frac{1}{2}(\mathbf{C}_w + \mathbf{C}_P)(\ln \varrho_w - \ln \varrho_P) - \left(\frac{\mathbf{U}_w\mathbf{C}_w}{\mathbf{r}_w} + \frac{\mathbf{U}_P\mathbf{C}_P}{\mathbf{r}_P}\right)\frac{\Delta \mathbf{t}}{2} \tag{4.3.15}$$

- and the characteristic line SW :

$$\mathbf{r}_S = \mathbf{r}_w - (\mathbf{U}_w + \mathbf{U}_S)\frac{\Delta \mathbf{t}}{2} \tag{4.3.16}$$

with density change correlation :

$$\ln \varrho_w - \ln \varrho_S = -\mathbf{G_k}\left(\frac{1}{\mathbf{C}_w{}^2} + \frac{1}{\mathbf{C}_S{}^2}\right)\frac{\Delta \mathbf{t}}{2} \tag{4.3.17}$$

The velocity $\mathbf{U}_w$ at the bund depends on the bund height, as in the case of non-boiling liquid shock flow. For infinitely-high bunds, in which overflow does not occur, $\mathbf{U}_w$ is taken to be zero, as already mentioned in the Section 4.2. If the bund is so low that overflow takes place, the overflow velocity is also estimated by Greenspan and Young's theory, as described in Chapter 2. According to this theory, the velocity at the bund is estimated from equation (2.4.9) :

$$\mathbf{U}_w = \frac{\left(\mathbf{C}_w{}^2 - \mathbf{C}_d{}^2\right)^{1.5}}{\mathbf{C}_w{}^2} \quad .$$

The limit of applicability of equation (2.4.9) has already been mentioned in Chapter 2. This limit is also applied to the cryogenic liquid shock flow. If the upstream flow rate is less than total overflow, as shown in equation (2.5.5), the velocity at bund is estimated by using equation (2.5.6) :

$$\mathbf{U}_w = \mathbf{U}_f \left(\frac{\mathbf{r}_s}{\mathbf{r}_w}\right) \left(\frac{\mathbf{C}_f}{\mathbf{C}_w}\right)^2 \quad .$$

With four equations : (4.3.14) to (4.3.17) together with the equation for $\mathbf{U}_w$, the five unknown variables : $\mathbf{r}_P$, $\mathbf{r}_S$, ϱ_w, $\mathbf{U}_w$ and $\mathbf{C}_w$ can be determined.

The conditions at the bund under the vapour-release regime to be determined involves only $\mathbf{U}_w$ and $\mathbf{C}_w$, because ϱ_w is equal to ϱ_{smin}. In this case, only the positive characteristic line is needed, which is given by equation (4.3.14). Here, the corresponding Riemann invariant is given by :

$$\begin{aligned} \mathbf{U}_w + 2\mathbf{C}_w = \mathbf{U}_P \; + \; & 2\mathbf{C}_P - \mathbf{K}_{vs}\left(\frac{1}{\mathbf{C}_w} + \frac{1}{\mathbf{C}_P}\right)\frac{\Delta t}{2} \\ & - \left(\frac{\mathbf{U}_w\mathbf{C}_w}{\mathbf{r}_w} + \frac{\mathbf{U}_P\mathbf{C}_P}{\mathbf{r}_P}\right)\frac{\Delta t}{2} \end{aligned} \qquad (4.3.18)$$

Variables $\mathbf{U}_w$, $\mathbf{C}_w$ and $\mathbf{r}_P$ can be determined from equations (4.3.14), (4.3.18) and $\mathbf{U}_w$ equation.

4.3.2 The Shock Conditions

The method of determination of the shock conditions is essentially similar to that in non-boiling liquid shock flow. Figure 4.7 illustrates this method. Besides equations (4.2.6) and (4.2.7), the negative characteristic

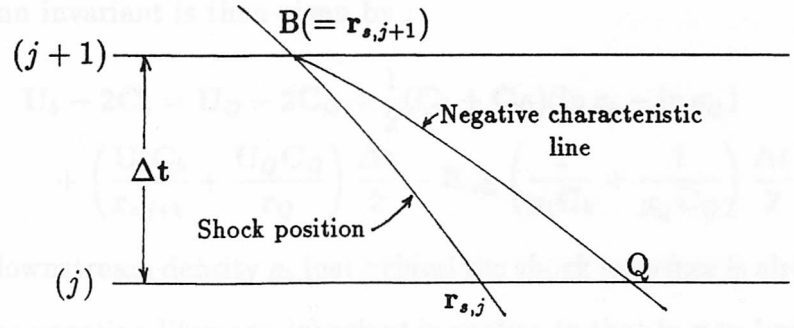


Figure 4.7: Determination of shock conditions

line that passes through the shock position and its Riemann invariant are needed. The shock position can be in the density-change or the vapour-release regimes. To cover both regimes, the negative Riemann invariant equation can be written in the form of :

$$\mathbf{U}_b - 2\mathbf{C}_b = \mathbf{U}_Q - 2\mathbf{C}_Q + \frac{K_1}{2}(\mathbf{C}_b + \mathbf{C}_Q)(\ln \varrho_b - \ln \varrho_Q) + \left(\frac{\mathbf{U}_b\mathbf{C}_b}{\mathbf{r}_{s,j+1}} + \frac{\mathbf{U}_Q\mathbf{C}_Q}{\mathbf{r}_Q}\right)\frac{\Delta \mathbf{t}}{2} + K_2.\mathbf{K}_{\mathbf{vs}}\left(\frac{1}{\mathbf{C}_b} + \frac{1}{\mathbf{C}_Q}\right)\frac{\Delta \mathbf{t}}{2} \quad (4.3.19)$$

where K_1 and K_2 are constants, which depend on the regimes. For the density-change regime, $K_1 = 1$ and $K_2 = 0$ and for the vapour-release regime, $K_1 = 0$ and $K_2 = 1$. Here, the corresponding negative characteristic line is given by :

$$\mathbf{r}_Q = \mathbf{r}_{s,j+1} - (\mathbf{U}_b - \mathbf{C}_b + \mathbf{U}_Q - \mathbf{C}_Q)\frac{\Delta \mathbf{t}}{2} \quad (4.3.20)$$

The new shock position $\mathbf{r}_{s,j+1}$ is estimated by using :

$$\mathbf{r}_{s,j+1} = \mathbf{r}_{s,j} + (\mathbf{U}_{s,j} + \mathbf{U}_{s,j+1})\frac{\Delta \mathbf{t}}{2} \quad (4.3.21)$$

With five equations :(4.2.6), (4.2.7) and (4.3.19) to (4.3.21), five unknown variables $\mathbf{U}_b$, $\mathbf{C}_b$, $\mathbf{U}_{s,j+1}$, $\mathbf{r}_{s,j+1}$ and $\mathbf{r}_Q$ can be determined. The detail of the numerical solution procedure was already described in Chapter 2.

A special case is when the shock position $\mathbf{r}_s$ is just less than 1. Here, the density will increase ; the shock is in the density-increase regime. Its Riemann invariant is then given by :

$$\mathbf{U}_b - 2\mathbf{C}_b = \mathbf{U}_Q - 2\mathbf{C}_Q + \frac{1}{2}(\mathbf{C}_b + \mathbf{C}_Q)(\ln \varrho_b - \ln \varrho_Q) + \left(\frac{\mathbf{U}_b\mathbf{C}_b}{\mathbf{r}_{s,j+1}} + \frac{\mathbf{U}_Q\mathbf{C}_Q}{\mathbf{r}_Q}\right)\frac{\Delta t}{2} - \mathbf{K_{vb}}\left(\frac{1}{\varrho_b\mathbf{C}_b} + \frac{1}{\varrho_Q\mathbf{C}_Q}\right)\frac{\Delta t}{2} \quad (4.3.22)$$

If the downstream density ϱ_b just behind the shock interface is already equal to 1, the negative Riemann invariant is similar to that in non-boiling liquid shock flow. This can also be achieved by taking $K_1 = K_2 = 0$ in equation (4.3.19).

4.3.3 The Initial Conditions

Unlike the case of non-boiling liquid shock flow, there is no approximate analytical solution which can be used to set up the initial conditions for the cryogenic liquid shock flow in the early stage of shock formation. In this case, the initial condition will be set up by using the second method of initialization of the shock conditions in non-boiling liquid shock flow, described in Section 2.5.1. This method is based on the assumption that the shock height is uniform in the early stage of shock formation, as illustrated in Figure 4.8.

The shock level is determined from a mass balance over the shock and equation for the shock propagation velocity $\mathbf{U}_s$ (equation (4.2.4)). To simplify the setting up of the initial conditions, it is assumed that the shock density is uniform, i.e. the density at the shock interface is equal to the density at the bund. The shock density is determined from the upstream

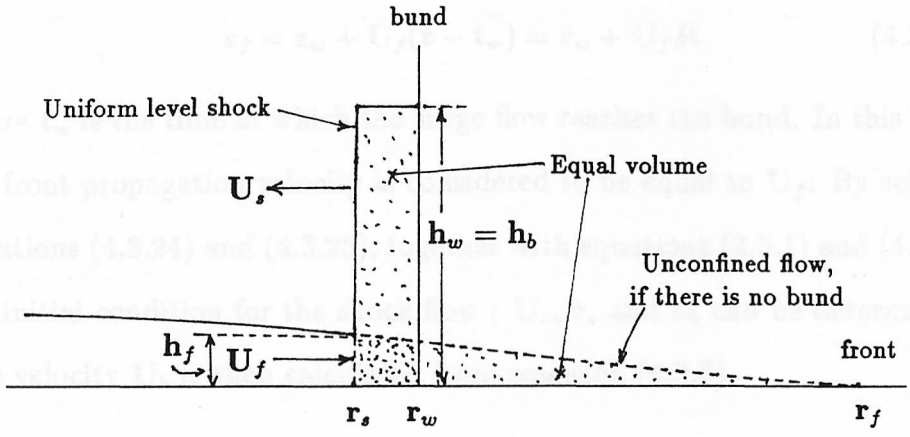


Figure 4.8: Uniform shock level assumption in the early stage of shock formation

density ϱ_f : for ϱ_f greater than the minimum shock density ϱ_{smin}, the shock density $\varrho_b = \varrho_f$ and, for ϱ_f less than ϱ_{smin}, then $\varrho_b = \varrho_{smin}$.

As soon as the shock is formed, boiling occurs at the bund surface. This causes mass loss in the shock flow due to vaporization, which reduces the total mass of the shock flow. In this initialization, such mass loss is assumed to be very small and hence neglected from the mass balance. From Figure 4.8, the total mass of the shock flow is estimated from the total mass of the dotted area for unconfined flow, from the shock position $\mathbf{r}_s$ to the front position $\mathbf{r}_f$. The mass balance mentioned is given by :

$$\pi \varrho_b \mathbf{h}_b \left(\mathbf{r}_w{}^2 - \mathbf{r}_s{}^2 \right) = 2\pi \int_{\mathbf{r}_s}^{\mathbf{r}_f} \varrho \mathbf{h} \mathbf{r} \, d\mathbf{r} \qquad (4.3.23)$$

The RHS of equation (4.3.23) can also be approximated by using :

$$\pi \varrho_b \mathbf{h}_b \left(\mathbf{r}_w{}^2 - \mathbf{r}_s{}^2 \right) = \frac{\pi}{2} \bar{\varrho}_f \mathbf{h}_f \left(\mathbf{r}_f{}^2 - \mathbf{r}_s{}^2 \right) \qquad (4.3.24)$$

with $\bar{\varrho}_f$ being the average density along $\mathbf{r}_s$ to $\mathbf{r}_f$. The front position $\mathbf{r}_f$ in unconfined flow is essentially determined by numerical solution, and depends on parameter $\mathbf{K_v}$. The other alternative for determination of $\mathbf{r}_f$

is by approximation with :

$$\mathbf{r}_f = \mathbf{r}_w + \mathbf{U}_f(\mathbf{t} - \mathbf{t}_w) = \mathbf{r}_w + \mathbf{U}_f\delta\mathbf{t} \qquad (4.3.25)$$

where $\mathbf{t}_w$ is the time at which the surge flow reaches the bund. In this case, the front propagation velocity is considered to be equal to $\mathbf{U}_f$. By solving equations (4.3.24) and (4.3.25), together with equations (2.5.1) and (4.2.4), the initial condition for the shock flow : $\mathbf{U}_s$, $\mathbf{r}_s$ and $\mathbf{h}_b$ can be determined. The velocity $\mathbf{U}_b$ is then calculated from equation (4.2.5).

4.4 Results And Discussion

4.4.1 Vapour Concentration

As in the case of unconfined flow of cryogenic liquids, the description of the two-phase shock flow is also concerned with the vapour concentration in the two-phase layer and in the vapour-release region, which depends on the vapour motion in the shock flow. The vapour motion is mainly affected by buoyancy and turbulence, as already discussed in Chapter 3 (Section 3.5.1). Buoyancy causes the vapour to move upward, while turbulence may slow down or may accelerate the upward motion of the vapour, and may break up the vapour into bubbles. The degree of turbulence depends on the flow conditions.

Abbott (1966) described that the surge flow (i.e. unconfined flow) is characterized by $\frac{U}{\sqrt{gh}}$ or $\frac{\mathbf{U}}{\mathbf{C}} > 1$, which is called supercritical flow, and that the shock flow is characterized by $\frac{\mathbf{U}}{\mathbf{C}} < 1$, so-called subcritical flow. The surge flow is relatively shallow with a relatively high horizontal velocity, while the shock flow is deeper with a lower horizontal velocity. This difference in condition between the surge flow and the shock flow may lead to the result that the vapour concentration in the two-phase layer of the surge flow may also differ from that in the shock flow. As the surge flow

is relatively shallow, the vapour in the two-phase layer of the surge flow may reach the free or top surface rather quickly and escape. On the other hand, the residence time for the vapour in the shock flow is longer than that in the surge flow, because the shock flow is deeper than the surge flow. This may in turn affect the vapour motion, where the vapour may break up into bubbles before reaching the free surface. The vapour concentration may therefore greatly vary throughout the height of the two-phase layer of the shock flow, where the vapour concentration is high at the bottom. In reality, the shock flow may also be turbulent, which promotes mixing of vapour and liquid. However, all these factors cannot be used to estimate quantitatively the vapour distribution and concentration in the two-phase layer and in the vapour-release region of the shock flow. Furthermore, no related and reliable, previous theoretical and experimental work has been found.

One rough method to estimate the vapour concentration in the two-phase layer and in the vapour-release region is by assuming that the vapour motion in the shock flow is analogous to the vapour motion in a bubble column or in pool boiling, i.e. in a deep liquid pool. As described above, the vapour may break up into bubbles before it reaches the free surface. If buoyancy indeed dominates the vapour motion, the vapour concentration (vapour void fraction) in the shock flow may be estimated from the upward motion of bubbles in liquid, which has already been described in Chapter 3 (Section 3.5.1). On this basis, the estimates of vapour void fraction for methane liquid are: $\epsilon_v = 0.54$ (Wallis, 1969) and $\epsilon_v = 0.86$ (Levich, 1962).

Azbel (1981) analyzed theoretically the hydrodynamics of bubbling phenomena in a liquid pool, in steady condition. He divided the phenom-

ena into two cases: rapid bubbling and slow bubbling. Rapid bubbling is encountered in shallow liquid pools with a relatively high gas superficial velocity, such as in sieve trays of distillation columns. Slow bubbling is characterized by a deep pool and low gas superficial velocity, as encountered in a bubble column. Although there is no sharp transition between both bubbling phenomena, Azbel identified them as follows : for rapid bubbling, the depth is less than 15 cm with a superficial gas velocity of more than 0.5 m/s while for slow bubbling, the depth is greater than 15 cm with a gas superficial velocity less than 0.2 m/s. It appears that this is a rough description, as no physical properties and other factors that influence the bubbling phenomenon are involved.

To obtain a gas void fraction relation, Azbel used the principle that whenever a two-phase flow system is in steady-state, the total available energy is at a minimum. The energy considered comprises potential, dissipative and surface tension energies. Based on an energy balance, Azbel obtained an equation as a function of fluid properties (liquid and gas), void fraction and liquid height or pool depth. He then derived this equation by using a variational method (Lagrangian multiplier), corresponding to the condition of minimum energy level. Of interest to this study is his analysis in slow bubbling. At a minimum energy level, he found that the maximum gas void fraction ϵ_v is around 0.3–0.4. Although the condition of the shock flow is unsteady, bubble motion in the shock flow may be regarded as a slow bubbling phenomenon, as bubbles move upward in a deep liquid pool.

In summary, the vapour concentration in the two-phase layer and in the vapour-release region of the shock flow are still not yet known, as also emphasized in Section 3.5.1 of Chapter 3. Further thorough theoretical and experimental investigation is still needed. To give a general description of

the two-phase shock flow, the maximum value of the vapour void fraction in the two-phase layer and in the vapour-release region of the shock flow $\epsilon_v = 0.3$ is used in this study. With $(\rho_l/\rho_v) = 200$, this corresponds to $\varrho_{smin} = 0.7015$. The maximum vapour void fraction for the surge flow $\epsilon_v = 0.7$ is used for the calculation of the upstream conditions, as that is used in Chapter 3.

4.4.2 Mass Discrepancy and Mass Evaporated

The mass discrepancy and the mass evaporated for confined flow are only calculated after the shock has been formed. Similar to equation (3.4.38), the total mass is calculated numerically by using :

$$\mathbf{M}_{tot} = 2\pi \sum_{i=0}^{NW-1} \left[\varrho_i \mathbf{h}_i \mathbf{r}_i + \varrho_{i+1} \mathbf{h}_{i+1} \mathbf{r}_{i+1}\right] \frac{\Delta \mathbf{r}}{2} \qquad (4.4.1)$$

The dimensionless total initial mass is equal to π. The mass discrepancy, as also defined in Chapter 3, is equal to the difference between the calculated mass $\mathbf{M}_{tot}$ from equation (4.4.1) and the total initial mass π, expressed as a percentage of the total initial mass :

$$M_{discr} = \frac{(\mathbf{M}_{tot} - \pi)}{\pi} 100\,\% \qquad (4.4.2)$$

Unlike unconfined flow, the total evaporated mass in confined flow comprises the evaporated mass in the upstream flow and that in the downstream flow. The upstream evaporated mass will only be calculated if the vapour-release position $\mathbf{r}_{vr}$ is less than the shock position $\mathbf{r}_s$. This is given by :

$$\mathbf{M}_{vu} = \pi \frac{\mathbf{G_k}}{E_f} \int (\mathbf{r}_s{}^2 - \mathbf{r}_{vr}{}^2)\, dt \quad .$$

with $\mathbf{M}_{vu}$ being the upstream evaporated mass. The downstream evaporated mass $\mathbf{M}_{vd}$ is given by :

$$\mathbf{M}_{vd} = \pi \frac{\mathbf{G_k}}{E_f} \int (\mathbf{r}_w{}^2 - \mathbf{r}_{vs}{}^2)\, dt \quad .$$

The total evaporated mass is then :

$$\mathbf{M}_{vtot} = \mathbf{M}_{vu} + \mathbf{M}_{vd} \tag{4.4.3}$$

The total evaporated mass is also expressed in the same way as the mass discrepancy :

$$M_{evap} = \frac{(\mathbf{M}_{vtot} - \pi)}{\pi} 100\,\% \tag{4.4.4}$$

For infinitely-high bund case, the numerical calculation procedure is consistent with conservation of mass if the difference between the mass discrepancy M_{discr} calculated from equation (4.4.2) and the total mass evaporated M_{evap} is less than 1 % . In the case of low bunds, the total amount of overflow also has to be taken into account. Hence, the consistency of the numerical calculation is :

$$Consistency \equiv M_{discr} - M_{evap} - (\ Total\ overflow\ ) \quad .$$

An example of the result is shown in Table IV-1, for $\mathbf{r}_w = 2$ and several values of $\mathbf{G_k}$, in the case of infinitely-high bunds. Other results are enclosed in Appendix E. These results show that the difference between M_{discr} and M_{evap} is less than 1 %, meaning that the numerical calculation procedure is consistent with conservation of mass. This also shows that the numerical calculation procedure used in this study is satisfactory.

The results also show that, for $\mathbf{r}_w \leq 2$, the total evaporated mass at the moment the shock flow converges at the axis of symmetry is still less than 1 %. On the other hand, the total mass evaporated at the same instant is relatively high for $\mathbf{r}_w = 4$. As expected theoretically, greater bund distance $\mathbf{r}_w$ will result in greater amount of the total evaporated mass, due to wider boiling area (from $\mathbf{r} = 1$ to $\mathbf{r}_w$). The total evaporated mass is also presented in Figure 4.9, for $\mathbf{r}_w = 3$ and 4. It is shown that in

Table IV-1: Mass discrepancy and mass evaporated for $\mathbf{r}_w = 2$ and infinitely-high bund

Time	$\mathbf{G_k} = 0.01$		$\mathbf{G_k} = 0.05$		$\mathbf{G_k} = 0.10$	
(t)	M_{discr}	M_{evap}	M_{discr}	M_{evap}	M_{discr}	M_{evap}
0.60	-0.220	0.0006	0.123	0.0031	0.112	0.0096
0.80	-0.253	0.0006	-0.031	0.0033	-0.093	0.0105
1.00	-0.296	0.0006	-0.368	0.0035	-0.528	0.0119
1.20	-0.266	0.0006	-0.745	0.0036	-1.218	0.0147
1.40	-0.549	0.0006	-0.161	0.0036	-0.481	0.0193
1.50	-0.497	0.0006	-0.491	0.0036	-1.012	0.0224
1.60	-0.421	0.0006	-0.840	0.0036	0.089	0.0260
1.70	-0.338	0.0006	-0.213	0.0037	-0.517	0.0301
1.80	-0.444	0.0006	-0.593	0.0037	-1.143	0.0349
1.90	-0.355	0.0006	-0.970	0.0037	-0.056	0.0403
2.00	-0.276	0.0006	-0.376	0.0037	-0.719	0.0463
2.10	-0.399	0.0006	-0.764	0.0038	-1.393	0.0529
2.20	-0.319	0.0006	-1.160	0.0038	-0.394	0.0601
2.30	-0.245	0.0006	-0.625	0.0039	-1.104	0.0681
2.40	-0.366	0.0006	-1.089	0.0040	-0.215	0.0767
2.50	-0.266	0.0006	-0.609	0.0042	-0.956	0.0860
2.60	-0.374	0.0006	-1.164	0.0050	-0.233	0.0960
2.70	-0.251	0.0006	-0.822	0.0061	-1.001	0.1070
2.80	-0.349	0.0006	-1.632	0.0071	-0.423	0.1180
2.90	-0.206	0.0006	-1.372	0.0082	-1.208	0.1310
3.00	-0.296	0.0006	-0.999	0.0098	-0.739	0.1440
3.10	-0.157	0.0006	-1.400	0.0118	-0.313	0.1570
3.20	-0.241	0.0006	-0.919	0.0143	0.041	0.1710
3.30	-0.300	0.0006	-0.742	0.0173	0.013	0.1850
3.40	-0.266	0.0006	-0.044	0.0230	-0.175	0.1990
3.50	-0.285	0.0006	-0.255	0.0301	-0.284	0.2130
3.60	-0.263	0.0006	-0.425	0.0373	-0.405	0.2290
3.70	-0.255	0.0006	-0.494	0.0449	-0.439	0.2440
3.80	-0.250	0.0006	-0.507	0.0524	-0.428	0.2590
3.90	-0.245	0.0006	-0.496	0.0599	-0.470	0.2740
4.00	-0.246	0.0006	-0.515	0.0675	-0.457	0.2890
4.10	-0.242	0.0006	-0.521	0.0751	-0.394	0.3040
4.20	-0.242	0.0006	-0.505	0.0827	-0.230	0.3190
4.30	-0.239	0.0006	-0.479	0.0902	-0.092	0.3350

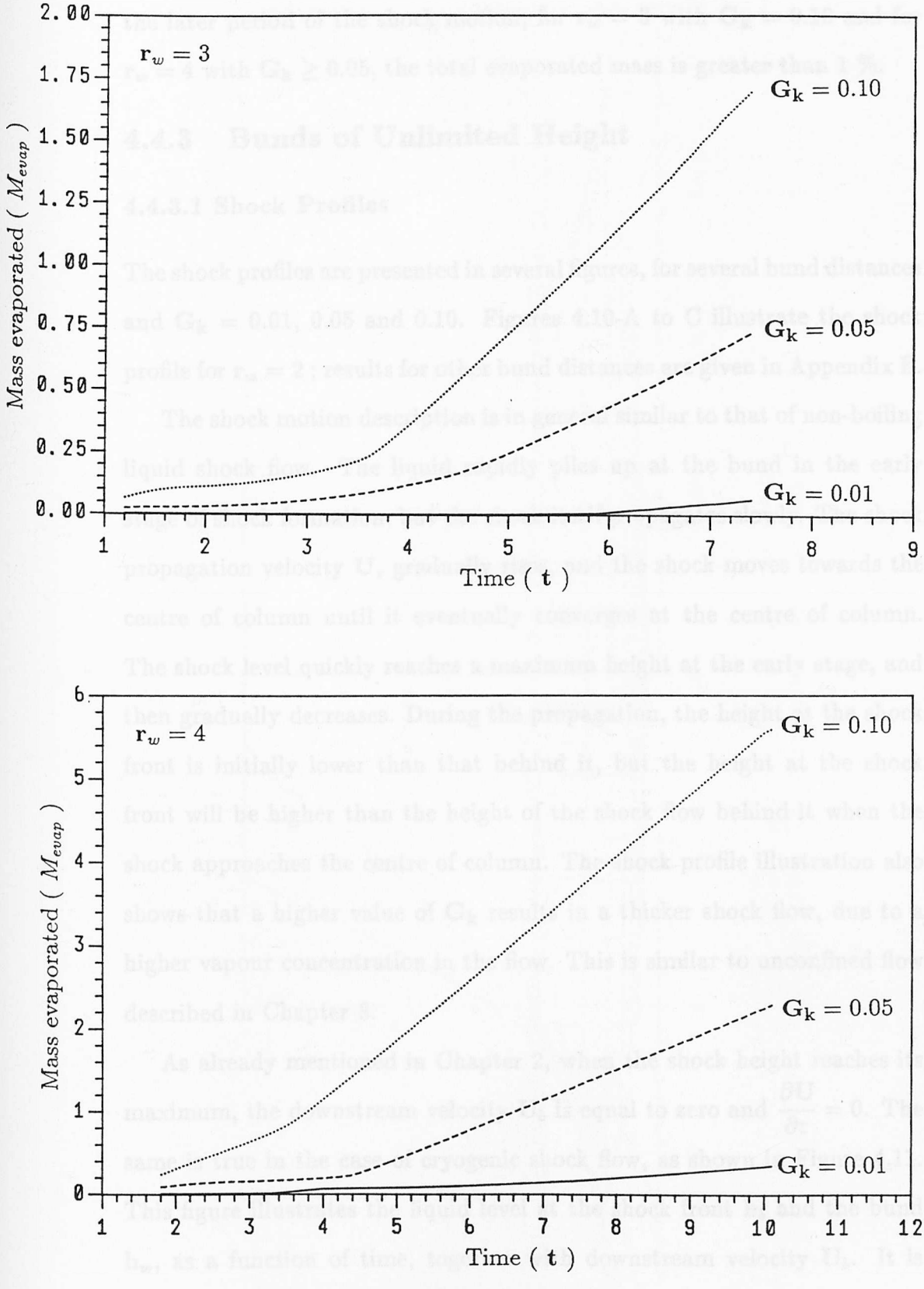


Figure 4.9: Mass evaporated for $r_w = 3$ and 4

the later period of the shock motion, for $\mathbf{r_w} = 3$ with $\mathbf{G_k} = 0.10$ and for $\mathbf{r_w} = 4$ with $\mathbf{G_k} \geq 0.05$, the total evaporated mass is greater than 1 %.

4.4.3 Bunds of Unlimited Height

4.4.3.1 Shock Profiles

The shock profiles are presented in several figures, for several bund distances and $\mathbf{G_k} = 0.01$, 0.05 and 0.10. Figures 4.10-A to C illustrate the shock profile for $\mathbf{r_w} = 2$; results for other bund distances are given in Appendix E.

The shock motion description is in general similar to that of non-boiling liquid shock flow. The liquid rapidly piles up at the bund in the early stage of shock formation, but the shock itself propagates slowly. The shock propagation velocity $\mathbf{U_s}$ gradually rises, and the shock moves towards the centre of column until it eventually converges at the centre of column. The shock level quickly reaches a maximum height at the early stage, and then gradually decreases. During the propagation, the height at the shock front is initially lower than that behind it, but the height at the shock front will be higher than the height of the shock flow behind it when the shock approaches the centre of column. The shock profile illustration also shows that a higher value of $\mathbf{G_k}$ results in a thicker shock flow, due to a higher vapour concentration in the flow. This is similar to unconfined flow described in Chapter 3.

As already mentioned in Chapter 2, when the shock height reaches its maximum, the downstream velocity $\mathbf{U_b}$ is equal to zero and $\frac{\partial \mathbf{U}}{\partial \mathbf{r}} = 0$. The same is true in the case of cryogenic shock flow, as shown in Figure 4.11. This figure illustrates the liquid level at the shock front $\mathbf{h_b}$ and the bund $\mathbf{h_w}$, as a function of time, together with downstream velocity $\mathbf{U_b}$. It is shown that at $\mathbf{U_b} = 0$, both $\mathbf{h_b}$ and $\mathbf{h_w}$ are still at their maximum values.

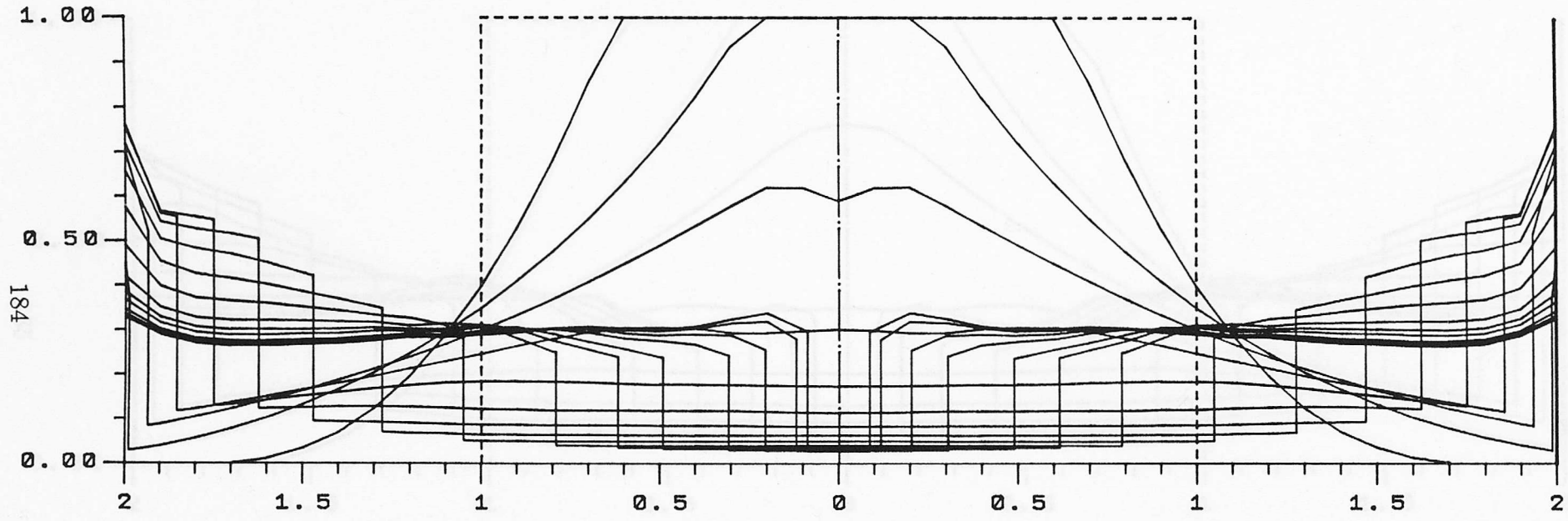


Figure 4.10-A: The shock profiles for $\mathbf{r}_w = 2$ and $\mathbf{G_k} = 0.01$

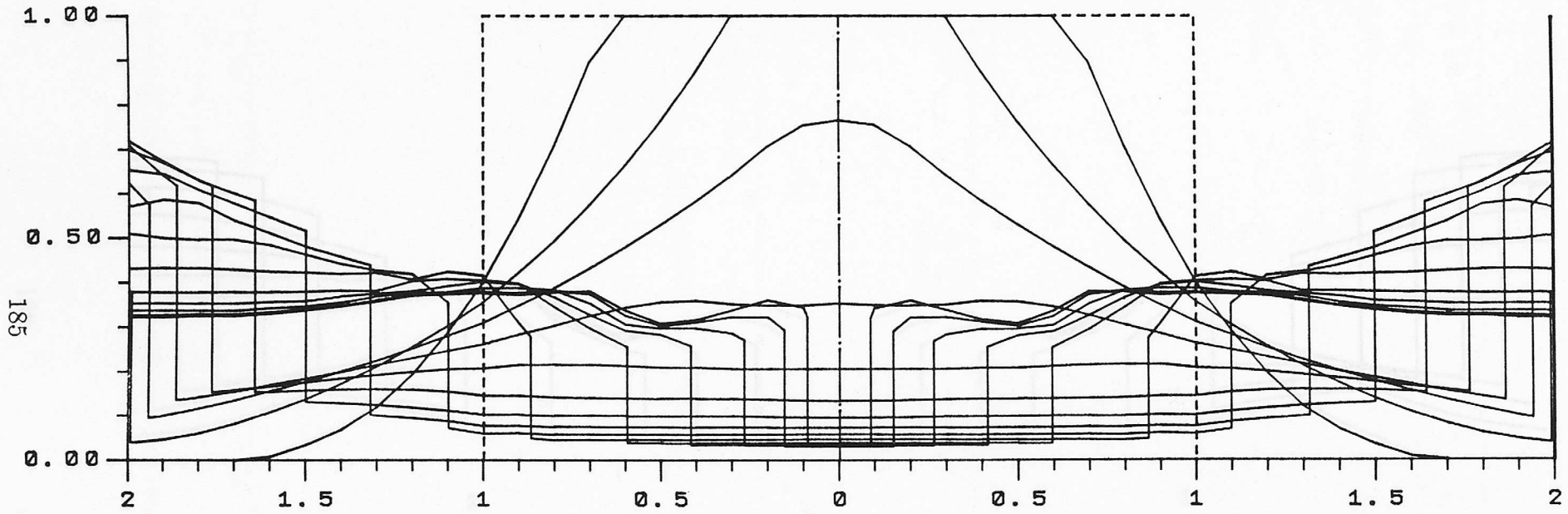


Figure 4.10-B: The shock profiles for $\mathbf{r}_w = 2$ and $\mathbf{G_k} = 0.05$

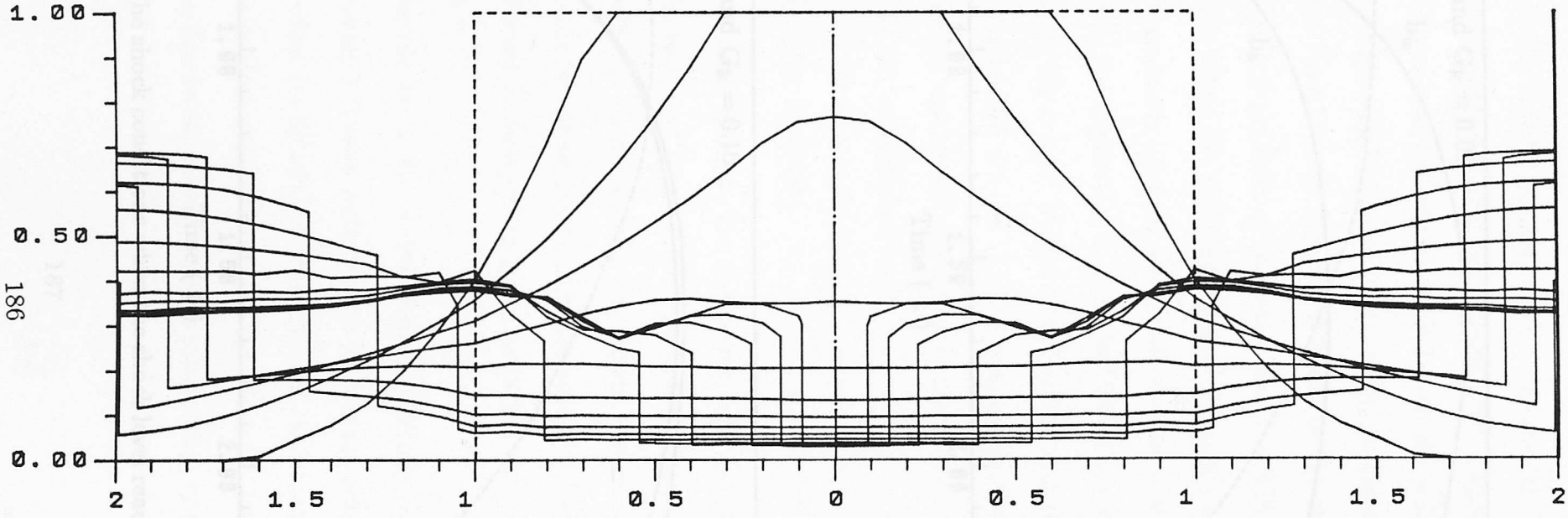


Figure 4.10-C: The shock profiles for $\mathbf{r}_w = 2$ and $\mathbf{G_k} = 0.10$

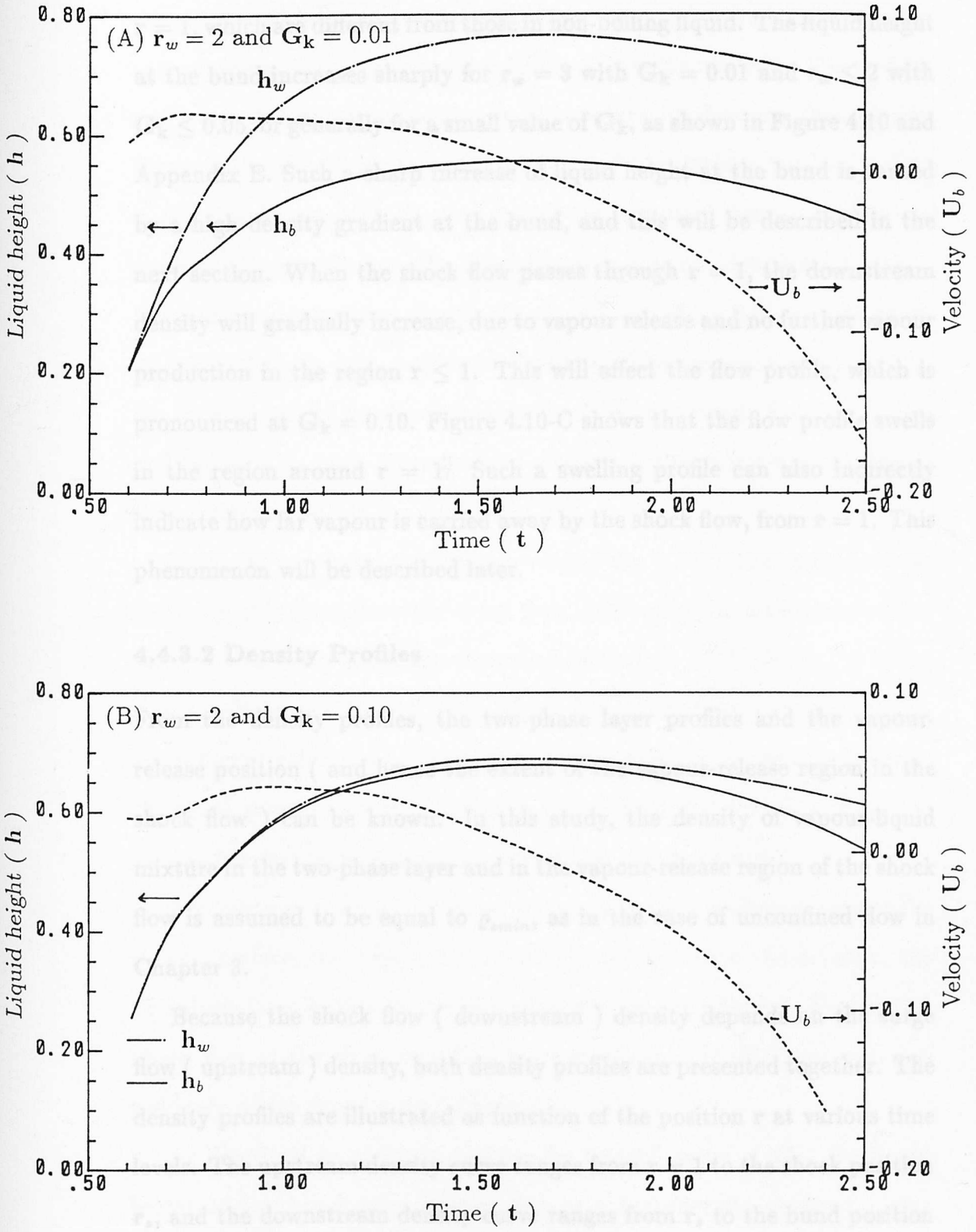


Figure 4.11: The shock conditions when the shock level reaches a maximum

Of particular significance are the shock profiles at the bund and around $\mathbf{r} = 1$, which are different from those in non-boiling liquid. The liquid height at the bund increases sharply for $\mathbf{r}_w = 3$ with $\mathbf{G_k} = 0.01$ and $\mathbf{r}_w \leq 2$ with $\mathbf{G_k} \leq 0.05$, or generally for a small value of $\mathbf{G_k}$, as shown in Figure 4.10 and Appendix E. Such a sharp increase of liquid height at the bund is caused by a high density gradient at the bund, and this will be described in the next section. When the shock flow passes through $\mathbf{r} = 1$, the downstream density will gradually increase, due to vapour release and no further vapour production in the region $\mathbf{r} \leq 1$. This will affect the flow profile, which is pronounced at $\mathbf{G_k} = 0.10$. Figure 4.10-C shows that the flow profile swells in the region around $\mathbf{r} = 1$. Such a swelling profile can also indirectly indicate how far vapour is carried away by the shock flow, from $\mathbf{r} = 1$. This phenomenon will be described later.

4.4.3.2 Density Profiles

From the density profiles, the two-phase layer profiles and the vapour-release position (and hence the extent of the vapour-release region in the shock flow) can be known. In this study, the density of vapour-liquid mixture in the two-phase layer and in the vapour-release region of the shock flow is assumed to be equal to ϱ_{smin}, as in the case of unconfined flow in Chapter 3.

Because the shock flow (downstream) density depends on the surge flow (upstream) density, both density profiles are presented together. The density profiles are illustrated as function of the position $\mathbf{r}$ at various time levels. The upstream density curve ranges from $\mathbf{r} = 1$ to the shock position $\mathbf{r}_s$, and the downstream density curve ranges from $\mathbf{r}_s$ to the bund position $\mathbf{r}_w$.

Due to very short range of of position $\mathbf{r}$ for $\mathbf{r}_w \leq 1.5$, the density profiles are not illustrated, because the figure is crowded with curves and hence becomes messy. The density profiles for $\mathbf{r}_w = 2$ are illustrated in Figure 4.12, and some of their corresponding two-phase layer profiles are illustrated in Figure 4.13. The illustration of upstream and dwonstream densitiy profiles is given in Figure 4.14. In this figure, the upstream density profiles are presented separately from the downstream one, to avoid crowded figure. Because the downstream density for $\mathbf{r}_w = 3$ and $\mathbf{G_k} \geq 0.05$, as well as for $\mathbf{r}_w = 4$ and $\mathbf{G_k} \geq 0.01$, quickly reaches the minimum shock density ϱ_{smin}, the density profiles for these conditions are not presented. Even for $\mathbf{r}_w = 4$ and $\mathbf{G_k} = 0.10$, both upstream and downstream densities are uniform at their minimum values.

It can be concluded that for $\mathbf{r}_w = 3$ and $\mathbf{G_k} \geq 0.05$, the vapour-release region quickly dominates the shock flow, and hence the total mass evaporated is also high, as already described in Section 4.2.2. For $\mathbf{r}_w \leq 2$, the vapour-release position $\mathbf{r}_{vs}$ in the shock flow depends on the value of $\mathbf{G_k}$. For a higher value of $\mathbf{G_k}$, the vapour-release position $\mathbf{r}_{vs}$ will be closer to the shock position $\mathbf{r}_s$. It is shown in Figure 4.12 that for $\mathbf{G_k} = 0.10$, the vapour-release region also quickly dominates the shock flow.

According to the Shallow Water theory, when a flow element crosses the shock interface, its shape will change into tall but slim. As a result, the two-phase layer profile at the shock interface is also affected. Figure 4.13 shows that at the shock interface, the two-phase layer thickness increases suddenly, which forms a step shape.

As described in previous section, for a small value of $\mathbf{G_k}$, the liquid height at the bund rises sharply, due to a high density gradient. This phenomenon is clearly shown in Figures 4.12 and 4.13 at $\mathbf{G_k} = 0.01$, in

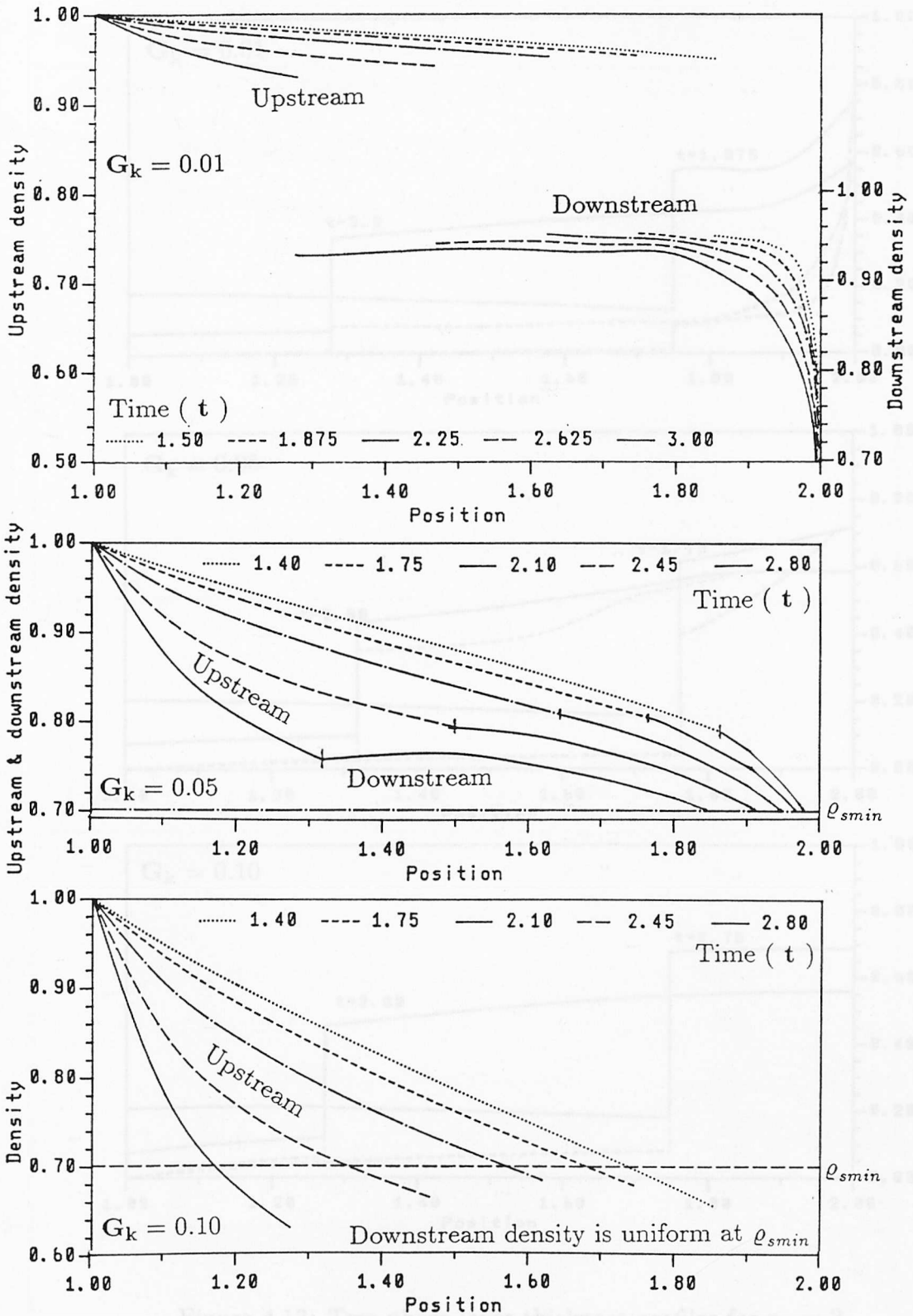


Figure 4.12: Density profiles for $r_w = 2$

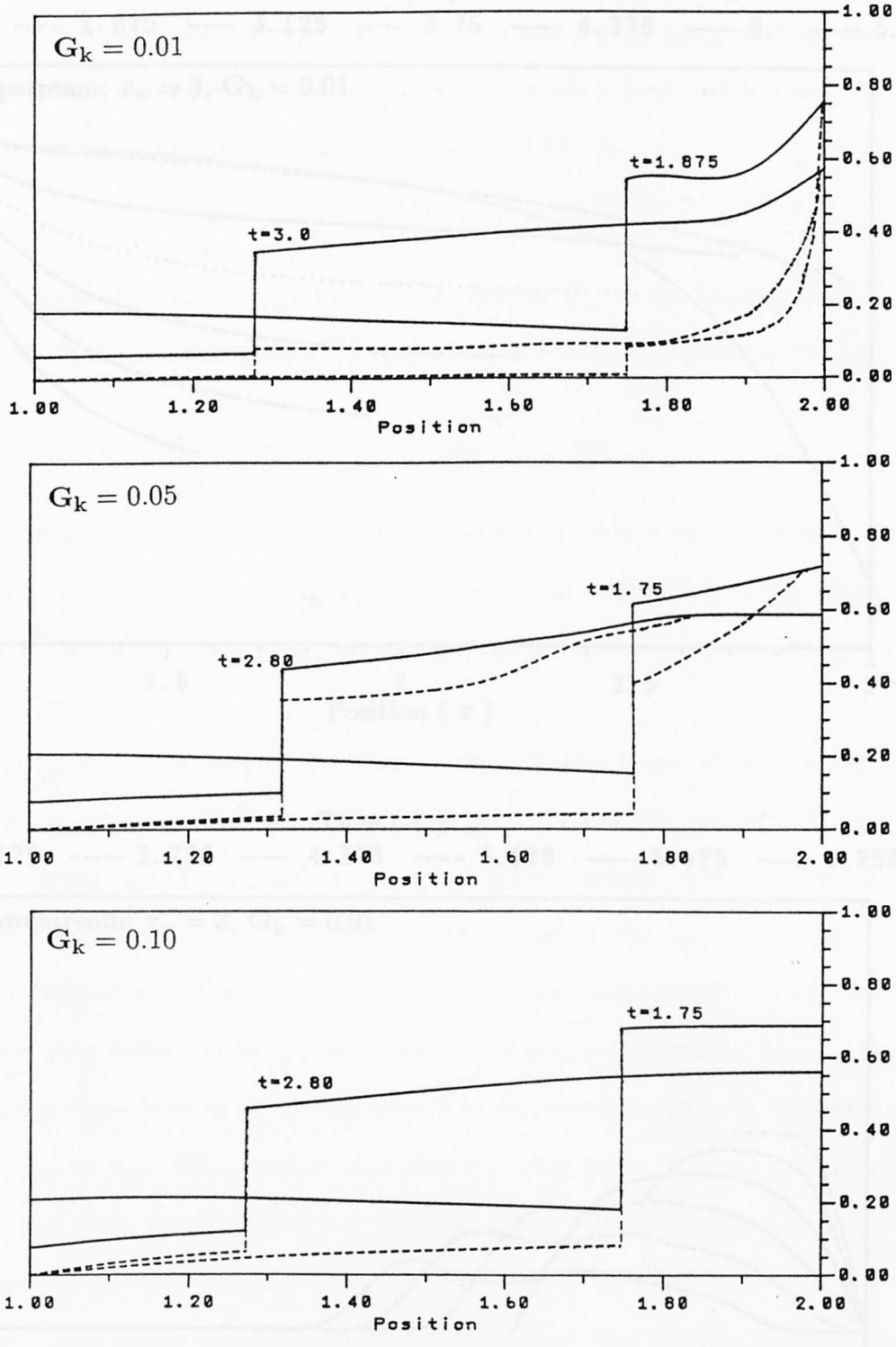


Figure 4.13: Two-phase layer thickness profiles for $\mathbf{r}_w = 2$

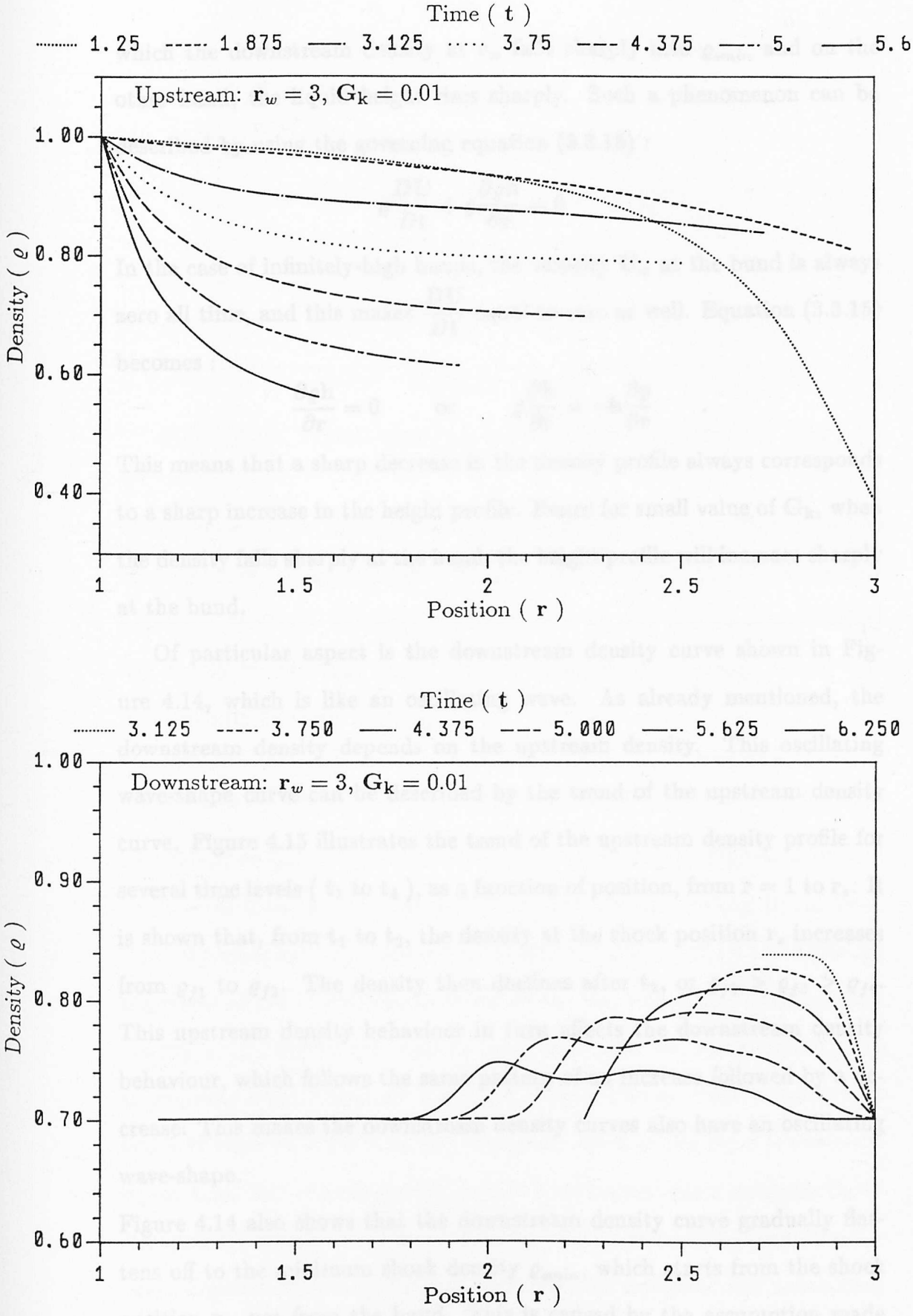


Figure 4.14: Upstream and downstream density profiles for $r_w = 3$ and $G_k = 0.01$

which the downstream density at $\mathbf{r}_w$ falls sharply into ϱ_{smin} and on the other hand, the liquid height rises sharply. Such a phenomenon can be described by using the governing equation (3.3.15) :

$$\varrho \frac{D\mathbf{U}}{D\mathbf{t}} + g \frac{\partial \varrho \mathbf{h}}{\partial \mathbf{r}} = 0 \quad .$$

In the case of infinitely-high bunds, the velocity $\mathbf{U}_w$ at the bund is always zero all time, and this makes $\frac{D\mathbf{U}}{D\mathbf{t}}$ equal to zero as well. Equation (3.3.15) becomes :

$$\frac{\partial \varrho \mathbf{h}}{\partial \mathbf{r}} = 0 \qquad \text{or} \qquad \varrho \frac{\partial \mathbf{h}}{\partial \mathbf{r}} = -\mathbf{h} \frac{\partial \varrho}{\partial \mathbf{r}} \quad .$$

This means that a sharp decrease in the density profile always corresponds to a sharp increase in the height profile. Hence for small value of $\mathbf{G_k}$, when the density falls sharply at the bund, the height profile will increase sharply at the bund.

Of particular aspect is the downstream density curve shown in Figure 4.14, which is like an oscillating wave. As already mentioned, the downstream density depends on the upstream density. This oscillating wave-shape curve can be described by the trend of the upstream density curve. Figure 4.15 illustrates the trend of the upstream density profile for several time levels ($\mathbf{t}_1$ to $\mathbf{t}_4$), as a function of position, from $\mathbf{r} = 1$ to $\mathbf{r}_s$. It is shown that, from $\mathbf{t}_1$ to $\mathbf{t}_2$, the density at the shock position $\mathbf{r}_s$ increases from ϱ_{f1} to ϱ_{f2}. The density then declines after $\mathbf{t}_2$, or $\varrho_{f2} > \varrho_{f3} > \varrho_{f4}$. This upstream density behaviour in turn affects the downstream density behaviour, which follows the same pattern of an increase followed by a decrease. This makes the downstream density curves also have an oscillating wave-shape.

Figure 4.14 also shows that the downstream density curve gradually flattens off to the minimum shock density ϱ_{smin}, which starts from the shock position $\mathbf{r}_s$, not from the bund. This is caused by the assumption made

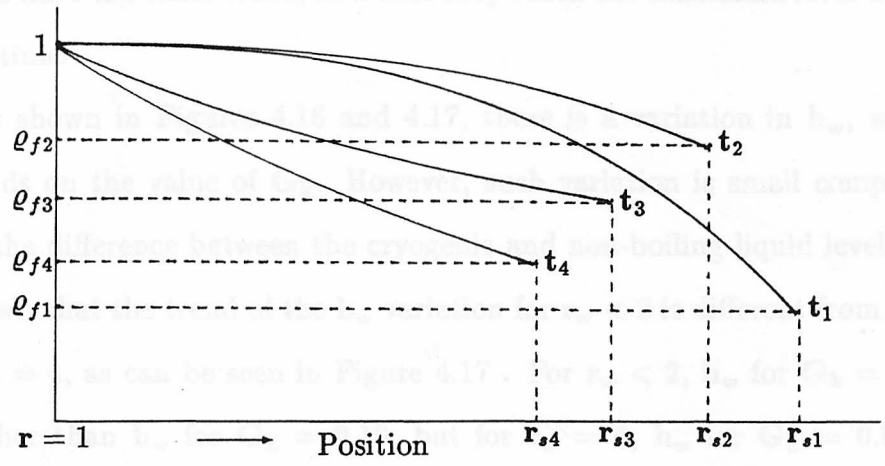


Figure 4.15: Typical upstream density profile ($t_1 < t_2 < t_3 < t_4$)

in Section 4.2.2, in which $\varrho_b = \varrho_{smin}$ whenever $\varrho_f < \varrho_{smin}$. Because in the later stages of the shock motion, the upstream density at the shock interface gradually decreases, as illustrated in Figure 4.15, and this upstream density will finally be less than ϱ_{smin}, the corresponding downstream density will consequently be equal to ϱ_{smin}.

4.4.3.3 Liquid Level, Hydrostatic and Impact Pressures at a Bund

The liquid height or level at the bund is presented in Figures 4.16 as a function of time, and is also compared with the non-boiling liquid level. The maximum level for a specific r_w is illustrated in Figure 4.17. Although the result of the calculation depends on the value of minimum shock flow density ϱ_{smin}, Figure 4.17 can be used as a basis for recommending the appropriate bund height for a cryogenic liquid storage tank. Figures 4.16 and 4.17 show that the level of a cryogenic liquid at the bund is obviously higher than that of a non-boiling liquid. This means that a cryogenic liquid storage tank requires a higher vertical bund than non-boiling liquid storage tank. Figure 4.16 also shows that the curves for cryogenic and non-boiling

liquids have the same trend, and that they reach the maximum level at the same time.

As shown in Figures 4.16 and 4.17, there is a variation in $\mathbf{h}_w$, which depends on the value of $\mathbf{G_k}$. However, such variation is small compared with the difference between the cryogenic and non-boiling liquid levels. It is shown that the trend of the $\mathbf{h}_w$ variation for $\mathbf{r}_w < 2$ is different from that for $\mathbf{r}_w = 4$, as can be seen in Figure 4.17 . For $\mathbf{r}_w < 2$, $\mathbf{h}_w$ for $\mathbf{G_k} = 0.01$ is higher than $\mathbf{h}_w$ for $\mathbf{G_k} = 0.10$, but for $\mathbf{r}_w = 4$, $\mathbf{h}_w$ for $\mathbf{G_k} = 0.01$ is less than that for $\mathbf{G_k} = 0.10$. This may be caused by the accuracy of the interpolation in the numerical calculation. The liquid level at the bund has essentially the same trend as for unconfined flow, i.e. a higher value of $\mathbf{G_k}$ results in a higher liquid level. As described in the Density Profiles section, the downstream density profiles for $\mathbf{r}_w = 4$ are uniform at ϱ_{smin}, regardless of the value of $\mathbf{G_k}$. Hence, the density gradient $\frac{\partial \varrho}{\partial \mathbf{r}}$ at the bund is zero, which makes the shock level relatively uniform. As a result, interpolation of ϱ and C in the bund and its surroundings can be carried out accurately. On the other hand, for $\mathbf{r}_w \leq 2$ and $\mathbf{G_k} \leq 0.05$, the density gradient is high and the liquid level profile at the bund rises sharply, as illustrated in Figure 4.18. Because of this drastic change in density and height close to the bund, their numerical interpolation is likely to be less accurate, which can lead to a spurious higher value of $\mathbf{h}_w$ at the next time step. A smaller $\mathbf{G_k}$ gives a greater density gradient, and this may result in a still higher value of $\mathbf{h}_w$. Apart from this, the variation in $\mathbf{G_k}$ only has little effect on the liquid level at bund.

Figures 4.16 are also used to estimate the hydrostatic pressure at the bund, as a function of time. Figures 4.19-A to D show a dimensionless hydrostatic pressure at the base of the bund. In this case, the dimensionless

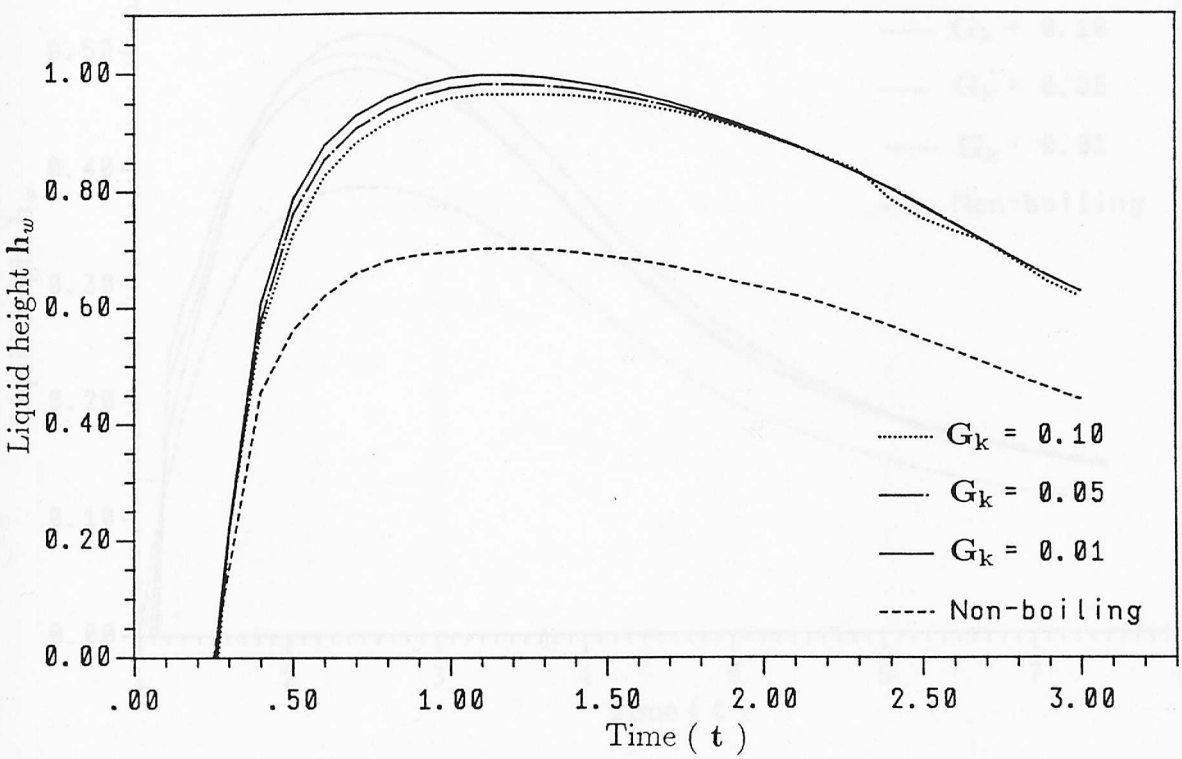


Figure 4.16-A: Liquid height at bund for $r_w = 1.5$

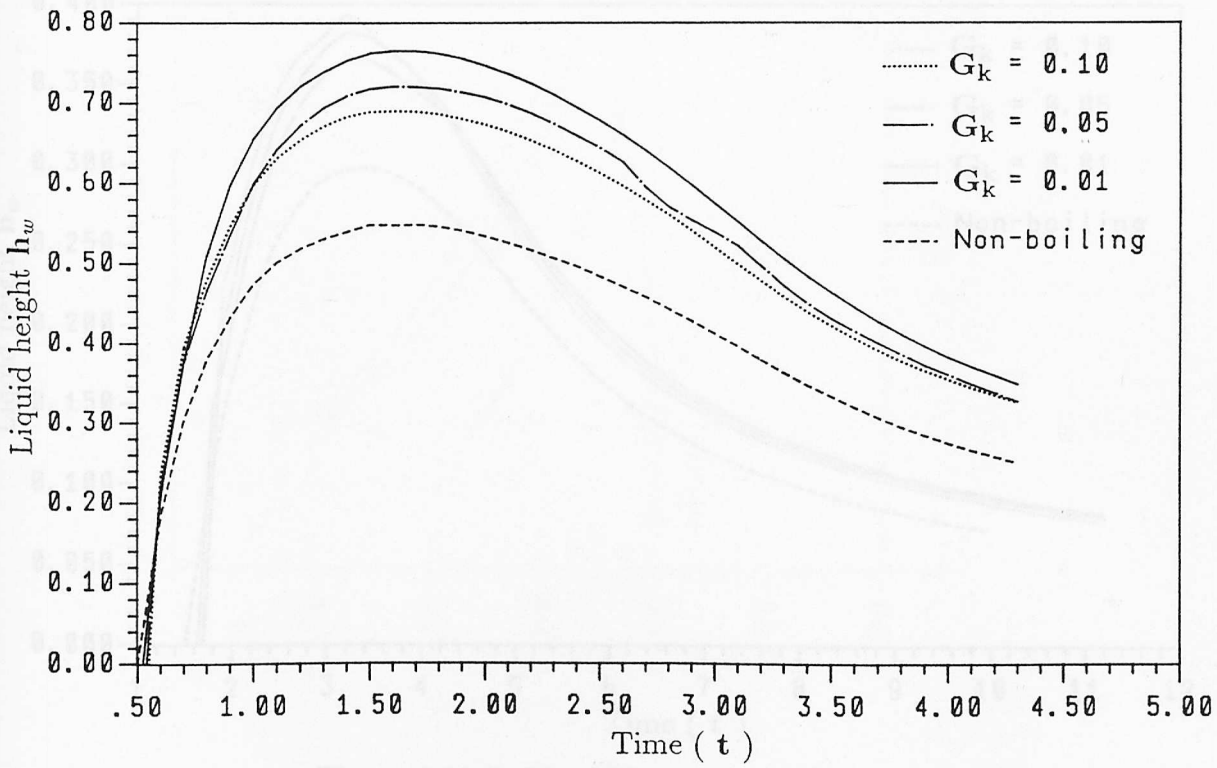


Figure 4.16-B: Liquid height at bund for $r_w = 2$

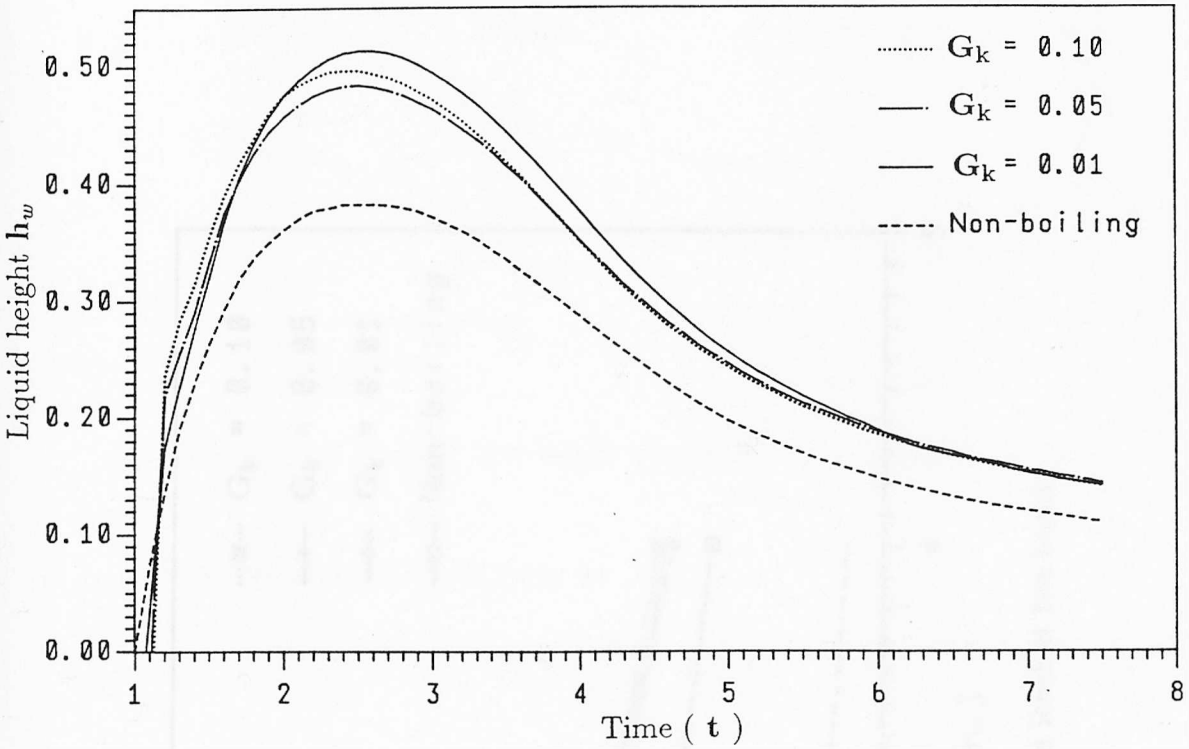


Figure 4.16-C: Liquid height at bund for $r_w = 3$

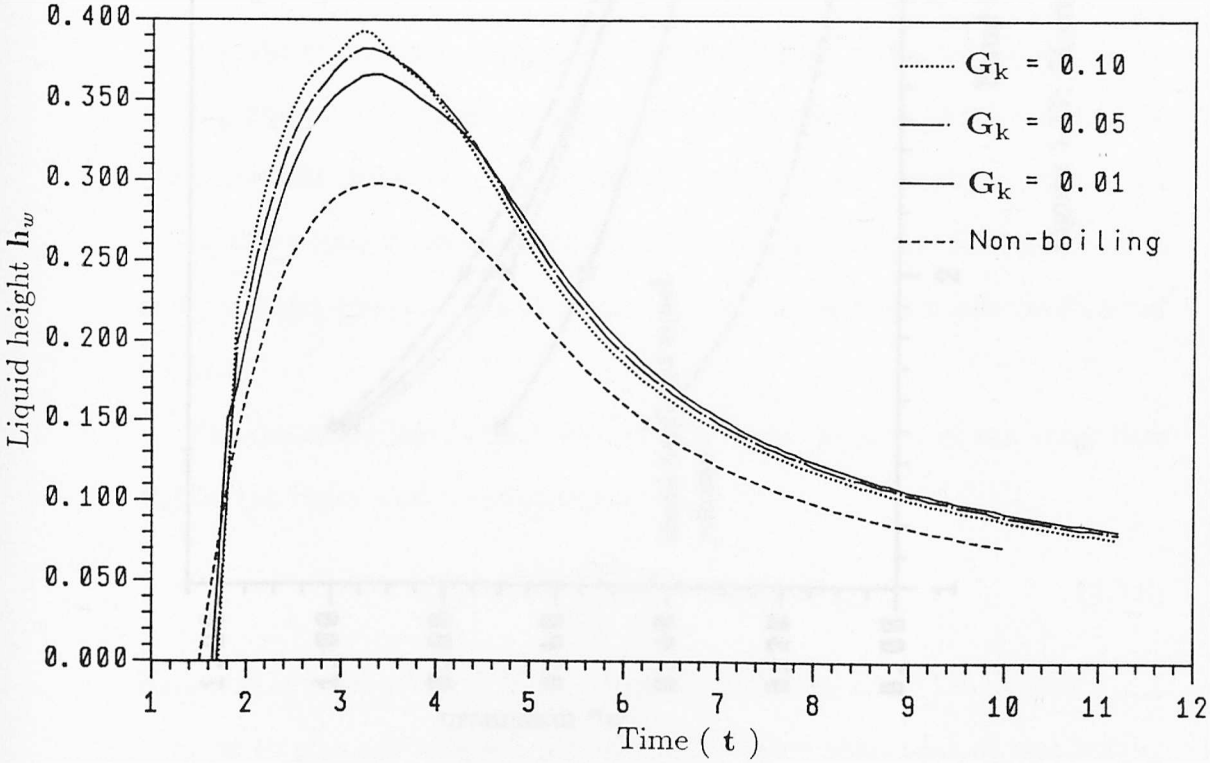


Figure 4.16-D: Liquid height at bund for $r_w = 4$

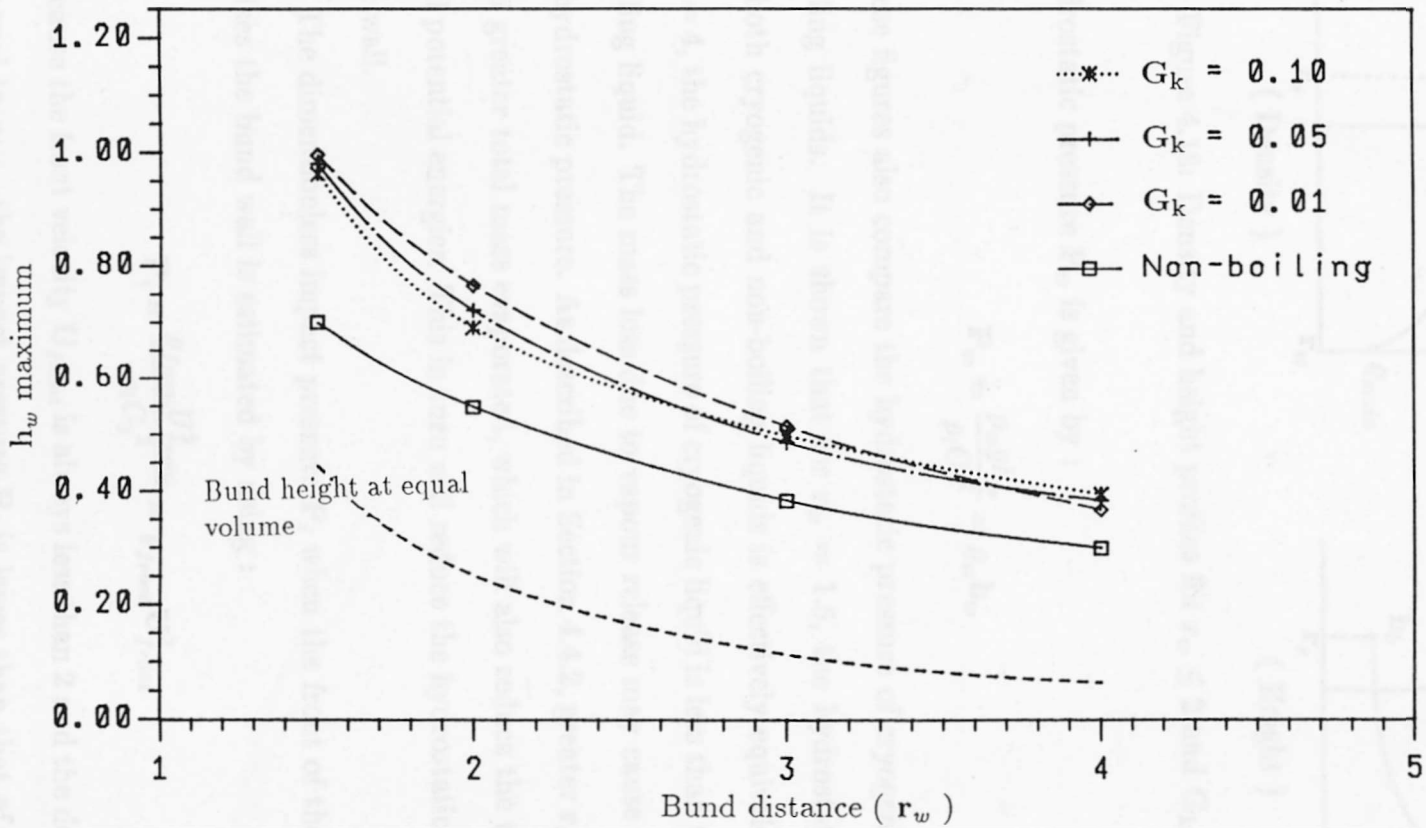


Figure 4.17: Maximum liquid level at the bund

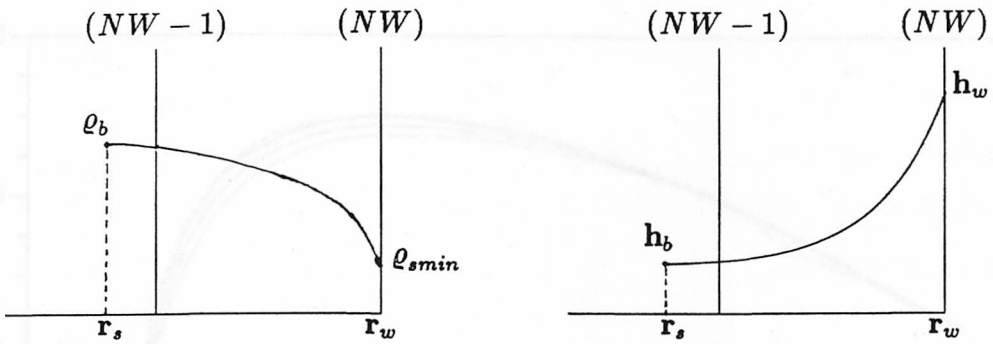


Figure 4.18: Density and height profiles for $\mathbf{r}_w \leq 2$ and $\mathbf{G_k} \leq 0.05$

hydrostatic pressure $\mathbf{P}_w$ is given by :

$$\mathbf{P}_w = \frac{\rho_w g h_w}{\rho_l C_0{}^2} = \varrho_w \mathbf{h}_w \tag{4.4.5}$$

These figures also compare the hydrostatic pressure of cryogenic and non-boiling liquids. It is shown that for $\mathbf{r}_w = 1.5$, the hydrostatic pressure of both cryogenic and non-boiling liquids is effectively equivalent, but for $\mathbf{r}_w = 4$, the hydrostatic pressure of cryogenic liquid is less than that of non-boiling liquid. The mass loss due to vapour release may cause a reduction of hydrostatic pressure. As described in Section 4.4.2, greater $\mathbf{r}_w$ will result in a greater total mass evaporated, which will also reduce the total kinetic and potential energies. This in turn will reduce the hydrostatic pressure at the wall.

The dimensionless impact pressure $\mathbf{P}_i$ when the front of the surge flow strikes the bund wall is estimated by using :

$$\mathbf{P}_i = \frac{\rho_{front} U_{front}^2}{\rho_l C_0{}^2} = \varrho_{front} \mathbf{U}_{front}^2 \tag{4.4.6}$$

Because the front velocity $\mathbf{U}_{front}$ is always less than 2 and the density ϱ_{front} is equal to ϱ_{min}, the impact pressure $\mathbf{P}_i$ is lower than that of non-boiling liquid flow. Table IV-2 presents the impact pressure for several values of

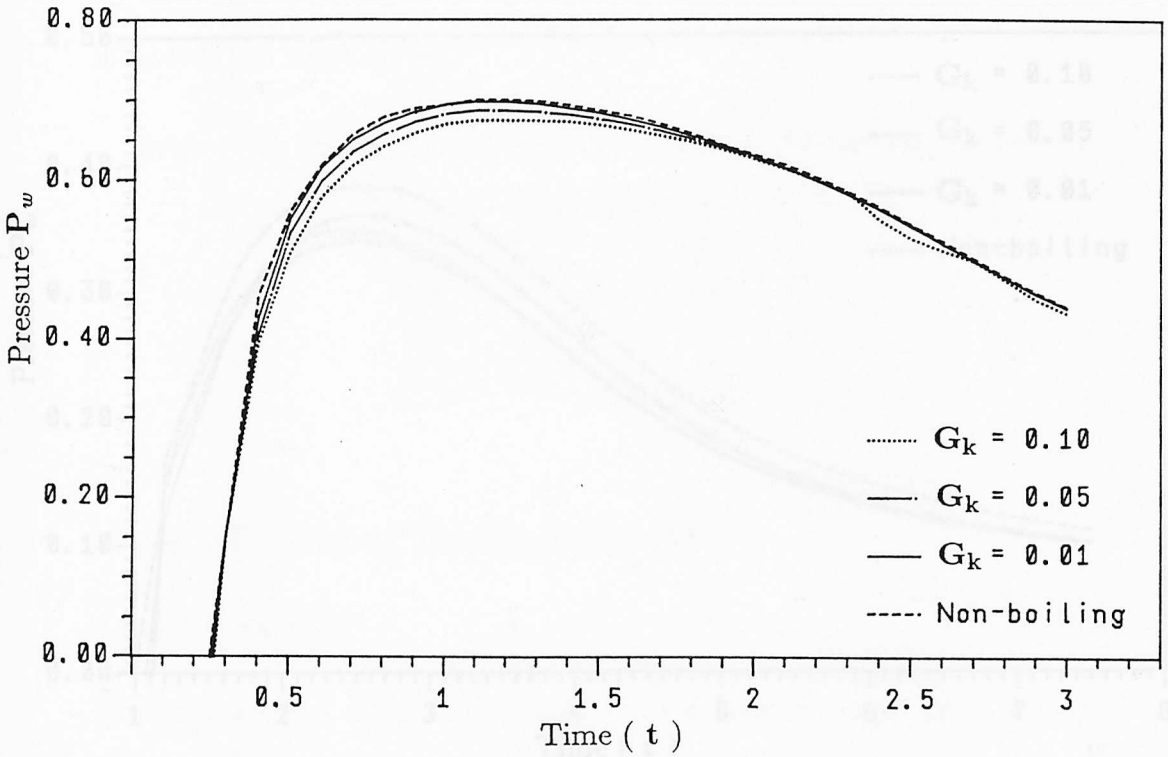


Figure 4.19-A: Dimensionless hydrostatic pressure at the base of bund for $\mathbf{r}_w = 1.5$

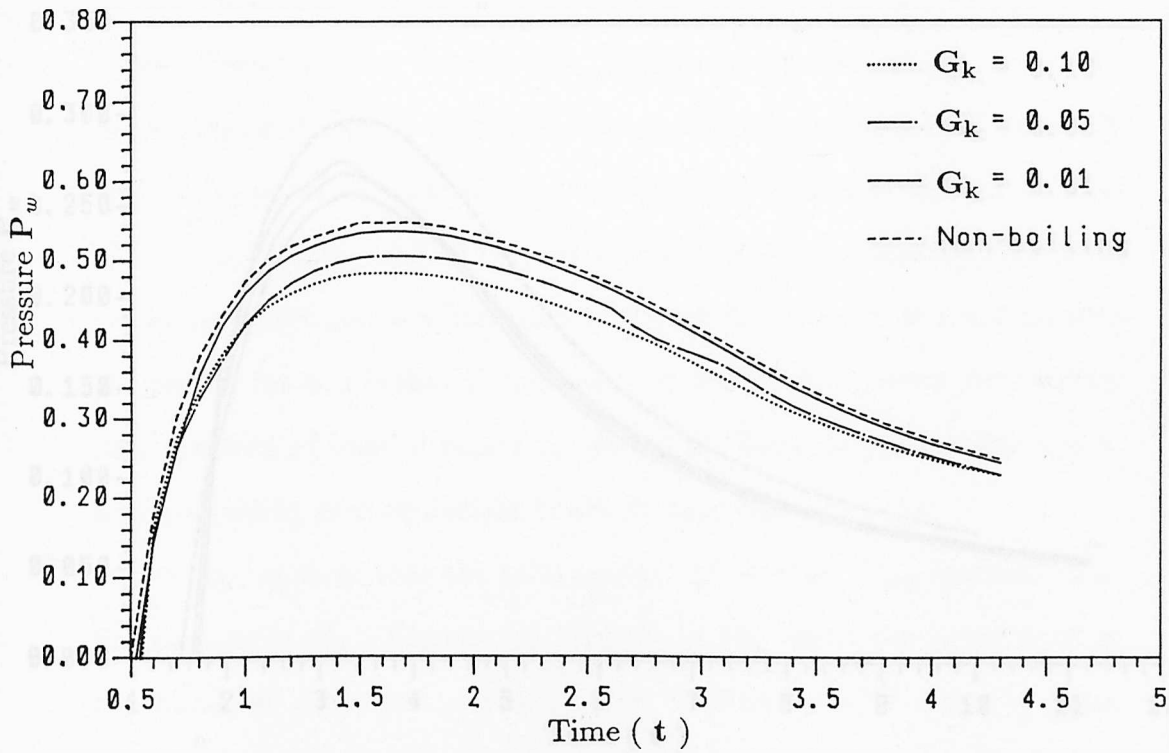


Figure 4.19-B: Dimensionless hydrostatic pressure at the base of bund for $\mathbf{r}_w = 2$

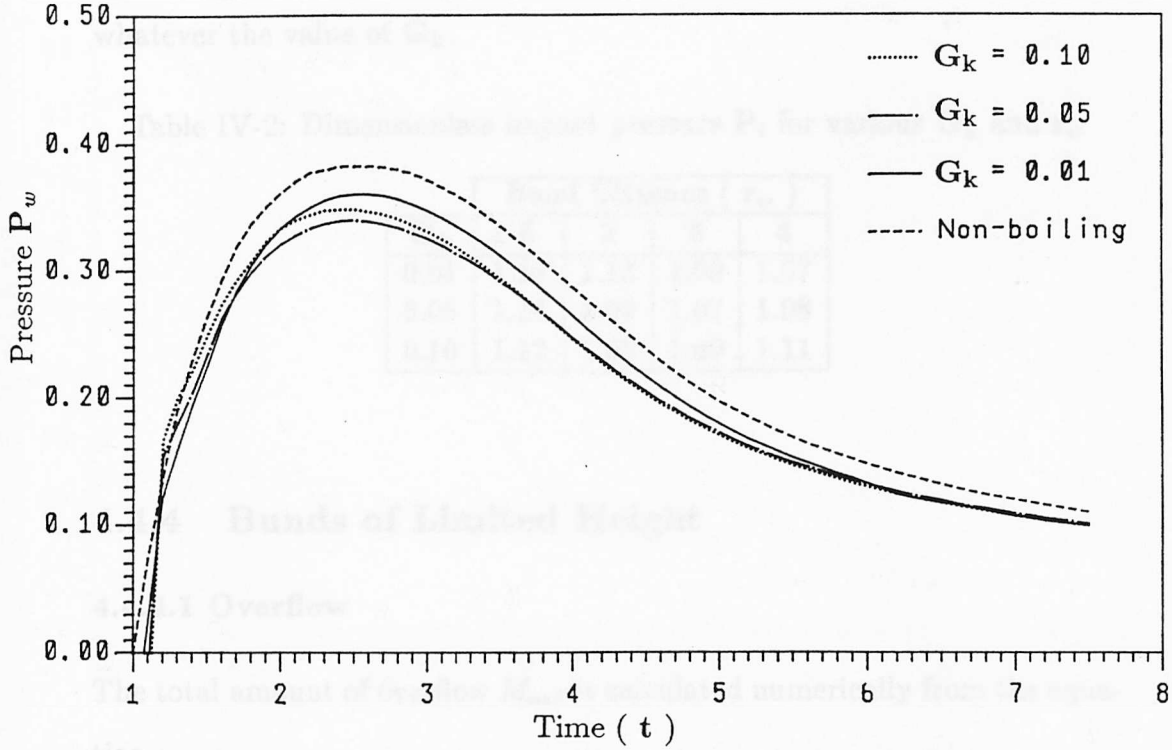


Figure 4.19-C: Dimensionless hydrostatic pressure at the base of bund for $r_w = 3$

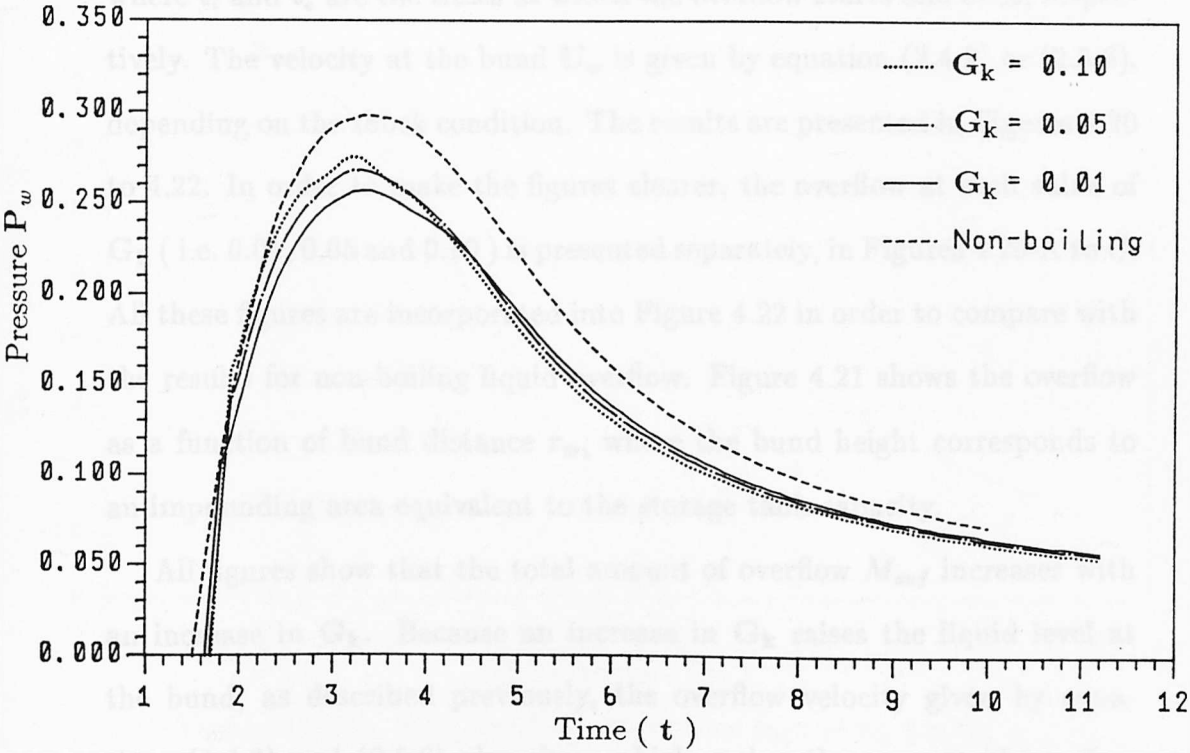


Figure 4.19-D: Dimensionless hydrostatic pressure at the base of bund for $r_w = 4$

$\mathbf{r}_w$ and $\mathbf{G_k}$. It is shown that the $\mathbf{P_i}$ of cryogenic liquids is only around 1.1, whatever the value of $\mathbf{G_k}$.

Table IV-2: Dimensionless impact pressure $\mathbf{P_i}$ for various $\mathbf{G_k}$ and $\mathbf{r}_w$

	Bund Distance ($\mathbf{r}_w$)			
$\mathbf{G_k}$	**1.5**	**2**	**3**	**4**
0.01	1.18	1.13	1.09	1.07
0.05	1.14	1.09	1.07	1.08
0.10	1.12	1.08	1.09	1.11

4.4.4 Bunds of Limited Height

4.4.4.1 Overflow

The total amount of overflow M_{ovf} is calculated numerically from the equation :

$$M_{ovf} = 2\pi \mathbf{r}_w \int_{\mathbf{t}_i}^{\mathbf{t}_e} \varrho_w \mathbf{U}_w \mathbf{h}_w \, d\mathbf{t} \tag{4.4.7}$$

where $\mathbf{t}_i$ and $\mathbf{t}_e$ are the times at which the overflow starts and ends, respectively. The velocity at the bund $\mathbf{U}_w$ is given by equation (2.4.9) or (2.5.6), depending on the shock condition. The results are presented in Figures 4.20 to 4.22. In order to make the figures clearer, the overflow at each value of $\mathbf{G_k}$ (i.e. 0.01, 0.05 and 0.10) is presented separately, in Figures 4.20-A to C. All these figures are incorporated into Figure 4.22 in order to compare with the results for non-boiling liquid overflow. Figure 4.21 shows the overflow as a function of bund distance $\mathbf{r}_w$, where the bund height corresponds to an impounding area equivalent to the storage tank capacity.

All figures show that the total amount of overflow M_{ovf} increases with an increase in $\mathbf{G_k}$. Because an increase in $\mathbf{G_k}$ raises the liquid level at the bund, as described previously, the overflow velocity given by equations (2.4.9) and (2.5.6) also rises, which makes the amount of overflow

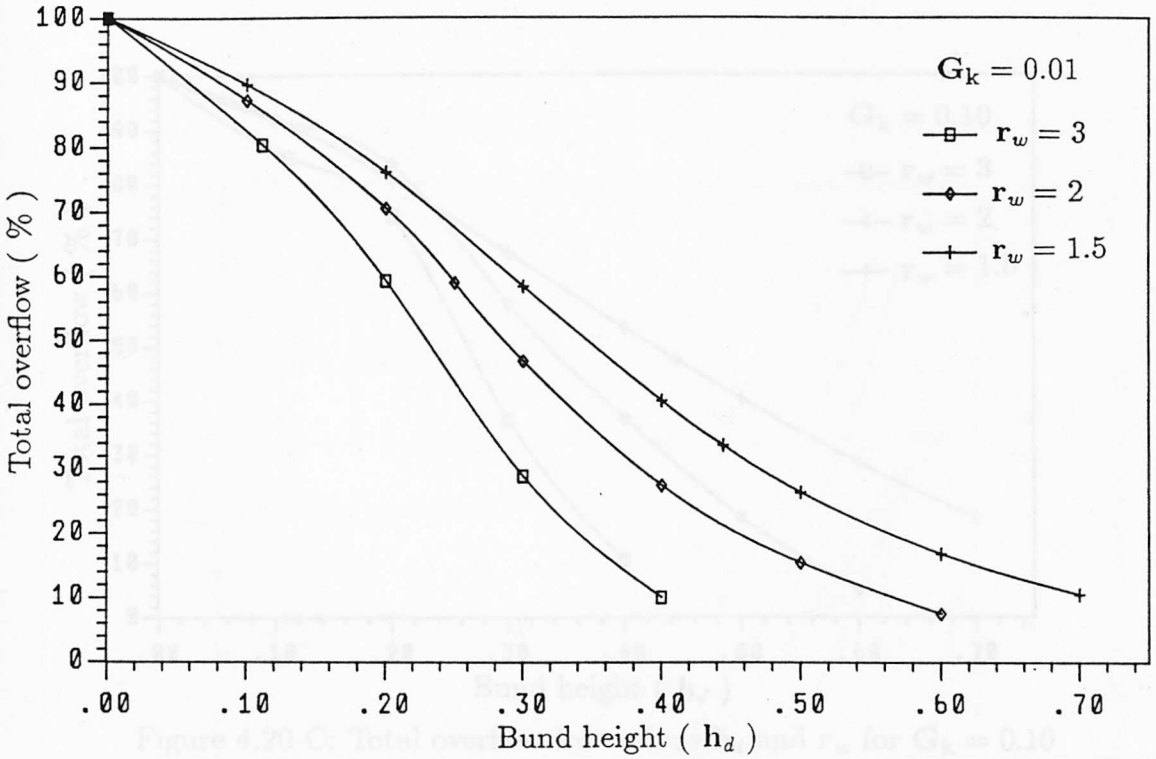


Figure 4.20-A: Total overflow for various $\mathbf{h}_d$ and $\mathbf{r}_w$ for $\mathbf{G}_k = 0.01$

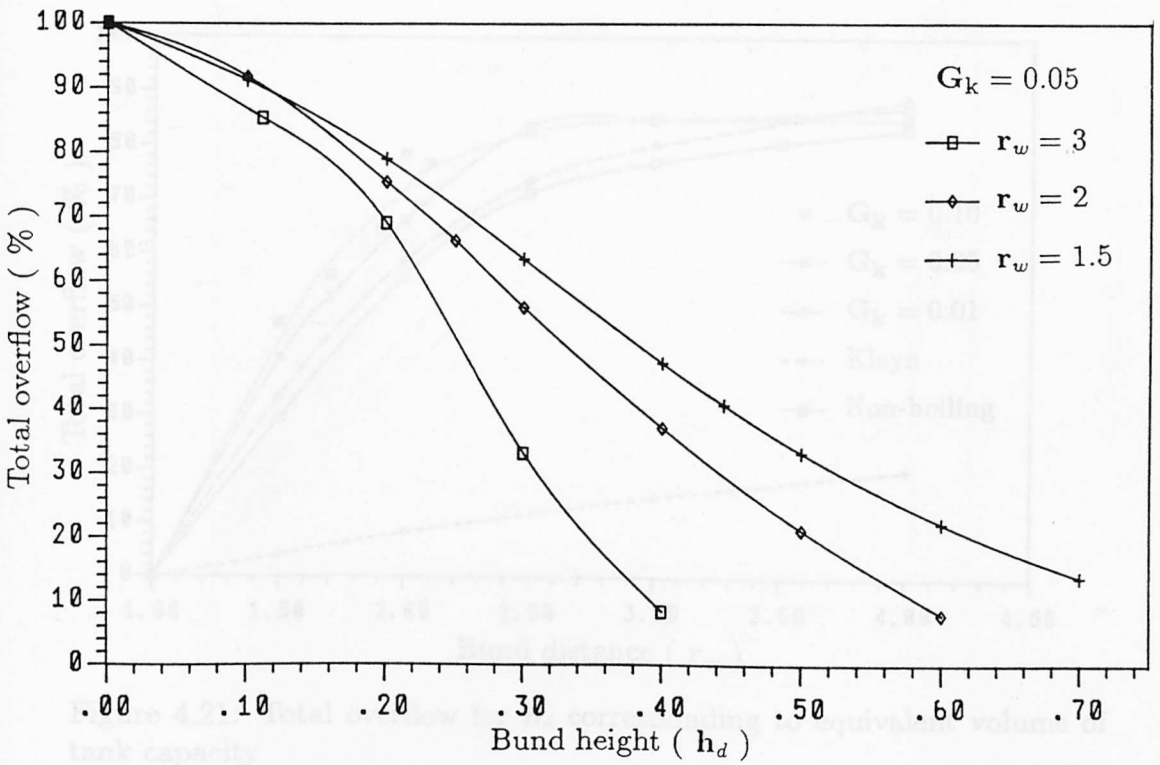


Figure 4.20-B: Total overflow for various $\mathbf{h}_d$ and $\mathbf{r}_w$ for $\mathbf{G}_k = 0.05$

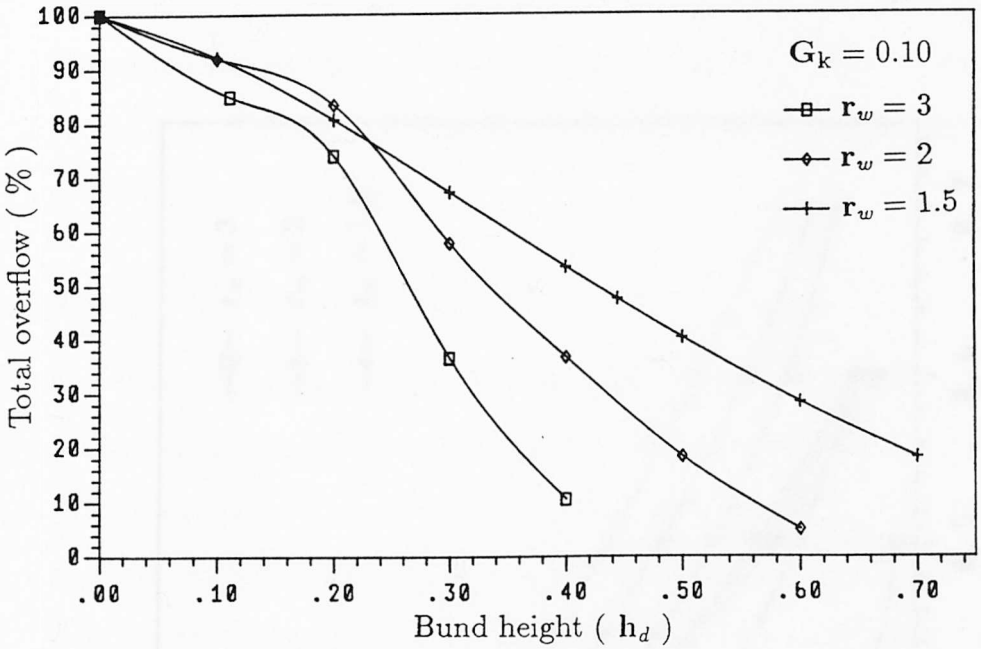


Figure 4.20-C: Total overflow for various h_d and r_w for $G_k = 0.10$

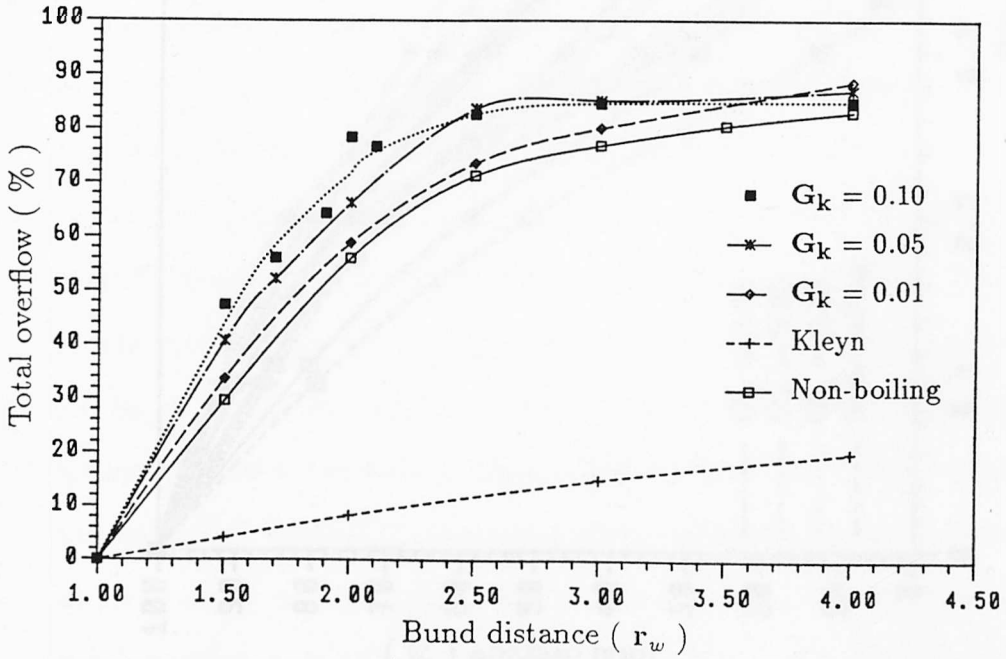


Figure 4.21: Total overflow for h_d corresponding to equivalent volume of tank capacity

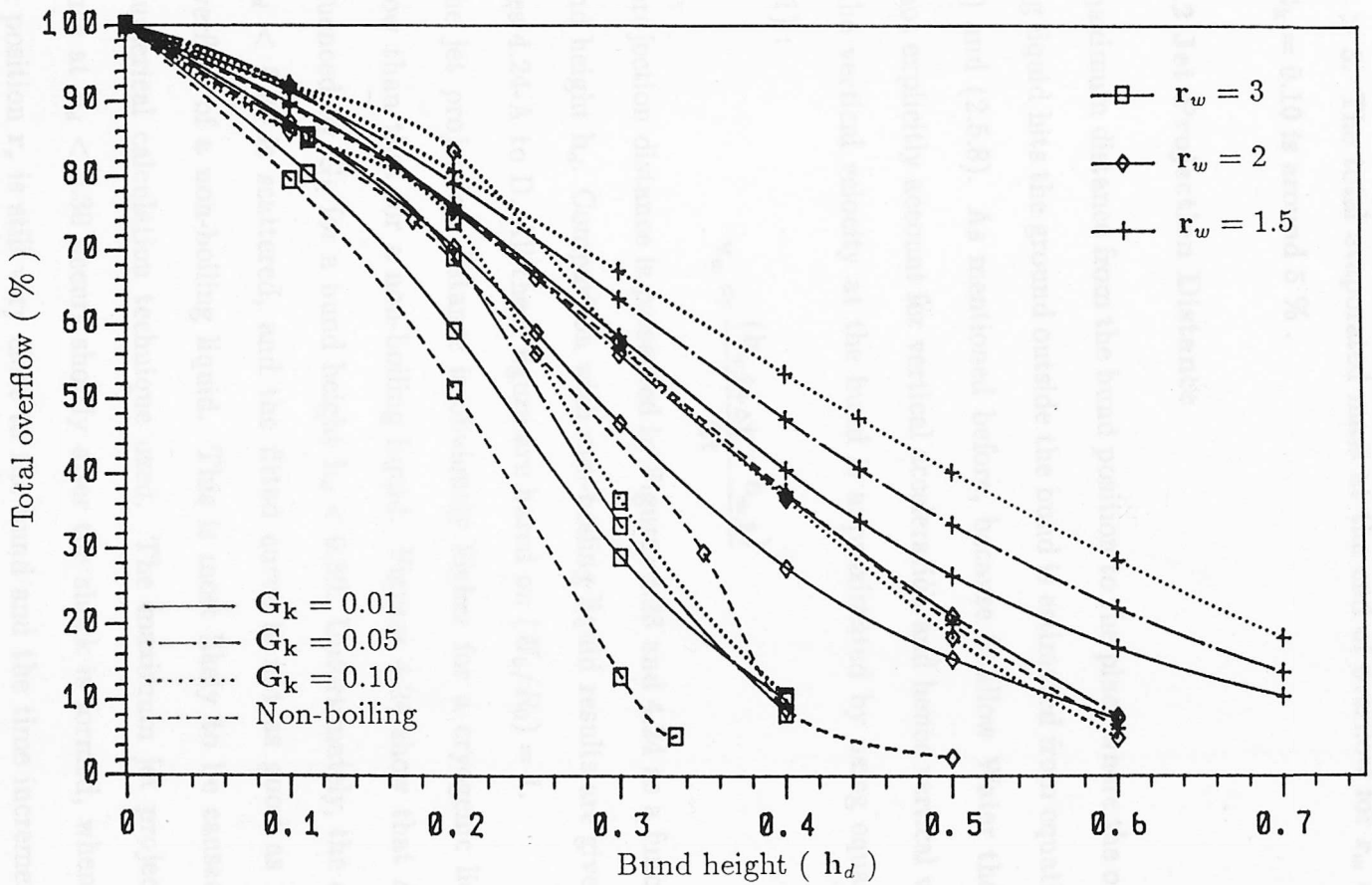


Figure 4.22: Total overflow comparison for various values of G_k

increase as well. Figure 4.21 shows that the increase of M_{ovf} is relatively small for $\mathbf{r_w} = 4$. This may be caused by the mass loss due to evaporation. It was already shown in Section 4.5.1 that significant evaporation occurs for $\mathbf{r_w} > 3$. The total evaporated mass at the end of overflow for $\mathbf{r_w} = 4$ and $\mathbf{G_k} = 0.10$ is around 5 % .

4.4.4.2 Jet Projection Distance

The maximum distance from the bund position to the place where the overflowing liquid hits the ground outside the bund is estimated from equations (2.5.7) and (2.5.8). As mentioned before, because Shallow Water theory does not explicitly account for vertical acceleration and hence vertical velocity, the vertical velocity at the bund is approximated by using equation (2.2.11) :

$$\mathbf{v_w} \approx \frac{(\mathbf{h_{w,t+\Delta t}} - \mathbf{h_{w,t}})}{\mathbf{\Delta t}} \quad .$$

The projection distance is presented in Figures 4.23 and 4.24 as a function of bund height $\mathbf{h_d}$. Comparison with non-boiling liquid results are given in Figures 4.24-A to D. All these figure are based on $(H_0/R_0) = 1$.

The jet projection distance is obviously higher for a cryogenic liquid overflow than that for a non-boiling liquid. Figures 4.24 show that $\Delta\mathbf{R_p}$ is influenced by $\mathbf{G_k}$ for a bund height $\mathbf{h_d} < 0.30$. Unfortunately, the data for $\mathbf{h_d} < 0.30$ is scattered, and the fitted curve is not as good as that for overflow of a non-boiling liquid. This is most likely to be caused by the numerical calculation technique used. The maximum jet projection distance at $\mathbf{h_d} < 0.30$ occurs shortly after the shock is formed, when the shock position $\mathbf{r_s}$ is still very close to the bund and the time increment is still refined. It seems that, in that period, the numerical calculation results in ripples in $\mathbf{h_w}$. This in turn affects the vertical velocity $\mathbf{v_w}$ estimated

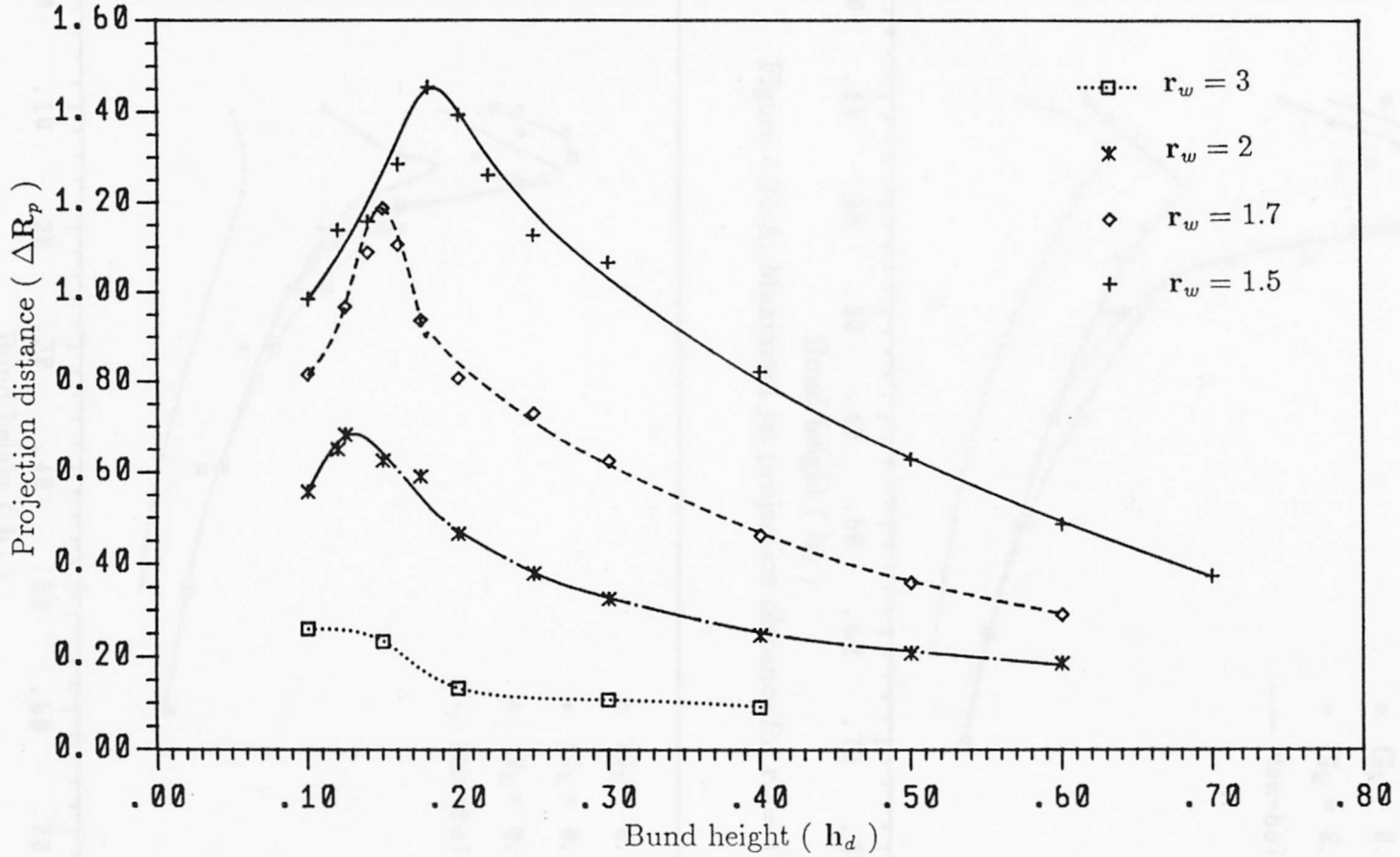


Figure 4.23: Maximum jet projection distance for $G_k = 0.01$

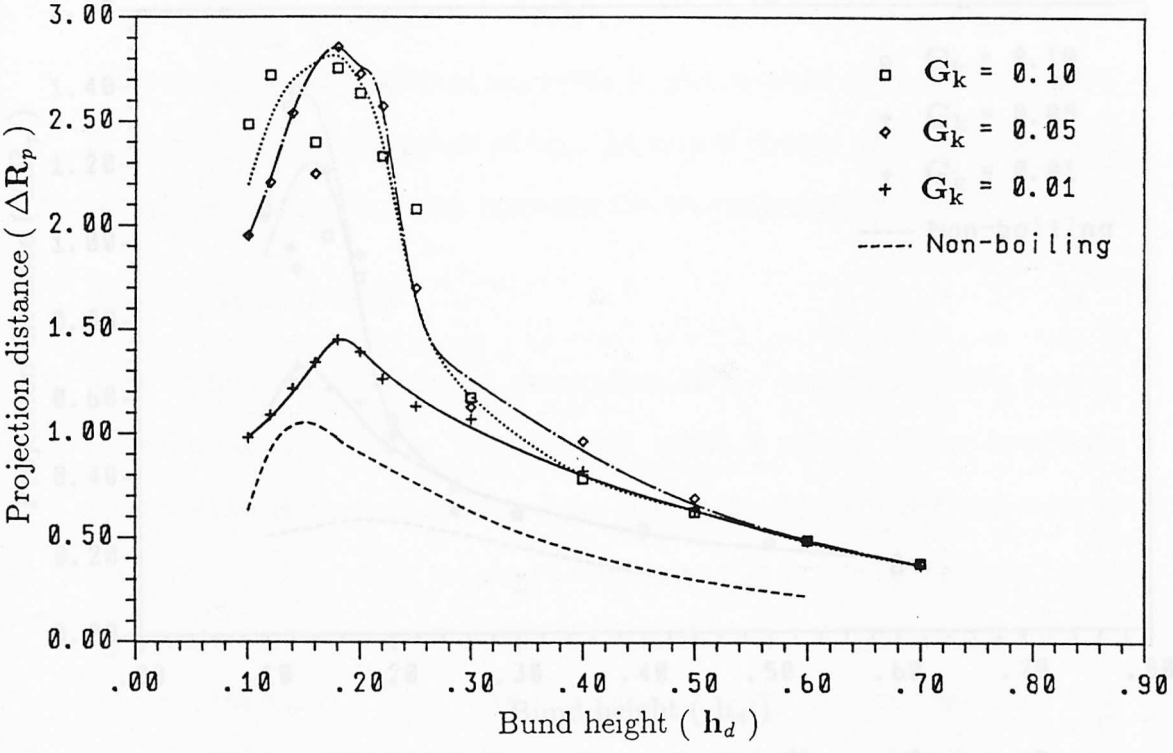


Figure 4.24-A: Maximum jet projection distance for $r_w = 1.5$

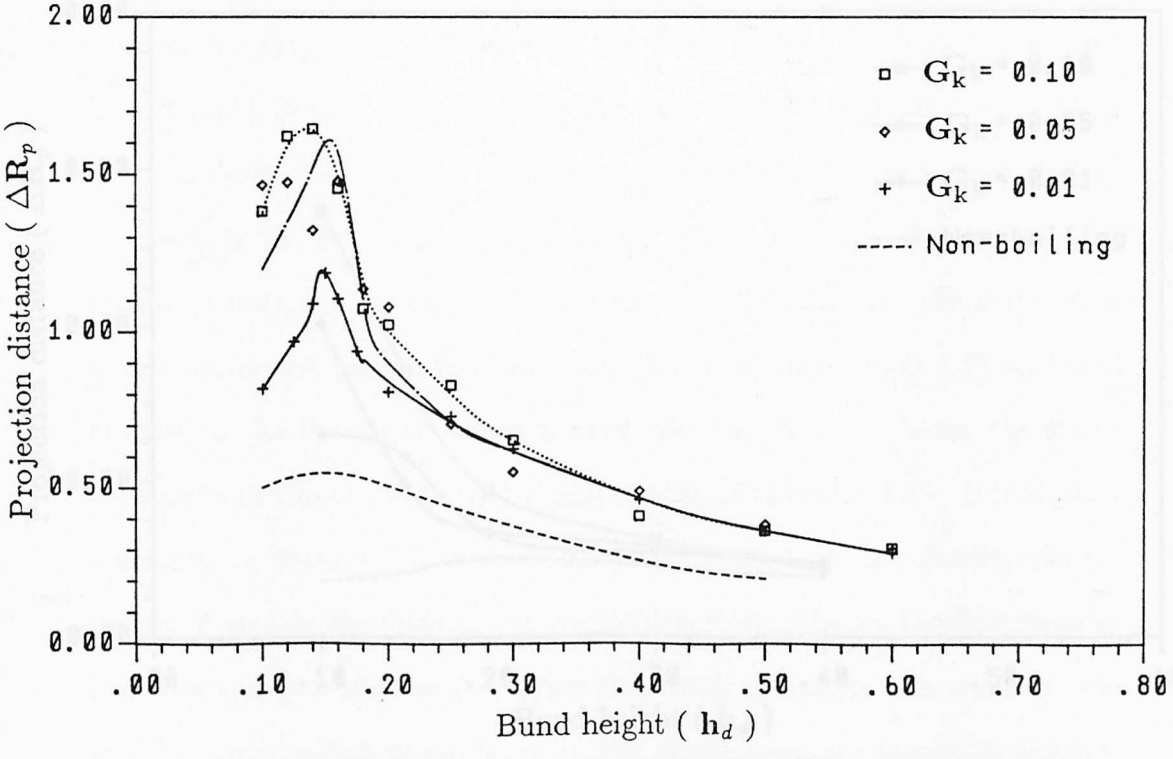


Figure 4.24-B: Maximum jet projection distance for $r_w = 1.7$

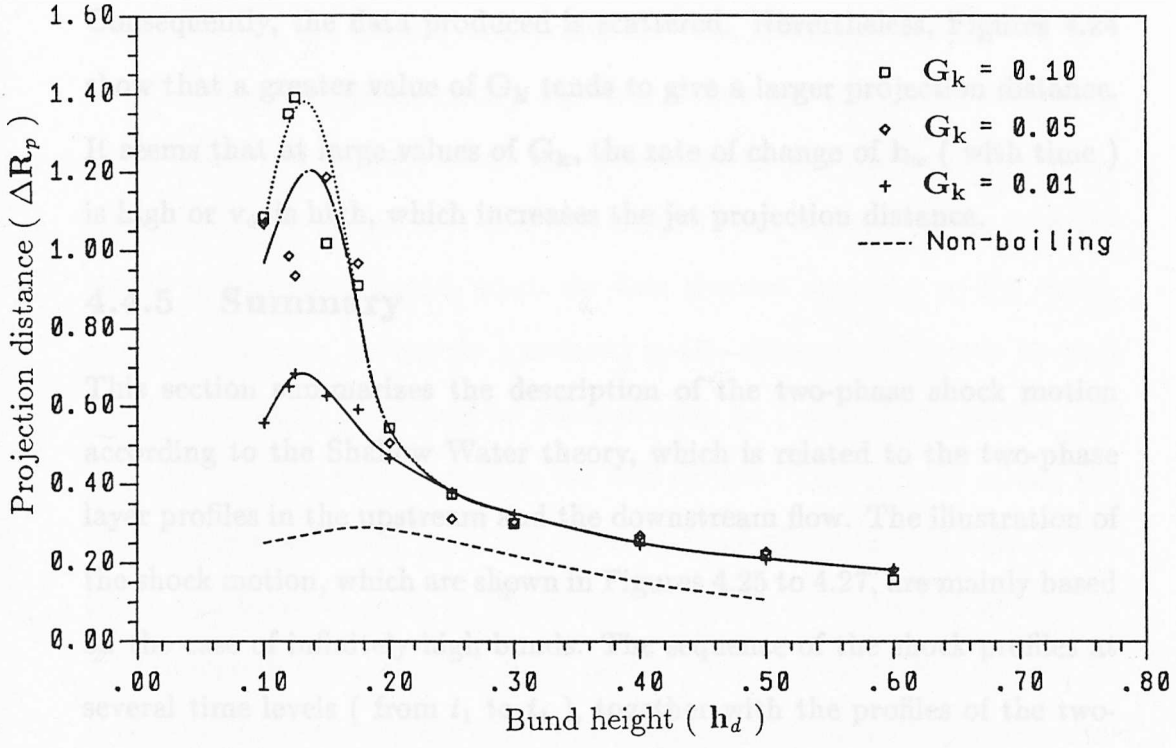


Figure 4.24-C: Maximum jet projection distance for $r_w = 2$

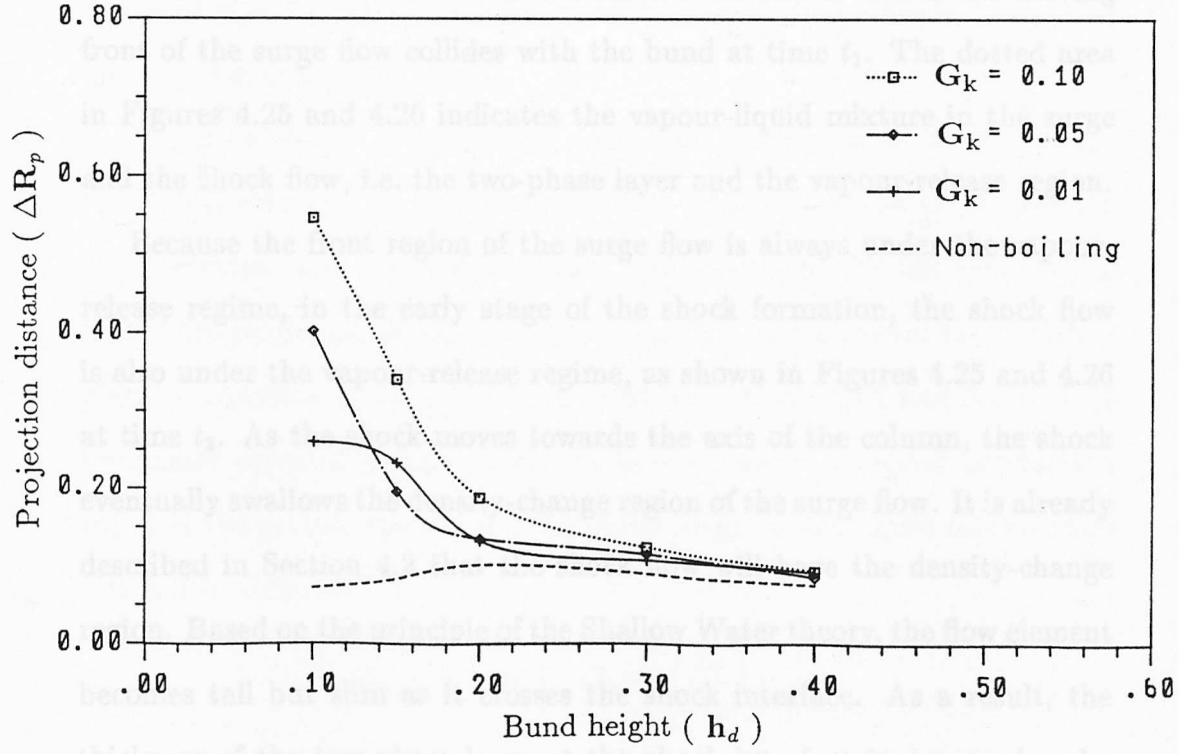


Figure 4.24-D: Maximum jet projection distance for $r_w = 3$

from equation (2.2.11), and also influences the jet projection distance $\Delta \mathbf{R}_p$. Consequently, the data produced is scattered. Nevertheless, Figures 4.24 show that a greater value of $\mathbf{G_k}$ tends to give a larger projection distance. It seems that at large values of $\mathbf{G_k}$, the rate of change of $\mathbf{h}_w$ (with time) is high or $\mathbf{v}_w$ is high, which increases the jet projection distance.

4.4.5 Summary

This section summarizes the description of the two-phase shock motion according to the Shallow Water theory, which is related to the two-phase layer profiles in the upstream and the downstream flow. The illustration of the shock motion, which are shown in Figures 4.25 to 4.27, are mainly based on the case of infinitely-high bunds. The sequence of the shock profiles at several time levels (from t_1 to t_4), together with the profiles of the two-phase layer and the vapour-release region, are illustrated in Figures 4.25 and 4.26. The illustration starts from the instant at which the moving front of the surge flow collides with the bund at time t_1. The dotted area in Figures 4.25 and 4.26 indicates the vapour-liquid mixture in the surge and the shock flow, i.e. the two-phase layer and the vapour-release region.

Because the front region of the surge flow is always under the vapour-release regime, in the early stage of the shock formation, the shock flow is also under the vapour-release regime, as shown in Figures 4.25 and 4.26 at time t_2. As the shock moves towards the axis of the column, the shock eventually swallows the density-change region of the surge flow. It is already described in Section 4.2 that the shock flow will have the density-change region. Based on the principle of the Shallow Water theory, the flow element becomes tall but slim as it crosses the shock interface. As a result, the thickness of the two-phase layer at the shock interface increases sharply, which forms a step-shape. The vapour-release position r_{vs} in the shock

flow depends on the magnitude of $\mathbf{G_k}$. At this stage, the shock flow region is divided into the density-change and the vapour-release regions.

The shape of the boundary line that shows the thickness of the two-phase layer will change, when the shock flow enters the region $r < R_0$. Because boiling at the base does not occur in the region $r < R_0$, no additional vapour is produced, when the flow element crosses $r = R_0$; meanwhile, the vapour previously contained in the element still moves upward due to buoyancy, which will be released later on (hence the density will increase), as the vapour reaches the free surface. This process causes the shape of the boundary line that shows the two-phase layer profile in the shock flow becomes curly, as illustrated in Figures 4.25 and 4.26 at time t_4. The change in the two-phase layer profile when the shock has crossed R_0 is also illustrated in Figure 4.27, which shows a sequence of the motion of flow elements 1 and 2. Element 1 initially comes from the upstream flow in region $r < R_0$, which does not contain vapour, and element 2 contains vapour (i.e. two-phase layer).

Figures 4.25 to 4.27 only show qualitative description of the two-phase layer thickness and of the vapour-release position, where the two-phase layer thickness and the vapour-release position depend on the value of $\mathbf{G_k}$ and of the minimum shock flow density ρ_{smin}. The parameter $\mathbf{G_k}$, which is given in equation (3.4.6), was mentioned in Sections 3.4.2 and 3.5.1. This parameter essentially depends on the boiling rate m (vapour production rate) at the ground surface and the initial height of the liquid column, and this can be described as:

$$\mathbf{G_k} \sim m \quad \text{and} \quad \mathbf{G_k} \sim \left(\frac{R_0}{H_0}\right) \frac{1}{\sqrt{gH_0}}$$

Hence, higher boiling rate and smaller column gives greater value of $\mathbf{G_k}$, and vice versa.

It is concluded that greater values of $\mathbf{G_k}$ and of bund distance $\mathbf{r_w}$ results in greater domination of the vapour-release regime, and consequently, higher loss of mass evaporated at the free surface. For $\mathbf{r_w} \geq 3$ and $\mathbf{G_k} \geq 0.05$, domination of the vapour-release regime is pronounced in the later stages of the shock motion.

In the case of liquid height $\mathbf{h_w}$ for infinitely-high bunds, $\mathbf{h_w}$ is effectively independent on $\mathbf{G_k}$. For a small value of $\mathbf{G_k}$, especially for $\mathbf{r_w} \leq 2$ and $\mathbf{G_k} \leq 0.05$, the height profile at the bund shows that $\mathbf{h_w}$ increases sharply, due to a high density gradient.

When the shock flow passes through $r = R_0$, the shock flow density will decrease, due to vapour release and no further vapour production in the region $r < R_0$. This will in turn affect the shock profile, which is pronounced at $\mathbf{G_k} = 0.10$. Because greater value of $\mathbf{G_k}$ indicates higher vapour concentration in the flow, and hence higher flow profile, the decrease in vapour concentration (due to vapour release) will result in the decrease in the flow height. This phenomenon is shown in Figure 4.10-C and in Appendix-E, where the flow height in region $r < R_0$ gradually decreases.

The minimum density in the surge flow and in the shock flow affect the two-phase layer thickness, as shown in equation (3.3.17). This also affect the vapour-release position, which indicates the extent of the vapour-release region. Lower value of the minimum density results in thinner two-phase layer and smaller vapour-release region.

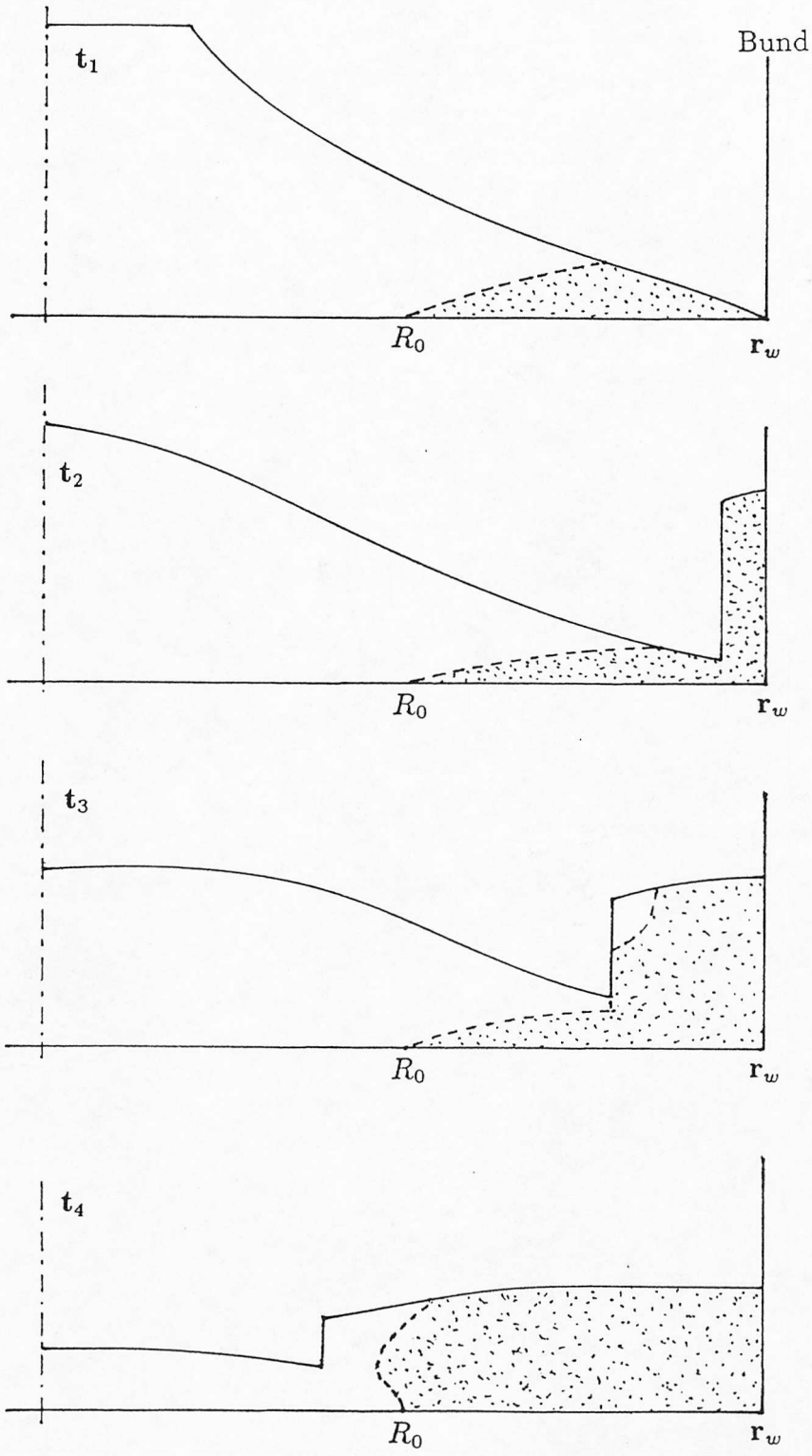


Figure 4.25: Illustration of two-phase shock flow according to the Shallow Water theory

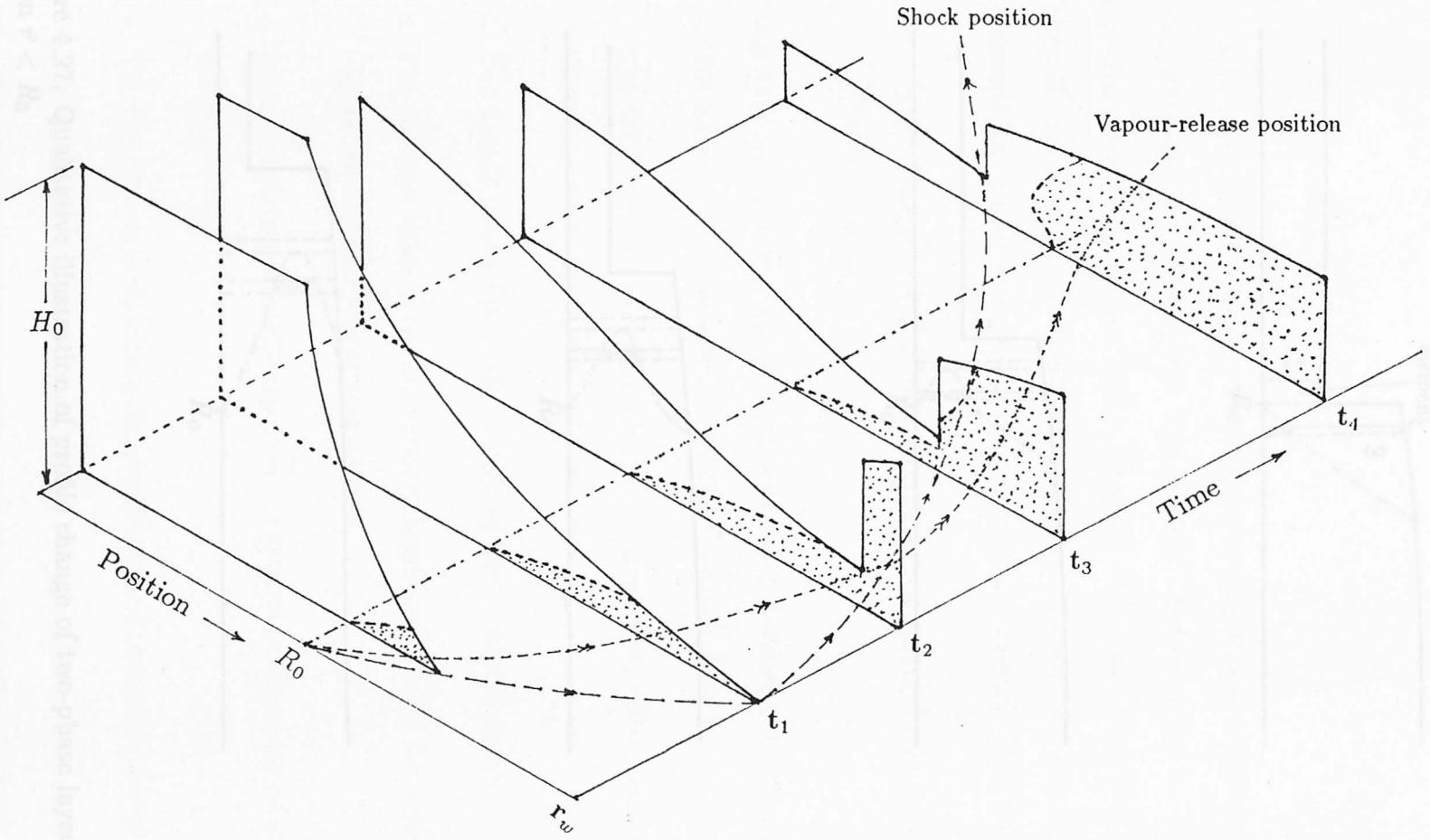


Figure 4.26: The corresponding illustration given by Figure 4.25

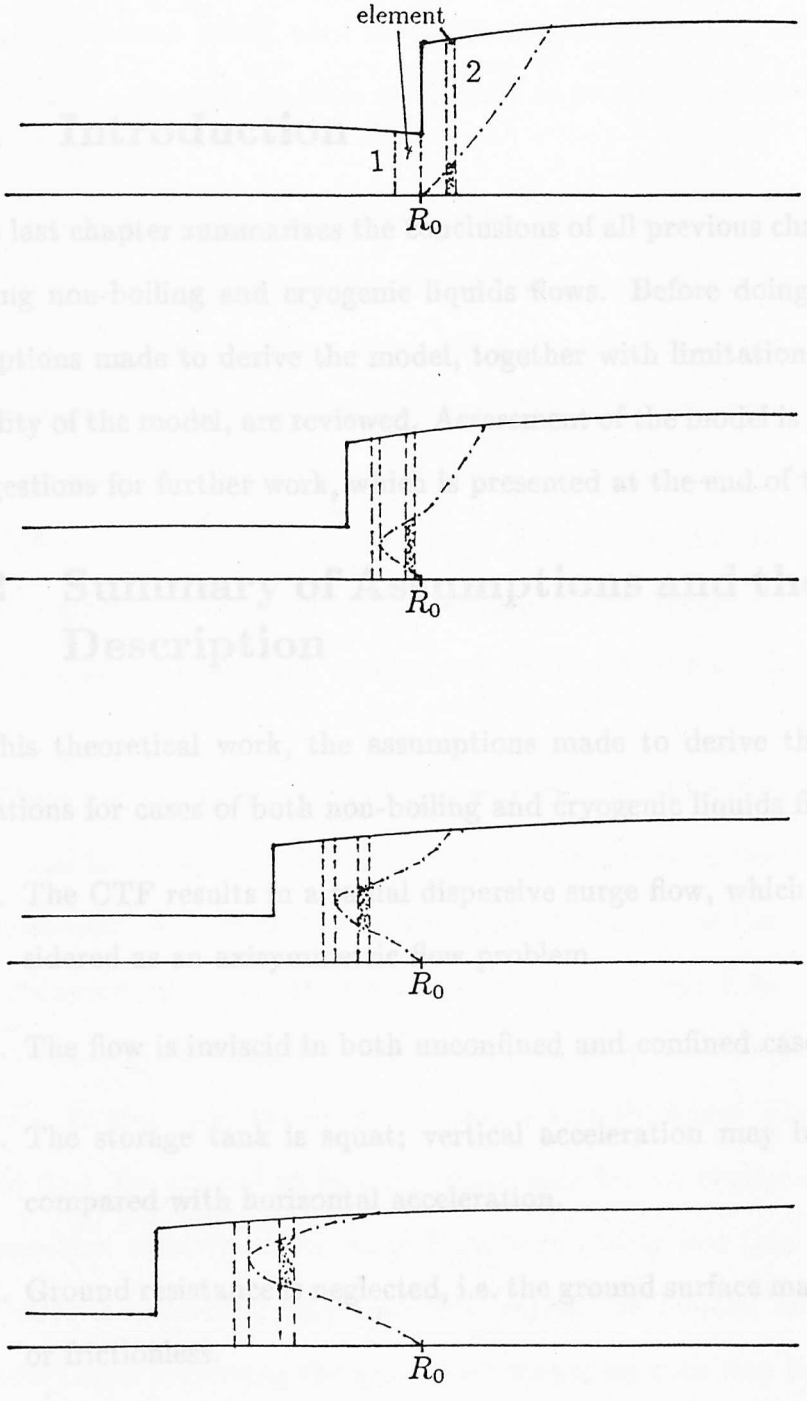


Figure 4.27: Qualitative illustration of profile change of two-phase layer in region $r < R_0$

CHAPTER 5

CONCLUSIONS

5.1 Introduction

This last chapter summarizes the conclusions of all previous chapters, comprising non-boiling and cryogenic liquids flows. Before doing so, the assumptions made to derive the model, together with limitations and applicability of the model, are reviewed. Assessment of the model is given before suggestions for further work, which is presented at the end of this chapter.

5.2 Summary of Assumptions and the Model Description

In this theoretical work, the assumptions made to derive the governing equations for cases of both non-boiling and cryogenic liquids flows are:

1. The CTF results in a radial dispersive surge flow, which can be considered as an axisymmetric flow problem.

2. The flow is inviscid in both unconfined and confined cases.

3. The storage tank is squat; vertical acceleration may be neglected, compared with horizontal acceleration.

4. Ground resistance is neglected, i.e. the ground surface may be smooth or frictionless.

5. The bund is vertical, with a circular shape and concentric to the tank.

Points 1) and 5) represent the scope of investigation in this theoretical work. The asymmetric flow problem, such as liquid release through a gap

or hole in a tank shell, and the interaction of the surge flow with square bunds are not easily analysed by mathematical methods. The solution of both problems would need extensive mathematical and computational efforts, and a physical model is more likely to produce realistic results than theoretical ones.

Points 2) and 3) are obviously valid for almost all vertical storage tanks. The surge flows resulting from the failure of such tanks have very high Reynolds numbers (greater than 10^4), meaning that the inviscid flow assumption is acceptable. Brighton and Webber (1986) described that the early stages of flow from the collapse of a liquid column are controlled by a balance of gravity and inertia forces. The assumption that the tank is squat implies that the height-diameter ratio of the storage tank is not more than 1, which is commonly encountered in industrial and terminal storage tanks.

These two assumptions lead to the introduction of Shallow Water Equations and to the application of Shallow Water theory to describe the CTF phenomenon. According to Shallow Water theory, once the liquid column has collapsed and resulted in a radial dispersive surge flow, the propagation velocity of the surge front on the frictionless ground surface is equal to $2\sqrt{gH_0}$. In this case, the surge front has a zero thickness. For non-boiling liquid flow, the ground surface resistance may be not negligible, hence the propagation velocity of the surge front is in reality less than $2\sqrt{gH_0}$. As this work is concerned only with flow within the bunded area, the error incurred from neglecting the ground resistance on such flow is still acceptable, as argued by Greenspan and Young (1978). For cryogenic liquid flows, this assumption is evenmore justified, since a vapour layer formed at the ground surface will reduce the ground resistance appreciably.

As pointed out in the Introduction chapter, this study considers CTF as a collapse of a liquid column under its own weight, i.e. only concerned with liquid releases from atmospheric tanks. In the case of cryogenic liquid flow, this implies that the liquid is released at its boiling temperature. Hence, the model used in this study should not be applied to describe cryogenic release from pressurized storage tanks, in which the tank pressure would affect the rate of liquid release and flashing would also contribute to the liquid evaporation.

For both unconfined and confined flow of cryogenic liquids, the model accounts for the boiling rate of cryogenic liquid spills on land, which is very high in the early stages of spills. Besides horizontal velocity U and liquid height h, the average density ρ of the liquid-vapour mixture along h is also considered as a dependent variable.

The model considers that the surge flow of cryogenic liquids contains vapour, in the form of a two-phase layer. This two-phase layer, which is the essential aspect of the model, flows parallel to the bulk flow, beneath the liquid layer. The two-phase layer thickness is zero at $r = R_0$ (i.e. at the initial radius of the column) and increases gradually along the flow. In the region near the moving front, vapour is released at the free surface and escapes into the air. The position at which vapour begins to escape at the free surface is called the vapour-release position (r_{vr}). As in the non-boiling flow case, the moving front is considered to have zero thickness. Thus the model divides the region of unconfined flow into 3 regions :

- the non-boiling region ($0 \leq r \leq R_0$), where no boiling occurs.
- the density-change region ($R_0 < r \leq r_{vr}$), where the two-phase layer is formed but vapour does not yet reach the free surface.

- the vapour-release region ($r_{vr} < r \leq r_f$), where vapour is formed at the base and simultaneously released at the surface.

The extent of the two-phase layer essentially depends on: the boiling rate, the horizontal flow velocity, dimension of column (H_0 and R_0), physical properties of vapour and liquid, and the vapour motion in the flow. As the shock flow is formed from the surge flow, its region is also divided into: density-change and vapour-release regions, but the region boundaries and some details change.

Each region, in unconfined and confined flow, has a set of governing equations. The governing equations for the density-change region use dimensionless parameter $\mathbf{G_k}$ (defined in equation (3.4.6)). This parameter is a function of the boiling rate, the physical properties of liquid and the column dimension (i.e. H_0 and R_0). The magnitude of the parameter $\mathbf{G_k}$, which represents the ratio of superficial velocity of vapour and horizontal flow velocity, indicates the intensity of boiling rate effect upon the flow. Dimensionless parameter $\mathbf{K_v}$ (for the surge flow) and $\mathbf{K_{vs}}$ (for the shock flow) are used in the governing equations for the vapour-release region. Both parameters are related to the parameter $\mathbf{G_k}$ in equation (3.4.37). Summary of the theoretical description of the cryogenic liquid shock flow is given in Section 4.4.5 and its illustration is shown in Figures 4.26 to 4.27.

5.3 Discussion of Results

5.3.1 Non-boiling Liquid Flow

In this work, the accuracy and consistency of the numerical calculation results was checked by comparing the mass (volume) and energy content of the flow calculated at every time level with the initial (theoretical) mass and energy content of the liquid column. This method, which was

apparently not applied in previous work, is based on mass and energy conservation.

In the case of unconfined flow, if the differences between the calculated and the initial masses and energy contents (i.e. V_{err} and E_{err}) are less than 1 %, the numerical calculation results are considered to be consistent with mass and energy conservations, for within the accuracy of the calculation method, there is no mass loss (i.e. no evaporation) and no energy loss (frictionless flow) during the process. In the case of confined flow, some energy is lost at the shock and overflow takes place if the bund is low. Checking the accuracy and consistency of the results in confined flow includes calculation of the total energy loss at the shock and the amount of the overflowing liquid. For infinitely high bunds, i.e. no overflow, the calculated energy loss $\mathbf{E}_{loss}$ at the shock must agree well (within 1 % accuracy) with the discrepancy between the calculated and initial energy contents E_{discr}, and so must the calculated mass inside the bund with the initial (theoretical) mass. If overflow occurs, the calculated amount of the overflowing liquid also agrees well with the discrepancy between the calculated and initial masses.

The results of this work, in unconfined and confined flow, showed the consistency with mass and energy conservation, where :

- the differences between the calculated and initial masses and energy contents (V_{err} and E_{err}) in unconfined flow are less than 1 %, and hence agree,
- the calculated energy loss $\mathbf{E}_{loss}$ at the shock agrees very well (i.e. within 1 %) with the discrepancy between the calculated and initial energy contents E_{discr}, and
- the calculated amount of the overflowing liquid agrees very well (i.e.

within 1 %) with the discrepancy between the calculated and initial masses.

By the time the shock converges at the axis, the system has lost a considerable amount of its energy. With little energy remaining available, the subsequent flow (i.e. reflection of the shock from the axis and sloshing) is weaker than the surge flow, hence the interaction of sloshing flow with the bund is less important than that of the surge flow. Based on this consideration, such sloshing flow is regarded as irrelevant in this study.

Comparison with Trbojevic and Slater's results (the MAC method) showed that the Shallow Water theory can describe the flow resulting from CTF as well as the MAC method. Furthermore, the solution of SWEs by the Method of Characteristics is much simpler than the MAC method. Comparison with Sharifi's experimental results (the flow profile in unconfined flow and the liquid motion at the bund) showed that the flow profile given by this theoretical work has the same trend as that obtained by Sharifi. She observed that the propagation velocity of the surge front is $1.4\sqrt{gH_0}$, which is different from that predicted by this theoretical study. This difference has already been discussed in the previous section (i.e. the ground surface is assumed to be smooth and frictionless). The Shallow Water theory description of the motion of the column collapse only differs significantly from reality in the early stages of the column collapse, but agrees well after that, as was shown in the comparison of Martin and Moyce's (1952) data with the results of this study.

The amount of overflowing liquid predicted in this work roughly agrees with the experimental results of Greenspan and Johansson (1981) and of Sharifi (1987). In this case, Greenspan and Young's (1978) theoretical approximation of the overflow rate (equation (2.2.3)) needs further ex-

amination, as it tends to overestimate the amount of overflowing liquid for very low bunds and to under estimate that for high bunds. Further experimental results on the overflow are also needed, to re-examine the existing theoretical and experimental results.

It was shown that Kleyn underestimated the amount of overflow, as also confirmed by Sharifi. However, Kleyn's estimate on the maximum liquid level at the bund is exactly equal to that of this work. Jet projection distances estimated in this work are higher than those estimated by Kleyn. There is unfortunately no experimental data on jet projection distance, so this theoretical estimate cannot be compared with reality.

5.3.2 Cryogenic Liquid Flow

In the case of cryogenic liquid flow, the density of vapour-liquid phase is one of the important dependent variables to be calculated. From the density profiles, the two-phase layer thickness can be determined if the vapour concentration in the two-phase layer is known. In this case, the vapour concentration in the two-phase layer depends on the vapour motion in the flow, which is influenced by buoyancy, turbulence and acceleration of the flow resulting from the collapse of a liquid column. Vapour moves upward due to buoyancy, where turbulence may slow down the upward motion of vapour (i.e. in balance with buoyancy) and may break up vapour into bubbles. Unfortunately, no reliable theoretical or experimental work is available that can be used to determine precisely the vapour motion, and hence the accurate estimate of the vapour concentration in the two-phase layer is not yet known.

To give description of the two-phase layer in unconfined flow, the results presented in Chapter 3 are based on the maximum estimated vapour void fraction in the two-phase layer $\epsilon_v = 0.7$. This vapour void fraction cor-

responds to the minimum (dimensionless) density $\varrho_{min} = 0.3035$, and is assumed to be constant throughout the two-phase layer and the vapour-release region in unconfined flow. The results presented in Chapter 4 are based on the maximum vapour void fraction $\epsilon_v = 0.3$, which corresponds to the minimum (dimensionless) density $\varrho_{smin} = 0.7015$.

Of particular interest is the governing momentum equation for the density-change region, which depends on the vertical position z. Having investigated the influence of z, as described in Appendix F, it is concluded that for the case of unconfined flow, cryogenic liquid flow does not appreciably depend on z. In the case of confined flow, the estimate for the required bund height depends significantly on the value of z for bund distance $\mathbf{r}_w \leq 2$, but less so for $\mathbf{r}_w \geq 3$. In this case, neglecting the vertical position from the governing momentum equation gives the highest estimate for the required bund height. Safety considerations in bund design have to consider the conservative, worst case, i.e. choose the highest estimate for the required bund height. Hence, this work has neglected the vertical position z from the governing momentum equation for the density-change region, both for unconfined and confined flows, which as a maximum overestimates bund height requirement by approximately 20% (see Figure 1 in Appendix F).

As in the case of non-boiling liquid flow, the accuracy and consistency of the numerical calculation results were also checked by using mass conservation. This includes the calculation of the amount of evaporated mass caused by vapour release at the top surface. Once again, the results are considered to be consistent with mass conservation if the difference between the mass discrepancy M_{discr} (i.e. the calculated total mass at any time level less the initial mass) and the calculated evaporated mass M_{evap} is less than 1 %. For the overflow case, the mass discrepancy M_{discr} includes the amount of

the overflowing liquid. The results of this work, both in unconfined and confined flow cases, showed their consistency with mass conservation.

The results of both unconfined and confined flow of cryogenic liquids were only compared with those of non-boiling liquid, as no other theoretical and experimental results are available to date. This comparison can at least show how far the cryogenic liquids flow behaviour differs from the non-boiling liquid one.

The values of $\mathbf{G_k}$ in the investigation of unconfined flow ranges from 0.005 to 0.5, with the span of dimensionless time $\mathbf{t}$ from 0 to 2.5. It is shown that within the time span of investigation, the flow profile for unconfined flow of cryogenic liquids with $\mathbf{G_k} \leq 0.01$ is similar to that for non-boiling liquid. In this case, the two-phase layer is much thinner than the liquid layer, hence its effect on the flow profile is insignificant. For $\mathbf{G_k} = 0.5$, the flow is dominated by the two-phase layer, where the vapour-release region effectively covers the flow area from the point close to $r = R_0$ to the front position r_f. This is regarded as an extreme condition of cryogenic liquids release, which is likely to occur from the collapse of a small column of cryogenic liquids with very high boiling rate. At this condition, the amount of evaporated mass due to vapour release at the free surface is relatively high, around 5 % at (dimensionless) time $\mathbf{t} = 2.5$.

Within the range of $\mathbf{G_k}$ values and of time, the dimensionless velocity of the moving front is around 1.70–1.83; it is higher for small values of $\mathbf{G_k}$, i.e. the velocity is 1.83 for for $\mathbf{G_k} = 0.005$. It appears that the magnitude of $\mathbf{G_k}$ has little effect on the front velocity. On the other hand, the vapour-release position r_{vr} strongly depends on the value of $\mathbf{G_k}$. Larger values of $\mathbf{G_k}$ cause r_{vr} to move closer to $r = R_0$, which indicates that the vapour-release regime dominates the surge flow.

Shock flow results (i.e. in the confined flow case) indicated that the shock flow of cryogenic liquids behaves differently from that of non-boiling liquid. The results showed that the liquid height of the cryogenic liquid shock flow at infinitely-high bunds is generally higher than that of the non-boiling liquid shock flow and depends slightly on the value of $\mathbf{G_k}$. This means that the elementary requirements for complete containment of a cryogenic liquid release must differ from that of a non-boiling liquid release, or the bund height for cryogenic liquid storage tanks must be higher than that for non-boiling liquid.

As expected theoretically, greater bund distance r_w and $\mathbf{G_k}$ increases the importance of the vapour-release regime for both the surge and shock flows, which in turn increases the amount of mass evaporated. For $r_w \geq 3R_0$ and $\mathbf{G_k} \geq 0.05$, the domination of the vapour-release regime is pronounced and the amount of evaporated mass is relatively high.

Other aspects of cryogenic liquid shock flow (the amount of the overflowing liquid and the jet projection distance) are also higher than those of the non-boiling liquid shock flow. The amount of the overflowing liquid and the jet projection distance depend on the value of $\mathbf{G_k}$, where higher value of $\mathbf{G_k}$ gives larger amount of the overflowing liquid and larger jet projection distance.

It is concluded that the cryogenic liquids flow resulting from CTF and its interaction with the bund cannot generally be estimated by the model used in non-boiling liquid flow case, although the prediction of this theoretical study for cryogenic liquids depend on the uncertain values of maximum vapour concentration in the surge flow and in the shock flow, which are not yet known and need further investigation.

5.4 Assessment of the Model

The theoretical description of unconfined and confined flows given by this application of Shallow Water theory may differ from the realty in some aspects.

As observed experimentally (Martin and Moyce, 1952; Sharifi, 1987), for the case of unconfined flow, all parts of the column top move down simultaneously since the beginning of the column collapse. According to the Shallow Water theory, the process of the column collapse starts from outer element of the column ($r = R_0$) and gradually moves towards the column axis ($r = 0$). Hence, the column top does not collapse simultaneously. This different description occurs until the liquid height at the axis, as calculated by Shallow Water theory, begins to collapse at $t = (R_0/\sqrt{gH_0})$. As discussed previously, the Shallow Water theory description of the motion of the column collapse only differs from experiment in the early stages of the column collapse, but agrees well after that, as shown in the comparison with Martin and Moyce's (1952) experimental data. Furthermore, the length of the period over which this different description occurs is relatively short, compared with the whole time span of interest of this study.

In the early stage of shock formation, i.e. when the shock interface is close to the bund, vertical motion dominates the shock flow. Shallow Water theory considers that the shock is formed by horizontal arrangement of flow elements, and that in the shock, the height of flow elements changes instantaneously. However, the length of the period at which vertical motion dominates the shock flow is relatively short compared with the whole period of the shock motion (from its formation until it converges at the axis of the column). Hence, within the whole time span of interest of this study, both different descriptions are acceptable.

In the case of the cryogenic liquid shock flow, the description of the two-phase layer based on Shallow Water theory, which is illustrated in Figures 4.25 and 4.26, may differ from the reality in some further aspects. In all confined flow cases, when the shock position is not far from the bund wall, the incoming liquid from the upstream penetrates the shock interface and may reach the bund wall, which causes flow reversal (flow backward) in the upper part of the shock flow. Due to such circulation flow in the shock, the vapour carried by the reversed flow in the upper part of the shock flow may be released throughout the free surface of the shock flow. As described before, the Shallow Water theory only considers horizontal velocity, and hence cannot describe such flow reversal in the shock flow. However, this theoretical study considers that there is a vapour-release region, where vapour is released at the free surface, although the extent of the vapour-release region depends on the magnitude of $\mathbf{G_k}$. In this case, quantitative experimental data both for vapour void fraction and for the whole phenomenon is apparently needed, to compare with this theoretical estimate.

The other aspect is that according to this theoretical description, the two-phase layer thickness rises abruptly at the shock interface. This is likely to differ from the reality, in which the two-phase layer thickness may change gradually. In this case, it is difficult to estimate the extent of the region where gradual change of the two-phase layer thickness takes place. However, when the shock position is far from the bund, the extent of such a region is more likely to be small, compared with the whole region of the shock flow, which this theoretical study is interested in.

In conclusion, the Shallow Water theory used in this study can generally describe the cryogenic liquid releases from CTF, although further investi-

gation of the aspect of vapour motion in the surge flow and in the shock flow is needed.

5.5 Suggestions For Further Work

As mentioned previously, further theoretical and experimental investigations are still needed, which can precisely describe the nature of the two-phase, unconfined and confined flow. In the case of theoretical investigation on cryogenic liquid flow resulting from the CTF, improvement of the theoretical description of the flow may be made by considering the following aspects :

1). The nature of the two-phase, unconfined and confined flow.

The validity of the description given by the model proposed in this study depends partly on the nature of the two-phase layer in the surge flow and of the two-phase shock flow. This study only gives general description of both two-phase flows, where the maximum vapour void fraction is taken to be equal to 0.7 for the surge flow and 0.3 for the shock flow. The vapour concentration in both the surge flow and the shock flow will either be better estimated by considering turbulence, buoyancy and acceleration of the flow, or by experimentation. This will hopefully give more realistic description of the cryogenic liquid flow resulting from the CTF.

2). Modelling with two-space variables r and z (horizontal and vertical).

As described before, the Shallow Water theory only considers r as independent space variable, where vertical motion is represented by the change of liquid height, and vertical acceleration is considered to be negligible. Although this model is generally satisfactory for the description of the CTF, a model based on r and z is expected to give better description, as it would

account for vertical acceleration. Taking vertical acceleration into account may address the following problems :

1. The column collapse motion description in the early stage, where the experimental observation differs from that given by the Shallow Water theory.

2. The hydrodynamic pressure at the bund and overflow for low bunds in the early stages of shock formation, where the liquid height rises rapidly while the shock itself propagates very slowly. In this case, Shallow Water theory can only estimate the hydrostatic pressure, which is likely to be less than the hydrodynamic pressure in the early stages of shock formation.

3. The shock motion againts an inclined bund surface, which cannot be easily solved by the Shallow Water theory.

4. Circulation motion in the shock flow when it is close the the bund wall, which determines the nature of the two-phase cryogenic liquid shock flow.

3). Refined Estimation of Overflow Rate

Although the amount of overflow estimated by equations (2.4.9) and (2.5.6) agrees roughly with experimental results, the trend of the overflow prediction at extreme bund conditions (very low and very high) seems to differ from experimental result. As pointed out in 2) above, accounting for vertical acceleration may help to solve this problem, and may give more realistic estimates of the jet projection distance.

REFERENCES

1. ABBOTT, M.B. and TORBE, I. (1963) "On Flows and Fronts in a Stratified Fluid", *Proc. Roy. Soc.*, **A,273**, 12-40.

2. ABBOTT, M.B. (1966) *An Introduction to The Method of Characteristics*, Thames and Hudson, London.

3. ABBOTT, M.B. (1979) *Computational Hydraulics*, Pitman Publishing Ltd., London.

4. AZBEL, D. (1981) *Two-phase Flows in Chemical Engineering*, Cambridge University Press, Cambridge.

5. BARNEA, D. (1986) "Transition from Annular and from Dispersed Bubble Flow – Unified Models for The Whole Range of Pipe Inclinations", *Int.J.Multiphase Flow*, **12**,733-744.

6. BERENSON, P.J. (1961) "Film Boiling Heat Transfer From a Horizontal Surface", *J.Heat Transfer*, **81**(1),1-12.

7. BIRD, R.B., STEWARD, W.E. and LIGHTFOOT, E.N. (1966) *Transport Phenomena*, John Wiley, New York.

8. CARNAHAN, B., LUTHER, H.A. and WILKES, J.O. (1969) *Applied Numerical Methods*, John Wiley, New York.

9. CARSLAW, H.S. and JAEGER, J.C. (1959) *Conduction of Heat in Solids*, 2nd ed., Oxford University Press, Oxford.

10. CHAN, A.M.C. and BANERJEE, S. (1981) "Refilling and Rewetting of a Hot Horizontal Tube – Part I : Experiments", *J.Heat Transfer*, **103**, 281-286.

11. CHAN, A.M.C. and BANERJEE, S. (1981) "Refilling and Rewetting of a Hot Horizontal Tube – Part II : Structure of a Two-Fluid Model", *J.Heat Transfer*, **103**,287-292.

12. CHAN, A.M.C. and BANERJEE, S. (1981) "Refilling and Rewetting of a Hot Horizontal Tube – Part III : Application of a Two-Fluid Model to Analyze Rewetting", *J.Heat Transfer*, **103**,653-659.

13. DHIR, V.K. AND CATTON , I. (1982) "Boiling in a Porous Bed", *Appl.Sci.Res.*, **38**,69-76.

14. DRAKE, E.M., HARRIS, S.H. and REID, R.C. (1974) "Analysis of Vapor Dispersion Experiments", *LNG Safety Program , Interim Report on Phase II Work* , **AGA Project IS-3-1**.

15. DRAKE, E.M. and REID, R.C. (1975) "How LNG Boils on Soils", *Hydrocarbon Processing*, **54**(May),191-194.

16. DRESSLER, R.F. (1952) "Hydraulic Resistance Effect Upon The Dam-break Functions", *J.Res.Nat.Bur.Stand.*, **49**(3),217-225.

17. FANNELOP, T.K. and WALDMAN, G.D. (1971) "Dynamics of Oil Slicks", *AIAA J.*, **10**(4),506-510.

18. GREENSPAN, H.P. and BUTLER, D.S. (1962) "On The Expansion of a Gas into Vacuum", *J.Fluid Mech.*, **12**,101-120.

19. GREENSPAN, H.P. and JOHANSSON, A.V. (1981) "An Experimental Study of Flow Over an Impounding Dike", *Stud. Appl. Math.*, **64**, 211-223.

20. GREENSPAN, H.P. and YOUNG, R.E. (1978) "Flow Over a Containment Dyke", *J.Fluid Mech.*, **87**,179-192.

21. HILL, G.A., CHENIER, C.L., SHOOK, C.A. and ESMAIL, M.N. (1980) "Numerical and Experimental Study of a Falling Liquid Column", *Can.J.Chem.E.*, **58**,3-11.

22. KLEYN, O.H.F. (1983) "Hydrodynamic Modelling of Catastrophic Failure of Cylindrical Fuel Storage Tanks", *PhD. Thesis*, Dept.Chem. Eng., Imperial College, London.

23. LARSEN, P.S. and TONG , L.S. (1969) "Void Fractions in Subcooled Flow Boiling", *J.Heat Transfer*, **91**,471-476.

24. LEAF, G.K., CHAWLA, T.C. and MINKOWYCZ, W.J. (1979) "Numerical Methods for Hydraulic Transients", *J.Num.Heat Transfer*, **2**, 1-34.

25. LEVICH, V.G. (1962) *Physicochemical Hydrodynamics*, Prentice-Hall, Englewood Cliffs, New York.

26. MARTIN, J.C. and MOYCE, W.J. (1952) "An Experimental Study of The Collapse of Liquid Columns on a Rigid Horizontal Plane", *Phil.Trans.Roy.Soc.*, **A244**,312-324.

27. PENNEY, W.G. and, THORNHILL, C.K. (1952) "The Dispersion, Under Gravity, of a Column of Fluid Supported on a Rigid Horizontal Plane", *Phil.Trans.Roy.Soc.*, **A244**,285-311.

28. RAJ, P.K. (1981) "Models for Cryogenic Liquid Spill Behaviour on Land and Water", *J.Hazardous Materials*, **5**,111-130.

29. REID, R.C. and WANG, R. (1978) "The Boiling Rate of LNG on Typical Dike Floor Materials", *Cryogenics*, **18**,401-404.

30. SHARIFI, T. (1987) "An Experimental Study of Catastrophic Failure of Liquid Storage Tanks", *PhD. Thesis*, Dept.Chem.Eng., Imperial College, London.

31. SHAW, P. and BRISCOE, F. (1978) "Evaporation from Spills of Hazardous Liquids on Land and Water", *SRD* **R-100**.

32. SMITH, G.D. (1978) *Numerical Solution of Partial Differential Equations : Finite Difference Methods* , 2nd ed., Clarendon Press, Oxford.

33. STOKER, J.J. (1957) *Water Waves*, Interscience Publishers Inc., New York.

34. TRBOJEVIC, V.M. and SLATER, D.H. (1989) "Tank Failure Modes and Their Consequences", *Plant/Operations Progress*, **8**(2),84-87.

35. WALLIS, G.B. (1969) *One-dimensional Two-phase Flow*, McGraw-Hill Book Company, London, p255.

36. WEBBER, D.M. and BRIGHTON, P.W.M. (1986) "A Mathematical Model of a Spreading, Vaporising Liquid Pool", *Heavy Gas and Risk Assessment III*, ed. S.Hartwig, D.Reidel Publishing Company, pp.223-232.

37. WEBBER, D.M. and BRIGHTON, P.W.M. (1986) "Inviscid Similarity Solutions for Slumping From a Cylindrical Tank", *J.Fluid Eng.*, **108**,238-240.

38. WEISMAN, J., DUNCAN, D., GIBSON, J. and CRAWFORD T. (1979) "Effects of Fluid Properties and Pipe Diameter on Two-phase Flow Patterns in Horizontal Lines", *Int. J. Multiphase Flow*, **5**,437-462.

39. WEISMAN, J.and PEI, B.S. (1983) "Prediction of CHF in Flow Boiling at Low Qualities", *Int.J.Heat Mass Transfer*, **26**,1463-1477.

40. WHITHAM, G.B. (1955) "The Effects of Hydraulic Resistance in The Dam-break Problem", *Proc.Roy.Soc.,Ass.*, **7**,399-407.

41. ZUBER, N. (1958) "Stability of Boiling Heat Transfer", *Trans.ASME*, **80**,711-720.

APPENDIX A

NEWTON - RAPHSON METHOD

If there are a set of n equations :

$$\begin{aligned} F_1(x_1, x_2, \ldots, x_n) &= 0 \quad , \\ F_2(x_1, x_2, \ldots, x_n) &= 0 \quad , \\ &\vdots \\ F_n(x_1, x_2, \ldots, x_n) &= 0 \quad , \end{aligned}$$

and they are independent of each other, their roots x_1 to x_n can be determined. If F_1 to F_n are linear equations, they are easily solved by using any matrix solution, such as the Gaussian elimination method. For non-linear equations, such as some equations in this study, they are difficult to solve directly.

The Newton-Raphson method is one of several methods that can be used to solve such non-linear equations. This method is based on linearization of (non-linear) equations. The following gives the principle of the Newton-Raphson method.

By Taylor expansion, $F_i(x_1, x_2, \ldots, x_n) = 0$ is expanded around point $P(x_{1,P}, x_{2,P}, \ldots, x_{n,P})$:

$$\begin{aligned} F_i = F_{i,P} \quad + \quad & \Big[\frac{\partial F_i}{\partial x_1}\Delta x_1 + \frac{\partial F_i}{\partial x_2}\Delta x_2 + \cdots \\ & \cdots + \frac{\partial F_i}{\partial x_n}\Delta x_n\Big]_P + O\left((\Delta x_i)^2\right) = 0 \end{aligned} \tag{A.1}$$

$$\text{with} \begin{cases} \Delta x_1 = x_1 - x_{1,P} \quad , \\ \Delta x_2 = x_2 - x_{2,P} \quad , \\ \quad \vdots \\ \Delta x_n = x_n - x_{n,P} \quad . \end{cases}$$

In order to *linearize* it, equation (A.1) is truncated from the second order term of RHS. Expansion and truncation of F_1 to F_n results in:

$$\begin{aligned}
\frac{\partial F_1}{\partial x_1}\Delta x_1 + \frac{\partial F_1}{\partial x_2}\Delta x_2 + \cdots + \frac{\partial F_1}{\partial x_n}\Delta x_n &= -F_{1,P} \\
\frac{\partial F_2}{\partial x_1}\Delta x_1 + \frac{\partial F_2}{\partial x_2}\Delta x_2 + \cdots + \frac{\partial F_2}{\partial x_n}\Delta x_n &= -F_{2,P} \\
&\vdots \quad \vdots \\
\frac{\partial F_n}{\partial x_1}\Delta x_1 + \frac{\partial F_n}{\partial x_2}\Delta x_2 + \cdots + \frac{\partial F_n}{\partial x_n}\Delta x_n &= -F_{n,P}
\end{aligned} \tag{A.2}$$

This can be written in a matrix form :

$$\begin{vmatrix} \frac{\partial F_1}{\partial x_1} & \frac{\partial F_1}{\partial x_2} & \cdots & \frac{\partial F_1}{\partial x_n} \\ \frac{\partial F_2}{\partial x_1} & \frac{\partial F_2}{\partial x_2} & \cdots & \frac{\partial F_2}{\partial x_n} \\ \vdots & \vdots & \ddots & \vdots \\ \frac{\partial F_n}{\partial x_1} & \frac{\partial F_n}{\partial x_2} & \cdots & \frac{\partial F_n}{\partial x_n} \end{vmatrix} \cdot \begin{vmatrix} \Delta x_1 \\ \Delta x_2 \\ \vdots \\ \Delta x_n \end{vmatrix} = \begin{vmatrix} F_{1,P} \\ F_{2,P} \\ \vdots \\ F_{n,P} \end{vmatrix}$$

or in simpler form :

$$\begin{aligned}
\mathbf{J}(\mathbf{x}).\mathbf{\Delta x} &= \mathbf{F}(\mathbf{x}) \\
\mathbf{\Delta x} &= \mathbf{J}(\mathbf{x})^{-1}.\mathbf{F}(\mathbf{x})
\end{aligned} \tag{A.3}$$

Equation (A.3) is the principle of Δx_i calculation, which is also used in the Newton-Raphson iteration method. In the iteration, Δx_i is equal to $(x_i^{m+1} - x_i^m)$, where m is the iteration step number. Equation (A.3) is in fact equal to :

$$\mathbf{x}^{m+1} = \mathbf{x}^m - \mathbf{J}(\mathbf{x}^m)^{-1}.\mathbf{F}(\mathbf{x}^m) \tag{A.4}$$

The iteration is continuously performed until $\mathbf{x}^{m+1}$ is essentially equal to $\mathbf{x}^m$, or alternatively $\mathbf{F}(\mathbf{x}) = 0$. The following is the procedure of iteration :

1. To initialize the iteration ($m = 1$), take arbitrary values of $\mathbf{x}^m$, namely $\mathbf{x}^1 = (x_1, x_2, \ldots, x_n)$.

2. Calculate F_i and $\frac{\partial F_i}{\partial x_j}$ at point $\mathbf{x}^m$.

3. Calculate $\mathbf{x}^{m+1}$ by using equation (A.4). If$|\mathbf{F}(\mathbf{x}^{m+1})| \leq \epsilon$ (very small number), point $\mathbf{x}^{m+1}$ is regarded as one root of the equations, and the iteration is stopped.

4. If criterion in step 3 is not satisfied, then $\mathbf{x}^m = \mathbf{x}^{m+1}$ and step 2 onwards is repeated, until the criterion is satisfied.

The partial derivative $\frac{\partial F_i}{\partial x_j}$ sometimes cannot be easily evaluated analytically. In this case, such a partial derivative is better approximated numerically, by using :

$$\frac{\partial F_i}{\partial x_j} \approx \frac{\left(F_i|_{x_j+\delta x_j} - F_i|_{x_j}\right)}{\delta x_j}$$

where δx_j is very small (relative to x_j).

If there are only two equations, such as $F(x,y)$ and $G(x,y)$, equation (A.3) can be simplified. Rewriting equation (A.2) :

$$\frac{\partial F}{\partial x}\Delta x + \frac{\partial F}{\partial y}\Delta y = -F_0 \quad ,$$

$$\frac{\partial G}{\partial x}\Delta x + \frac{\partial G}{\partial y}\Delta y = -G_0 \quad ,$$

and this can be arranged into :

$$\Delta x = -\left[F_0\frac{\partial G}{\partial y} - G_0\frac{\partial F}{\partial y}\right] \Big/ \left[\frac{\partial F}{\partial x}\frac{\partial G}{\partial y} - \frac{\partial F}{\partial y}\frac{\partial G}{\partial x}\right] \quad ,$$

$$\Delta y = +\left[F_0\frac{\partial G}{\partial x} - G_0\frac{\partial F}{\partial x}\right] \Big/ \left[\frac{\partial F}{\partial x}\frac{\partial G}{\partial y} - \frac{\partial F}{\partial y}\frac{\partial G}{\partial x}\right] \quad .$$

APPENDIX B

NORMALISATION OF TIME REFERENCE

1. Trbojevic and Slater's Work

In this work (Trbojevic and Slater, 1989), the freeze frames are presented at time : 1.5 , 2. , 2.5, 3. and 4 (seconds). Here, at time just after zero, the column still stands, and the front edge may not move yet. Yet the SWE's theory implies that the front edge suddenly moves with a dimensionless velocity 2 as soon as the column collapses. Hence, the time references are different from each other, and comparison cannot be based on absolute zero time.

Although there is no explicit statement about the time reference and dimensionless time, they can be approximated by the following way :

- The tank diameter = 30 m ($R_0 = 15$ m).
- Initial liquid height $H_0 = 10.5$ m $\rightarrow C_0 = \sqrt{gH_0} = 10.15$ m/s .
- Bund diameter = 76.6 m or $\mathbf{r}_w = 2.55$.
- Front velocity (when reaching the bund) = 14.6 m/s . This is assumed constant along its motion. In dimensionless, $\mathbf{U}_{front} = 1.44$.
- The front arrives at the bund at 2 seconds (Frame 3). This must be equivalent to dimensionless time $\mathbf{t} = (\mathbf{r}_w - 1)/\mathbf{U}_{front}$. Hence, $\mathbf{t} = (2.55 - 1)/1.44 = 1.076$, or 2 seconds $\equiv 1.08$.

Based on this time reference, other frame times correspond to dimensionless time $\mathbf{t}$:

Original time :	1.5	2.	2.5	3.	4.
Equivalent **t**:	0.80	1.08	1.35	1.61	2.15

In Figure 1.4 (Chapter 1), **t** is rounded into the multiplication of $\mathbf{t} = 0.05$.

2. Martin and Moyce's Work

The copy of their results (Martin and Moyce, 1952) are enclosed in this Appendix. The following explains some of their notation, with the equivalent notation of this study.

Z = the position of moving front, dimensionless,
H = column crest/top height, dimensionless,
T = dimensionless time,
τ = dimensionless time , equal to T/n,
n^2 = ratio of initial column height to radius ($\equiv H_0/R_0$),
a = initial column width ($\equiv R_0$).

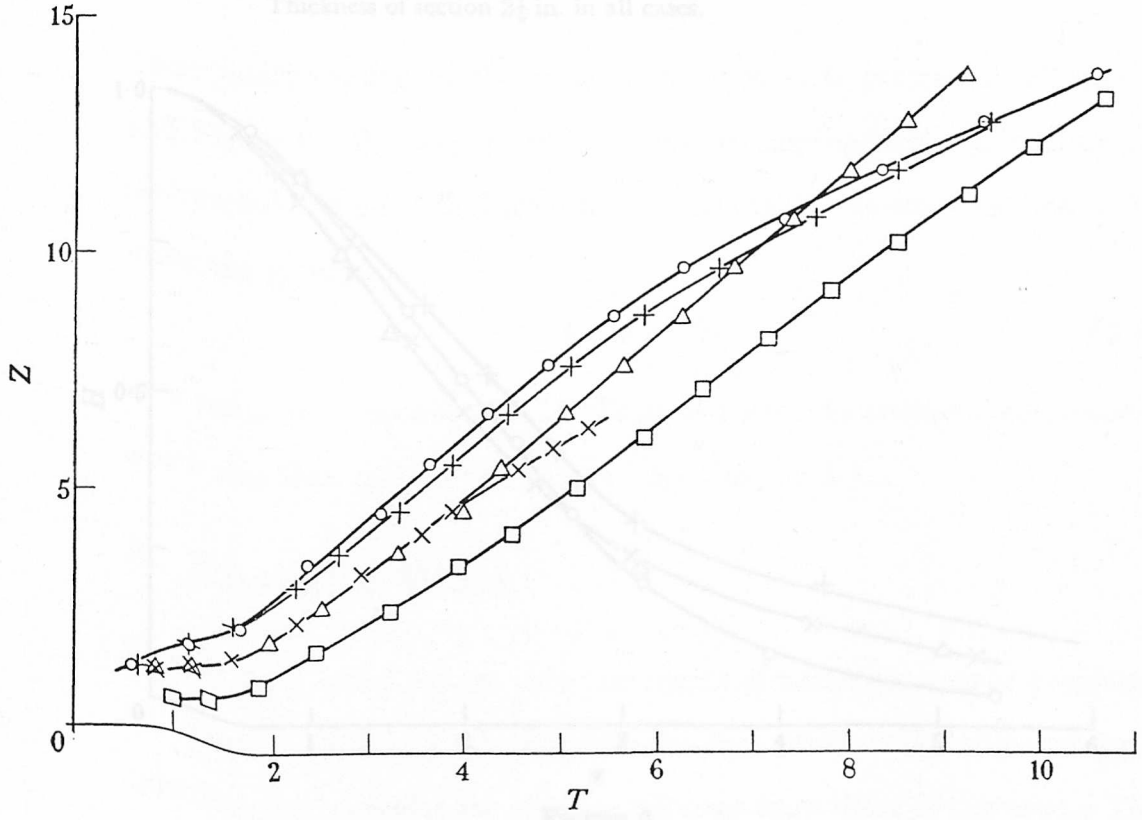


FIGURE 3. Rectangular sections.

key	+	○	×	△	□
n^2	1	1	2	2	4
a (in.)	$2\frac{1}{4}$	$4\frac{1}{2}$	$1\frac{1}{8}$	$2\frac{1}{4}$	$1\frac{1}{8}$

Note. In the case of $n^2 = 4$, $Z/2$ is plotted against $T/2$.

TABLE 6. MOTION OF TOP OF COLUMN. RECTANGULAR SECTION, PLANE SYMMETRY

$\tau = t(g/a)^{\frac{1}{2}} = T/n$

	$n^2=1$, $a=2\frac{1}{4}$ in.			$n^2=2$, $a=2\frac{1}{4}$ in.			$n^2=4$, $a=1\frac{1}{8}$ in.		
H			mean			mean			mean
1·00*	0	0	0	0	0	0	0	0	0
0·94	—	—	—	—	0·56	0·56	0·61	0·65	0·63
0·89	0·85	0·75	0·80	0·76	0·79	0·77	0·87	0·93	0·90
0·83	—	—	—	—	0·96	0·93	1·11	1·17	1·14
0·78	1·31	1·28	1·29	1·05	1·11	1·08	1·30	1·30	1·30
0·72	—	—	—	—	1·33	1·28	1·43	1·48	1·46
0·67	1·74	1·74	1·74	1·44	1·47	1·46	1·61	1·67	1·64
0·61	—	—	—	—	1·68	1·66	1·76	1·85	1·81
0·56	2·16	2·14	2·15	1·81	1·86	1·84	1·98	1·98	1·98
0·50	—	—	—	—	2·00	2·00	2·07	2·19	2·13
0·44	2·58	2·55	2·57	2·18	2·23	2·21	2·32	2·32	2·32
0·39	—	—	—	—	2·49	2·45	2·50	2·46	2·48
0·33	3·08	3·08	3·08	2·65	2·75	2·70	2·69	2·69	2·69
0·28	—	—	—	—	3·08	3·06	2·87	2·87	2·87
0·22	4·36	4·17	4·27	3·41	3·47	3·44	3·11	3·15	3·13
0·17	—	—	—	—	4·09	4·20	3·46	3·37	3·42
0·11	6·09	6·48	6·29	5·20	5·30	5·25	3·80	4·07	3·94
0·06	—	—	—	—	7·40	7·40	5·74	5·00	5·37
†motion began at or before $\tau =$			0·2			0·16			0·2

* $\tau = 0$ taken as the time when heater current was applied.

† As indicated by change in appearance of fluid meniscus in reservoir.

Thickness of section $2\frac{1}{4}$ in. in all cases.

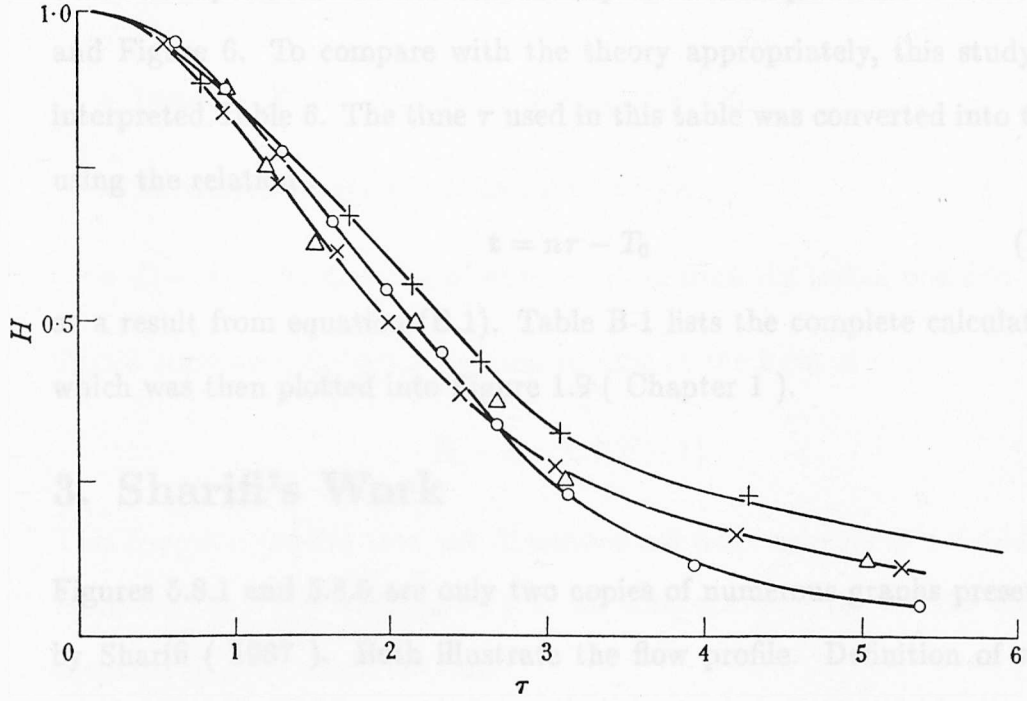


FIGURE 6

	n^2	a (in.)	
+	1	$2\frac{1}{4}$	rectangular section
×	2	$2\frac{1}{4}$	rectangular section
○	4	$1\frac{1}{8}$	rectangular section
△	—	2	semicircular section

Figure 3 shows the relation between the front edge position and time. Martin and Moyce estimated the front velocity $\mathbf{U}_{front} = 1.62 - 1.71$ based on this graph. This figure indicates that the curves do not start at point ($T = 0$, $Z = 1$), as commonly encountered in the experimental result. To compare with the SWE's theory, the front position correlation is normalised to :

$$Z - 1 = \mathbf{U}_{front}\mathbf{t} \tag{B.5}$$

Here, by extrapolating with a straight-line in Figure 3 into $Z = 1$, the correction for T can be approximated by inspection.

n^2	a,inch	T_0(approx.)
1	2.25	0.70
2	2.25	1.40
4	1.125	2.80

Their interpretation of the column top motion is presented in Table 6 and Figure 6. To compare with the theory appropriately, this study re-interpreted Table 6. The time τ used in this table was converted into $\mathbf{t}$, by using the relation :

$$\mathbf{t} = n\tau - T_0 \tag{B.6}$$

as a result from equation (B.1). Table B-1 lists the complete calculation, which was then plotted into Figure 1.9 (Chapter 1).

3. Sharifi's Work

Figures 5.8.1 and 5.8.5 are only two copies of numerous graphs presented by Sharifi (1987). Both illustrate the flow profile. Definition of some dimensionless variables she used are different from those of this study. The following are some of her definitions :

- Time $T = t\sqrt{g/H_0}$,

Table B-1: Interpretation of Martin and Moyce's data

	$n^2 = 1$		$n^2 = 2$		$n^2 = 4$	
H	τ	t	τ	t	τ	t
0.94	–	–	0.56	-0.6	0.63	-1.54
0.89	0.80	0.10	0.77	-0.31	0.90	-1.
0.83	–	–	0.93	-0.08	1.14	-0.52
0.78	1.29	0.59	1.08	0.13	1.30	-0.2
0.72	–	–	1.28	0.40	1.46	0.12
0.67	1.74	1.04	1.46	0.66	1.64	0.48
0.61	–	–	1.66	0.95	1.81	0.82
0.56	2.15	1.45	1.84	1.20	1.98	1.16
0.50	–	–	2.0	1.43	2.13	1.46
0.44	2.57	1.87	2.21	1.73	2.32	1.84
0.39	–	–	2.45	2.06	2.48	2.16
0.33	3.08	2.38	2.70	2.42	2.69	2.58
0.28	–	–	3.06	2.93	2.87	2.94
0.22	4.27	3.57	3.44	3.46	3.13	3.46
0.17	–	–	4.20	4.54	3.42	4.04
0.11	6.29	5.59	5.25	6.02	3.94	5.08
0.06	–	–	7.40	9.07	5.37	7.94

- Distance X (or Z or R) = (distance x)$/H_0$,
- The initial height to radius ratio = H/A ,
- $D - A$ = the distance of front position from the initial position.

Sharifi correlated the front position to time in the form of :

$$D - A = 1.4(T - 1) \tag{B.7}$$

This equation implies that the dimensionless front velocity is 1.4 and the "time-lag" is 1 (= zero time T_0). To compare with the SWE's theory, equation (B.3) is converted into :

$$D - A \simeq \frac{\Delta r_f}{H_0} = \frac{\Delta r_f}{R_0}(\frac{R_0}{H_0}),$$

$$\frac{\Delta r_f}{R_0} = 1.4(\frac{H_0}{R_0})(T - 1).$$

Here, the corrected dimensionless time $\mathbf{t} = (\frac{H_0}{R_0})(T-1)$. The distance X (Z and R) needs to be corrected as well :

$$X_{corrected} = X_{Sharifi}(\frac{H_0}{R_0}).$$

As an example, for $H/A = 2$, $T = 2$ is equivalent to $\mathbf{t} = 2$. But for $H/A = 1$, $T = 3$ is equivalent to $\mathbf{t} = 2$.

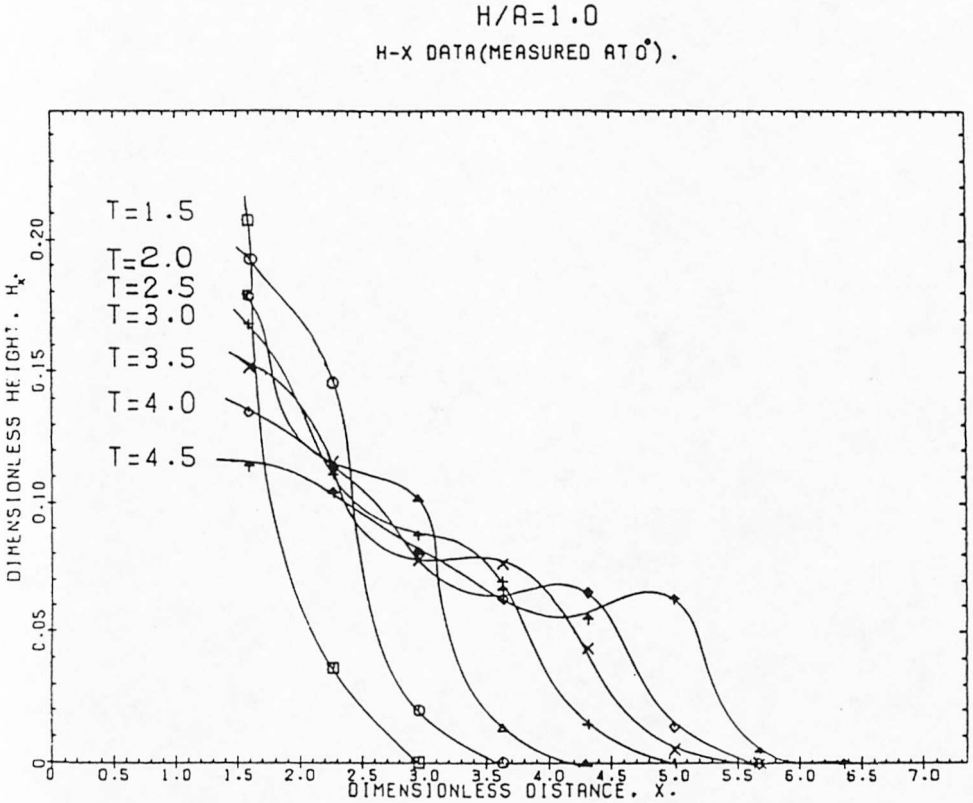


FIGURE 5.8.1 Dimensionless Height profiles (H_X vs. X) for runs measured at θ =0°.

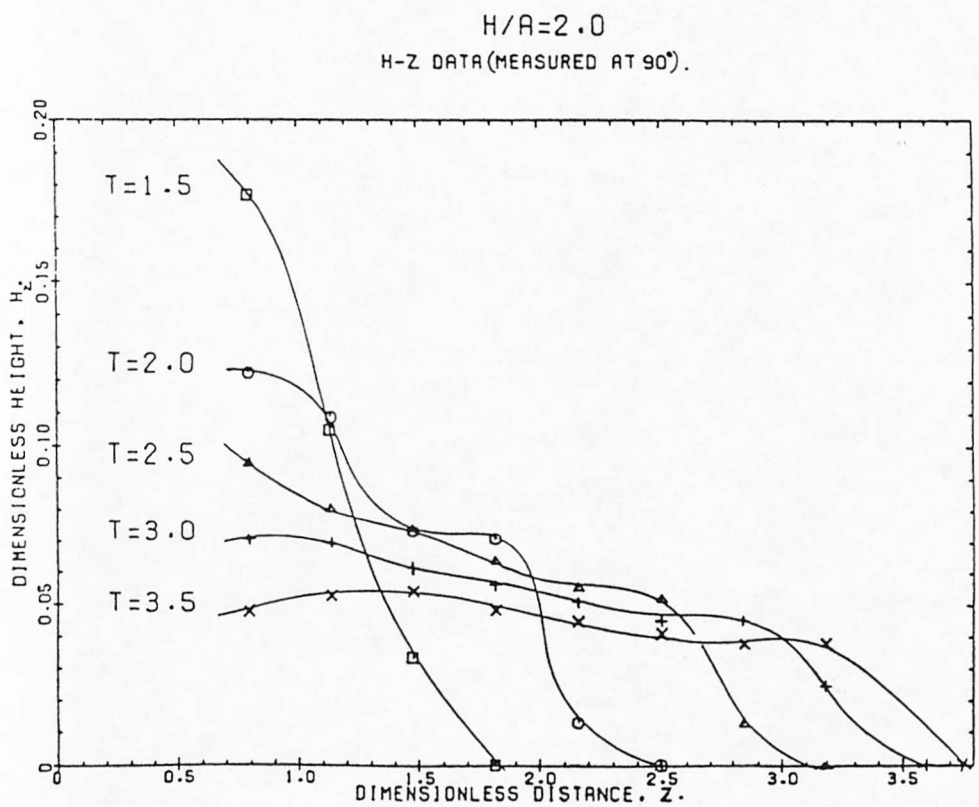


FIGURE 5.8.5 Dimensionless Height profiles (H_Z vs. Z) for runs measured at θ = 90°.

APPENDIX C

The contents of this Appendix are :

Tables :

- C-1: Mass error, energy discrepancy and loss for $\mathbf{r}_w = 2$
- C-2: Mass error, energy discrepancy and loss for $\mathbf{r}_w = 3$
- C-3: Mass error, energy discrepancy and loss for $\mathbf{r}_w = 4$

Figures :

- C-1: The shock profiles for $\mathbf{r}_w = 2$
- C-2: The shock profiles for $\mathbf{r}_w = 4$
- C-3: Hydrostatic pressure at the base P_w and total load at the bund F_w for $\mathbf{r}_w = 1.5$
- C-4: Hydrostatic pressure at the base P_w and total load at the bund F_w for $\mathbf{r}_w = 3$
- C-5: Hydrostatic pressure at the base P_w and total load at the bund F_w for $\mathbf{r}_w = 4$
- C-6: Maximum jet projection distance for $H_0/R_0 = 0.5$
- C-7: Maximum jet projection distance for $H_0/R_0 = 1.5$
- C-8: Maximum jet projection distance for $H_0/R_0 = 2$

Table C-1: Mass error, energy discrepancy and loss for $\mathbf{r}_w = 2$

Time(t)	V_{error}	E_{discr}	E_{loss}
0.60	-0.04	-0.34	0.27
0.70	-0.09	-2.22	2.09
0.80	-0.12	-5.26	5.07
0.90	-0.15	-8.89	8.67
1.00	-0.18	-12.82	12.58
1.10	-0.09	-16.70	16.61
1.20	-0.05	-20.63	20.58
1.30	-0.10	-24.52	24.42
1.40	-0.15	-28.24	28.08
1.50	-0.18	-31.76	31.55
1.60	-0.22	-35.08	34.83
1.70	-0.20	-38.16	37.92
1.80	-0.19	-41.04	40.81
1.90	-0.18	-43.73	43.51
2.00	-0.17	-46.23	46.01
2.10	-0.16	-48.54	48.33
2.20	-0.15	-50.65	50.45
2.30	-0.15	-52.58	52.39
2.40	-0.14	-54.32	54.13
2.50	-0.14	-55.87	55.68
2.60	-0.14	-57.22	57.03
2.70	-0.14	-58.39	58.21
2.80	-0.13	-59.41	59.24
2.90	-0.12	-60.30	60.13
3.00	-0.10	-61.08	60.91
3.20	-0.11	-62.38	62.21
3.40	-0.10	-63.39	63.23
3.60	-0.08	-64.19	64.02
3.80	-0.05	-64.81	64.65
4.00	-0.04	-65.29	65.13
4.20	-0.01	-65.67	65.51
4.40	0.00	-65.95	65.79
4.60	0.01	-66.08	65.98

Table C-2: Mass error, energy discrepancy and loss for $\mathbf{r}_w = 3$

Time(t)	V_{error}	E_{discr}	E_{loss}
1.10	0.05	0.10	0.11
1.20	0.15	-0.38	0.70
1.30	0.17	-1.63	1.97
1.40	0.17	-3.57	3.90
1.50	0.16	-6.02	6.34
1.60	0.14	-8.91	9.20
1.70	0.11	-12.17	12.43
1.80	0.08	-15.67	15.90
1.90	0.04	-19.32	19.51
2.00	0.00	-23.01	23.16
2.20	-0.14	-30.39	30.42
2.40	-0.10	-37.46	37.50
2.60	-0.14	-44.03	44.05
2.80	-0.16	-49.97	49.97
3.00	-0.13	-55.25	55.26
3.20	-0.13	-59.89	59.91
3.40	-0.17	-63.92	63.91
3.60	-0.17	-67.25	67.25
3.80	-0.07	-69.92	69.97
4.00	-0.11	-72.15	72.18
4.20	-0.10	-73.94	73.98
4.40	-0.10	-75.40	75.44
4.60	-0.10	-76.61	76.65
4.80	-0.09	-77.61	77.65
5.00	-0.08	-78.45	78.49
5.50	-0.08	-79.99	80.03
6.00	-0.07	-80.99	81.02
6.50	-0.08	-81.66	81.69
7.00	-0.08	-82.11	82.13
7.50	-0.09	-82.40	82.41
8.00	-0.10	-82.59	82.59
8.10	-0.10	-82.61	82.61

Table C-3: Mass error, energy discrepancy and loss for $\mathbf{r}_w = 4$

Time(t)	V_{error}	E_{discr}	E_{loss}
1.70	0.17	0.01	0.22
1.80	0.16	-0.59	0.81
1.90	0.14	-1.64	1.83
2.00	0.12	-3.09	3.25
2.10	0.10	-4.90	5.03
2.20	0.09	-7.04	7.15
2.30	0.06	-9.52	9.60
2.40	0.04	-12.28	12.34
2.50	0.02	-15.25	15.28
2.60	0.00	-18.34	18.36
2.70	-0.03	-21.53	21.53
2.80	-0.07	-24.80	24.76
2.90	-0.12	-28.10	28.02
3.00	-0.17	-31.39	31.28
3.20	-0.30	-37.85	37.65
3.40	-0.35	-43.96	43.74
3.60	-0.34	-49.68	49.46
3.80	-0.35	-54.95	54.73
4.00	-0.35	-59.72	59.50
4.20	-0.36	-63.96	63.74
4.40	-0.37	-67.67	67.44
4.60	-0.36	-70.83	70.61
4.80	-0.36	-73.50	73.28
5.00	-0.35	-75.75	75.54
5.50	-0.35	-79.94	79.73
6.00	-0.35	-82.73	82.52
6.50	-0.45	-84.65	84.42
7.00	-0.44	-85.98	85.75
7.50	-0.44	-86.93	86.69
8.00	-0.44	-87.60	87.36
8.50	-0.45	-88.10	87.86
9.00	-0.47	-88.48	88.22
9.50	-0.49	-88.75	88.50
10.00	-0.50	-88.97	88.70

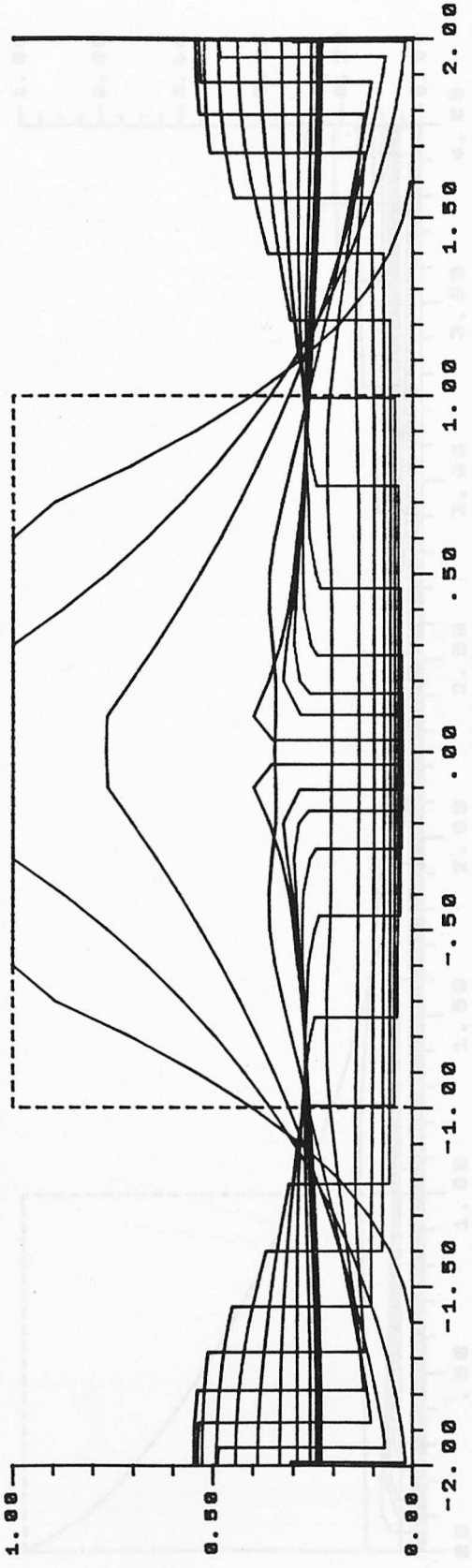


Figure C-1: The shock profiles for $\mathbf{r}_w = 2$

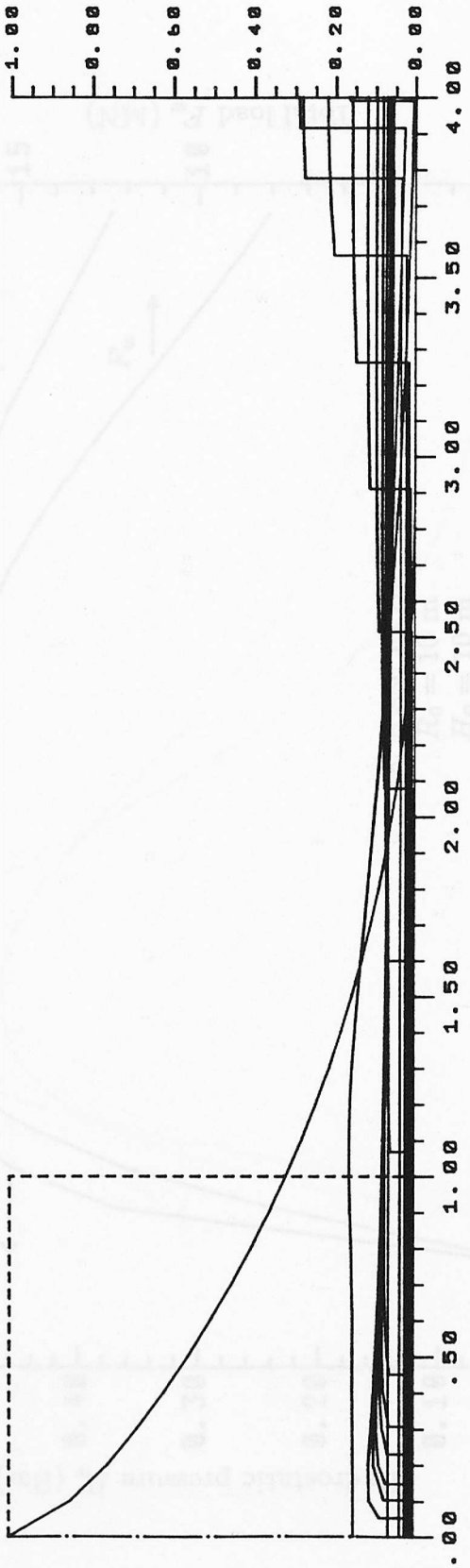


Figure C-2: The shock profiles for $\mathbf{r}_w = 4$

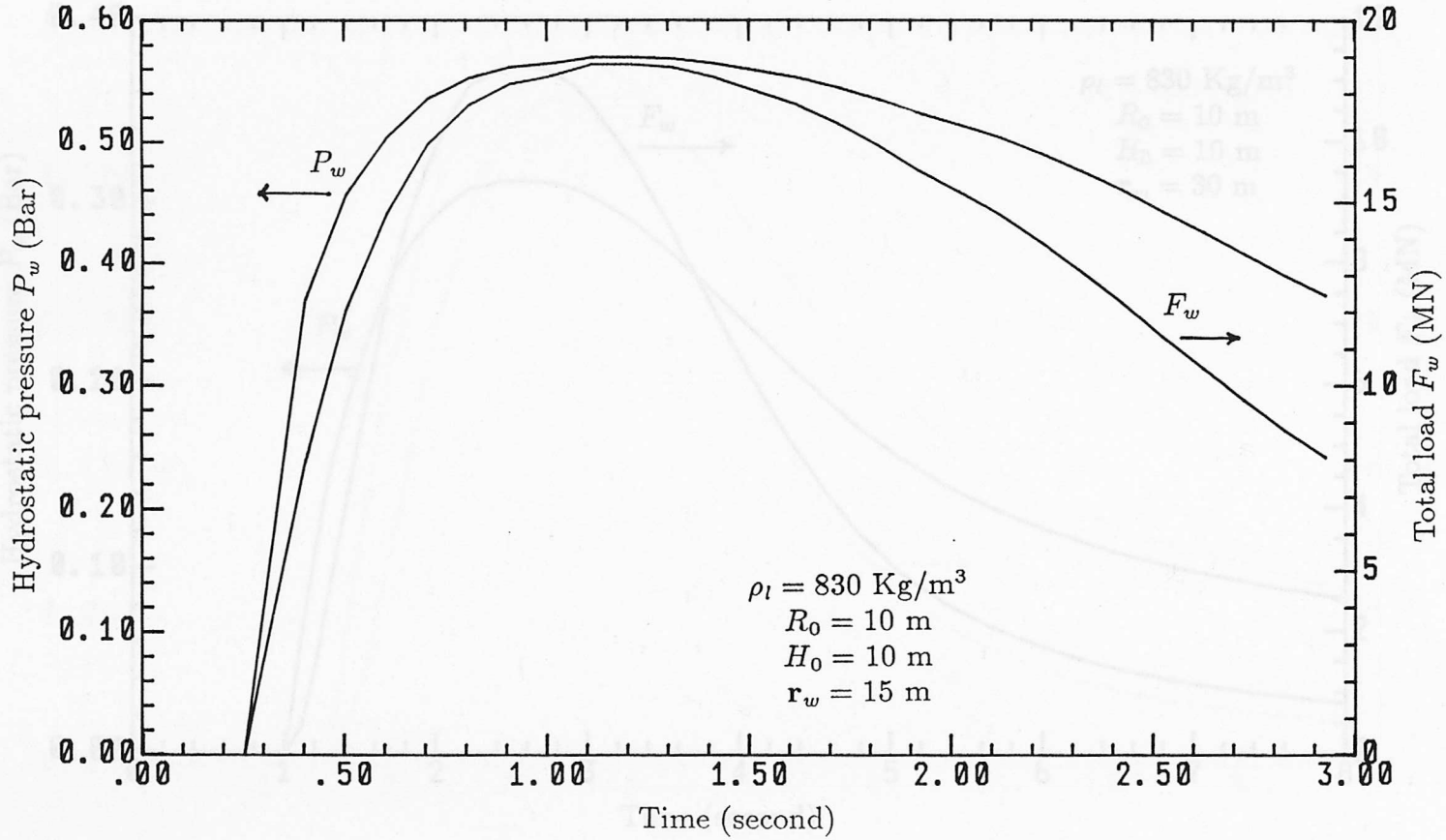


Figure C-3: Hydrostatic pressure at the base P_w and total load at the bund F_w for $\mathbf{r}_w = 1.5$

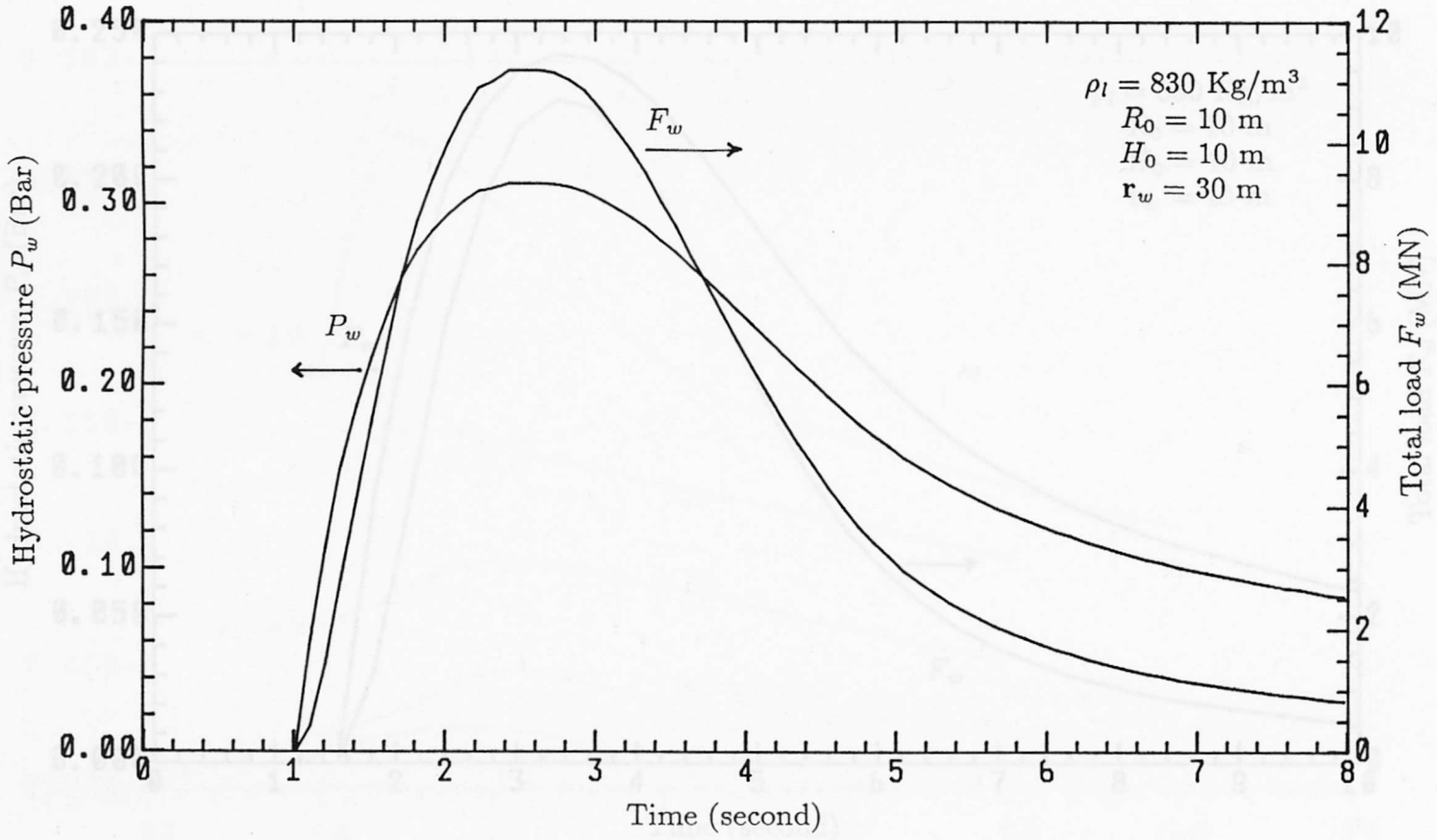


Figure C-4: Hydrostatic pressure at the base P_w and total load at the bund F_w for $\mathbf{r}_w = 3$

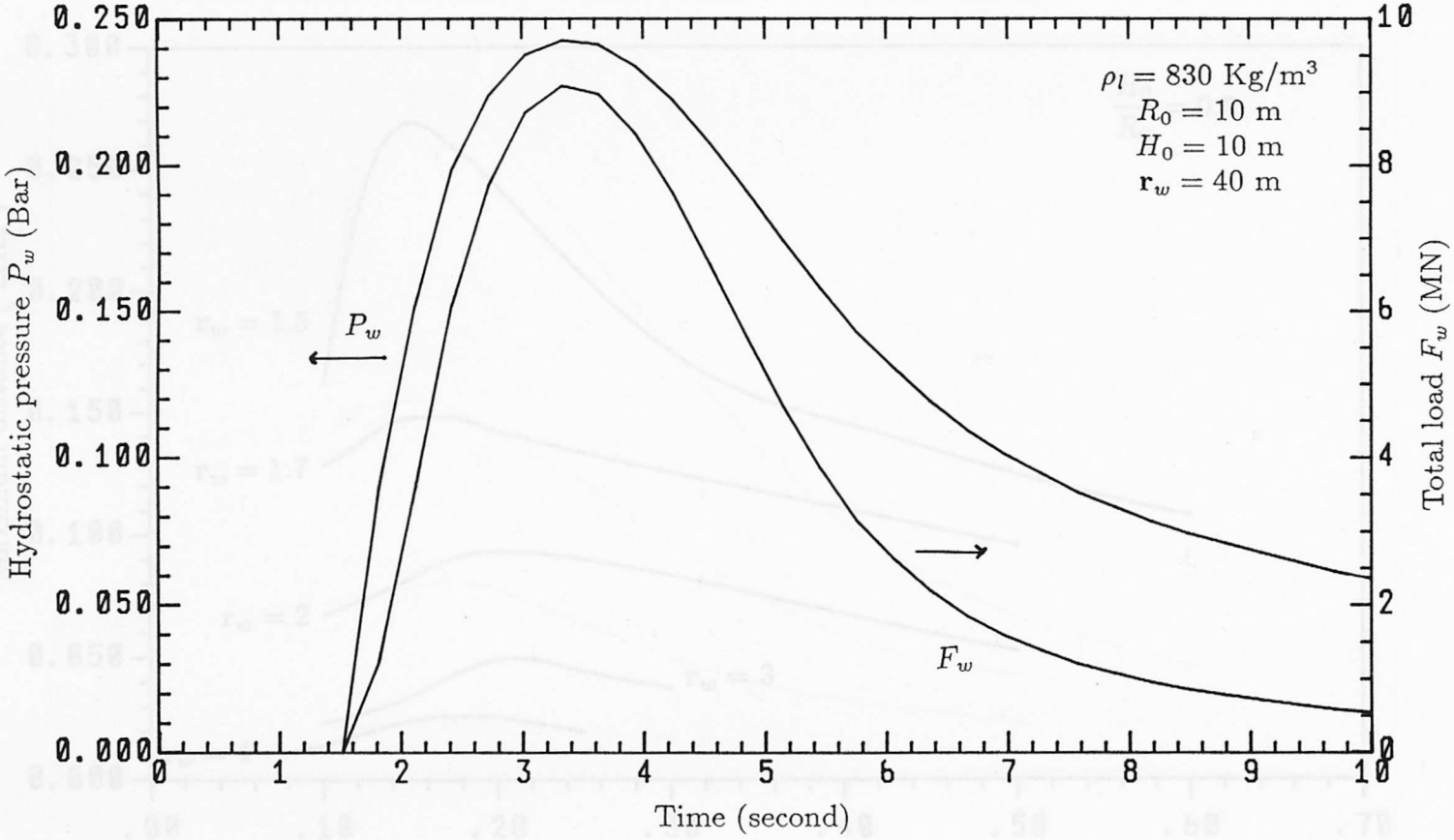


Figure C-5: Hydrostatic pressure at the base P_w and total load at the bund F_w for $\mathbf{r}_w = 4$

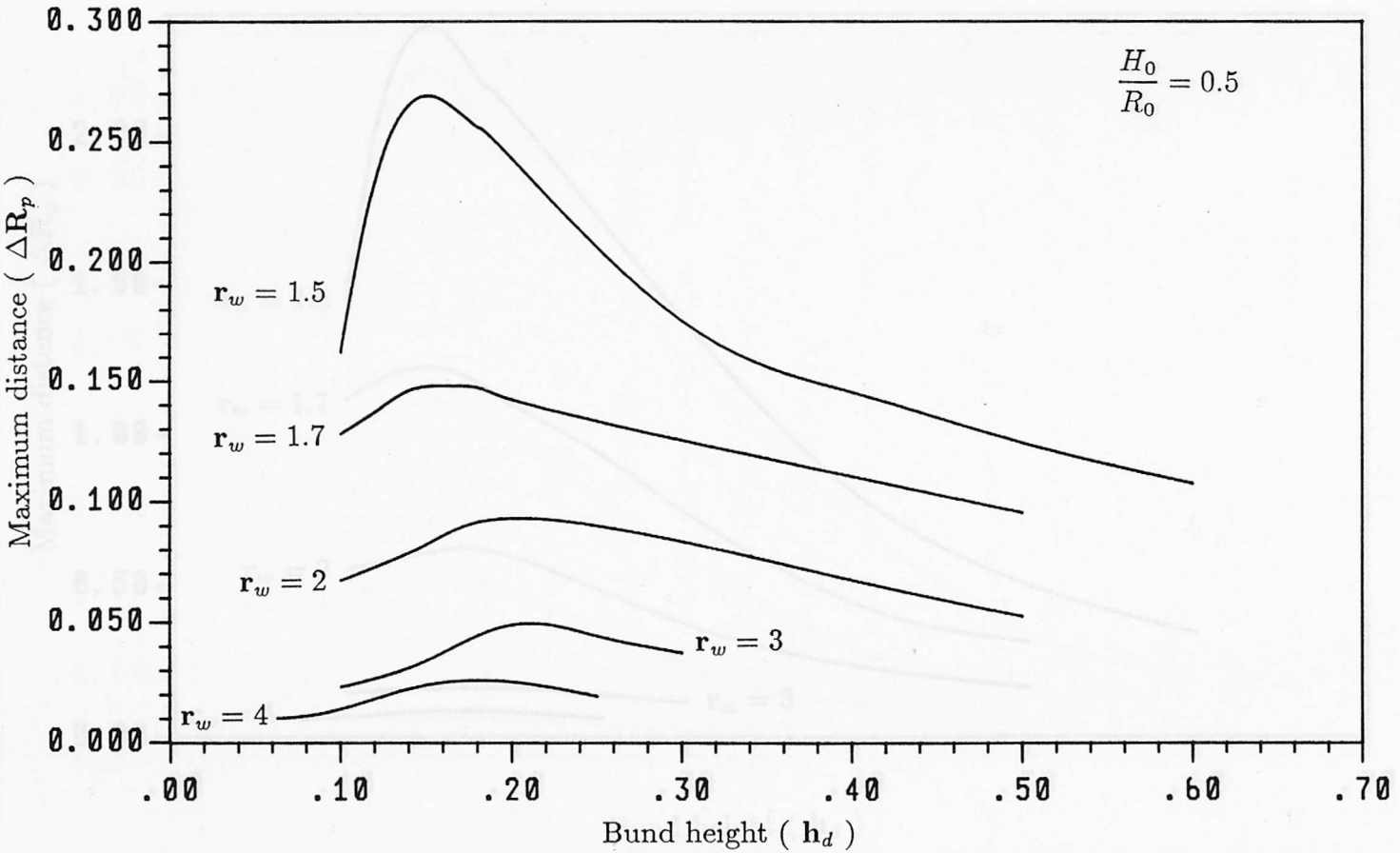


Figure C-6: Maximum jet projection distance for $(H_0/R_0) = 0.5$

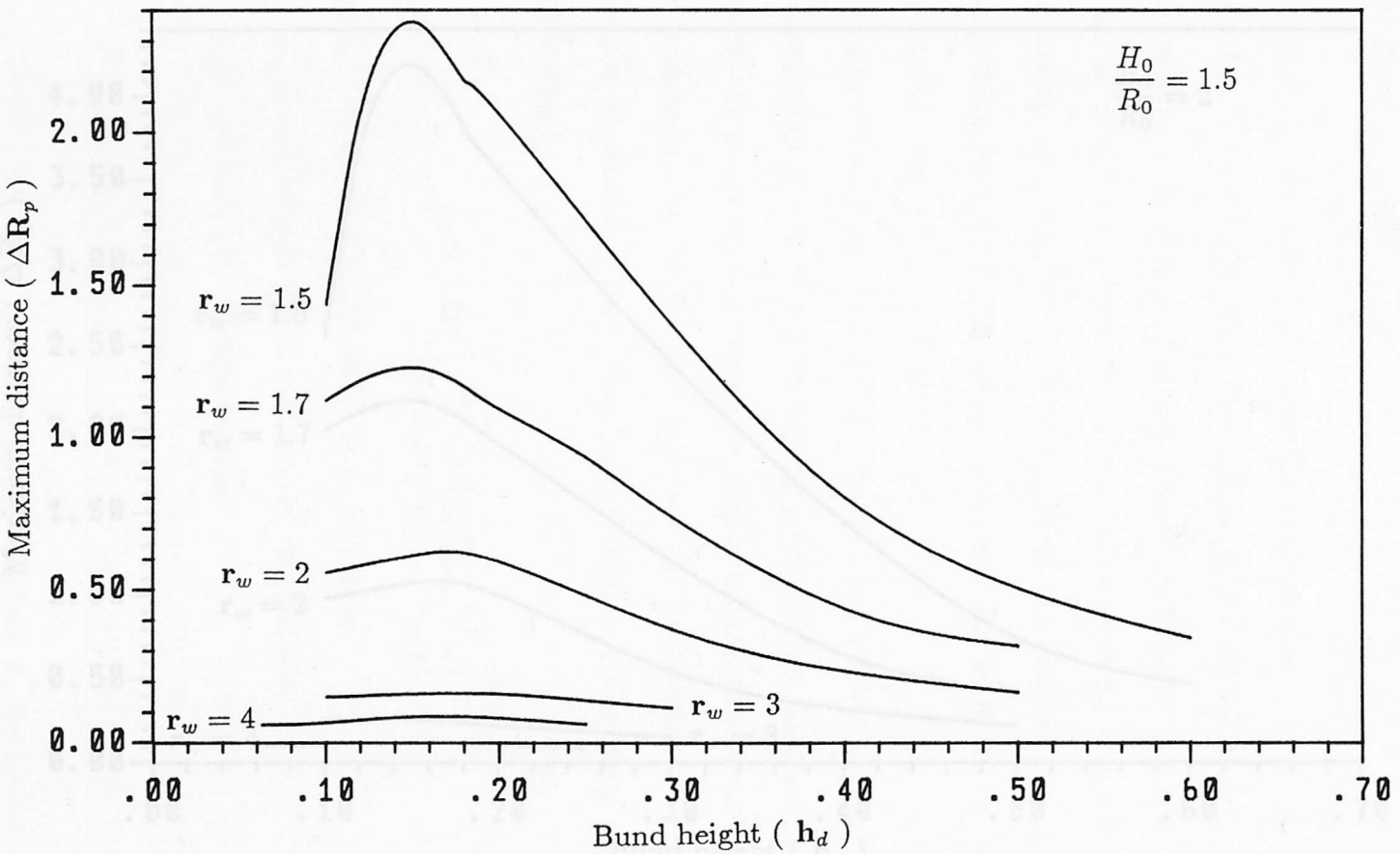


Figure C-7: Maximum jet projection distance for $(H_0/R_0) = 1.5$

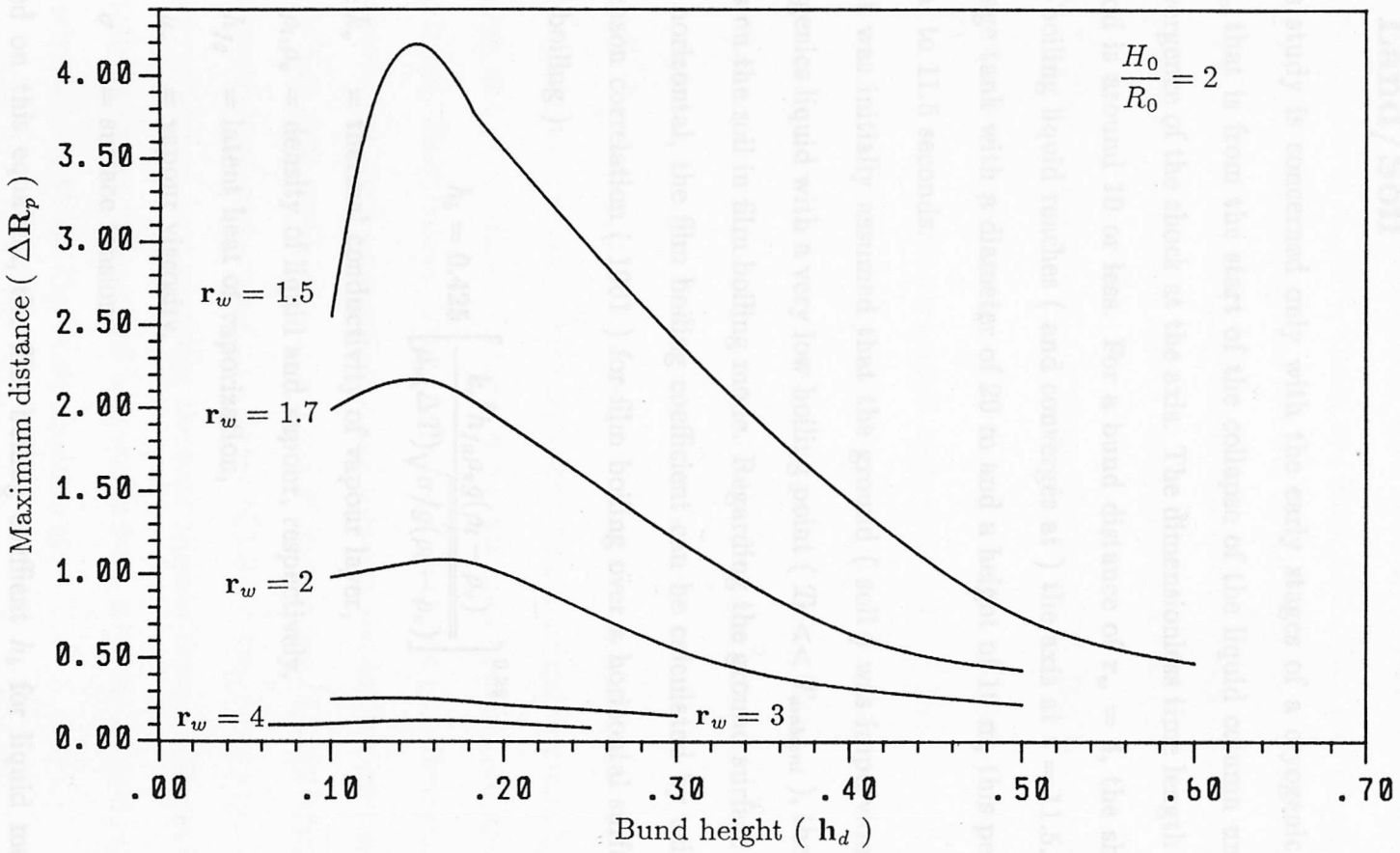


Figure C-8: Maximum jet projection distance for $(H_0/R_0) = 2$

APPENDIX D

D.1 Boiling Rate of Cryogenic Liquid Spills on Land/Soil

This study is concerned only with the early stages of a cryogenic liquid spill, that is from the start of the collapse of the liquid column until the convergence of the shock at the axis. The dimensionless time length of this period is around 10 or less. For a bund distance of $\mathbf{r}_w = 4$, the shock of non-boiling liquid reaches (and converges at) the axis at $\mathbf{t} = 11.5$. For a storage tank with a diameter of 20 m and a height of 10 m, this period is equal to 11.5 seconds.

It was initially assumed that the ground (soil) was impervious. For cryogenics liquid with a very low boiling point ($T_b << T_{ambient}$), the liquid boils on the soil in film boiling mode. Regarding the ground surface as flat and horizontal, the film boiling coefficient can be calculated by using the Berenson correlation (1961) for film boiling over a horizontal surface(in pool boiling):

$$h_b = 0.425 \left[\frac{{k_v}^3 h_{fg} \rho_v g(\rho_l - \rho_v)}{\mu_v (\Delta T) \sqrt{\sigma / g(\rho_l - \rho_v)}} \right]^{0.25}$$

with k_v = thermal conductivity of vapour layer,

ρ_l,ρ_v = density of liquid and vapour, respectively,

h_{fg} = latent heat of vaporization,

μ_v = vapour viscosity,

σ = surface tension.

Based on this equation, the film boiling coeffient h_b for liquid methane is 0.14 kW/m^2 °C. If the ground surface temperature is assumed to be

constant along the early stage of spill (the early period), the heat flux from the ground will be around 26 kW/m^2, or the boiling rate of methane on soil is around 0.05 kg/m^{2}s. This estimate is much lower than the actual boiling rate of methane evaluated experimentally. Research on LNG spills on land (Drake et al. ,1974; Drake and Reid, 1975; Reid and Wang, 1978) has shown that the boiling rate of LNG at the early stage of spill is in the order of 1 kg/m^{2}s. Hence, using simple film boiling theory is not satisfactory to approximate the boiling rate of cryogenic liquid spills on land.

D.1.1 The Nature of Cryogenic Liquid Boiling on Soil

Numerous experiments on crygenic liquid spills on land have been carried out. Most of them are concerned with LNG spills (Drake et al. ,1974; Drake and Reid, 1975; Reid and Wang, 1978). It is observed that the spills proceed with vigorous boiling and a high boiling rate at the early period, after which the boiling rate gradually decreases. The initial period at which vigorous boiling occurs lasts from 10 seconds to one minute. Reseachers agree that the high boiling rate at this initial period is caused by soil cracking and percolation, which is observed in the experiments. The soil cracking and percolation enhance the contact area between soil and cryogenic liquid. Furthermore, Drake and Reid have shown that their sample of compacted soil, used to investigate and measure the boiling rate of LNG, was riddled with small holes at the end of observation. Liquid apparently percolates/penetrates the soil to a depth of 1.2–1.8 cm.

All researchers have modelled the heat transfer from the ground as an unsteady quasi one-dimensional heat conduction, with the ground regarded as a semi infinite solid. The basic equation is :

$$\frac{\partial^2 T}{\partial z^2} = \frac{1}{\alpha}\frac{\partial T}{\partial t} \tag{D.1}$$

with z being the depth of soil (from the ground surface). They generally considered that the ground surface temperature changes rapidly to become equal to the crygenic liquid boiling temperature, as the spill occurs. By using this model, the heat flux from the ground surface is given by :

$$q_s = \left(\frac{\rho k c_p}{\pi}\right)^{\frac{1}{2}} \frac{\Delta T}{t^{0.5}} \tag{D.2}$$

or the boiling rate can be expressed by using :

$$m = \frac{q_s}{h_{fg}} = F t^{-0.5} \tag{D.3}$$

with $F = \left(\frac{\rho k c_p}{\pi}\right)^{\frac{1}{2}} \frac{\Delta T}{h_{fg}}$.

Drake et al. considered the effects of film boiling and ice formation (from the moisture in the soil). Drake and Reid evaluated the constant F in equation (D.3) from the experimental results. They showed that the value of F determined experimentally is two to three times that calculated from the data of soil from reference (Carslaw and Jaeger, 1959). Researchers pointed out that the moisture content increases the effective thermal conductivity of soil, and the heat released by the freezing process may also contribute to the high value of F. Briefly, F depends on the nature of soil. For engineering purposes, Reid and Wang have suggested that F is about 0.4 - 0.6 kg/m^{2}s$^{0.5}$.

The boiling rate prediction from equation (D.3) implicitly ignored the early stage of spill (i.e. vigorous boiling), because this period is short compared with the whole time of span of interest of the investigation, which is of the order of several minutes. If equation (D.3) is used to estimate the boiling rate m at $t = 0$, m is infinite. On the other hand, at time $t = 10$ seconds, with $F = 0.5$ kg/m^{2}s$^{0.5}$, m is 0.16 kg/m^{2}s. Shaw and Briscoe (1978) predict the LNG boiling rate at 1 second after spill to be 0.7 kg/m^{2}s.

D.1.2 Boiling in a Porous Bed

Many researchers have been investigating the phenomenon of boiling in a porous bed/layer. Here, Dhir and Catton's work (1982) is considered to be most relevant to this study. Their experiment aims to simulate cooling of a bed of fuel debris resulting from a nuclear reactor accident. Because the debris generates heat, it must be cooled.

Dhir and Catton investigated the effects of particle size and the depth of a bed (shallow and deep). In their experiment, heat is generated in a bed of metal particles by using a inductive microwave generator. Boiling occurs in the bed, where liquid flows down through the capillary conduites of the porous bed and the vapour produced flows up countercurrently. Dhir and Catton suggested that this countercurrent flow through the porous bed controls the boiling rate, rather than heat transfer. When the vapour production is high enough, liquid cannot reach the lower part of the bed. This condition is defined as dryout, which is analogous to a maximum critical condition in pool boiling. Dhir and Catton observed that in dryout condition, the vapour produced in a small particle bed (particle diameter $d_p < 1$ mm) flows through channels. These channels are free from particles. Furthermore, the particles in the top layer fluidize. In a deep bed (bed depth/particle diameter ratio much greater than 10), the vapour channels extend only part-way towards the bottom of the bed, while in a shallow bed, the channels are well formed throughout the depth of the bed. This is illustrated in Figure D-1. Dhir and Catton gave a correlation for the dryout heat flux in a deep bed of small particles:

$$\frac{q_{do}}{q_c} = C_1 K d^2 \Gamma^{0.5} M \tag{D.4}$$

with q_{do} = dryout heat flux (per cross sectional area),

q_c = Zuber's correlation for critical heat flux in boiling,

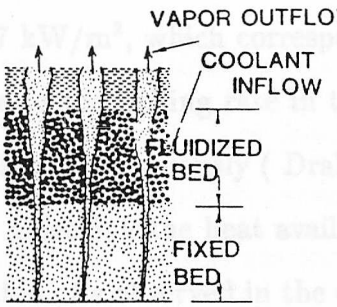


Figure D-1: Boiling phenomenon in a small particle bed (Dhir and Catton, 1982)

C_1 = dimensionless constant (determined experimentally), equal to 7.5×10^{-4},

$$K = \frac{\epsilon^3}{(1-\epsilon)^2}$$

$$d = \frac{d_p}{(\sigma/[g(\rho_l - \rho_v)])^{0.5}}$$

$$\Gamma = \rho_l/\rho_v$$

$$M = \left[\frac{{\rho_l}^4 \sigma^3}{{\mu_l}^4 g(\rho_l - \rho_v)^3}\right]^{0.25}$$

where d_p is the average particle diameter and ϵ is the void fraction of the porous bed. The Zuber critical heat flux q_c is given by (Zuber, 1958):

$$q_c = \frac{\pi}{24}\sqrt{\rho_v} h_{fg}[\sigma g(\rho_l - \rho_v)]^{0.25} \quad .$$

Based on the Dhir and Catton's description, boiling of cryogenic liquid spills on soil is considered as a boiling phenomenon in a deep bed of small particles, where the soil bed is a source of heat, and cryogenic liquid penetrates into the soil (percolation). As described earlier, the soil is riddled with small holes, which proves that the vapour produced forms channels in the soil bed, and the boiling rate is high in the early stages of a spill. All these aspects confirm that dryout occurs in the early stages of cryogenic liquid spills on soil.

For LNG (represented by methane), with a soil particle diameter d_p

of 1 mm and void fraction ϵ of 0.47, the dryout heat flux calculated from equation (D.4) is 277 kW/m^2, which corresponds to a boiling rate of 0.54 kg/m^{2}s. This is close to the boiling rate in the early stages of LNG spills of the experiment described previously (Drake and Reid, Reid and Wang, Shaw and Briscoe). Checking the heat available in the top soil layer also supports this prediction. As observed in the experiment, the top soil layer thickness (the depth of liquid penetration) is about 0.5 inch (1.25 cm). The bulk density and heat capacity of the soil are 2500 kg/m^3 and 0.836 kJ/kg°C, respectively. If the soil layer is to be cooled until its temperature equals to the LNG boiling temperature (-161°C), the available heat is :

$$\begin{aligned} Q &= (0.0125\,\mathrm{m^3/m^2})(2500\,\mathrm{kg/m^3})(0.836\,\mathrm{kJ/kg°C})(161+25)°\mathrm{C} \\ &= 4859\ \mathrm{kJ/m^2} \quad . \end{aligned}$$

This amount of heat is enough to supply heat of boiling in dryout condition along the early period of spill (around 10 seconds). Furthermore, as the temperature of the top soil layer approaches the LNG temperature, heat will be supplied by soil beneath the top layer.

In conclusion, this study employs Dhir and Catton's dryout correlation (equation (D.4)) to estimate the boiling rate at the early stages of cryogenic liquid spills on land. This also implies that the boiling rate is constant during this phase, as is justified, since the available heat is enough to supply the heat of boiling in dryout condition. The other liquified energy gas which is commonly stored in a large atmospheric tank is LPG. In general, propane is the main component. With its boiling temperature of $-42°$C, the available heat in the top soil layer is 1750 kJ/m^2. The dryout heat flux q_{do} is 230 kW/m^2, corresponding to a boiling rate of 0.54 kg/m^{2}s. Although this rate is lower than that of LNG, it still can be assumed that the boiling rate is constant along the early period of spill, especially since the heat is also supplied from the deep part of the soil.

D.2 Stratified Flow Model

Derivation of the governing equations for the stratified flow model is equivalent to those for non-boiling liquid flow described in Chapter 1. Equations of continuity and of motion are applied to each phase/layer. Essential symbols used in the stratified flow model are shown in Figure D-2.

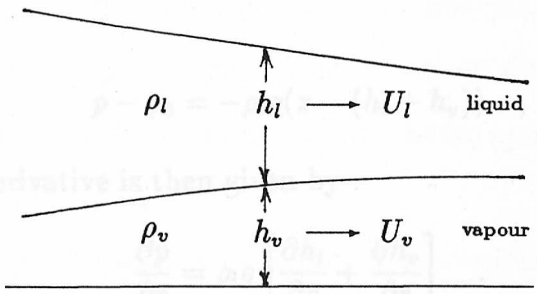


Figure D-2: The stratified flow model

Upper-layer: liquid.

The equation of continuity is integrated along the height of liquid layer h_l :

$$\begin{aligned} \frac{1}{r}\frac{\partial rU}{\partial r} + \frac{\partial v}{\partial z} &= 0 \\ \int_{h_v}^{h_l+h_v} \frac{1}{r}\frac{\partial rU}{\partial r}\, dz + \int_{h_v}^{h_l+h_v} dv &= 0 \\ \frac{h_l}{r}\frac{\partial rU_l}{\partial r} + v|_{h_l+h_v} - v|_{h_v} &= 0 \end{aligned}$$

For this preliminary investigation, the vaporization at the top surface (i.e. liquid-air) is neglected. As described in Chapter 1, the boundary condition at the top surface is $v|_{h_l+h_v} = \dfrac{Dh_l}{Dt}$. As there is a vaporization at the liquid-vapour interface, the boundary condition at this interface is $v|_{h_v} = \dfrac{m}{\rho_l}$, where m is the rate of mass vaporization (per unit area). The above

equation becomes :

$$\frac{Dh_l}{Dt} + h_l \frac{\partial U_l}{\partial r} + \frac{h_l U_l}{r} = -\frac{m}{\rho_l} \tag{D.5}$$

Derivation from equations of motion is given by :

- z component :

$$\rho_l \frac{Dv}{Dt} = -\frac{\partial p}{\partial z} - \rho_l g \quad .$$

Vertical acceleration is neglected ($\frac{Dv}{Dt} << |g|$). Integration along z results in :

$$p - p_0 = -\rho_l g(z - (h_l + h_v)) \quad ,$$

and the r derivative is then given by :

$$\frac{\partial p}{\partial r} = \rho_l g \left[\frac{\partial h_l}{\partial r} + \frac{\partial h_v}{\partial r} \right] \quad .$$

- r component :

$$\rho_l \frac{DU_l}{Dt} = -\frac{\partial p}{\partial r}$$

Substitution of $\frac{\partial p}{\partial r}$ from the above equation results in :

$$\frac{DU_l}{Dt} + g \left[\frac{\partial h_l}{\partial r} + \frac{\partial h_v}{\partial r} \right] = 0 \tag{D.6}$$

Equations (D.5) and (D.6) are the governing equations of upper-layer.

Lower-layer: vapour.

The method of derivation is the same as that for upper-layer. The governing equations of lower-layer or vapour layer are given by :

$$\frac{Dh_v}{Dt} + h_v \frac{\partial U_v}{\partial r} + \frac{h_v U_v}{r} = +\frac{m}{\rho_v} \tag{D.7}$$

$$\frac{DU_v}{Dt} + g \left[\frac{\rho_l}{\rho_v} \frac{\partial h_l}{\partial r} + \frac{\partial h_v}{\partial r} \right] = 0 \tag{D.8}$$

These two sets of governing equations (equations (D.5) to (D.8)) are solved by using the Method of Characteristics (see Abbott, 1966). By

substitution of $C_l = \sqrt{gh_l}$ and $C_v = \sqrt{gh_v}$ into the governing equations, four slopes of characteristic lines are given by :

$$\left[\left(U_l - \frac{dr}{dt}\right)^2 - {C_l}^2\right]\left[\left(U_v - \frac{dr}{dt}\right)^2 - {C_v}^2\right] - \frac{\rho_l}{\rho_v}{C_l}^2{C_v}^2 = 0$$

The solution of this equation depends on $\frac{\rho_l}{\rho_v}$. Because $\frac{\rho_l}{\rho_v}$ is clearly greater than 1, some slopes of the characteristic lines are imaginair (see Abbott and Torbe, 1963). This means that the governing equations, which are of hyperbolic partial differential equations, are unsolvable. Such imaginair characteristic lines is typical of the behaviour of an elliptic partial differential equation, where a discontinuity at the initial/boundary condition is not propagated.

The governing equations can be solved, if the vapour-layer thickness is much smaller than the liquid-layer height ($h_v << h_l$). Equations (D.5) to (D.8) are then modified into :

- Upper-layer (liquid) :

$$\frac{Dh_l}{Dt} + h_l\frac{\partial U_l}{\partial r} + \frac{h_l U_l}{r} = -\frac{m}{\rho_l} \qquad \text{(D.9)}$$

$$\frac{DU_l}{Dt} + g\frac{\partial h_l}{\partial r} = 0 \qquad \text{(D.10)}$$

- Lower-layer (vapour) :

$$\frac{Dh_v}{Dt} + h_v\frac{\partial U_v}{\partial r} + \frac{h_v U_v}{r} = +\frac{m}{\rho_v} \qquad \text{(D.11)}$$

$$\frac{DU_v}{Dt} + g\frac{\rho_l}{\rho_v}\frac{\partial h_l}{\partial r} = 0 \qquad \text{(D.12)}$$

It is clear that equations (D.9) and (D.10) can be solved independently from equations (D.11) and (D.12). For a preliminary investigation, equations (D.9) to (D.12) are solved to describe the nature of the flow of liquid methane resulting from a CTF. The radii of of the tanks or columns to be investigated are 10 m and 10 cm, with the initial liquid height equal to the

column radius. The rate of methane vaporization is taken to be constant, $m = 0.5\,\mathrm{kg/m^2s}$. An example of the results is shown in Table D-1 and Figure D-3. The results show that the velocity of both liquid and vapour layers as well as the height of liquid-layer are not effectively influenced by the size of the column, as represented in Figure D-3 and Table D-1. On the other hand, the vapour-layer thickness depends on the size of the column, as shown in Table D-1.

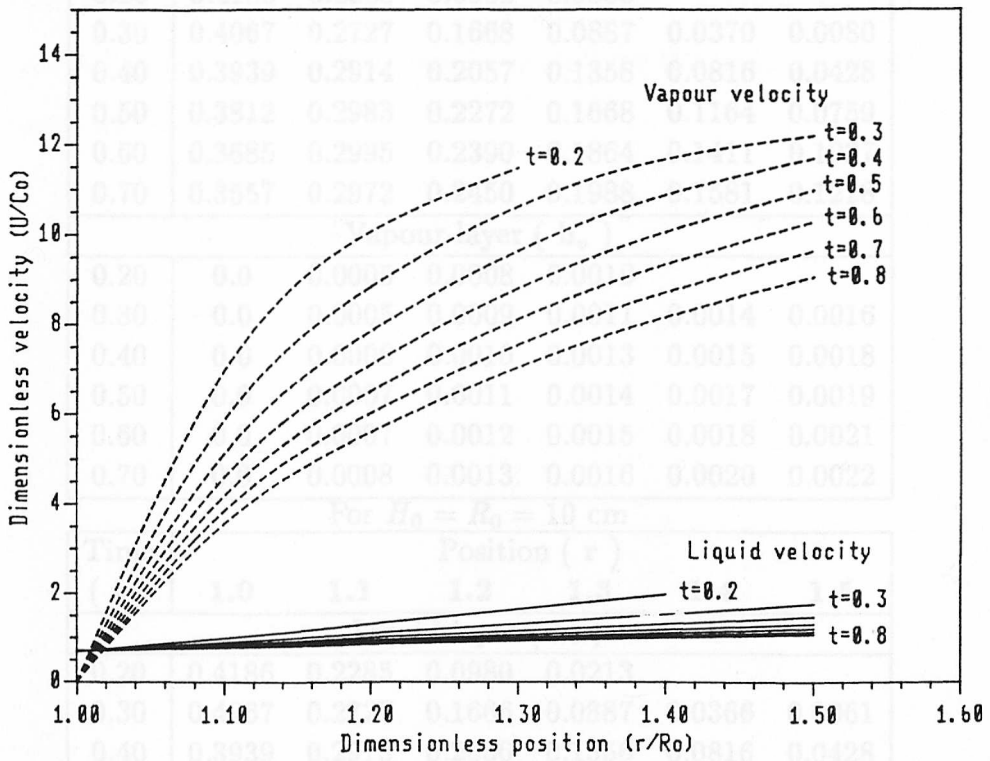


Figure D-3: Velocity of liquid and vapour layers at several dimensionless times

Table D-1: The thickness of liquid and vapour layers

For $H_0 = R_0 = 10$ m

Time	Position (r)					
(t)	**1.0**	**1.1**	**1.2**	**1.3**	**1.4**	**1.5**
Liquid-layer (h_l)						
0.20	0.4185	0.2285	0.0982	0.0230		
0.30	0.4067	0.2727	0.1668	0.0887	0.0370	0.0080
0.40	0.3939	0.2914	0.2057	0.1358	0.0816	0.0428
0.50	0.3812	0.2983	0.2272	0.1668	0.1164	0.0759
0.60	0.3685	0.2995	0.2390	0.1864	0.1411	0.1027
0.70	0.3557	0.2972	0.2450	0.1988	0.1581	0.1228
Vapour-layer (h_v)						
0.20	0.0	0.0005	0.0008	0.0010		
0.30	0.0	0.0005	0.0009	0.0011	0.0014	0.0016
0.40	0.0	0.0006	0.0010	0.0013	0.0015	0.0018
0.50	0.0	0.0007	0.0011	0.0014	0.0017	0.0019
0.60	0.0	0.0007	0.0012	0.0015	0.0018	0.0021
0.70	0.0	0.0008	0.0013	0.0016	0.0020	0.0022

For $H_0 = R_0 = 10$ cm

Time	Position (r)					
(t)	**1.0**	**1.1**	**1.2**	**1.3**	**1.4**	**1.5**
Liquid-layer (h_l)						
0.20	0.4186	0.2285	0.0980	0.0213		
0.30	0.4067	0.2727	0.1666	0.0887	0.0366	0.0061
0.40	0.3939	0.2913	0.2056	0.1356	0.0816	0.0428
0.50	0.3812	0.2982	0.2270	0.1666	0.1161	0.0756
0.60	0.3685	0.2994	0.2388	0.1861	0.1409	0.1024
0.70	0.3557	0.2970	0.2448	0.1985	0.1578	0.1224
Vapour-layer (h_v)						
0.20	0.0	0.0046	0.0075	0.0100		
0.30	0.0	0.0054	0.0087	0.0113	0.0137	0.0171
0.40	0.0	0.0061	0.0098	0.0127	0.0152	0.0175
0.50	0.0	0.0067	0.0108	0.0139	0.0167	0.0192
0.60	0.0	0.0073	0.0117	0.0152	0.0181	0.0208
0.70	0.0	0.0078	0.0126	0.0163	0.0195	0.0223

D.3 Additional Results

The description of flow resulting from CTF of LNG container with a height of 0.1 m, 1 m and 10 m are presented in this appendix. For $(H_0/R_0) = 1$, these correspond to the values of G_k of 0.3, 0.096 and 0.03, respectively. Although the results presented in Chapter 3 is based on the vapour void fraction $\epsilon_v = 0.7$ (in the two-phase layer), other values of vapour void fraction (0.5 and 0.7) are also used in the calculation, which are presented in this Appendix. This results may be usefull for the next investigation or future work.

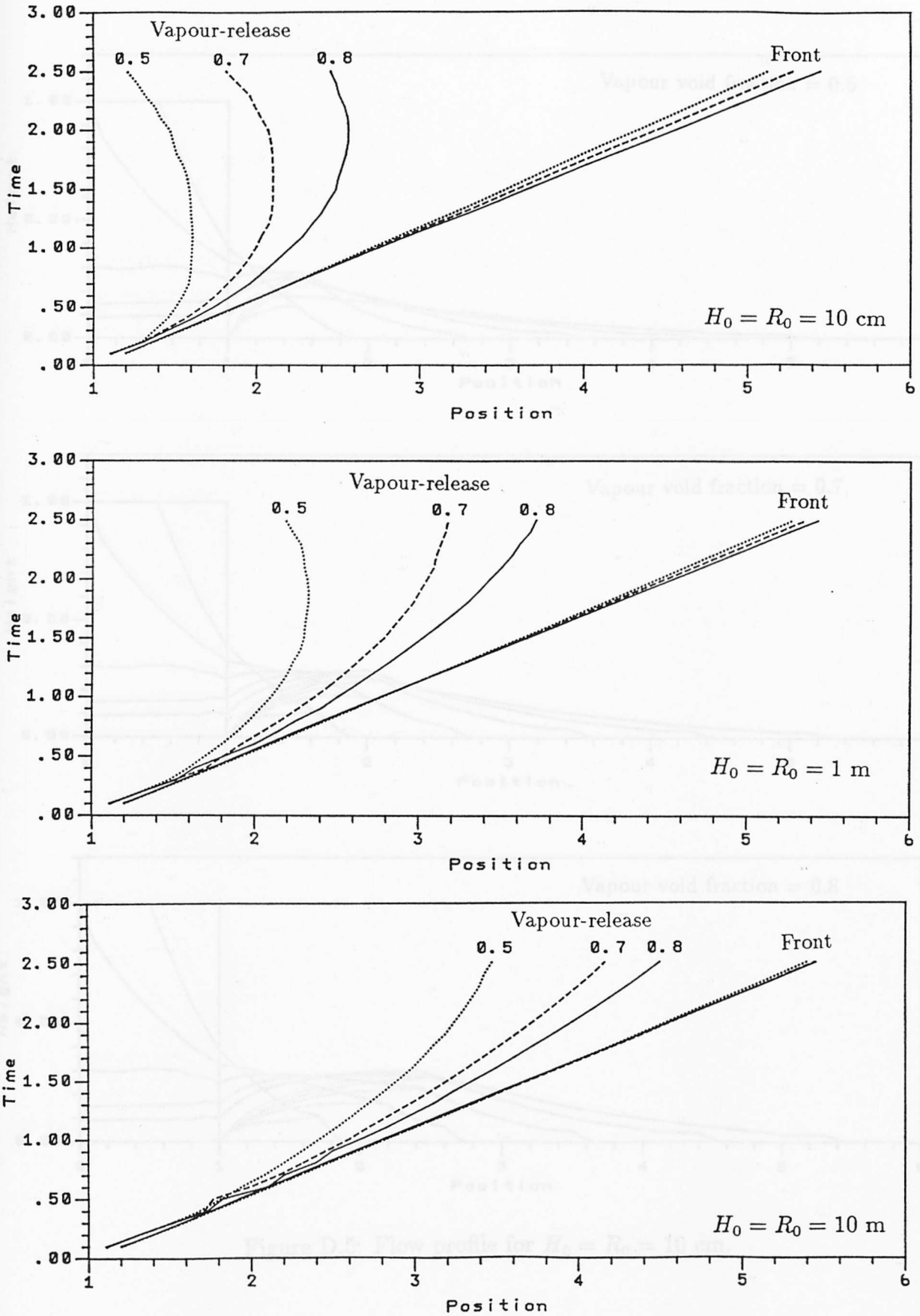


Figure D.4: Vapour-release and front positions

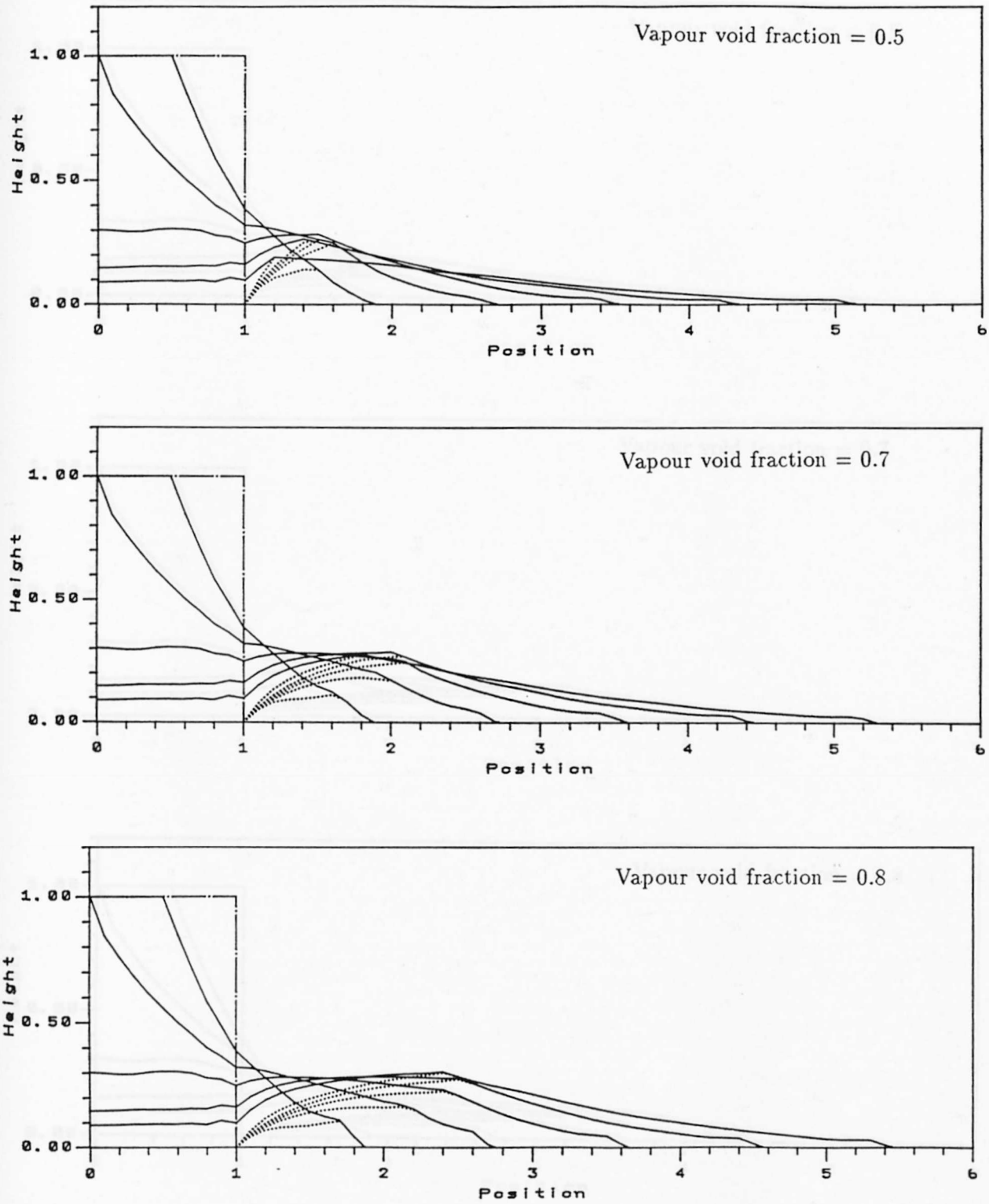


Figure D.5: Flow profile for $H_0 = R_0 = 10$ cm.

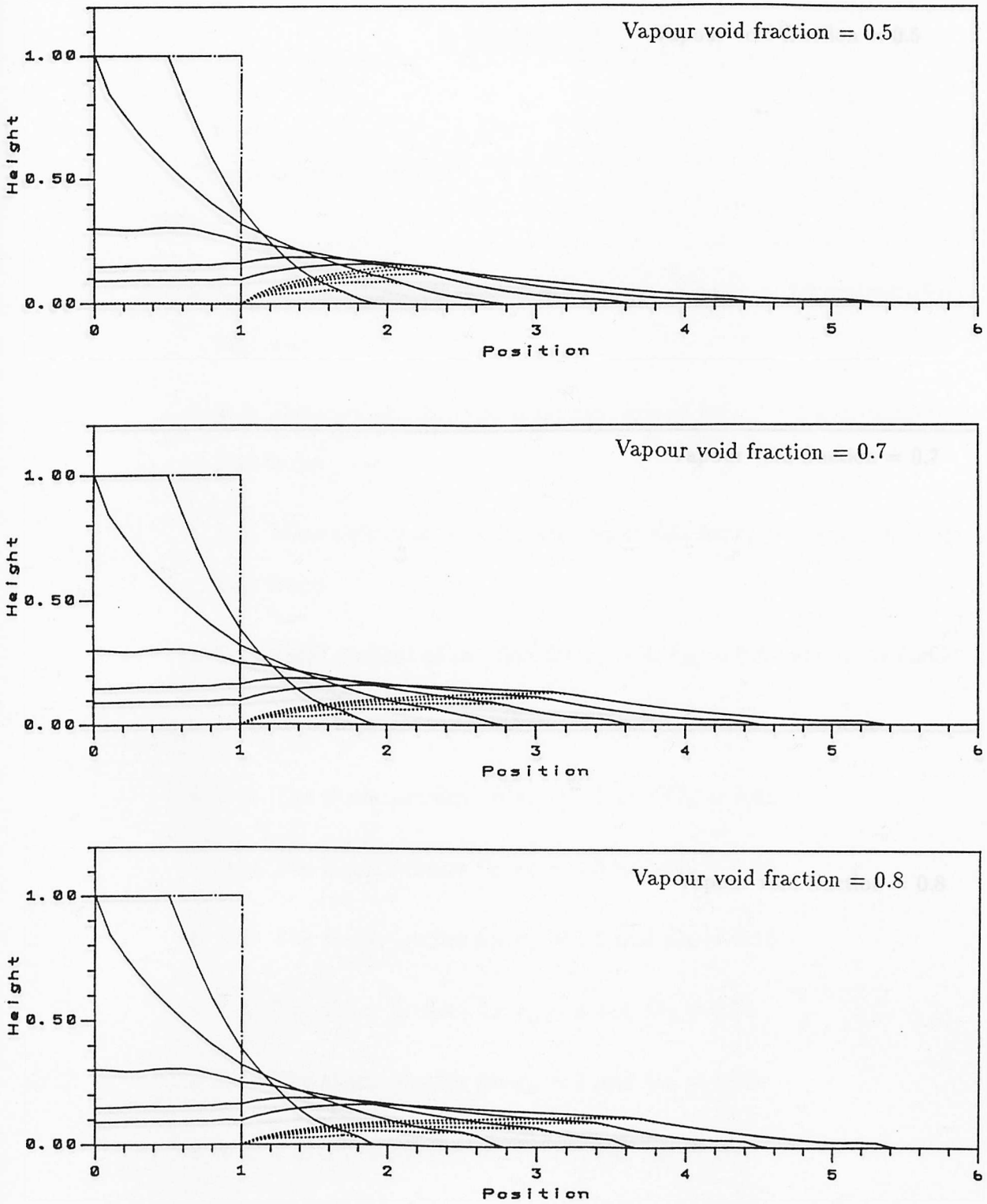


Figure D.6: Flow profile for $H_0 = R_0 = 1$ m.

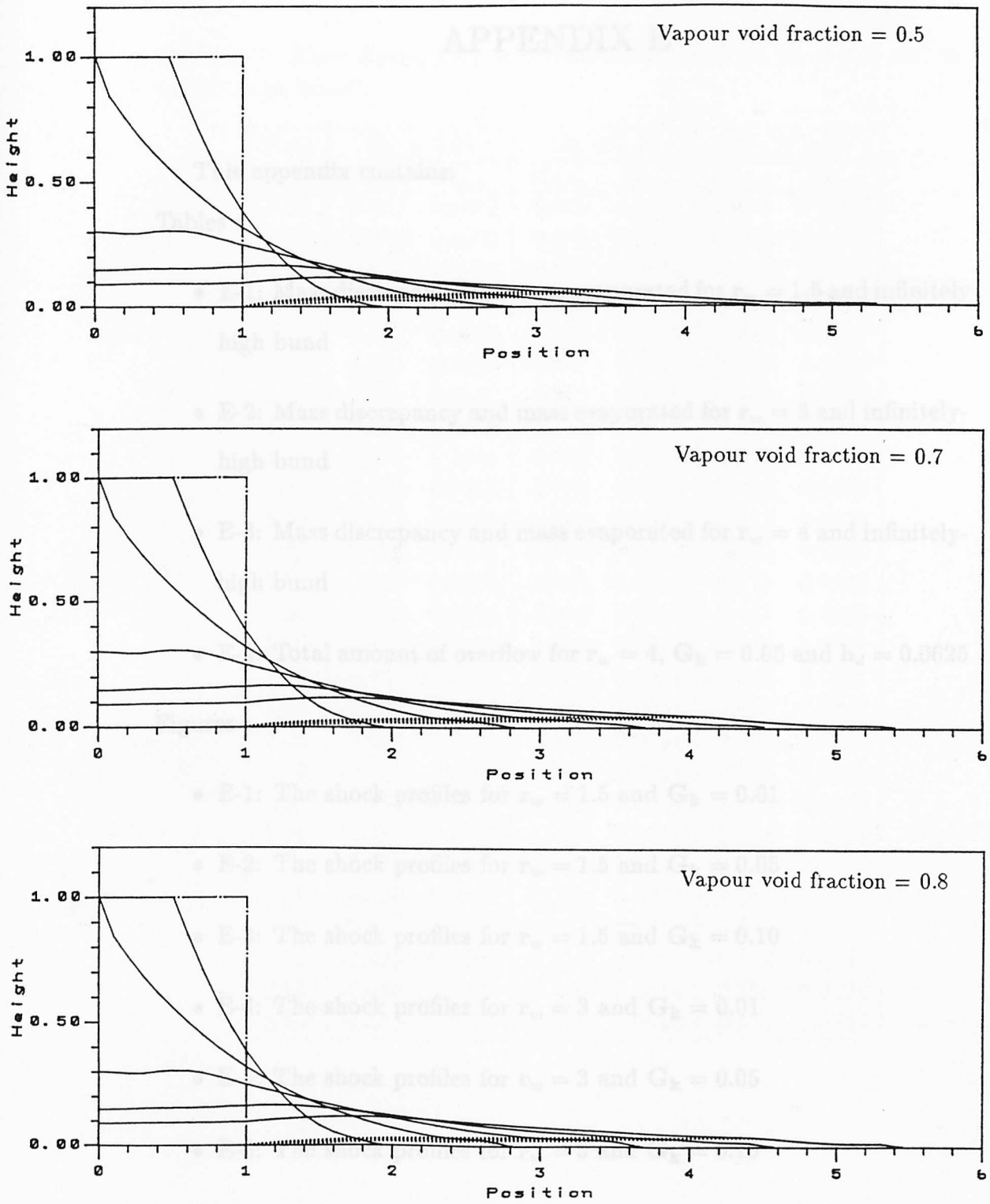


Figure D.7: Flow profile for $H_0 = R_0 = 10$ m.

APPENDIX E

This appendix contains:

Tables :

- E-1: Mass discrepancy and mass evaporated for $\mathbf{r}_w = 1.5$ and infinitely-high bund
- E-2: Mass discrepancy and mass evaporated for $\mathbf{r}_w = 3$ and infinitely-high bund
- E-3: Mass discrepancy and mass evaporated for $\mathbf{r}_w = 4$ and infinitely-high bund
- E-4: Total amount of overflow for $\mathbf{r}_w = 4$, $\mathbf{G_k} = 0.05$ and $\mathbf{h}_d = 0.0625$

Figures :

- E-1: The shock profiles for $\mathbf{r}_w = 1.5$ and $\mathbf{G_k} = 0.01$
- E-2: The shock profiles for $\mathbf{r}_w = 1.5$ and $\mathbf{G_k} = 0.05$
- E-3: The shock profiles for $\mathbf{r}_w = 1.5$ and $\mathbf{G_k} = 0.10$
- E-4: The shock profiles for $\mathbf{r}_w = 3$ and $\mathbf{G_k} = 0.01$
- E-5: The shock profiles for $\mathbf{r}_w = 3$ and $\mathbf{G_k} = 0.05$
- E-6: The shock profiles for $\mathbf{r}_w = 3$ and $\mathbf{G_k} = 0.10$
- E-7: The shock profiles for $\mathbf{r}_w = 4$ and $\mathbf{G_k} = 0.01$
- E-8: The shock profiles for $\mathbf{r}_w = 4$ and $\mathbf{G_k} = 0.05$
- E-9: The shock profiles for $\mathbf{r}_w = 4$ and $\mathbf{G_k} = 0.10$

Table E-1: Mass discrepancy and mass evaporated for $\mathbf{r}_w = 1.5$ and infinitely-high bund

Time	$\mathbf{G_k} = 0.01$		$\mathbf{G_k} = 0.05$		$\mathbf{G_k} = 0.10$	
(t)	M_{discr}	M_{evap}	M_{discr}	M_{evap}	M_{discr}	M_{evap}
0.30	-0.117	0.0003	-0.023	0.0010	0.028	0.0037
0.40	-0.223	0.0003	-0.034	0.0010	-0.040	0.0037
0.50	-0.313	0.0003	-0.032	0.0010	-0.209	0.0038
0.60	-0.369	0.0003	0.025	0.0010	-0.401	0.0038
0.70	-0.447	0.0003	0.081	0.0010	-0.617	0.0038
0.80	-0.551	0.0003	-0.455	0.0010	0.262	0.0038
0.90	-0.721	0.0003	-0.331	0.0010	-0.085	0.0038
1.00	-0.695	0.0003	-0.145	0.0010	-0.479	0.0039
1.10	-0.576	0.0003	-0.329	0.0010	-0.056	0.0039
1.20	-0.564	0.0003	-0.075	0.0011	-0.488	0.0039
1.30	-0.497	0.0003	0.117	0.0011	-0.817	0.0039
1.40	-0.524	0.0003	-0.058	0.0011	-0.465	0.0040
1.50	-0.489	0.0003	0.068	0.0011	-0.671	0.0040
1.60	-0.522	0.0003	-0.056	0.0011	-0.447	0.0041
1.70	-0.498	0.0003	0.015	0.0011	-0.542	0.0041
1.80	-0.495	0.0003	0.011	0.0011	-0.548	0.0041
1.90	-0.482	0.0003	0.058	0.0011	-0.630	0.0042
2.00	-0.465	0.0003	0.089	0.0011	-0.695	0.0043
2.10	-0.457	0.0003	0.091	0.0011	-0.674	0.0045
2.20	-0.448	0.0003	0.082	0.0011	-0.649	0.0047
2.30	-0.437	0.0003	0.126	0.0011	-0.704	0.0057
2.40	-0.433	0.0003	0.106	0.0011	-0.633	0.0073
2.50	-0.430	0.0003	0.083	0.0011	-0.662	0.0089
2.60	-0.435	0.0003	-0.031	0.0011	-0.457	0.0110
2.70	-0.439	0.0003	-0.113	0.0011	-0.163	0.0140
2.80	-0.449	0.0003	-0.209	0.0011	-0.759	0.0180
2.90	-0.453	0.0003	-0.277	0.0012	-0.932	0.0243

Table E-2: Mass discrepancy and mass evaporated for $\mathbf{r}_w = 3$ and infinitely-high bund

Time	$\mathbf{G_k} = 0.01$		$\mathbf{G_k} = 0.05$		$\mathbf{G_k} = 0.10$	
(t)	M_{discr}	M_{evap}	M_{discr}	M_{evap}	M_{discr}	M_{evap}
1.30	-0.151	0.0022	-0.042	0.0256	-0.068	0.076
1.50	-0.108	0.0023	-0.080	0.0275	-0.132	0.093
1.70	-0.143	0.0023	-0.115	0.0285	-0.122	0.104
1.90	-0.224	0.0023	-0.148	0.0301	-0.166	0.109
2.10	-0.335	0.0023	-0.166	0.0325	-0.159	0.113
2.30	-0.482	0.0023	-0.108	0.0359	-0.119	0.120
2.50	-0.447	0.0023	-0.092	0.0403	-0.105	0.129
2.70	-0.363	0.0023	-0.108	0.0460	0.087	0.141
2.90	-0.359	0.0023	-0.157	0.0529	-0.195	0.154
3.10	-0.257	0.0023	-0.066	0.0611	0.022	0.171
3.30	-0.287	0.0023	-0.250	0.0709	-0.309	0.191
3.50	-0.131	0.0024	0.078	0.0823	-0.110	0.214
3.70	-0.133	0.0024	-0.058	0.0954	-0.122	0.259
3.90	-0.140	0.0024	-0.365	0.1100	-0.224	0.323
4.10	-0.145	0.0024	-0.296	0.1270	-0.105	0.392
4.30	-0.137	0.0024	-0.252	0.1460	0.000	0.465
4.50	-0.179	0.0024	-0.218	0.1670	-0.076	0.539
4.70	-0.193	0.0026	-0.171	0.1960	-0.135	0.614
4.90	-0.141	0.0029	-0.158	0.2290	-0.151	0.690
5.10	-0.100	0.0032	-0.174	0.2640	-0.087	0.765
5.30	-0.072	0.0038	-0.219	0.3000	0.029	0.841
5.50	0.003	0.0046	-0.275	0.3370	-0.358	0.917
5.70	0.085	0.0057	-0.163	0.3730	-0.203	0.993
5.90	-0.257	0.0074	0.053	0.4110	-0.201	1.070
6.10	-0.058	0.0147	-0.043	0.4490	-0.328	1.150
6.30	0.158	0.0219	-0.231	0.4870	-0.784	1.230
6.50	-0.137	0.0284	-0.173	0.5270	-0.982	1.310
6.70	-0.051	0.0355	-0.055	0.5710	-0.834	1.400
6.90	0.002	0.0435	-0.111	0.6160	-0.877	1.490
7.10	-0.030	0.0494	-0.061	0.6610	-0.888	1.580
7.30	-0.057	0.0579	-0.111	0.7060	-0.919	1.660

Table E-3: Mass discrepancy and mass evaporated for $\mathbf{r_w} = 4$ and infinitely-high bund

Time	$\mathbf{G_k} = 0.01$		$\mathbf{G_k} = 0.05$		$\mathbf{G_k} = 0.10$	
(t)	M_{discr}	M_{evap}	M_{discr}	M_{evap}	M_{discr}	M_{evap}
1.90	-0.087	0.0084	0.043	0.099	-0.052	0.273
2.30	-0.202	0.0087	-0.114	0.134	-0.464	0.408
2.70	-0.514	0.0094	-0.520	0.151	-0.927	0.535
3.10	-0.472	0.0108	-0.437	0.159	-1.060	0.666
3.50	-0.497	0.0267	-0.669	0.170	-1.652	0.827
3.90	-0.139	0.0587	-0.454	0.187	-1.796	1.080
4.30	0.066	0.0694	-0.472	0.213	-1.991	1.360
4.70	0.078	0.0754	-0.669	0.320	-2.192	1.650
4.90	0.159	0.0789	-0.659	0.388	-2.235	1.790
5.10	-0.116	0.0829	-0.760	0.458	-2.314	1.940
5.50	-0.166	0.0922	-0.822	0.601	-2.298	2.230
5.90	-0.198	0.1030	-0.905	0.745	-2.491	2.520
6.10	-0.193	0.1100	-0.963	0.818	-2.738	2.670
6.30	-0.177	0.1170	-1.003	0.891	-3.025	2.820
6.50	-0.273	0.1240	-1.033	0.964	-3.310	2.970
6.70	-0.265	0.1320	-0.922	1.040	-3.436	3.120
6.90	-0.253	0.1400	-0.938	1.110	-3.666	3.260
7.10	-0.237	0.1490	-0.962	1.180	-3.883	3.410
7.30	-0.220	0.1580	-1.007	1.260	-4.083	3.560
7.50	-0.191	0.1680	-1.109	1.330	-4.262	3.710
7.70	-0.169	0.1800	-1.236	1.400	-4.458	3.860
7.90	-0.152	0.1930	-1.380	1.480	-4.683	4.010
8.10	-0.137	0.2070	-1.522	1.550	-4.890	4.150
8.30	-0.126	0.2200	-1.640	1.630	-5.076	4.300
8.50	-0.121	0.2340	-1.746	1.700	-5.249	4.450
8.70	-0.120	0.2480	-1.871	1.770	-5.411	4.600
8.90	-0.127	0.2620	-1.996	1.850	-5.565	4.750
9.10	-0.139	0.2770	-2.092	1.920	-5.715	4.890
9.30	-0.157	0.2910	-2.163	2.000	-6.035	5.040
9.50	-0.181	0.3050	-2.216	2.070	-6.145	5.190
9.70	-0.217	0.3200	-2.265	2.140	-6.255	5.340
9.90	0.008	0.3340	-2.510	2.220	-6.335	5.490
10.10	-0.043	0.3490	-2.472	2.290	-6.599	5.600
10.30	-0.068	0.3640	-2.609	2.330	-6.702	5.610

Table E-4: Total amount of overflow for $\mathbf{r}_w = 4$, $\mathbf{G_k} = 0.05$ and $\mathbf{h}_d = 0.0625$

Time	M_{discr}	M_{ovl}	M_{evap}
3.30	-27.61	27.56	0.155
3.40	-30.30	30.27	0.155
3.50	-32.99	32.97	0.155
3.60	-35.66	35.65	0.155
3.70	-38.33	38.29	0.155
3.80	-40.92	40.83	0.155
3.90	-43.44	43.33	0.156
4.00	-45.93	45.79	0.158
4.10	-48.33	48.16	0.162
4.20	-50.65	50.44	0.168
4.30	-52.88	52.62	0.177
4.40	-55.09	54.69	0.194
4.50	-57.12	56.65	0.220
4.60	-59.03	58.50	0.251
4.70	-60.81	60.25	0.284
4.80	-62.48	61.89	0.318
4.90	-64.06	63.43	0.352
5.00	-65.54	64.88	0.387
5.10	-66.93	66.24	0.422
5.20	-68.24	67.52	0.457
5.30	-69.47	68.72	0.493
5.40	-70.64	69.85	0.529
5.50	-71.74	70.92	0.565
5.60	-72.78	71.93	0.601
5.70	-73.76	72.88	0.636
5.80	-74.68	73.78	0.672
5.90	-75.58	74.63	0.709
6.00	-76.42	75.44	0.745
6.20	-77.95	76.93	0.818
6.40	-79.33	78.28	0.891
6.50	-79.96	78.91	0.928
6.60	-80.56	79.51	0.964
6.80	-81.68	80.62	1.037
7.00	-82.71	81.64	1.110

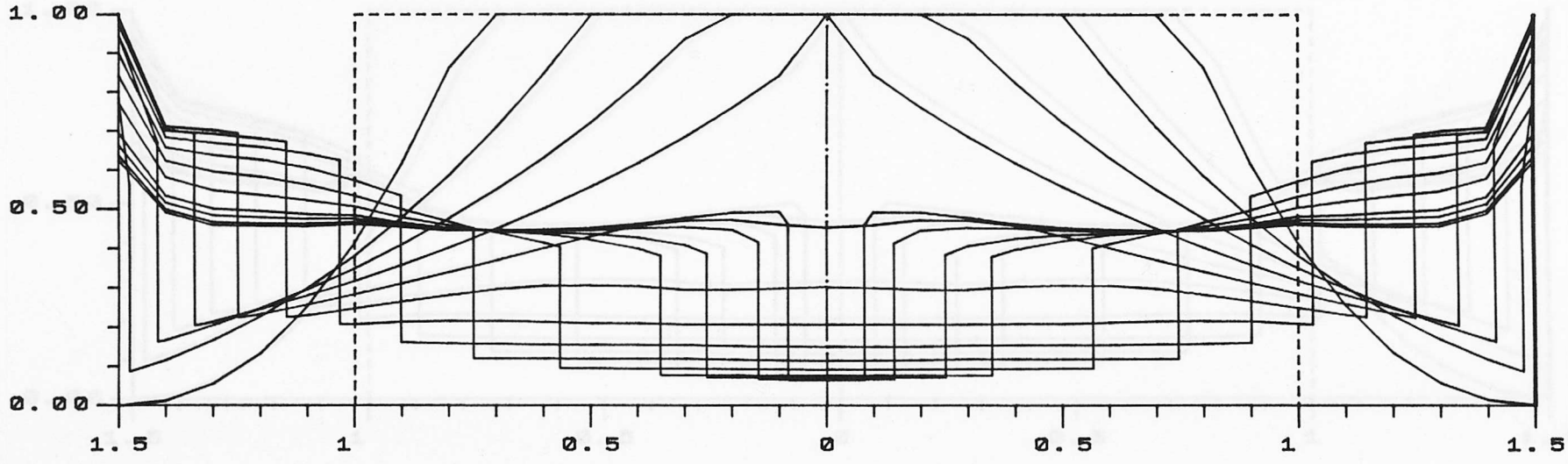


Figure E-1: The shock profiles for $\mathbf{r}_w = 1.5$ and $\mathbf{G_k} = 0.01$

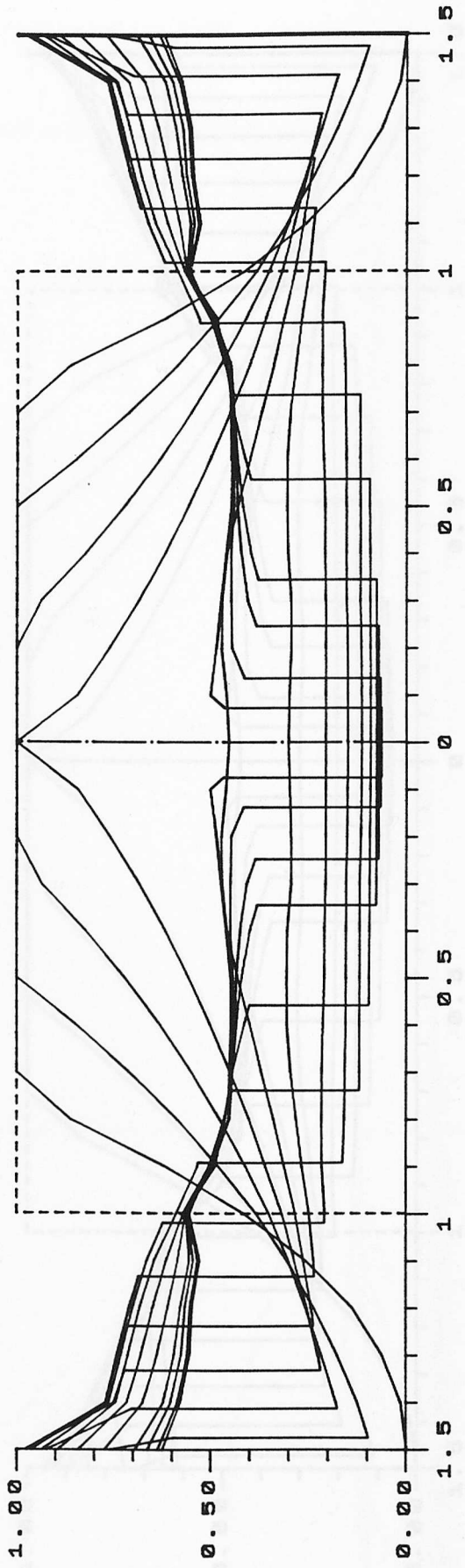


Figure E-2: The shock profiles for $\mathbf{r}_w = 1.5$ and $\mathbf{G}_\mathbf{k} = 0.05$

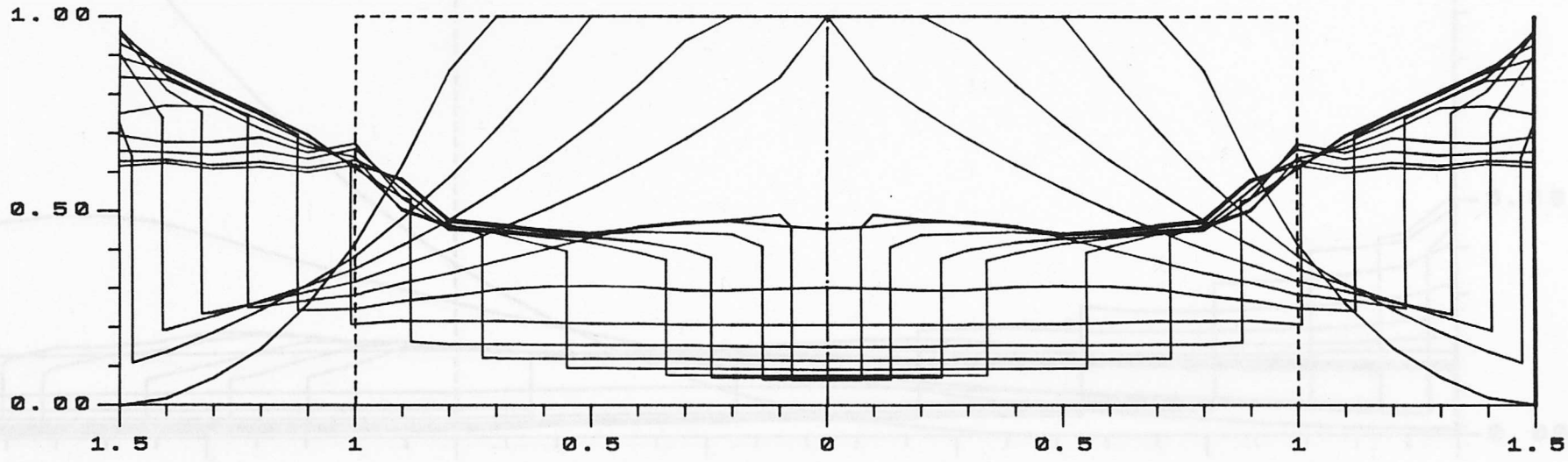


Figure E-3: The shock profiles for $\mathbf{r}_w = 1.5$ and $\mathbf{G_k} = 0.10$

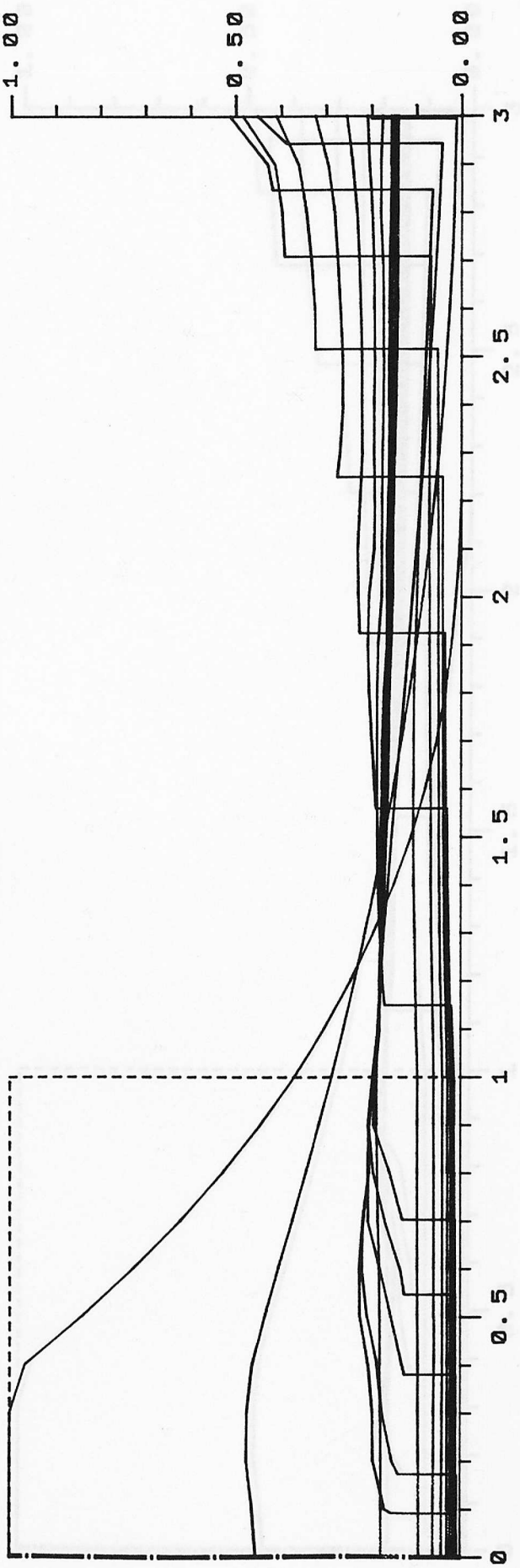


Figure E-4: The shock profiles for $\mathbf{r}_w = 3$ and $\mathbf{G}_\mathbf{k} = 0.01$

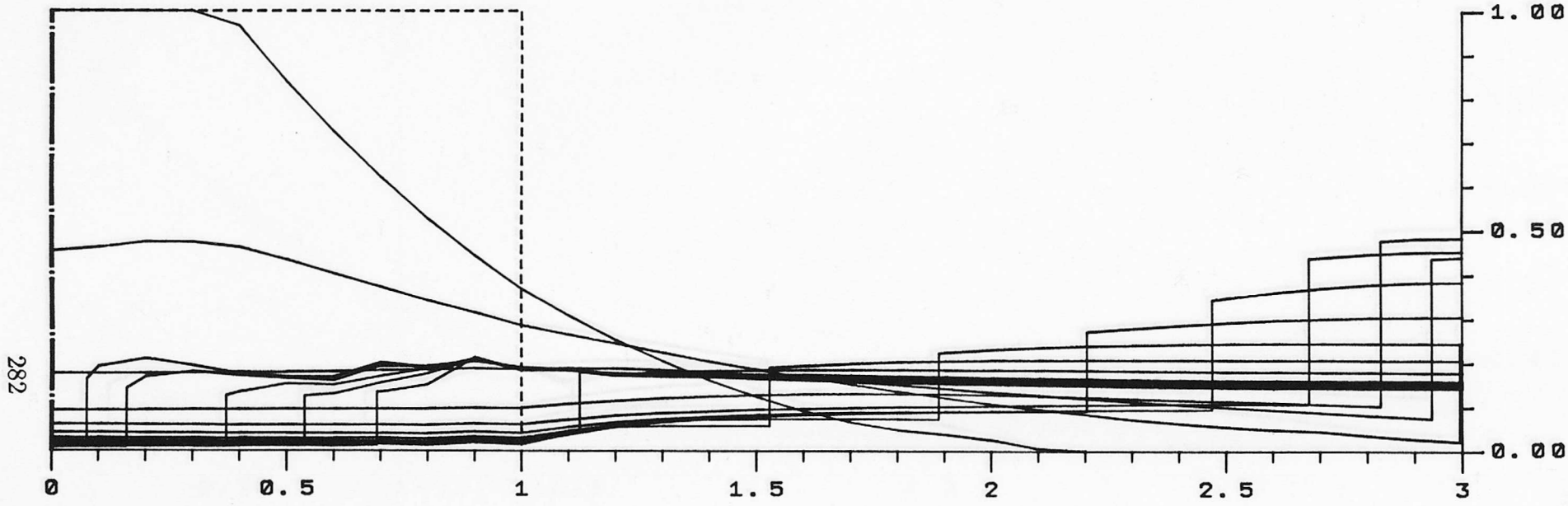


Figure E-5: The shock profiles for $\mathbf{r}_w = 3$ and $\mathbf{G_k} = 0.05$

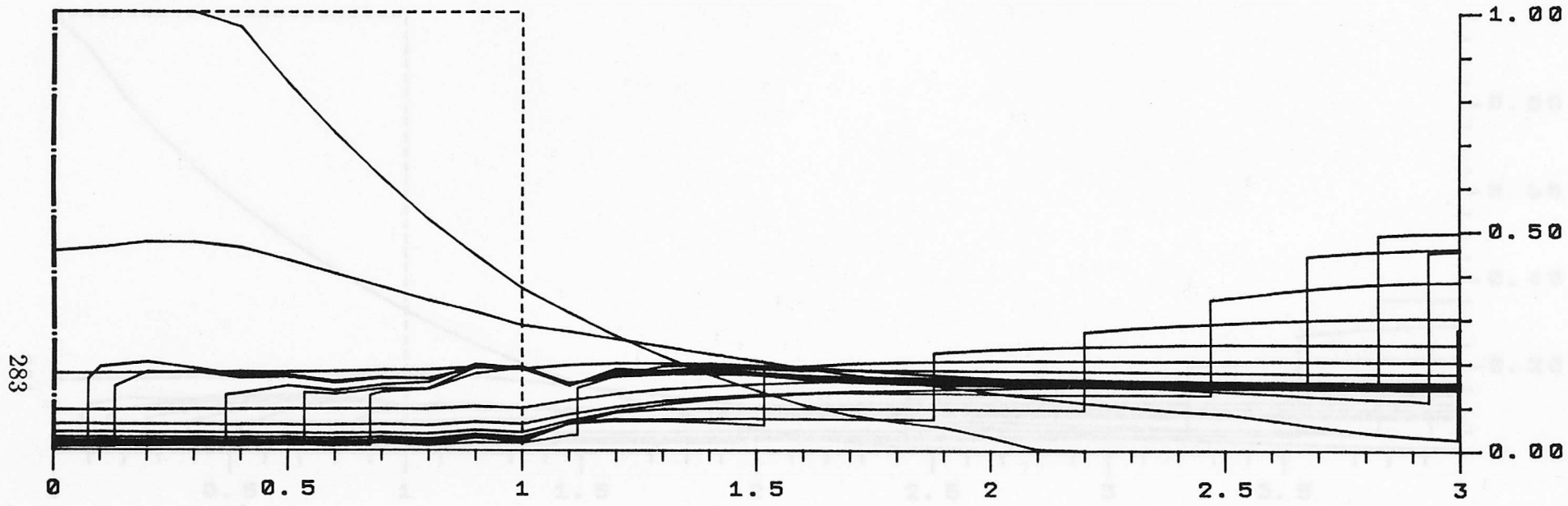


Figure E-6: The shock profiles for $\mathbf{r}_w = 3$ and $\mathbf{G_k} = 0.10$

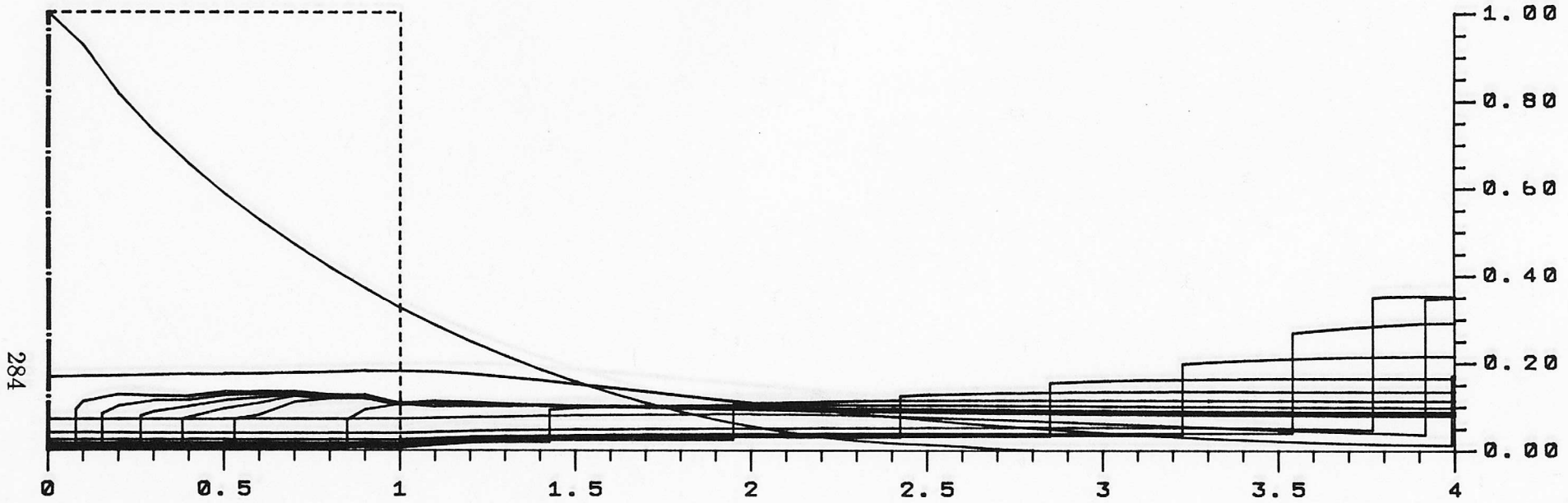


Figure E-7: The shock profiles for $\mathbf{r}_w = 4$ and $\mathbf{G_k} = 0.01$

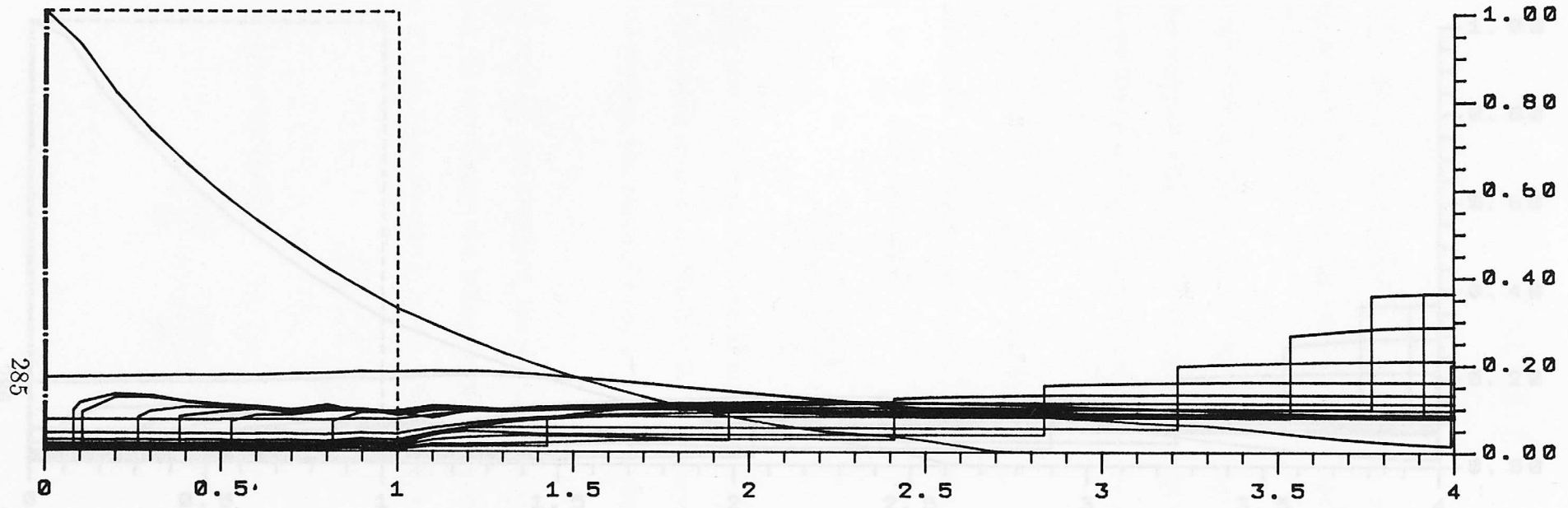


Figure E-8: The shock profiles for $\mathbf{r}_w = 4$ and $\mathbf{G_k} = 0.05$

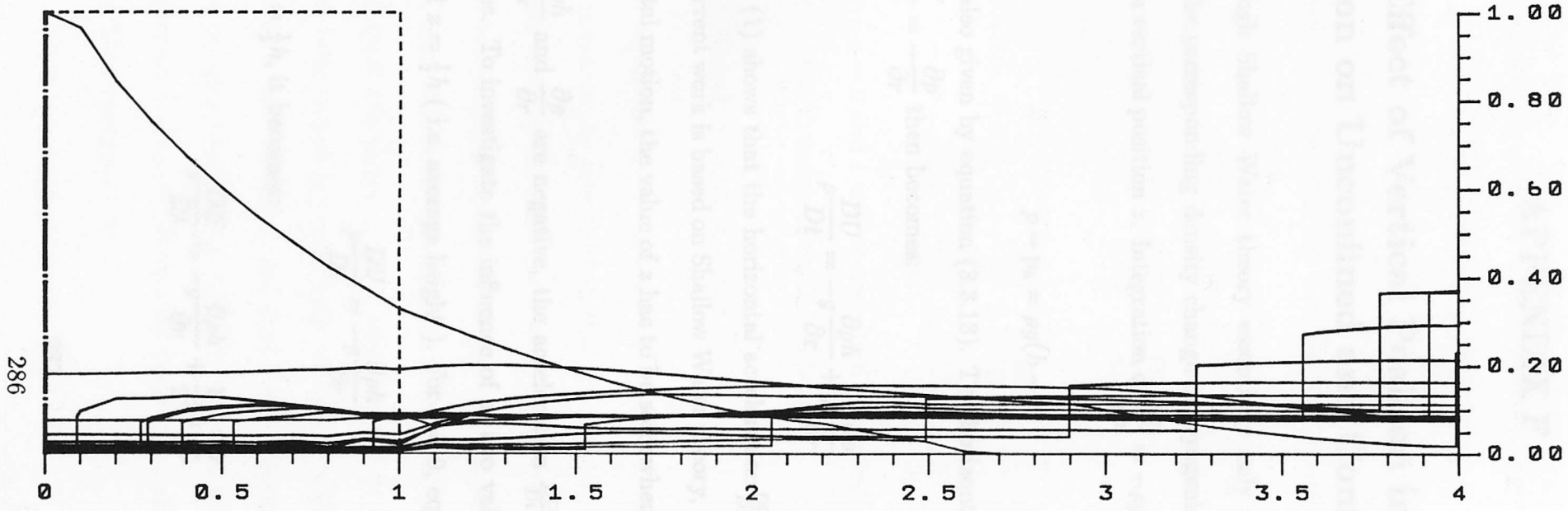


Figure E-9: The shock profiles for $\mathbf{r}_w = 4$ and $\mathbf{G_k} = 0.10$

APPENDIX F

The Effect of Vertical Position in Density-change Region on Unconfined and Confined Flows

Although Shallow Water theory essentially only considers horizontal motion, the corresponding density change in cryogenic liquid flow still introduces a vertical position z. Integration of $\frac{\partial p}{\partial z} = -\rho g$ along z to h results in:

$$p - p_h = \rho g(h - z)$$

which is also given by equation (3.3.13). The horizontal momentum equation $\rho\frac{DU}{Dt} = -\frac{\partial p}{\partial r}$ then becomes:

$$\rho\frac{DU}{Dt} = -g\frac{\partial \rho h}{\partial r} + gz\frac{\partial \rho}{\partial r} \tag{1}$$

Equation (1) shows that the horizontal acceleration $\frac{DU}{Dt}$ still depends on z. As the current work is based on Shallow Water theory, which only considers a horizontal motion, the value of z has to be somewhere between $z = 0$ and $z = h$.

As $\frac{\partial \rho h}{\partial r}$ and $\frac{\partial \rho}{\partial r}$ are negative, the acceleration $\frac{DU}{Dt}$ will decrease when z increases. To investigate the influence of z, two values of z are chosen: $z = 0$ and $z = \frac{1}{2}h$ (i.e. average height). For $z = 0$, equation (1) becomes:

$$\rho\frac{DU}{Dt} = -g\frac{\partial \rho h}{\partial r} \tag{2}$$

and for $z = \frac{1}{2}h$, it becomes:

$$\rho\frac{DU}{Dt} = -g\frac{\partial \rho h}{\partial r} + \frac{1}{2}gh\frac{\partial \rho}{\partial r} \tag{3}$$

The governing equations for the density-change region are:

$$\rho\frac{Dh}{Dt}+\frac{\rho h}{r}\frac{\partial rU}{\partial r}+h\frac{D\rho}{Dt} = 0 \quad (4)$$

$$\frac{1}{\rho}\frac{D\rho}{Dt} = -\frac{K_b}{h} \quad (5)$$

together with equation (2) or (3). The dimensionless forms of the governing equations are:

$$2\frac{DC}{Dt}+C\frac{\partial U}{\partial r}=-\frac{UC}{r}-\frac{C}{\varrho}\frac{D\varrho}{Dt}$$

$$\frac{1}{\varrho}\frac{D\varrho}{Dt}=-\frac{G_k}{C^2}$$

with

$$z=0 \quad : \quad \frac{DU}{Dt}+2C\frac{\partial C}{\partial r}=-\frac{C^2}{\varrho}\frac{\partial \varrho}{\partial r}$$

$$z=\frac{1}{2}h \quad : \quad \frac{DU}{Dt}+2C\frac{\partial C}{\partial r}=-\frac{C^2}{2\varrho}\frac{\partial \varrho}{\partial r}$$

Both cases ($z=0$ and $z=\frac{1}{2}h$) are solved numerically for unconfined and confined flows (with bunds of unlimited height).

Unconfined Flow Case

In Table-I, results are given for G_k=0.01 and 0.10. Although acceleration for $z=0$ is essentially greater than that for $z=\frac{1}{2}h$, the results for $z=0$ do not differ much from those for $z=\frac{1}{2}h$, as shown for both cases; the differences between the vapour-release position r_{vr} and the front position r_f are less than 2%. Note also that for both cases, the mass discrepancy (i.e. total mass calculated − total initial mass) is less than 1%, which means that both results are essentially consistent with mass conservation.

From this it may be concluded that the predictions of the model for unconfined cryogenic liquid flow, which is based on Shallow Water theory, do not significantly depend on vertical position z, and therefore $g\frac{\partial \rho}{\partial r}$ can be omitted from equation (1).

Confined Flow Case with Bunds of Unlimited Height

The most important result for bunds of unlimited height is the value of the maximum liquid height $\mathbf{h}_{w,max}$ at the bund, as for a given bund distance $\mathbf{r}_w$, this gives an indication of the bund height required to prevent overspill. The results calculated for $z = 0$ and $z = \frac{1}{2}h$ are illustrated in Figure 1. Unlike the case of unconfined flow, this one shows a dependency on the value of z. Figure 1 shows that values of $\mathbf{h}_{w,max}$ for $z = 0$ are higher than for $z = \frac{1}{2}h$. As already described, the acceleration for $z = 0$ is higher than that for $z = \frac{1}{2}h$, consequently $\mathbf{h}_{w,max}$ for $z = 0$ is higher as well. However, Figure 1 also shows that, as maybe expected when the bund is relatively far removed from the original tank position, the difference between $\mathbf{h}_{w,max}$ values for both cases is relatively small. For $\mathbf{r}_w \geq 3$, the front region of unconfined flow is dominated by the vapour-release regime. Hence, when the shock height at the bund reaches its maximum, the shock flow is effectively dominated by the vapour-release regime, which governing equation is the same for both cases. The difference is only pronounced for $\mathbf{r}_w \leq 2$. In this case, the vapour-release region at the bund is so narrow that the density-change region dominates the shock flow. Hence, the value of z still affects $\mathbf{h}_{w,max}$ for $\mathbf{r}_w \leq 2$, which is caused by a relatively high density gradient $\frac{\partial \rho}{\partial r}$ near the bund when the shock height reaches its maximum (i.e. $\mathbf{h}_{w,max}$).

The conservative and safest approach is always to consider the worst case, i.e. to consider the highest estimate for the required bund height. Hence, although $\mathbf{h}_{w,max}$ values depend on the value of z, in view of safety and bund design considerations, this work only considers $z = 0$, which gives highest $\mathbf{h}_{w,max}$ values.

Table -I: Results for $z = 0$ and $z = \frac{1}{2}h$ in equation (1)

Vapour-release position $\mathbf{r}_{vr}$

	$z = 0$		$z = \frac{1}{2}h$	
Time	$\mathbf{G_k} = 0.01$	$\mathbf{G_k} = 0.10$	$\mathbf{G_k} = 0.01$	$\mathbf{G_k} = 0.10$
0.20	1.302	1.305	1.302	1.305
0.40	1.707	1.737	1.707	1.723
0.60	1.960	1.915	1.950	1.908
0.80	2.424	2.148	2.397	2.131
1.00	2.734	2.351	2.722	2.333
1.10	2.881	2.443	2.865	2.424
1.20	3.032	2.529	3.022	2.511
1.30	3.191	2.611	3.167	2.596
1.40	3.321	2.694	3.309	2.671
1.50	3.462	2.762	3.443	2.727
1.60	3.605	2.817	3.589	2.795
1.70	3.734	2.886	3.718	2.846
1.80	3.873	2.925	3.851	2.896
1.90	4.004	2.983	3.988	2.932
2.00	4.123	3.007	4.111	2.980

Front position $\mathbf{r}_f$

	$z = 0$		$z = \frac{1}{2}h$	
Time	$\mathbf{G_k} = 0.01$	$\mathbf{G_k} = 0.10$	$\mathbf{G_k} = 0.01$	$\mathbf{G_k} = 0.10$
0.20	1.394	1.382	1.394	1.382
0.40	1.772	1.737	1.771	1.737
0.60	2.141	2.085	2.140	2.081
0.80	2.505	2.430	2.502	2.421
1.00	2.866	2.775	2.861	2.760
1.10	3.045	2.947	3.039	2.930
1.20	3.223	3.121	3.217	3.100
1.30	3.401	3.294	3.393	3.269
1.40	3.579	3.467	3.569	3.439
1.50	3.756	3.641	3.745	3.607
1.60	3.933	3.814	3.920	3.777
1.70	4.110	3.988	4.095	3.946
1.80	4.286	4.162	4.270	4.116
1.90	4.462	4.337	4.444	4.286
2.00	4.638	4.510	4.618	4.456

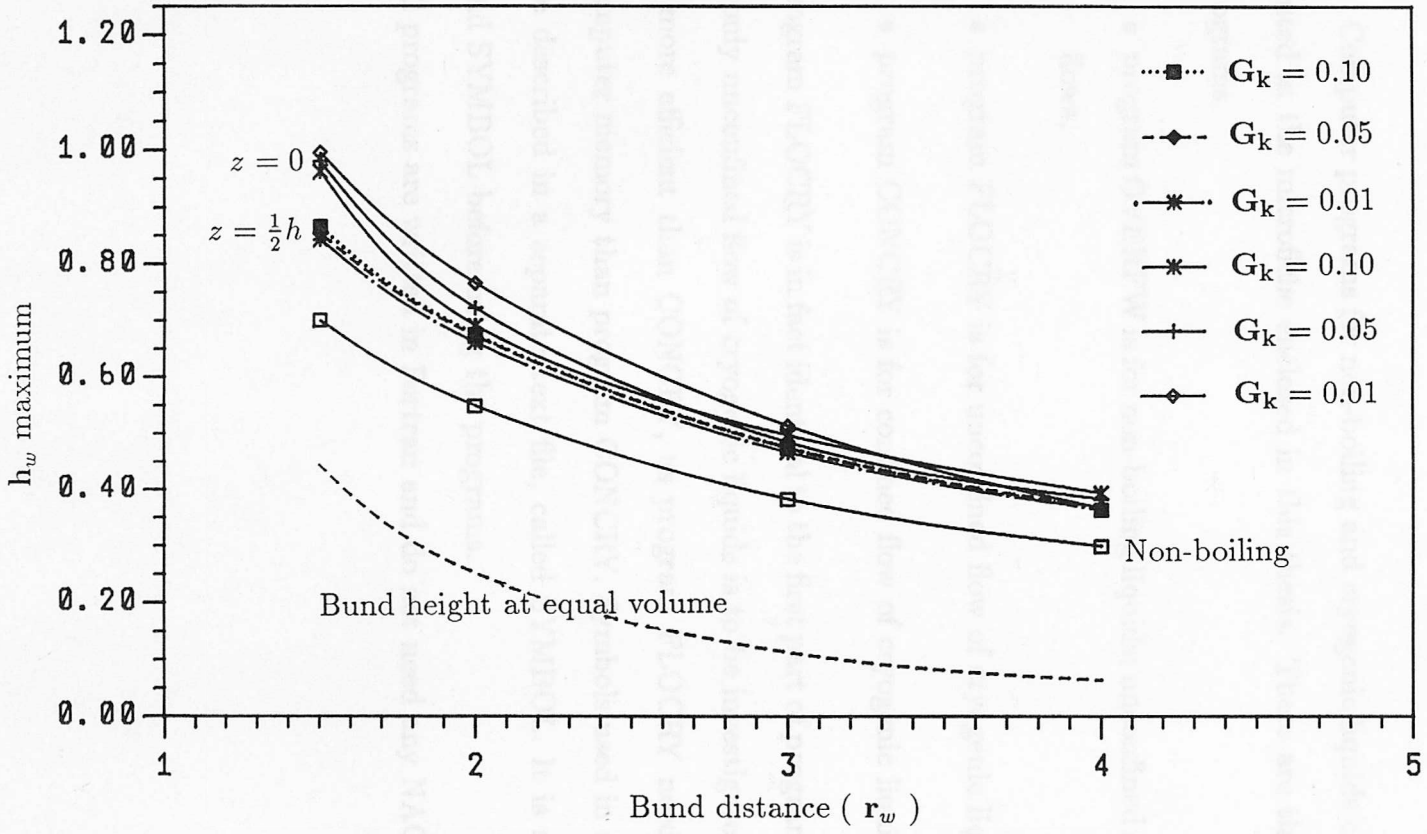


Figure 1: Maximum liquid height at the bund wall

APPENDIX G

COMPUTER PROGRAMS

Computer programs for non-boiling and cryogenic liquids cases are presented in the microfiche enclosed in this thesis. There are three separate programs:

- program OVERFW is for non-boiling liquids; unconfined and confined flows,
- program FLOCRY is for unconfined flow of cryogenic liquids,
- program CONCRY is for confined flow of cryogenic liquids.

Program FLOCRY is in fact identical to the first part of program CONCRY. If only unconfined flow of cryogenic liquids is to be investigated, FLOCRY is more efficient than CONCRY, as program FLOCRY needs much less computer memory than program CONCRY. Symbols used in all programs are described in a separate text file, called SYMBOL. It is suggested to read SYMBOL before using the programs.

All programs are written in Fortran and do not need any NAG Library.

BRITISH LIBRARY

ETHOS

Boston Spa, Wetherby
West Yorkshire, LS23 7BQ
www.bl.uk

The following page has been copied from microfiche.

This is the best copy available.

U.L.C.C. MICROFICHE
UMECB72 BUBZ
90/12/10 21.14.37

COMPUTER PROGRAMS

